



The
University
Of
Sheffield.

**Tribological characteristics of the wheel-rail interface
with the evolution of surface topography**

Shinya Fukagai

Thesis submitted for the degree of Doctor of Philosophy

The University of Sheffield
Faculty of Engineering
Department of Mechanical Engineering

30 June 2021

SUMMARY

The margin of safety for wheel climb-up derailments decreases with an increase of friction coefficient between the wheel flange and the rail. In order to reduce the risk of derailment, it is important to keep the friction coefficient low. Derailment accidents have sometimes been observed within a relatively short running distance after wheel re-profiling, and an increase in the friction coefficient is suspected to be a contributing factor. However, the relationship between these surface conditions and the friction coefficient has not been fully understood.

The aim of this work was to reduce the incidence of climb-up derailments and further improve railway safety. This required a better understanding of the tribological mechanisms at the wheel-rail interface just after wheel re-profiling. A range of test approaches (small-scale twin-disk and high-pressure torsion (HPT) and full-scale wheel/rail interface) and novel measurement techniques have made this possible.

The twin-disk tests, simulating a freshly machined wheel, revealed how the friction coefficient rises during the running-in period. The running-in curve of the friction coefficient showed a momentary rise and a peak value was observed to decrease with the increase in magnitude of the wheel surface texture. The change of the subsurface hardness and the microstructure were also dependent on the initial surface texture coincidentally and the work-hardening layer of the textured surface was thicker than that of a smooth surface.

The application of ultrasound reflectometry to a sliding interface enabled the in-situ evaluation of contact stiffness changes. A contact pressure representative of that in a wheel-rail interface was achieved by using a high-pressure torsion (HPT) test approach. The dynamic change of contact stiffness was found to be dependent on the initial surface topography, indicating that the friction mode can be different. The change of the friction coefficient during the repeated sliding tests was in general agreement with the trend of the twin-disk tests, and the dynamic evaluation of the contact stiffness provided a more detailed understanding of the interfacial change during the running-in process. The micro-fracture of the surface at low initial roughness and the plastic deformation of the

asperities at high initial roughness are considered to be the dominant factors to the running-in.

Tests with the full-scale rig enabled understanding of the changes in the running-in process in the actual wheel-rail contact. The ultrasound measurements using an arrayed probe provided the change of the contact stiffness distribution in the contact area. The change of the mean value of contact stiffness showed a similar trend to the HPT tests. In the tests with the re-profiled wheels, it was possible to understand the friction coefficient increase characteristics with the deformation of the machining marks.

The above test results indicated that the increase in the friction coefficient is due to the temporary stiffer contact conditions at the interface. Therefore, it was thought that the lubrication of the wheel flange just after the wheel re-profiling would be effective in preventing the wheel climb-up derailment, as the friction coefficient could be high when clean metal surfaces are exposed by machining.

CONTENTS

Summary	i
Contents.....	iii
Acknowledgement	vii
1 Introduction.....	1
1.1 Background.....	1
1.2 Aims and objectives	1
1.3 Novelty and impact.....	2
1.4 Thesis layout	2
References.....	6
2 Literature Review	7
2.1 Outline	7
2.2 Wheel-rail contact.....	7
2.2.1 Railway wheel and rail	7
2.2.2 Contact position and contact condition.....	9
2.2.3 Traction (Creep) force	11
2.3 Flange climb-up derailment	12
2.3.1 Types of derailments	12
2.3.2 Typical mechanisms of flange climb derailment.....	14
2.3.3 Case studies of derailment just after wheel re-profiling.....	17
2.4 Running-in phenomenon.....	22
2.4.1 Model for running-in	22
2.4.2 Roughness parameters to evaluate the surface geometry during running-in..	25
2.4.3 Running-in behaviour of the wheel-rail contact	25
2.5 Experimental measurement of the wheel-rail interface	34
2.6 Ultrasound reflectometry	40
2.6.1 Acoustic impedance and reflection coefficient.....	40
2.6.2 Spring model.....	40
2.6.3 Evaluation for wheel-rail contact.....	42
2.7 Summary.....	48
References.....	50
3 Understanding the change of friction coefficient and surface condition after wheel re-profiling	56
Abstract.....	56
3.1 Introduction.....	56

3.2	Methodology.....	58
3.2.1	Apparatus.....	58
3.2.2	Test disks.....	59
3.2.3	Test procedure	60
3.3	Results	62
3.3.1	Effect of initial surface texture on traction coefficient	62
3.3.2	Surface texture	63
3.3.3	Hardness.....	66
3.3.4	Metallic structure.....	66
3.3.5	Amount of wear particle.....	69
3.3.6	Chemical composition.....	69
3.4	Discussion	71
3.5	Conclusions.....	74
	References.....	75
	Appendix A.....	77
4	In-situ evaluation of a sliding interface with different roughness conditions using ultrasound reflectometry.....	78
	Abstract.....	78
4.1	Introduction.....	79
4.2	Methodology.....	80
4.2.1	HPT testing equipment.....	80
4.2.2	Ultrasonic measurement.....	83
4.2.3	Specimens	85
4.2.4	Test procedure	88
4.2.5	Numerical simulation	88
4.3	Results	91
4.3.1	Change in the contact stiffness during normal force loading.....	91
4.3.2	Change in the contact stiffness under tangential force	91
4.3.3	Change in the contact stiffness during normal force unloading	94
4.3.4	Change in the roughness profile after the cycle	95
4.3.5	Comparison of experimental and numerical simulation results	98
4.4	Discussion	101
4.5	Conclusions.....	105
	References.....	106
5	Transition of the friction behaviour and interface topography due to repeated high-pressure contact and sliding.....	110
	Abstract.....	110
5.1	Introduction.....	110

5.2	Methodology.....	112
5.2.1	HPT testing equipment.....	112
5.2.2	Ultrasonic measurement.....	113
5.2.3	Specimens.....	115
5.2.4	Test procedure.....	117
5.3	Results.....	119
5.3.1	Topography dependence on contact stiffness and friction coefficient during running-in.....	119
5.3.2	Contact pressure dependence on contact stiffness and friction coefficient during running-in.....	121
5.3.3	Change in the surface roughness during repetitive cycles.....	123
5.4	Discussion.....	126
5.5	Conclusions.....	129
	References.....	131
	Appendix B.....	134
6	Applying the evaluation technique using ultrasound reflectometry to the actual wheel-rail interface.....	140
	Abstract.....	140
6.1	Introduction.....	140
6.2	Methodology.....	142
6.2.1	Full-scale dynamic wheel/rail rig.....	142
6.2.2	Ultrasound technique.....	144
6.2.3	Test rail and wheel.....	146
6.2.4	Test procedure.....	148
6.3	Results.....	149
6.3.1	Change of traction coefficient with cyclic rolling.....	149
6.3.2	Change of contact stiffness with cyclic rolling.....	150
6.3.3	Change of surface topography with cyclic rolling.....	153
6.4	Discussion.....	158
6.5	Conclusions.....	162
	References.....	163
7	Influence of initial roughness of re-profiled wheels on friction coefficient.....	166
	Abstract.....	166
7.1	Introduction.....	166
7.2	Methodology.....	168
7.2.1	Full-scale rig.....	168
7.2.2	Ultrasound technique.....	170
7.2.3	Test rail and wheel.....	172

7.2.4	Test procedure	173
7.3	Results	174
7.3.1	Change of traction coefficient with cyclic rolling.....	174
7.3.2	Change of contact stiffness with cyclic rolling.....	175
7.3.3	Change of surface topography with cyclic rolling.....	176
7.4	Conclusions.....	177
	References.....	178
8	Discussion.....	180
8.1	Test conditions for contact stiffnesses evaluation.....	180
8.2	Relationship between contact stiffness and friction coefficient	181
8.2.1	Test 1: HPT.....	181
8.2.2	Test 2: FSR at Sheffield.....	183
8.2.3	Test 3: FSR at RTRI.....	185
8.2.4	General trend.....	187
8.3	Recommendation to the practical operation	188
	References.....	190
9	Conclusions	191

ACKNOWLEDGEMENT

Firstly, I would like to express my deep and sincere gratitude to my research supervisor, Professor Roger Lewis. It was a great honor to study under his guidance. My special thanks go to my secondary supervisor, Professor Matthew B. Marshall who gave me very thoughtful advice on how to understand and explain a phenomenon. I would like to take this opportunity to thank my examiners, Professor David Fletcher and Professor Alejandro Toro, for valuable comments and suggestions.

I spent 2017 and 2018 at the University of Sheffield (UoS) and had a great time studying about the wheel-rail tribology and research into "Tribo-Acoustic". This experience has developed me professionally and personally. I would like to express my deepest gratitude to the management of Railway Technical Research Institute (RTRI) for this opportunity and financial support.

I would also like to thank the academic staff and my fellow PhD students at UoS and my colleagues at RTRI for their friendship and input in the completion of this work.

Finally, I am very grateful to my family, Mari, Akari and Madoka for their understanding and continuous support to complete this research.

1 INTRODUCTION

1.1 Background

Among railway accidents, derailments involve the risk of losing many lives and must be avoided. To prevent derailment accidents due to faults of the train or track, such as melting damage of the axle, cracking of the bogie frame, and rail breakage, railway operators make inspection and maintenance a day-to-day task. However, derailments rarely occur even in the absence of special faults in the vehicle and track. This type of accident is mainly caused by the combination of multiple factors in a vehicle, track, or operation, coming together to cause a derailment phenomenon called “flange climb-up” derailment (see Fig. 1-1 [1]), which is unique to railways.

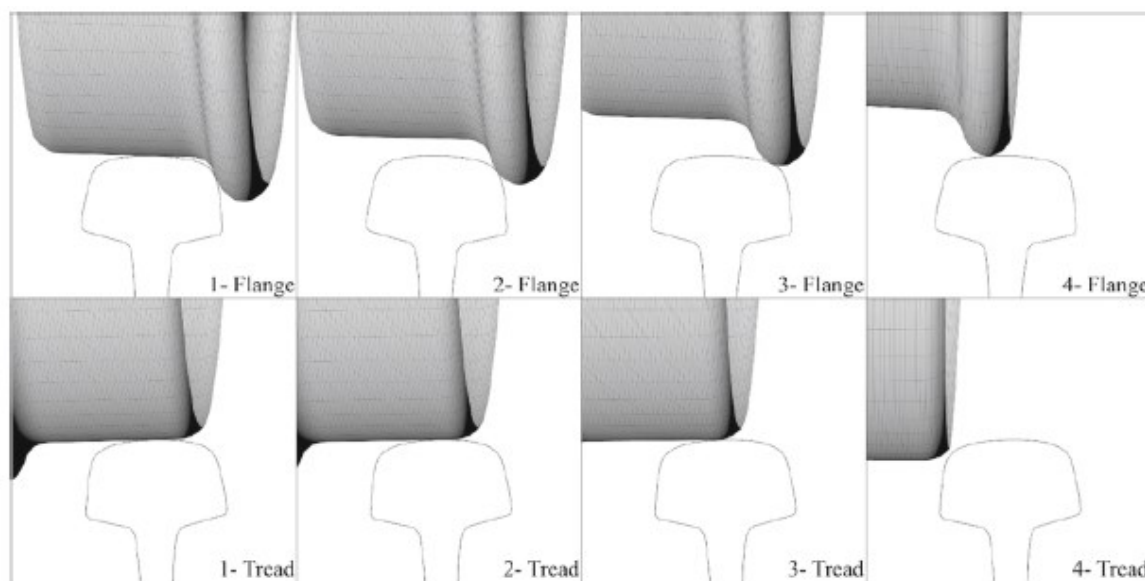


Fig. 1-1 Motion of both wheels during flange climb derailment predicted using a multi-body system model [1].

Every time a flange climb-up derailment occurs, the causes have been investigated and some measures taken to reduce future occurrences. As a result, the number of accidents has been decreasing, but the accidents still occur, even though rarely. In particular, it is known that derailments occur relatively soon after wheel re-profiling. The friction coefficient between wheel and rail is a parameter that has a significant influence on derailment, and one possibility is that the surface geometry of the wheel after wheel re-profiling is related to its friction coefficient, but their causal relationship is unknown.

1.2 Aims and objectives

This study was aimed at reducing the accident of climb-up derailments and further improving the safety of the railway. The climb-up derailment phenomenon is considered to occur when the balance between the frictional force (adhesion) between the wheel

flange and the rail, which is the source of the railway's traction force, is out of a certain range. In addition, the balance may become unstable, especially just after the wheel is re-profiled. To improve the safety of the railway, further basic knowledge on tribological mechanisms at the wheel-rail interface just after wheel re-profiling is necessary. Therefore, the objectives of this study were as follows;

- ◆ Experimental reproduction of the change in friction coefficient after wheel re-profiling
- ◆ In-situ measurement of the change in contact condition due to friction between wheel and rail
- ◆ Evaluation of the influence of surface topography on friction
- ◆ Development of hypotheses for the change in friction coefficient
- ◆ Recommendations for practical wheel management

1.3 Novelty and impact

Most of the studies on the frictional behaviour of the running-in process relate to lubricated interfaces, and few studies have focused on dry conditions. In addition, this study applies an ultrasonic evaluation technique to the in-situ measurement of wheel-rail contact conditions. While this has been used before, the relationship between the contact conditions obtained by ultrasound and frictional behaviour (static through to dynamic) has not been investigated so far.

Some railway operators apply oil to the wheel flanges just after re-profiling intending to stabilize the running-in process. However, oil and other lubricants still include the risk of crashes due to sliding. On the other hand, some railway operators set a standard value for roughness after wheel re-profiling and manage it so that the roughness will be less than the standard value in order to prevent climb-up derailment after re-profiling. However, it is not clear how surface roughness affects the friction coefficient in the first place. Therefore, understanding the change in the friction coefficient after wheel re-profiling and the factors that contribute to it will provide railway operators with an indication of appropriate surface treatment to prevent derailment.

1.4 Thesis layout

This thesis describes the frictional behaviour of a railway wheel during the running-in process. This thesis consists of seven chapters, the flow is as shown in Figs. 1-2. The main studies are Chapters 3 to 5, which were published individually as journal papers and conference papers. Table 1-1 shows the list of published papers included in this thesis and highlights the contributions made by the authors.

Chapter 1 is the introduction, which describes the background, the aims and objectives, the novelty and impact and the layout of this thesis.

Chapter 2 is the literature review, which describes the wheel-rail contact, the flange climb-up derailment, the running-in phenomenon, the experimental measurement of the wheel-rail interface and the ultrasound reflectometry.

The published/to be published papers that make up the main body of this thesis are divided into three parts.

Chapter 3 [2] belongs to the first part, which describes work done to understand the change of friction coefficient and surface condition after wheel re-profiling. In this study, rolling-sliding tests were conducted with a twin-disk machine and specimens which simulated wheel flange-rail gauge corner contact. The change of friction coefficient, surface topography, hardness and metallurgical structure during running-in, and the effect of initial surface topography were investigated.

Chapter 4 [3] and Chapter 5 [4] belong to the second part, which describes an evaluation of the transition of the slip interface during the running-in using ultrasound reflectometry. In this study, high-pressure torsion (HPT) tests were conducted, and the contact stiffness between the specimens was evaluated using ultrasound technique during the tests. The dynamic change of contact stiffness was found to be dependent on the initial surface topography, indicating that the friction mode can be different [3]. The running-in behaviour of friction coefficient and contact stiffness were investigated [4].

Chapter 6 [5] and Chapter 7 [6] belong to the third part which describes the application of ultrasound reflectometry to the actual wheel-rail interface. In this study, full-scale wheel-rail contact tests were conducted, and the contact patch and contact stiffness distributions at the actual wheel-rail interface were evaluated using the ultrasound technique during the tests. The dynamic measurement of the wheel-rail contact patch, running-in behaviour in the rolling-sliding contact patch [5] and evolution of surface topographies of the re-profiled wheel were investigated [6].

Chapter 8 is the discussion of this thesis in which the different strands are brought together and links, trends and mechanisms are described. Based on the findings, recommendations for practical operation are made.

Chapter 9 contains the concluding remarks and future challenges.

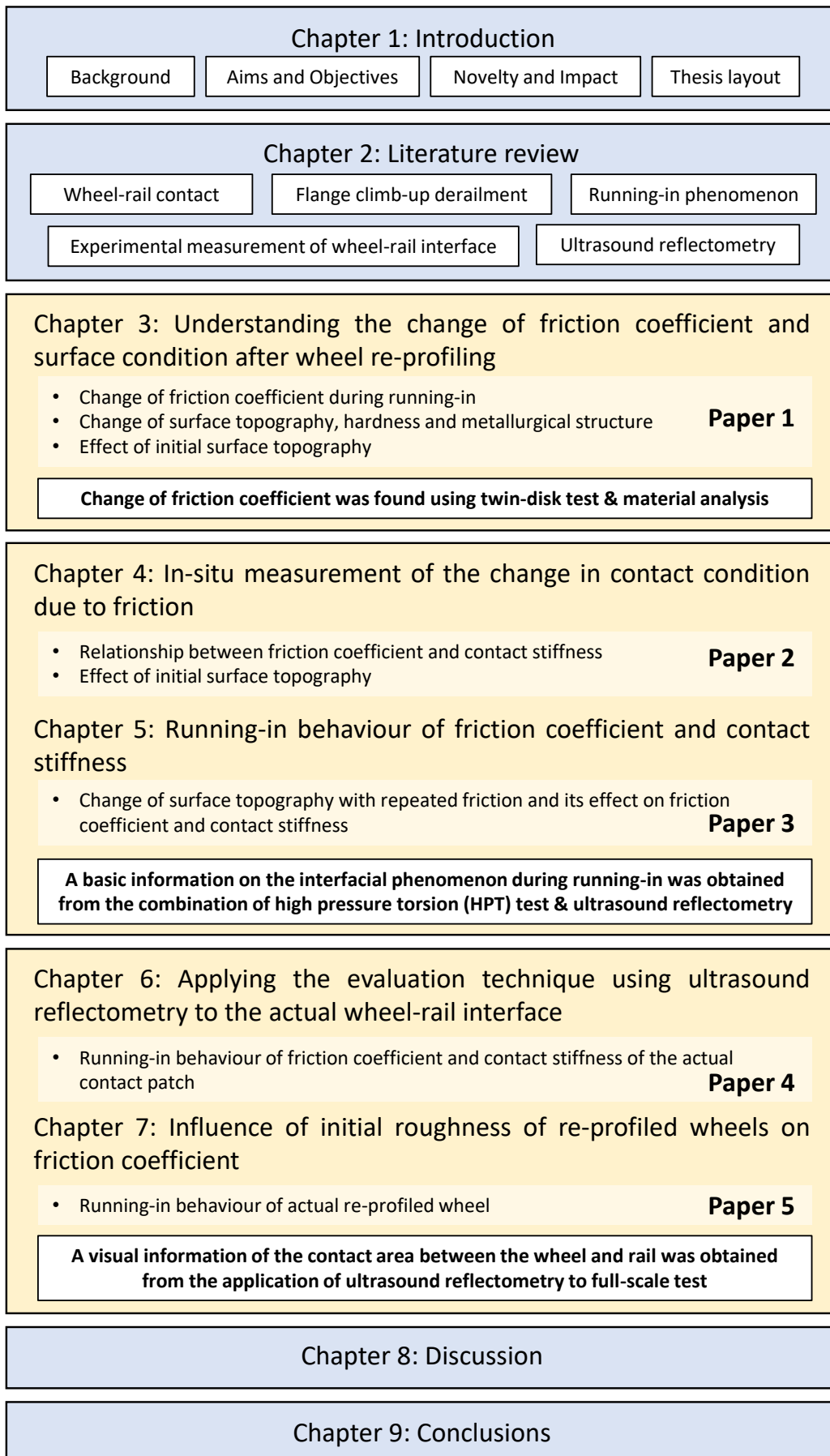


Fig. 1-1 Thesis layout.

Table 1-1 List of papers included in chapters in this thesis

ID	Title	Contribution
1 [2]	Tribological aspects to optimize traction coefficient during running-in period using surface texture	First author. The co-authors supported in one of the material analyses and in some of the discussion.
2 [3]	In-situ evaluation of a sliding interface with different roughness conditions using ultrasound reflectometry	First author. The co-authors supported in the numerical analysis, some of the methodology and the discussion.
3 [4]	Transition of the friction behaviour and interface topography due to repeated high-pressure contact and slideing	First author. The co-authors supported in some of discussion.
4 [5]	Transitions in rolling-sliding wheel/rail contact condition during running-in	First author. The co-authors supported in some of the methodology and the discussion.
5 [6]	Traction condition between wheel flange and rail gauge corner during running-in	First author. The co-author supported in some of the discussion.

References

- [1] J. J. O'Shea and A. A. Shabana, "Analytical and numerical investigation of wheel climb at large angle of attack," *Nonlinear Dyn.*, vol. 83, no. 1–2, pp. 555–577, 2016.
- [2] S. Fukagai, L. Ma, and R. Lewis, "Tribological aspects to optimize traction coefficient during running-in period using surface texture," *Wear*, vol. 424–425, no. January, pp. 223–232, 2019.
- [3] S. Fukagai, M. Watson, H. P. Brunskill, A. K. Hunter, M. B. Marshall, and R. Lewis, "In-situ evaluation of a sliding interface with different roughness conditions using ultrasound reflectometry," *Submitt. to Proc. R. Soc. A*, 2021.
- [4] S. Fukagai, M. B. Marshall, and R. Lewis, "Transition of the friction behaviour and interface topography due to repeated high-pressure contact and slide," *To be Submitt.*
- [5] S. Fukagai, H. P. Brunskill, A. K. Hunter, R. S. Dwyer-Joyce, and R. Lewis, "Transitions in rolling-sliding wheel/rail contact condition during running-in," *Tribol. Int.*, vol. 149, no. August 2018, p. 105679, 2020.
- [6] S. Fukagai and R. Lewis, "Traction Condition between Wheel Flange and Rail Gauge Corner during Running-in," in *Railway Engineering 2019*, 2019.

2 LITERATURE REVIEW

2.1 Outline

In this doctoral thesis, an increase in the coefficient of friction, which remains an undetermined factor in the occurrence of flange climb derailment, was studied. For this purpose, the literature review first addressed basic contact behaviours such as wheel-rail contact position, contact state and traction (creep) force. Subsequently, the mechanisms and actual cases of flange climb derailment, one of the many types of derailment in railways, were investigated.

The running-in phenomenon related to interacting surfaces was investigated from the general behaviour of mechanical elements to the interface between the wheel and rail, since it was noted that flange derailment tends to occur relatively often in a short distance after wheel re-profiling.

Finally, to understand the running-in process of the wheel-rail interface, experimental evaluation methods for assessing changes in the contact condition were investigated. In particular, the direct evaluation method for the wheel-rail interface using ultrasonic waves was investigated and its usefulness was reviewed.

2.2 Wheel-rail contact

2.2.1 Railway wheel and rail

The railway wheel and the rail play vital roles in rail operation, such as bearing the vehicle load, guiding the vehicle and transmitting the driving and braking forces. Therefore, these components are considered to be the most safety-conscious of all the components of a railway.

Figure 2-2-1 shows a simplified configuration of the wheelset. The wheelset of a railway vehicle consists of a single round axle with wheels mounted on both sides by press fits. Bearings are located at both ends of the axle to maintain the smooth rotation of the wheels. The part where the bearings are located is called the journal. On the other hand, wheels of the same shape are located back to back at symmetrical positions on both sides of the axle.

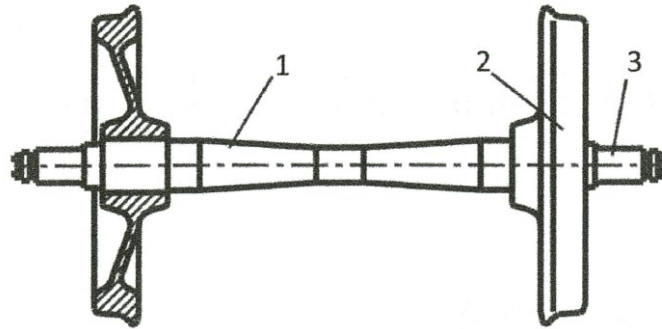


Fig. 2-2-1 Simplified configuration of the wheelset. (1) Axle; (2) Wheel; (3) Journal [1].

The wheels roll on the rails, and this rolling surface is called the tread, and the part that guides the wheelset between two rails is called the flange. Figure 2-2-2 shows a typical cross-sectional view of a wheel on a rail, with each component named. This is shown here with reference to the British Rail standard rail, BS113A [2].

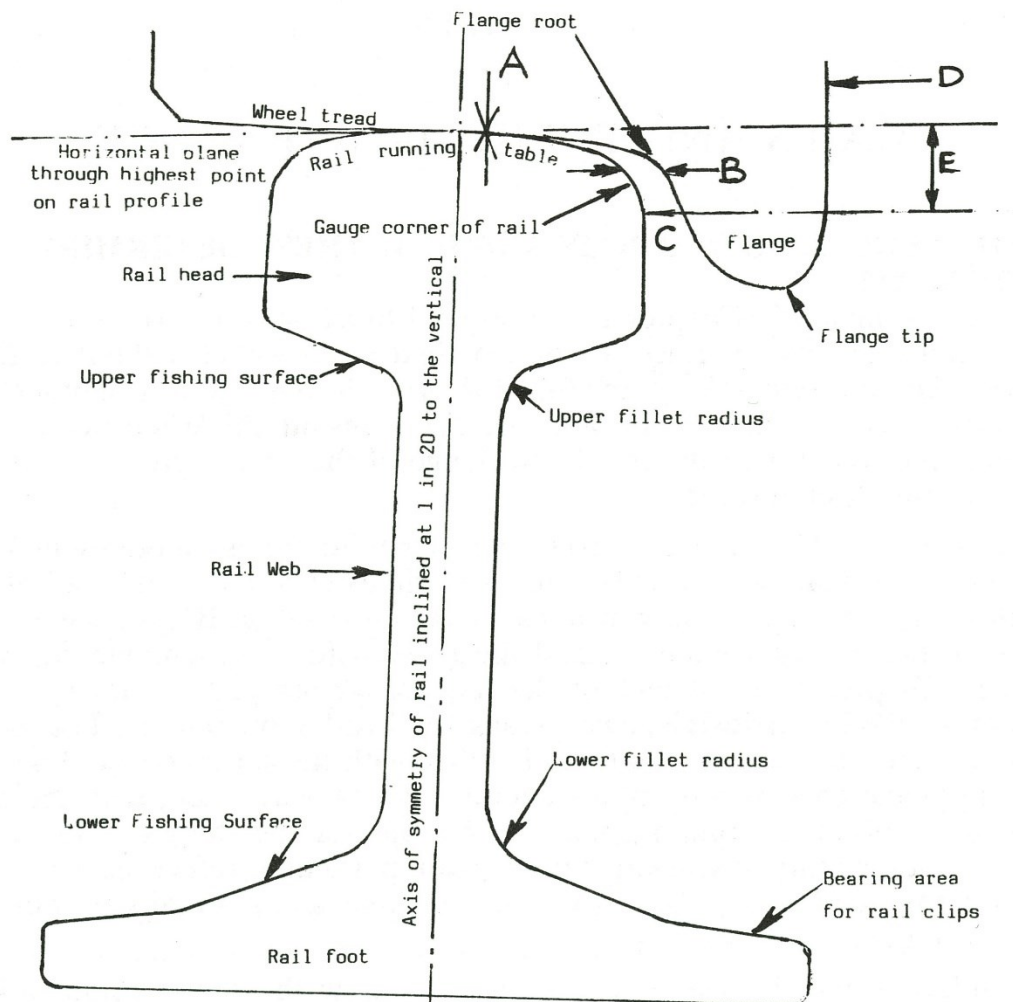


Fig. 2-2-2 Typical cross-sectional view of a wheelset on the track, with each component named. This is shown here with reference to the British Rail standard rail, BS113A [2].

2.2.2 Contact position and contact condition

As is well known, a wheel tread has a taper in the axle direction. When running on a straight track, the wheel tread makes contact with the rail head (Fig. 2-2-3 (a)). If there is a difference in angle between the longitudinal direction of the rail and the direction of travel, which is commonly referred to as the angle of attack, due to various forces applied to the vehicle, the taper acts to reduce the angle and helps the motion to reach a stable equilibrium state. On the other hand, when running on a curved track, the wheel diameter of a wheel rolling on the low rail (the inner rail of the curve) will be lower than that on the high rail (the outer rail of the curve). Hence, if the radius of curvature is large to some extent, the difference in wheel diameter should compensate for the difference in length between the high and low rail and can turn smoothly. However, when running on sharp curves or turnouts, the difference in wheel diameters shortage, and the wheel flange contacts the gauge corner of the high rail and guides the vehicle as it travels (Fig. 2-2-3 (b)), resulting in significant slip in the contact area.

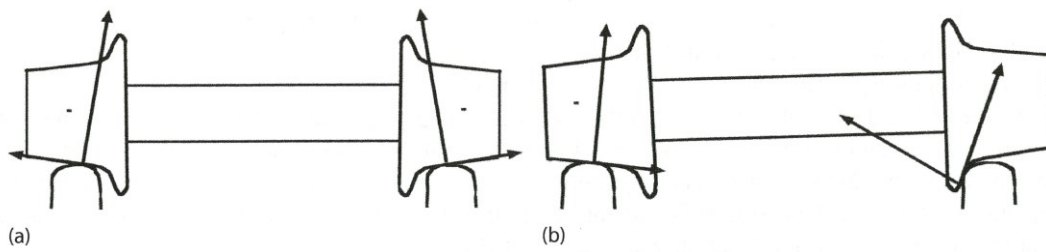


Fig. 2-2-3 Schematics of contact position and acting forces on wheelset in (a) a straight section (central position) and (b) a curve section (laterally displaced position) [1].

Figure 2-2-4 shows the calculated results of contact patches between a wheelset and rails using measured geometrical data [3]. In general, the contact ellipse between the wheel flange and rail gauge is elongated in the direction of the rail compared to that of the wheel tread and rail head due to the difference in the curvature of rail in the direction of sleeper, and the specific contact shape generates the higher contact pressure. Also, the differences in contact position affect the slipping velocity and thus the wear pattern. Figure 2-2-5 shows the wear map which has been laid over some predicted wheel-rail contact conditions. The correlation between the wear patterns, such as mild, severe and catastrophic wear, and contact conditions, such as contact pressure and sliding velocity, which are dependent on the contact position, are expressed.

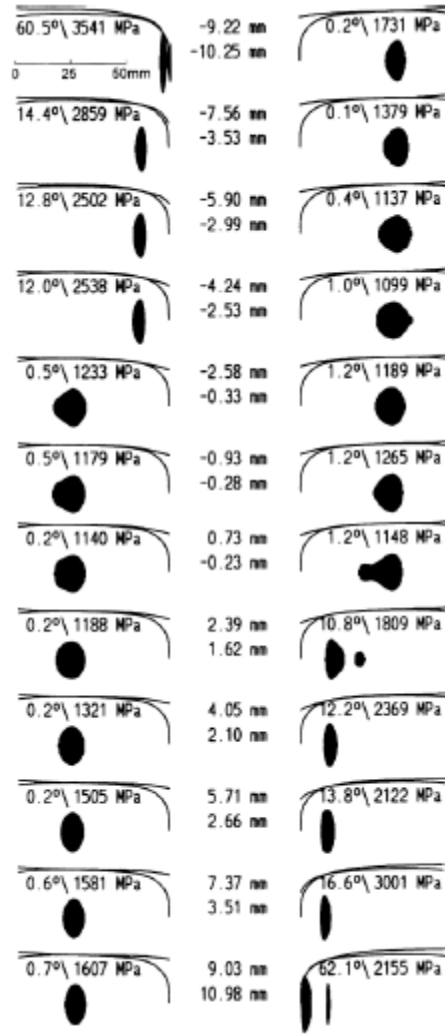


Fig. 2-2-4 Calculated contact patches for measured wheelset and track under normal load 105 kN [3].

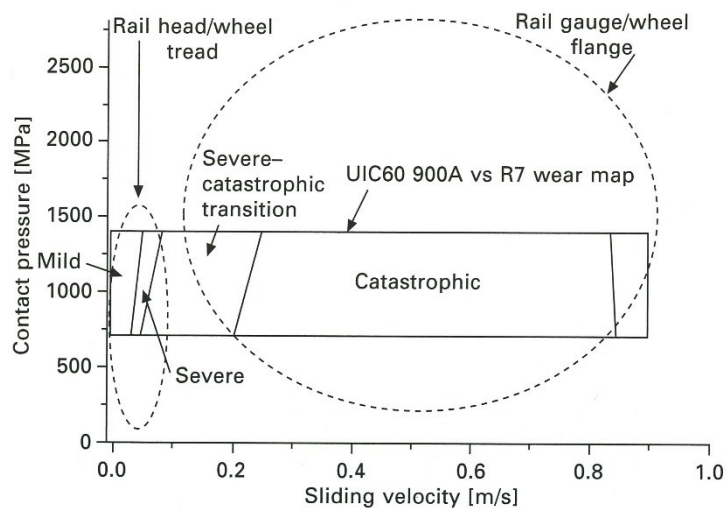


Fig. 2-2-5 Wear map which has been laid over some predicted wheel-rail contact conditions [4].

2.2.3 Traction (Creep) force

When the wheel actually rolls on the rails to generate the driving and braking forces, there is a small slip between the wheel and rail. This small slip is called creep. Creep (traction) forces increase with creep, but above a certain level, it shows a saturation trend. Figure 2-2-6 shows a schematic relationship between the creep and creep force [4]. There is a mixture of stick area and slip area in the contact patch and creep force is the sum of the tangential force or frictional force of the stick and slip areas [5]. As the creep increases, the stick area gradually decreases and the slip area increases. The creep force is considered to be a dynamic friction force when the whole contact area is fulfilled with the slip area. Therefore, the saturation trend is that the creep force tends to approach the dynamic friction force, in other words it can be said that the creep force does not exceed the dynamic friction force.

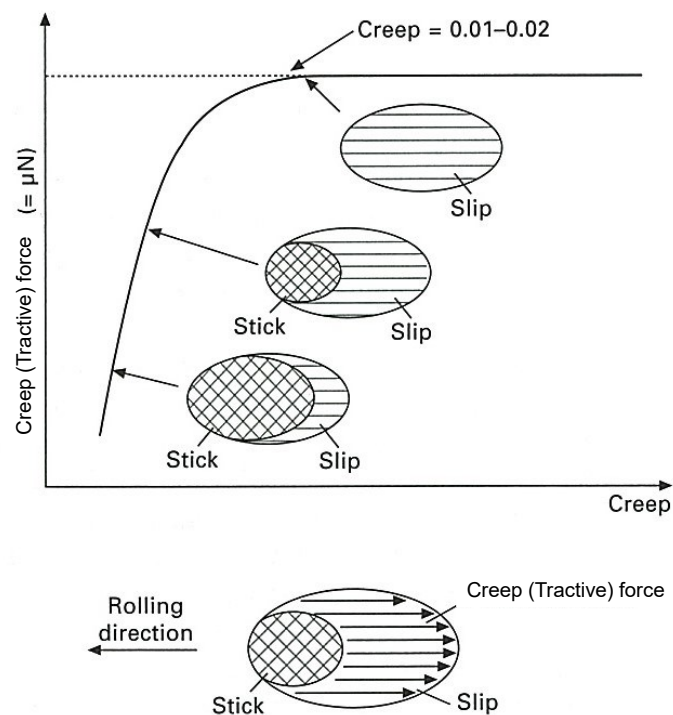


Fig. 2-2-6 Schematic relationship between the creep and creep force [4] (with some minor revisions).

Creep is determined for each direction, such as longitudinal and lateral, and affected by the wheel radius, contact angle, wheel yaw angle (angle of attack), roll angular velocity and the wheel-rail contact position. As an example, Fig. 2-2-7 shows the relationship between the angle of attack and the f_x/N or f_y/N at a high rail (f_x , f_y and N denote the longitudinal, lateral creep forces and normal force respectively) [6]. It can be found that f_x/N decreases with the angle of attack, while f_y/N increases with angle of attack. This indicates a decrease in turning performance as the angle of attack increases.

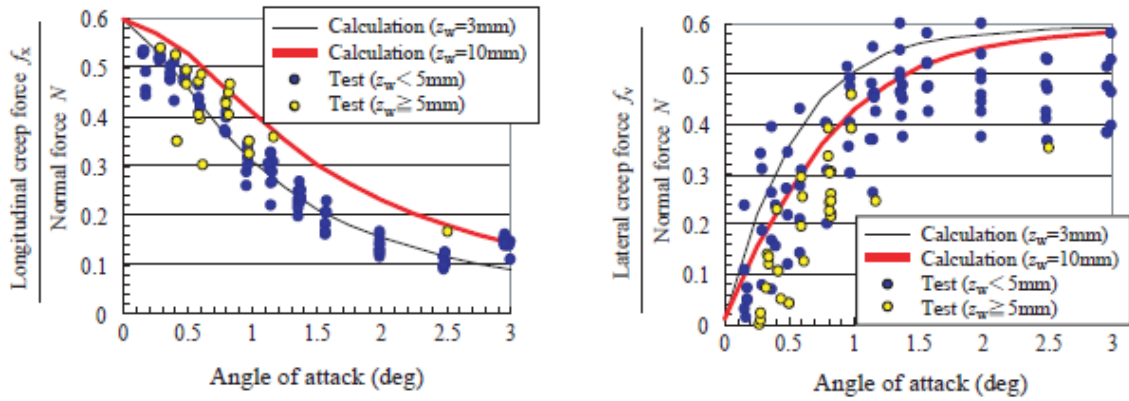


Fig. 2-2-7 Relationship between the angle of attack and the f_x/N or f_y/N at the high rail [6]. The data were obtained using a testing machine with a full-scale axle and a rollers rig of 1600 mm diameter. It can be seen that f_x/N decreases with the angle of attack, while f_y/N increases with angle of attack.

2.3 Flange climb-up derailment

2.3.1 Types of derailments

Derailments due to loss of lateral guidance at the wheel-rail interface can be categorized into three major mechanisms based on how the wheel-rail lateral restraint is lost [1]:

1. Flange climb derailment - A type of derailment in which the wheel climbs the railhead by itself and runs further down the field side of the rail as shown in Fig. 2-3-1. Flange climbing derailments typically occur when the lateral force of the wheel is high and the vertical force of the flanging wheel is reduced.

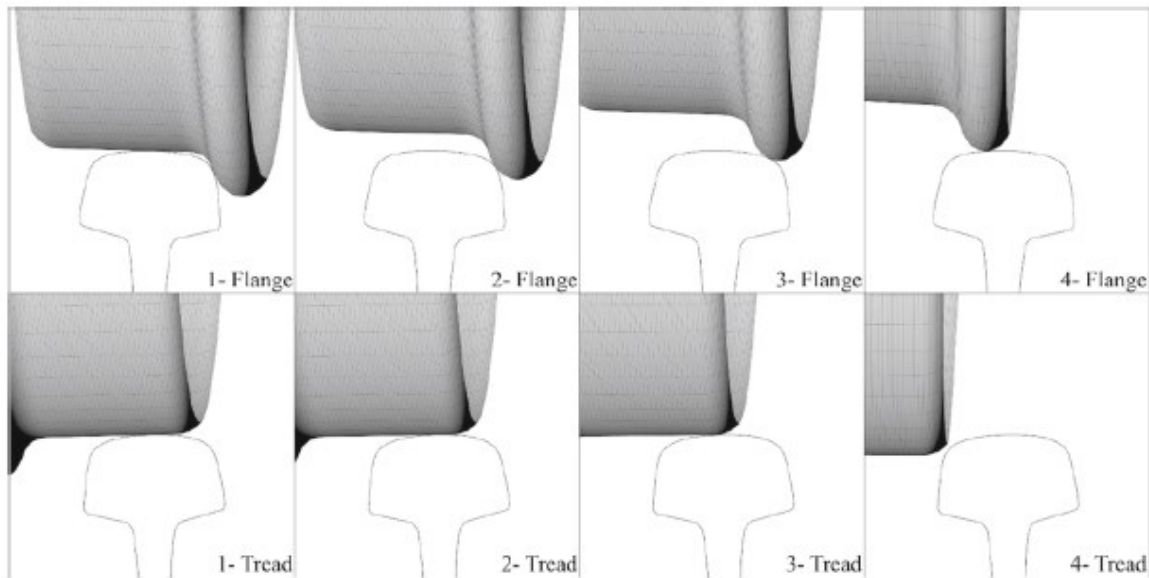


Fig. 2-3-1 Motion of both wheels during flange climb derailment predicted using a multi-body system model [7].

- Gauge widening - Derailments due to gauge widening are usually caused by a combination of wide gauge and large lateral rail deflections (rail rolls), as shown in Fig. 2-3-2. Both rails may experience significant lateral movement and/or railhead roll, and this often causes non-flanging wheels to fall between the rails.

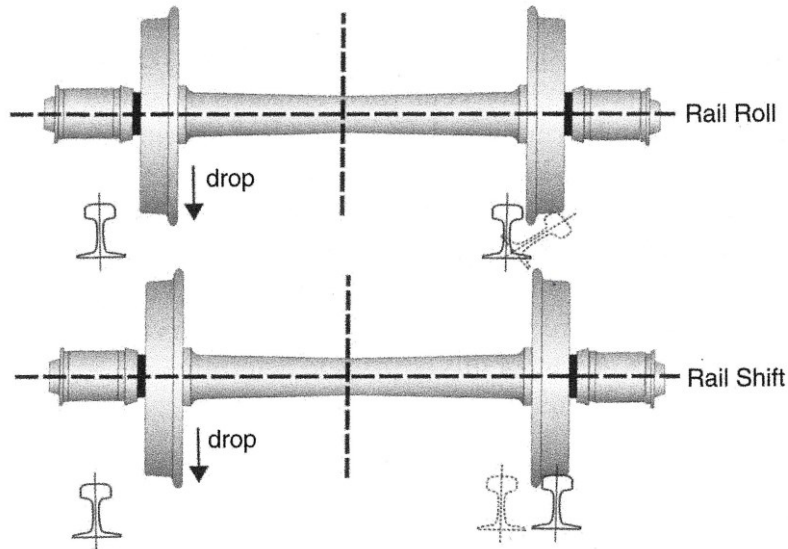


Fig. 2-3-2 Schematics of gauge widening derailment [1].

- Track panel shift - Track panel shift means the cumulative lateral displacement of the track panel, including rails, sleeper plates and sleepers on the ballast, as shown in Fig. 2-3-3. If these components are only slightly displaced, there is no immediate loss of guidance to the bogie. However, if the situation gradually deteriorates to a certain level, the wheels lose guidance at some speed and it could fall to the ground.

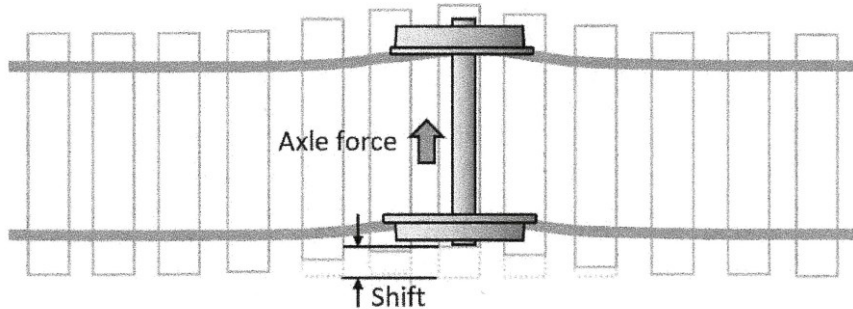


Fig. 2-3-3 Schematic of lateral panel shift [1].

Additionally, there are derailments due to the breakdown of track or rail, rocking derailments, etc. In particular, the risk of flange climb derailment is particularly high on lines in modern, densely populated urban areas, including subways, due to the high proportion of sharp curves. Also, it is recognized as an accident that can cause extensive damage [8][9][10].

2.3.2 Typical mechanisms of flange climb derailment

When a railway vehicle negotiates a sharp curve, the leading wheelset of the vehicle rolls toward the outside of the curve due to the insufficient difference in radius of rotation between the low and high rail. At this moment, an angle of attack occurs between the wheel and the high rail. Since the wheel on high rail rolls toward the outside of the curve while making contact with the rail at the flange, the wheel can climb up along the flange slope by itself. On the other hand, when the angle of attack is small as in a straight section, a climb derailment is less likely to occur.

Figure 2-3-4 shows a cross-sectional view of the wheel-rail on the high rail side, showing the forces acting on the wheel from the rail. According to this figure, it is found that the wheel flange on the high rail of the curve has a lateral creep force f_y in the direction that the wheel is going to climb up the rail gauge corner.

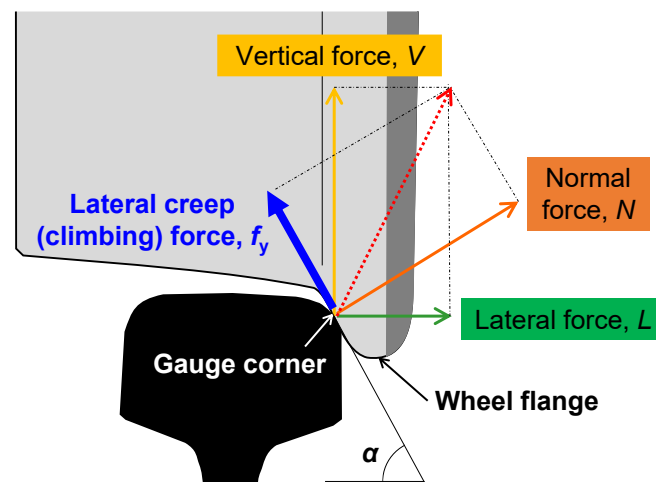


Fig. 2-3-4 A cross-sectional view of the wheel-rail on the high rail side, showing the forces acting on the wheel from the rail.

In this case, the relationship between the normal force N and the lateral creep force f_y acting on the wheel-rail contact and the vertical force V and the lateral force L is as follows:

$$L = N \sin \alpha - f_y \cos \alpha, \quad (1)$$

$$V = N \cos \alpha + f_y \sin \alpha, \quad (2)$$

$$\frac{L}{V} = \frac{\tan \alpha - (f_y/N)}{1 + (f_y/N) \tan \alpha} \quad (3)$$

where α is the contact angle between the wheel and the rail. Equation (3) is commonly known as Nadal's equation. Also, L/V , which is the ratio of lateral force L to vertical force V , is called derailment coefficient and is used as an index to evaluate the safety margin against derailment. When a flange climb derailment occurs, the wheel flange and rail gauge corner are in contact, so the contact angle α is consistent with the flange angle. Also, as mentioned in section 2.3.3, the creep force does not exceed the dynamic friction force. This means that the maximum value of f_y/N is the coefficient of friction. Therefore, the value calculated by substituting the flange angle for the contact angle α and the coefficient of friction for f_y/N is the minimum value of L/V that may derail. The minimum value is called the critical derailment coefficient, $(L/V)_{cr}$. Though the derailment coefficient L/V increases with the increase of lateral force or the decrease of vertical force, when L/V exceeds $(L/V)_{cr}$, a condition is established under which the wheel flange begins to climb up the gauge corner of the rail [6][8].

Figure 2-3-5 shows the relationship between flange angle and coefficient of friction and critical derailment coefficient [11]. The critical derailment coefficient depends on the flange angle and friction coefficient. The lower the flange angle and the higher the coefficient of friction, the lower the critical derailment coefficient, and the more likely the climb derailment will occur.

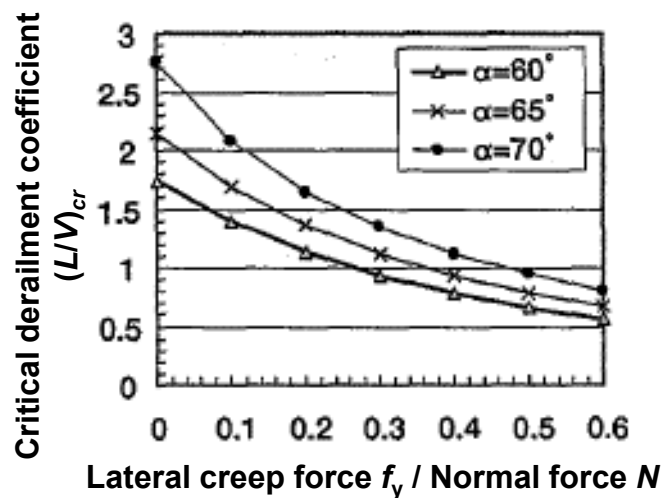


Fig. 2-3-5 Relationship between flange angle and coefficient of friction and critical derailment coefficient [11] (with some minor revisions).

Based on the above, it can be said that the methods to prevent flange climb derailment are to increase the contact angle α , to decrease the f_y/N , and to avoid increasing the L/V while driving. Increasing the flange angle is a relatively simple method and has already been done to some extent. The methods to reduce L/V include, for example, managing the imbalance of the left and right wheel loads, optimizing the springs of the bogie, and managing the twist of the track.

Furthermore, in recent years, Takai *et al.* developed the calculation method to estimate the critical derailment coefficient considering wheel flange angle, equivalent coefficient of friction and angle of attack, and proposed "Estimated derailment coefficient ratio", which is the ratio between the critical derailment coefficient and calculated derailment coefficient as a practical index to evaluate the safety of the system [12]. The above calculation method has been validated by experimental and numerical simulations [6] and the research is also being conducted to further improve accuracy [13].

On the other hand, the coefficient of friction between the wheel and the rail is generally difficult to manage because the coefficient of friction changes in response to various environmental factors, such as weather, worn profile and wheel-rail machining and the phenomenon is complex.

One major factor that influences the coefficient of friction for flange climb up derailment is that it is more likely to occur after wheel re-profiling (machining).

In Japan, wheels are normally manufactured using the following processes: blast furnace, converter, vacuum degassing, continuous casting, slicing and cutting, heating, blanking, rolling, dishing and punching, heat treatment, ultrasonic inspection, machining, imbalance measurement, final inspection and painting [14]. After that, they are installed and used in vehicles, where they are subject to wear and damage. In general, railway wheels have a metallurgical structure consisting mainly of pearlite [15], [16].

A railway wheel experiences re-profiling (Fig. 2-3-6) several times during its whole life to reset it to the designed profile from the worn profile or to remove damage, such as wheel flats and cracks (Fig. 2-3-7).

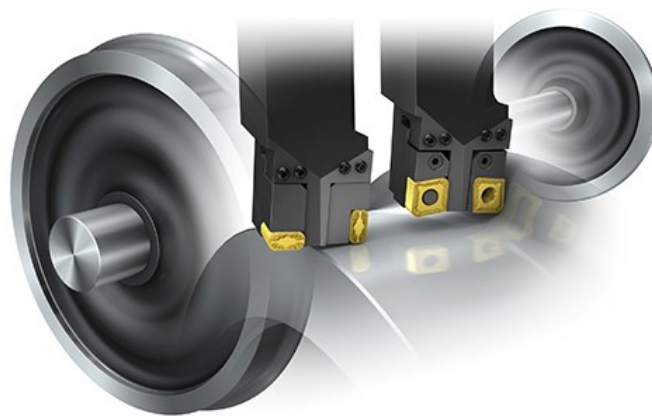


Fig. 2-3-6 A schematic of a railway wheel experiencing re-profiling [17].

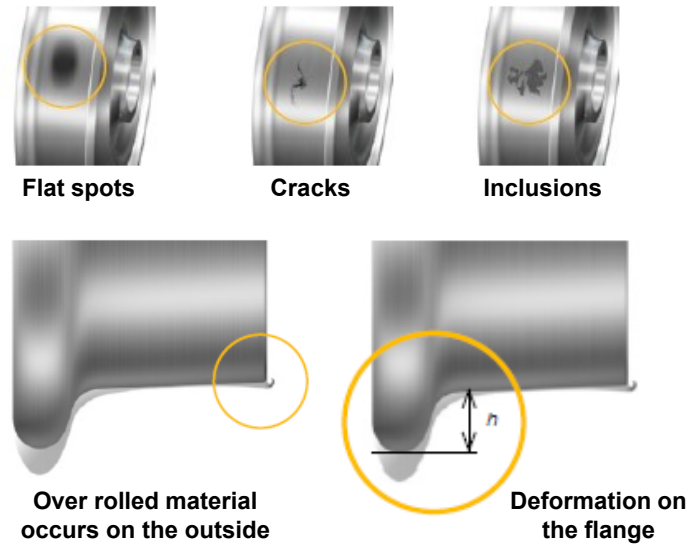


Fig. 2-3-7 Schematics of wheel damage and deformation/wear [18] (with some minor revisions).

It is known that some derailments have occurred relatively soon after the re-profiling of wheels [8][10]. Many of them are rarely made public as they occur within the railroad operator's rolling stock base, and there are no exact statistics. However, one company reported that about 90% of the climb derailments occurred within a relatively short travel distance after the wheel re-profiling [19]. Also, the other report mentioned that about 50% of the flange climb derailments that occurred when travelling a turnout in a trailing direction were just after wheel re-profiling [20]. Since the cycle of wheel re-profiling is several times a year, it is presumed that there is some causal relationship between derailment and wheel re-profiling, but the mechanism has not been clarified.

2.3.3 Case studies of derailment just after wheel re-profiling

Table 2-3-1 shows the list of derailments that occurred at turnouts in Japan between 2006 and 2011. It is noted that four of the eight cases were derailments just after wheel re-profiling (including wheel replacement). In addition, these included two cases of derailment after repeated runs on short sections.

Table 2-3-1 List of derailments that occurred at turnouts in Japan between 2006 and 2011 [10]

Date	Railway	Turnout type	Radius	Direction	Derailed point	Wheel tread	Wheel tread truing	Comments
2006.1	Private	37kg/ No.8/ simple (T-type)	107m	Trailing	Tongue (toe)	Conical (57.2deg)	just after (95km run)	
2006.2	same as above	same as above	107m	Facing	Lead rail	same as above	just after (35km run)	
2007.9	Private; LRT	37kg/ simple	46m	Trailing	Tongue	Conical (65deg)	No	
2008.2	JR	50N/ No.8(siding-type)/ simple	103m	Facing	Lead rail	JR-type arc (65deg)	2day after (394km run)	after 6 times - short distance shuttle; 5km
2008.7	Private; local	37kg/ simple	165m	Facing	Tongue (toe)	Conical (60deg, worn)	No	worn rail
2008.9	Private; urban	50N/curved in same direction	86m c=60mm	Facing	Tongue	Conical (68deg)	2day after (574km run)	after 16times - short distance shuttle; 2km; over super elevation
2011.12	Private; urban	50N/curved in same direction	184m c=54mm	Facing	Tongue	Conical (70deg)	No	
2009.8	Private; local	none	200m	none	Exit-side transient curve	Conical (60deg)	No	Incorrect setting of guard rail

In the following paragraphs, a few of these accidents are picked up and the specific circumstances are introduced.

[1] Arimaguchi station on the Arima Line (2006) [21]

On Sunday, 22nd January, 2006, the 12160 Kobe Electric Railway Company's train, a 4-car unit, from Arimaguchi Station to Suzurandai station on the Arima Line, departed from Arimaguchi Station, on time (12:24). The driver of the train felt a violent vibration just after the departure and applied the emergency brake. After stopping, it was found that the rear bogies of the first and third cars had derailed to the right, obstructing the other track. Only one driver was on board the train, but no injuries were reported.

It is believed that the accident has occurred when the right wheel of the rear bogies of the first and third cars derailed on the right stock rail because of the following reasons:

- i. When the train enters the turnout in the trailing direction, the right wheel load of the first axle decreased by the twist of the turnout
- ii. As the train moved from the right tongue rail to the right stock rail, a lateral impact load was created on the right wheel of the first axle. In addition, the coefficient of friction between wheel and rail was higher than usual because the wheels were close to a condition just after machining. Therefore, the turning lateral force was increased.
- iii. The large angle of attack between the right tongue rail and the right wheel of the first

axle and the increased coefficient of friction by the wheel machining reduced the critical derailment coefficient.

[2] Oku Station on the Tohoku Main Line (2008) [22]

On Saturday, 23rd February, 2008, the 9489 M train of the East Japan Railway Company, a 10-car unit from Ueno Station to Oku Station on the Tohoku Line, departed from Ueno Station, about 5 minutes after the scheduled time (14:51). When the train was coasting through the No. 537 turnout leading to the No. 8 line at Oku Station at a speed of about 23 km/h, all four axles of the fifth car derailed to the left and stopped. One driver and one instructional driver were on board the train, but there were no casualties.

The displacement of track and the ratio of wheel load imbalance (the ratio of large wheel weight to the average wheel weight of the left and right sides of the same axis) of the cars did not exceed the standard values of maintenance. However, the accident was believed to have been caused by the left wheel of the first axle of the front bogie of the fifth car riding up on the main lead rail and derailing to the left as the derailment coefficient increased and the critical derailment coefficient decreased while the train was passing through the lead section of the turnout.

The possible reasons for the increase in the derailment coefficient and the decrease in the critical derailment coefficient are as follows:

- i. The twist of turnout corresponding to the distance of fixed axles in the bogie caused a decrease in the wheel load of the left side. In addition, the derailment coefficient increased due to the rolling of the car body caused by the change in the cross level and the alignment, resulting in a decrease in the wheel load and an increase in the lateral force.
- ii. The equivalent coefficient of friction between the wheel flange and the rail increased and the critical coefficient derailment decreased.

Figure 2-3-8 shows the appearance of the wheel surface just after the accident. The wheels of the fifth car that derailed had just been re-profiled on 20th February, 2008.

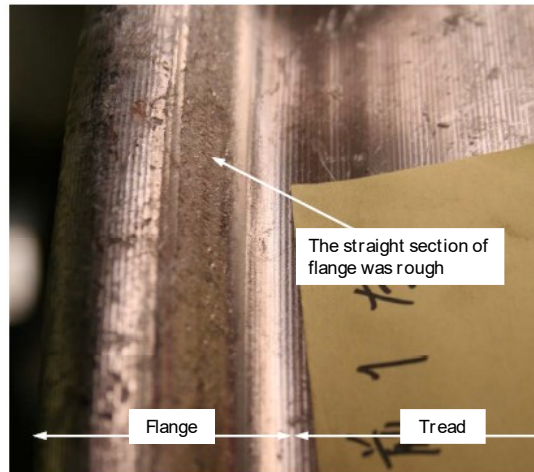


Fig. 2-3-8 Appearance of the wheel surface just after the accident [22] (with some minor revisions). Left wheel of the first axle of the front bogie of the fifth vehicle.

Similar accidents have occurred in the UK, and the following are some cases.

[3] Ordsall Lane Junction, Salford (2013) [23]

At 14:34, on Wednesday, 23rd January, 2013, the 5Z47 train operated by the West Coast Railway Company, derailed on a sharp curve, approaching Ordsall Lane Junction in Salford, and caught fire. The train departed Ardwick depot at 14:24 hrs, and was routed via Ardwick Junction, over the lines that lead into the terminal platforms at Manchester Piccadilly station, and onto the track towards the derailment site. Just before departure, the vehicle's wheels were re-profiled.

The immediate cause of the accident was a lateral force created by the 47500 locomotive as it passed the curve approaching to the Ordsall Lane junction, which caused the flange of the leading right wheel to climb up on the outer rail.

The cause was that even though the curve approaching the Ordsall Lane junction met the installation requirements, the check rail had not been installed.

The following factors were necessary to achieve a high L/V derailment quotient:

- i. A high friction condition was developing on the gauge corner of the high rail. The rail lubrication system did not prevent such a condition, and the inspection process was not able to identify.
- ii. A recent wheel re-profiling had removed any residual lubricant and dirt from the wheel surface. They would have helped to reduce the contact friction between the wheels and rails.
- iii. The relatively low contact angle of the flanges in the new P1 wheel profile makes them less resistant to derailment due to climbing.
- iv. The wider track gauge increases the risk of derailment.

The surface roughness of the wheels was slightly rougher than the N10 specified by West Coast Railways. It indicated that this is a potential cause of the derailment. However, precise quantification of the role of the wheel roughness conditions is required.

[4] Roberts Road Depot, Doncaster (2018) [24]

At 17:17, on Friday, 21st December, 2018, the train operated by Direct Rail Services (DRS), derailed on curves of around 200 metres radius or less, while departing the Roberts Road Depot, Doncaster, after a wheel re-profiling. The train consisted of four locomotives: a class 66, a class 20, a class 37 and another class 66. The train changed direction to York and was travelling through a sharp curve at 13mph (21 km/h) when the third locomotive of the formation derailed. No one was injured in the derailment, but the damage to the track and recovery work resulted in the Sheffield and Routes between Doncaster blocked for 36 hours, causing major disruption to passenger services.

The derailment may have been caused by a combination of some or all of the following factors:

- i. As a result of wheel re-profiling, the wheel surfaces were clean and dry at the time of the derailment, which increases the friction between the wheels and the rails and increases the likelihood of derailment.
- ii. The flange angle of the P1 wheel used on the vehicle was 62 degrees and smaller than that of the P8 wheel, 68-70 degree, which is a more modern profile.
- iii. The class 37 locomotive bogie has three wheels on each, and compared to a two-axle bogie, the overall wheelbase was longer and this would have negatively affected its cornering ability.

The wheel re-profiling was done properly and was within the correct geometric and surface finish tolerances.

2.4 Running-in phenomenon

When a machine is first used or when it is restarted after a long period of inactivity, it is widely known that various tribological problems such as initial severe wear, seizure, etc. can occur during the so-called running-in process. Derailment just after wheel re-profiling can also be a phenomenon of some kind of running-in process. According to OECD terminology [25], "running-in" is *the process by which machine parts improve in conformity, surface topography and frictional compatibility during initial stage of use*. Hirano [26] referred this OECD terminology and indicated that the "conformity" includes not only microscopic surface roughness, but also improvement of the macroscopic contact condition at the interface.

2.4.1 Model for running-in

Blau proposed a mathematical model of the running-in process of a friction interface based on examples of sliding friction coefficient versus time behaviour from published work and laboratory experiments [27]–[30]. The factors contributing to the coefficient of friction were expressed as in equation (4).

$$\mu = L(D + T + V) \quad (4)$$

where μ is the time-dependent coefficient of friction, L is a lubrication factor, D is the initial material deformation term, T is a transition term based on one of several candidate interfacial processes occurring during sliding, and V is the magnitude of the variability in friction coefficient which can also be derived from any of several sources.

The lubrication factor L changes from 0 to 1.0. If L is very small, the lubrication method in the system is effective and if L is very large, the lubrication effect is lost or the conditions are dry. The initial material deformation term D contains contributions from both work-hardening and near-surface microstructural reorientation from sliding-induced deformation.

A transition term T contains the phenomenon which appears after an "incubation period", such as the accumulation of sub-surface fatigue damage, coating wear, build-up of the transfer layer, debris deposit agglomeration, and even accumulation of the frictional heat.

The magnitude of the variability in friction coefficient, V , is the variation of the coefficient of friction in a sliding tribosystem. This variation is often caused by surface roughness in particular, and it affects momentary mechanical impedance to relative motion. This phenomenon is otherwise known as "asperity interlocking."

Blau presented examples of the types of the running-in curve based on Equation (4), as shown in Fig. 2-4-1 and Table 2-4-2.

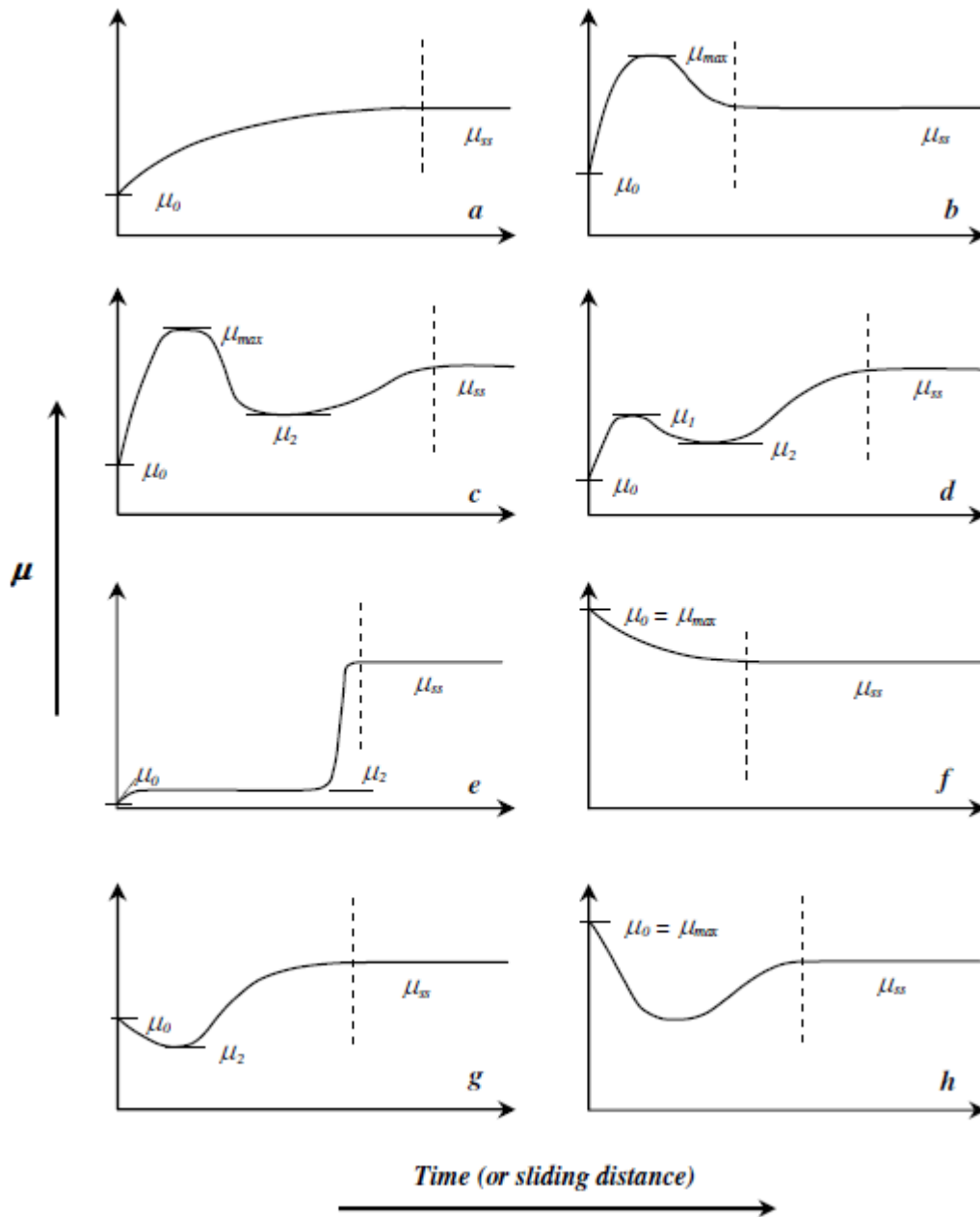


Fig. 2-4-1 Types of running-in curve shapes. The friction force is on the vertical axis and time or number of cycles is the horizontal axis [30].

Table 2-4-1 Possible causes for each running-in curve [30].

Type	Occurrence	Possible cause(s)
a	Contaminant surfaces.	A thin film of lubricious contaminant is worn off the sliding surface(s).
b	Boundary-lubricated metals.	Surfaces wear in; initial wear rate is high until the sharpest asperities are worn off and the surface becomes smoother.
c	Unlubricated oxidized metals, often observed in ferrous or ferrous/nonferrous pairs.	Wear-in, as in b, but with the subsequent development of a debris layer or excessive transfer of material.
d	Same as type c.	Similar to c, but the initial oxide film may be more tenacious and protective.
e	Coated systems; also, systems in which wear is controlled by subsurface fatigue processes.	Wear-through of a coating; or subsurface fatigue cracks grow until debris is first produced (the debris creates third bodies), which induce a rapid transition in friction
f	Clean, pure metals.	Changes in crystallographic orientation in near-surface layers reduce their shear strength and lower the friction.
g	Graphite on graphite; metal on graphite.	Creation of a thin film during running-in; debris or transfer produces a subsequent rise in friction.
h	Hard coatings on ceramics.	Roughness changes, then a fine-grained debris layer forms.

Blau has also presented the change of wear volume with test duration which has been typically observed for either a pin-on-disk or flat block-on-ring (Fig. 2-4-2). He noted that the wear rate can vary greatly depending on where in the overall test the test had been stopped and the amount of wear was evaluated because of their non-linearity.

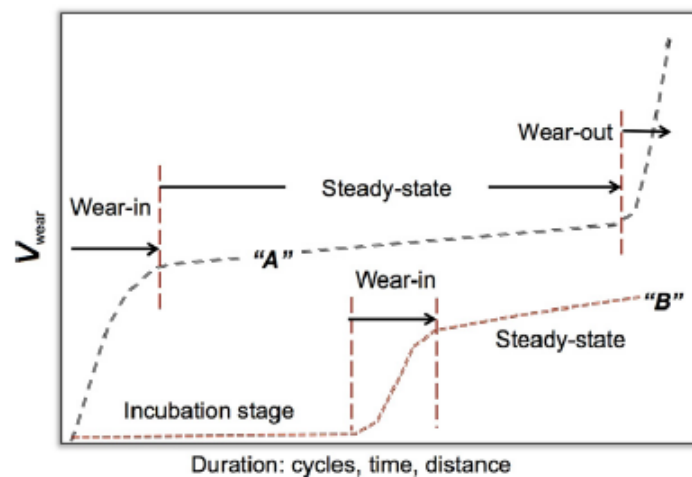


Fig. 2-4-2 Two sample cases of non-linear sliding wear behaviour. Curve “B” accounts for a zero wear stage in which surface and subsurface damage is building up, but no material has yet been lost. Other curve shapes exist, but this is a common one [31].

Blau takes into account the influence of various factors in the running-in process and it captures the characteristics to a certain extent. However, of course, the actual cases vary in individual complexity and the degree of influence of factors varies.

2.4.2 Roughness parameters to evaluate the surface geometry during running-in

In addition to the common roughness parameters RMS and Ra, skewness and kurtosis are reported to be useful parameters for assessing changes in surface topography during the running-in process [32]–[34]. Skewness is a parameter that evaluates the symmetry of the height distribution and is effective in monitoring geometry changes. Kurtosis is a parameter that evaluates the spikiness or scratchiness of the surface geometry. Stout *et al.* evaluated the evolution of roughness parameters by tracing the geometry changes of the friction surface of a pin-and-ring testing machine at exactly the same location. They mentioned that quoting skewness seems to be the most appropriate to quantify the geometry of a worn surface [32].

2.4.3 Running-in behaviour of the wheel-rail contact

Lundmark *et al.* investigated the change of surface topography of wheel and rail after wheel re-profiling and rail grinding in the field [35]. Lundmark *et al.* monitored changes in eight surface roughness parameters. These were Rk, Rpk, Rvk, Sa, Sku, Ssk, Sc and Sdq. Lundmark *et al.* explained that the changes in these surface roughness parameters all showed a similar trend, so only the Sa values were presented in the literature. They found that the roughness just after rail grinding, $Sa \sim 10 \mu\text{m}$, was dramatically reduced to $Sa \sim 1 \mu\text{m}$ in the first 35 hours, or 26,800 ton and the reduction was negligible until 10 weeks, or 2,070,000 ton later for both low and high rail with a 655-metre radius (Fig. 2-4-3). In the case of wheel roughness, although the initial topography differs between new and re-profiling, and different workshops (Fig. 2-4-4), the roughness decreases significantly at the beginning of the run and settles to almost the same value, $Sa \sim 1 \mu\text{m}$ after 5400 km (Fig. 2-4-5).

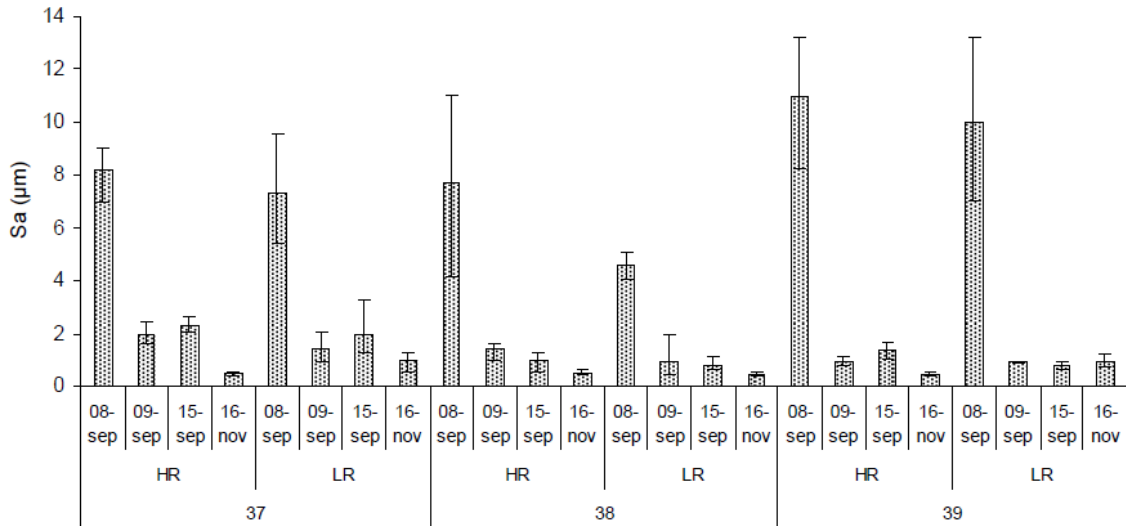


Fig. 2-4-3 Arithmetical mean height obtained from field measurements on the newly ground rails and its change during the initial running-in stage. (HR: High rail, LR: Low rail) [35].

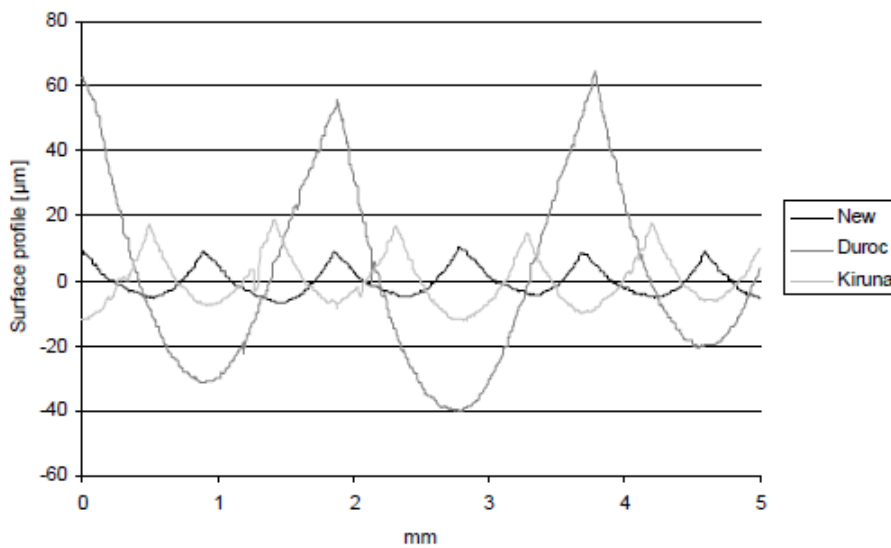


Fig. 2-4-4 Initial surface roughness on wheels [35]. It can be seen that the surface profile of the new wheel and the wheels that have been re-profiled at the two workshops in Durac and Kiruna are quite different.

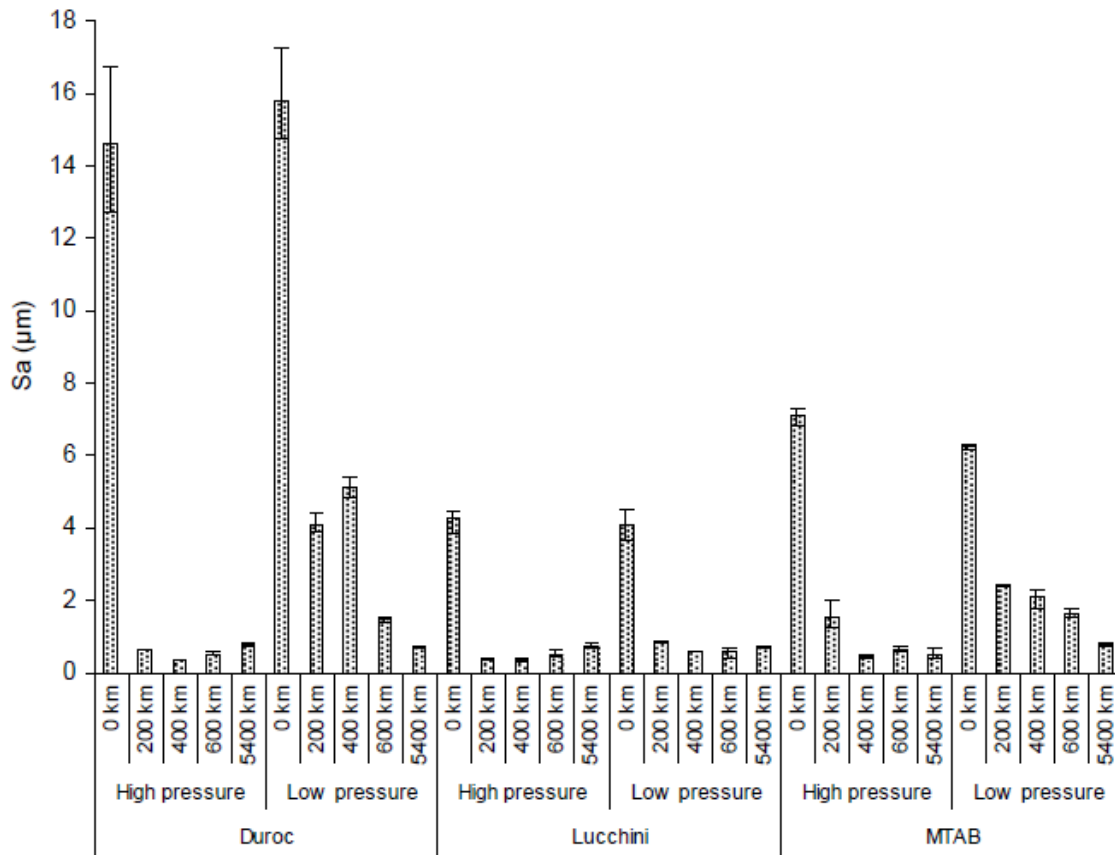


Fig. 2-4-5 Arithmetical mean height obtained from field measurements on the re-profiled wheels and its change during the initial running-in stage (Lucchini was a new wheel as a reference) [35]. The roughness decreases significantly at the beginning of the run and settles to almost the same value, $S_a \sim 1 \mu\text{m}$ after 5400 km.

Lundmark *et al.* also investigated the influence of the initial topography and material on the creep (traction) force during running-in using a twin-disk rolling/sliding machine [36]. Figure 2-4-6 shows an example of the twin disk test results. The first letter of the figure legend denotes the roughness of the wheel specimen and the second letter the roughness of the rail specimen, S, smooth and R, rough. The roughness' of the wheel specimens were $S_a = 14\mu\text{m}$ and $S_a = 2\mu\text{m}$, and that of the rail specimens were $S_a = 2\mu\text{m}$ on the rough specimens and $S_a = 0.5\mu\text{m}$ on the smooth. The wheel disks were finished to the same level of roughness as the wheels just after re-profiling and after travelling some distance, as measured in practice by the same authors (Fig. 2-4-5). On the other hand, the rail disks could not be ground to the same surface roughness as the newly ground rail, so they were ground to the roughest possible to simulate a rough rail. All cases except one have clear peaks within the first 2000 s (about 7000 rpm) of the test. The trend is well in line with one of the running-in models presented by Blau (Fig. 2-4-1 (b)).

A number of tests of combinations of rough wheel and smooth rail showed a lower coefficient of friction than the combinations of smooth wheel and smooth rail. Lundmark *et al.* attributed this to reduced adhesion compared to contact between smooth disks. Also, they pointed out the influence of the difference of work-hardened layers. However, they mentioned this was not clear, suggesting that challenges remain.

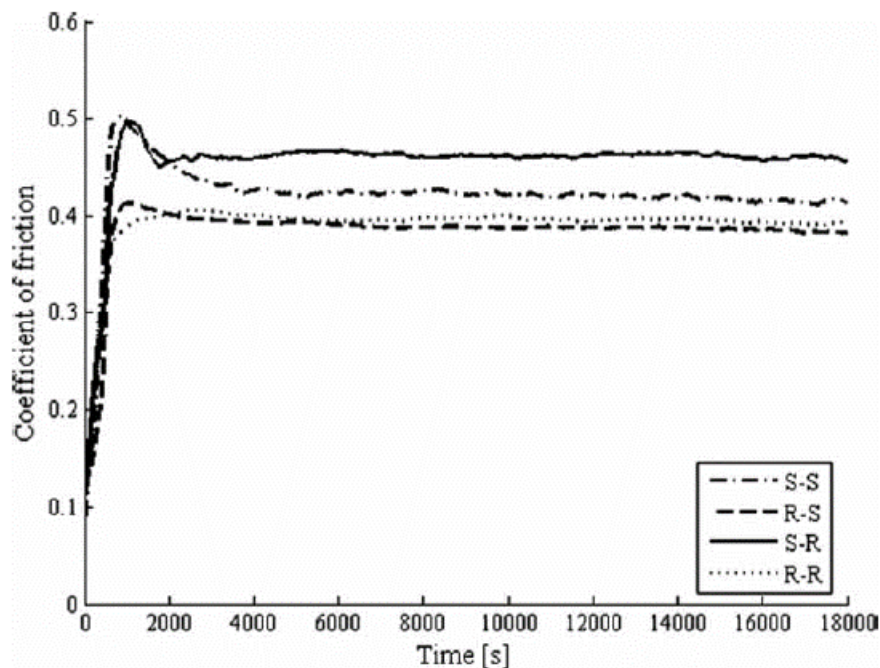


Fig. 2-4-6 Friction plots for different roughness combinations of blue light wheel – 1100 rail pairs. The first letter denotes the roughness of the wheel specimen and the second letter the roughness of the rail specimen, S, smooth and R, rough [36].

Baek *et al.* also investigated the traction curve during running-in [37]–[39] in the wake of the train accident caused by a derailment on the Tokyo Metro line on 8 March 2000. They conducted twin disk tests to investigate the effects of running speed, slip ratio, temperature, humidity and contact pressure on traction coefficient during running-in.

Figure 2-4-7 shows an example of traction curve with the vibration acceleration during the test, measured by an accelerometer installed near the rotating shaft. A peak in a traction coefficients can be seen at the beginning of the running in, as in Lundmark *et al.* [36]. As the traction coefficient decreases after reaching the peak, the vibration acceleration increases at the same time. Baek *et al.* indicated that significant wear began to occur as the traction coefficient decreased after the peak [38]. Figure 2-4-8 shows surface roughness profiles from A to E in Fig. 2-4-7. It can be seen that the surface roughness increases rapidly after the peak of the traction coefficient is reached.

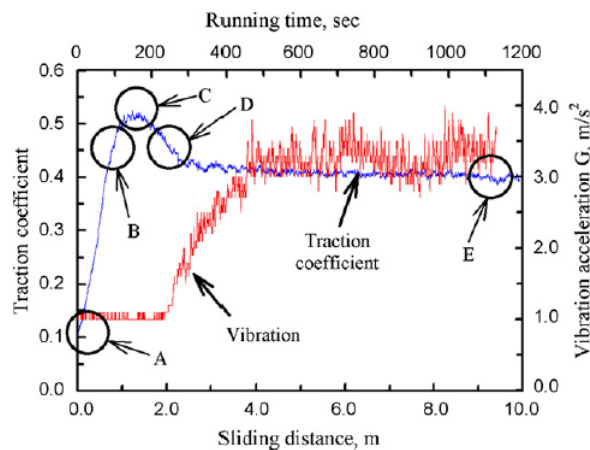


Fig. 2-4-7 Relationships of traction coefficient and vibration acceleration to sliding distance under the standard conditions (contact pressure of 800MPa, rolling speed of 1.26 m/s, slip ratio of 0.7 %, temperature of 30 °C, and relative humidity of 60 % RH) [38].

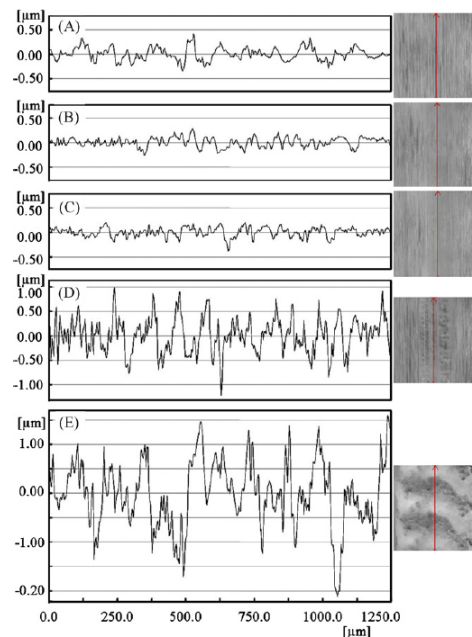


Fig. 2-4-8 Surface roughness profiles of the rail disk from A to E in Fig. 2-4-7 [38].

Mesaritis *et al.* also used a twin-disk test machine to investigate the changes in traction coefficient, roughness, and wear to reach a steady state. They also reported that during the running-in process, the surface once becomes smooth until the wear begins, but then wear becomes apparent and the roughness increases again [40].

Greene *et al.* mentioned the possibility that the residual machining marks just after wheel re-profiling may contribute to the increase in the coefficient of friction [8]. Figure 2-4-9 shows examples of wheel surfaces just after wheel re-profiling and after experiencing the damage resulting from operation. According to Greene *et al.*, for smooth steel-to-steel contact in dry conditions, the coefficient of friction is generally around 0.5, but can be higher if the surface roughness is higher. It has also been mentioned that the rougher surface created by wheel re-profiling can significantly reduce the L/V limit (Nadal criterion) and increase the risk of derailment.

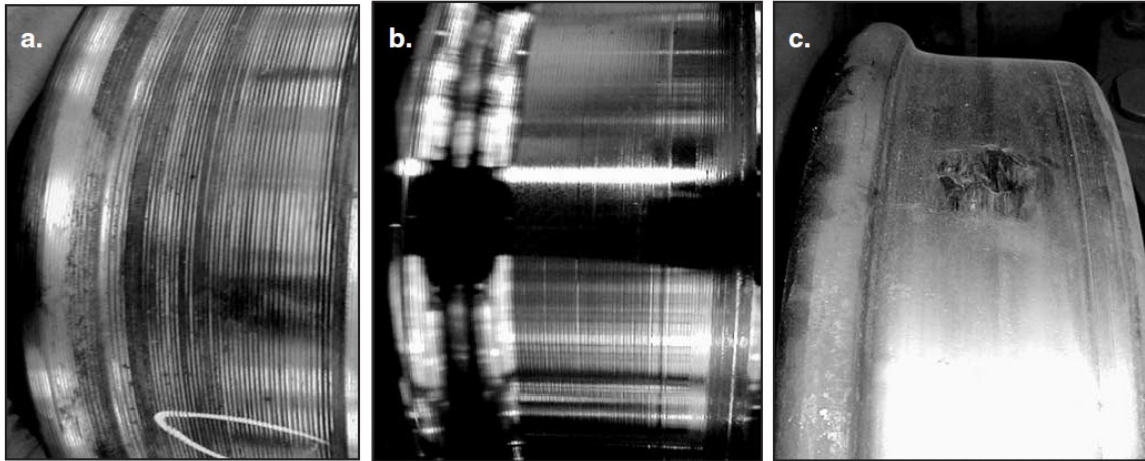


Fig. 2-4-9 Comparison of wheel surface roughness ([a] surface after wheel re-profiling from milling type machine, [b] surface after wheel re-profiling from lathe type machine, and [c] surface of wheel back from operation with a flat spot.) [8].

The above opinion is that, namely the spike-like by the machining marks ploughing into the rail material and increasing traction during the running-in period. This opinion is also found in other literature [1][41].

On the other hand, Ban *et al.* measured the coefficient of friction of an actual machined wheel using a tribometer and reported that the coefficient of friction was higher when the wheel was worn out by sliding than when the protrusions remained (Figs. 2-4-10 and 2-4-11) [42].

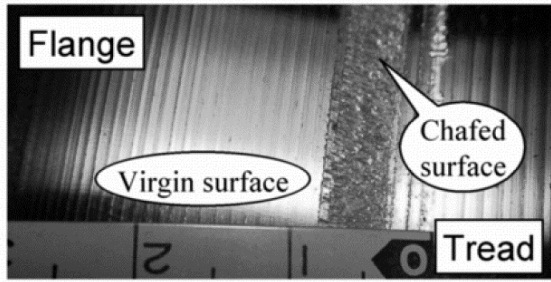


Fig. 2-4-10 Appearance of flange contact mark (1 mm/rev) just after the 20th loading cycle (Vertical load: 30 kN, Lateral load: 25 kN). The test was carried out using a full-scale wheel-rail contact machine[42].

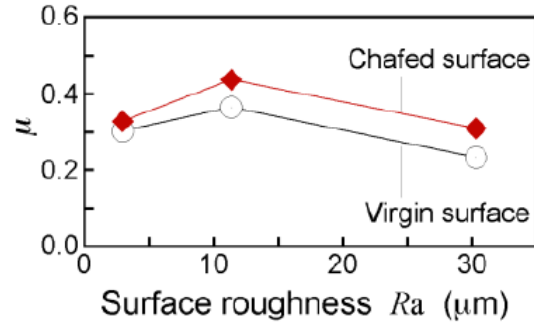


Fig. 2-4-11 Relationship between the tester the initial surface roughness of wheel flange and coefficient of friction measured by a tribometer [42].

Doi *et al.* ran an actual vehicle repeatedly at a curve to investigate changes in the surface condition of the wheels and frictional force after wheel re-profiling [43]. Figure 2-4-12 shows the change of surface profile of the wheel flange with the increasing number of passages at a curve after wheel re-profiling. Although the regular marks by the wheel re-profiling disappeared after the 5th pass, the irregular roughness appeared in the pattern after the 30th pass. Figure 2-4-13 shows the change of arithmetical mean roughness, Ra, of the wheel flange for different machining feed rate. It can be seen that the roughness is at its minimum value after about the fifth run for all machining rate. Even though the Ra is similar between the early and late stages of the repetitive tests, it is estimated that the surface topography is very different, having regular or irregular profiles. In other words, the large Ra at the early stage of the test was caused by machining marks, while the increase in Ra at the late stage of the test was thought to be caused by wear on the surface. Therefore, the interfacial condition of the two was significantly different.

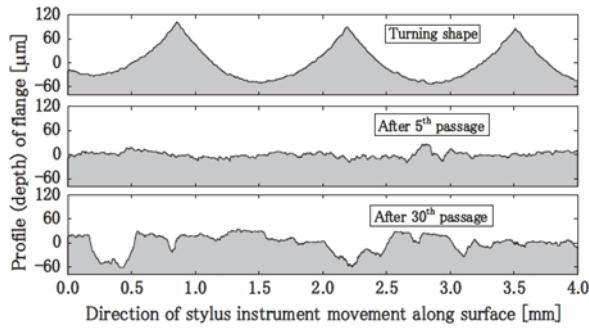


Fig. 2-4-12 Change of surface profile of the wheel flange with increasing number of passages at a curve after wheel re-profiling (Machining feed rate: 1.5mm/rev) [43].

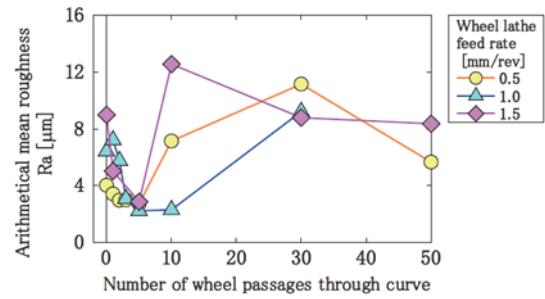


Fig. 2-4-13 Change of arithmetical mean roughness, Ra, of the wheel flange with increasing number of passages at a curve after wheel re-profiling [43].

Figure 2-4-14 shows $Y/Q(L/V \text{ on high rail})_{\max}$, $\kappa(L/V \text{ on low rail})$ and wheel climbing height, z_{\max} versus numbers of passage over the turnout. It can be thought that Y/Q_{\max} and κ represent the qualitative friction coefficient on high rail and low rail, respectively. Both Y/Q_{\max} , κ and z_{\max} tend to increase rapidly at the beginning of the test and then increases more slowly. Doi *et al.* also found that lubricating the wheel flanges prior to testing reduced flange climbing up.

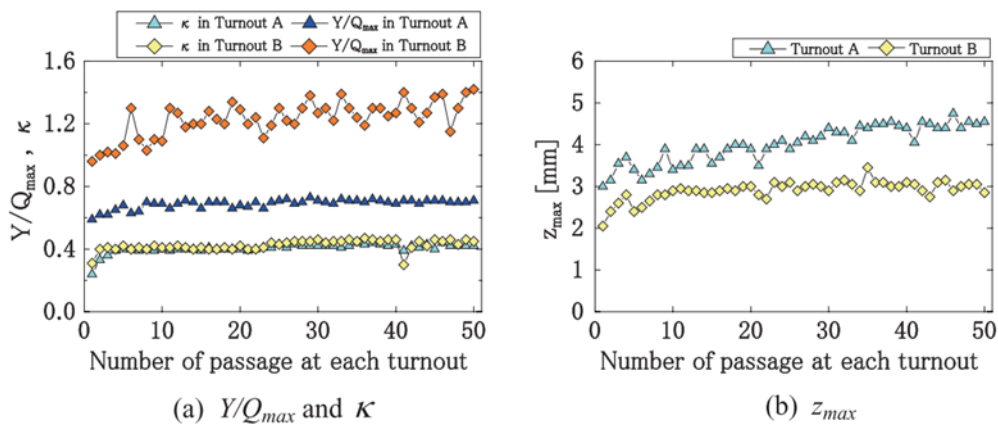


Fig. 2-4-14 Y/Q_{\max} , κ and z_{\max} versus numbers of passage over the turnout [43].

Kataori *et al.* also conducted tests to replicate the climb-up of the wheel at a turnout [44]. As shown in Fig. 2-4-15, they captured the increase in climbing height as the number of tests increased, too. Figures 2-4-16 and 2-4-17 shows the appearance of the test wheel and rail, respectively. It could be seen that the contact width of the wheel flanges gradually increased and a large amount of wear debris was observed after the test. They have also conducted climb-up tests on several wheels with different machining rates, but an effect of machining rate was not observed.

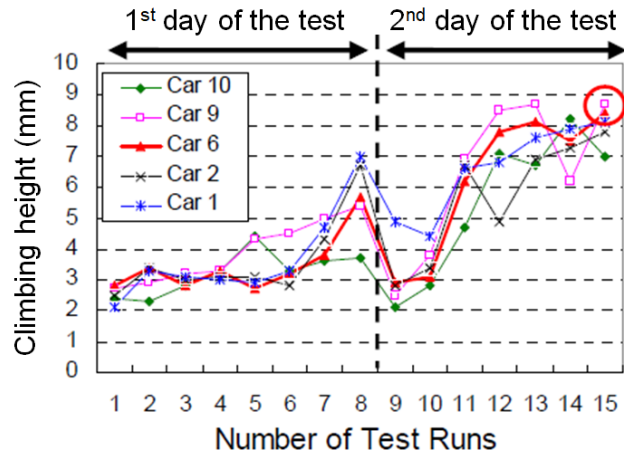


Fig. 2-4-15 Relationship between the number of test runs and climbing height of wheel [44]. The test vehicle was fitted with new lathe-machined wheels and the test vehicle travelled the same route repeatedly 15 times over two days (eight times on the first day and seven times on the second day). The test speed at the turnout was 20 km/h.

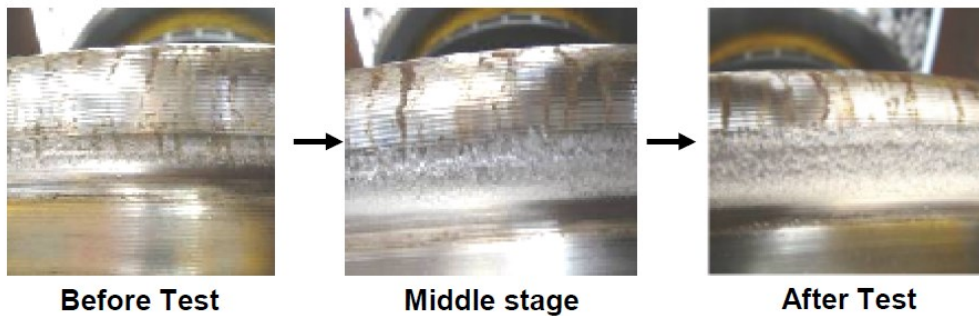


Fig. 2-4-16 Appearance of the flange of test wheel [44]. As the number of runs increased, the surface of the flange became progressively rougher and the rougher area extended.

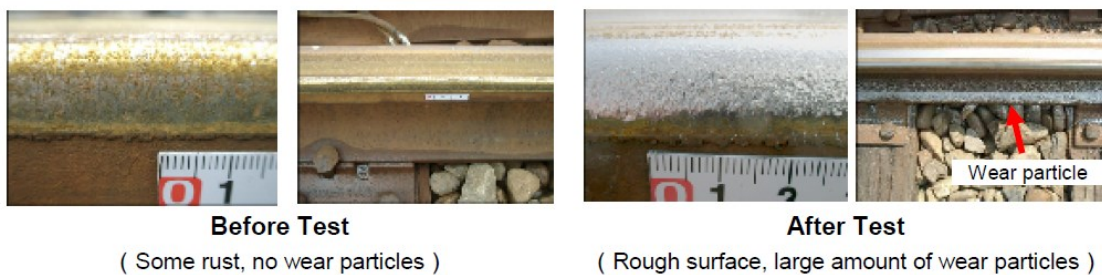


Fig. 2-4-17 Appearance of the test rail[44]. The gauge corner of the outer rail was heavily roughed up, producing a large amount of wear particles.

While these circumstantial evidences suggest that wheel climb-up is not necessarily due to the spike effect of the machining marks, the friction mechanism is still unclear.

2.5 Experimental measurement of the wheel-rail interface

During the running-in period, the microscopic and macroscopic topography, material properties such as hardness and microstructure change in relation to each other at the contact interface. These sensitive, multi-parameter phenomena are generally too complex to be reproduced numerically. On the other hand, as is well known, it is also very difficult to experimentally evaluate the contact interface due to the difficulty of measurement, and the number of reports is not large. This section presents a few examples of experimental evaluations of wheel-rail contact that have been conducted in the past.

Andrews [45] inserted a carbon sheet and ordinary paper between the wheel and rail and statically contacted the wheel and rail to transfer the contact shape and evaluate the contact area. He mentioned the differences in contact shape due to differences in wheel diameter and conditions (just after re-profiling and after wear, Figs. 2-5-1 and 2-5-2). He reported that the machining marks on a freshly turned wheel may increase the contact area, with a corresponding decrease in average pressure.

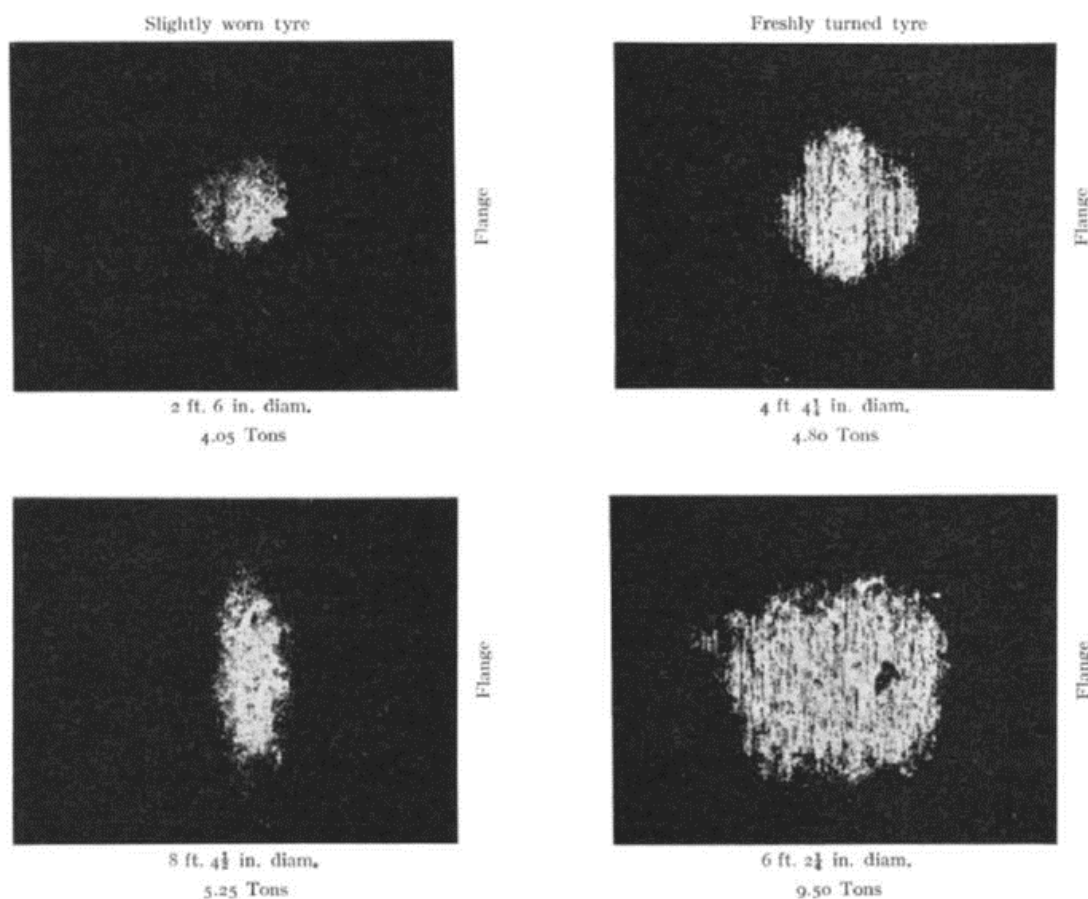


Fig. 2-5-1 Typical contact area between wheel and rail[45]. The contact area was obtained by inserting a carbon sheet and ordinary paper between the wheel and the rail.

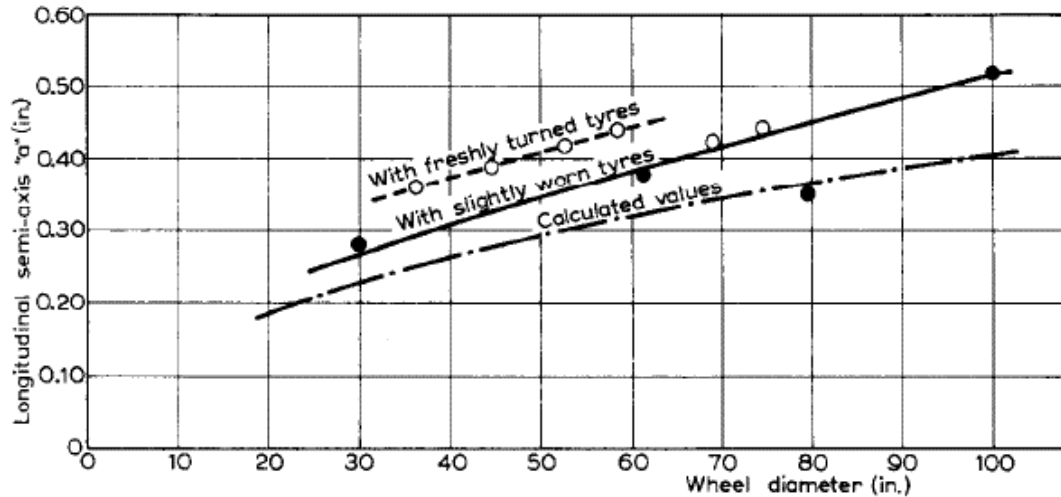


Fig. 2-5-2 Measurements with variable wheel diameter. Slightly worn or freshly turned tyre in contact with new rail. Relationship between longitudinal semi-axis a (corrected for 7 tons wheel load) and wheel diameter [45].

Kumar *et al.* [46] used SEM replica tape to conduct a similar evaluation. They showed changes in the contact area and contact pressure due to plastic deformation and wear with loading cycles. They used two types of tape of different thicknesses. Figure 2-5-3 showed the qualitative description of measured contact area growth with 1 mm and 5 mm replicating tapes in the laboratory. They reported that the stage of wear and the increase in roughness caused differences in the information on the contact area obtained from tapes of different thicknesses. The thin tape (1 mm) was effective for smooth surfaces and the thick tape (5 mm) for rough surfaces. Different correction factors were used for each tape of different thicknesses to convert the measured area to the real area.

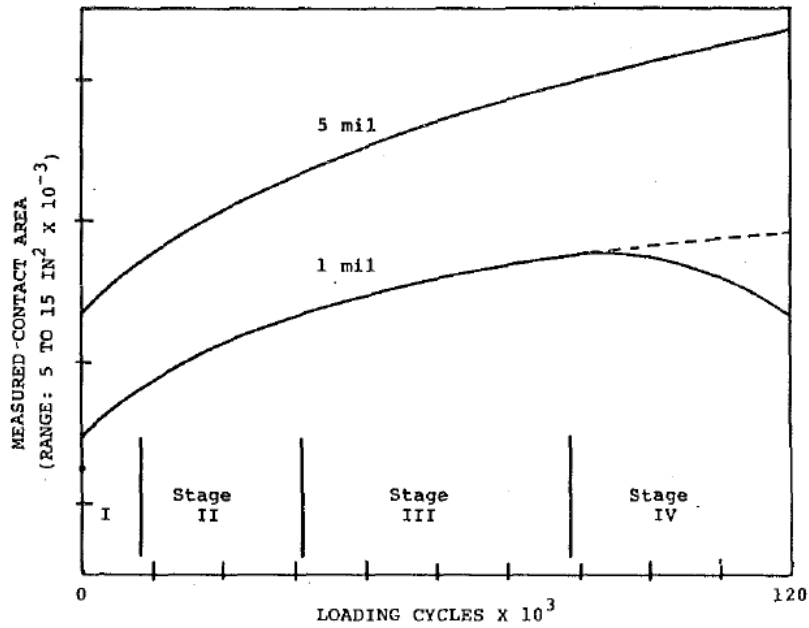


Fig. 2-5-3 Qualitative description of measured contact area growth with 1 mm and 5 mm replicating tapes in the laboratory [46].

Kleiner *et al.* [47] used Fuji Film's Prescale to evaluate the contact shape between the wheel and rail. The difference in the contact shape with the displacement in the direction of the sleeper (Fig. 2-5-4). They also reported the results of the contact pressure distribution by the image analysis using contact shape under different contact load (Fig. 2-5-5). Furthermore, Lekue *et al.* [48], [49] investigated in detail the magnitude of the system errors in this method for the efficient modelling of rough wheel-rail contacts.

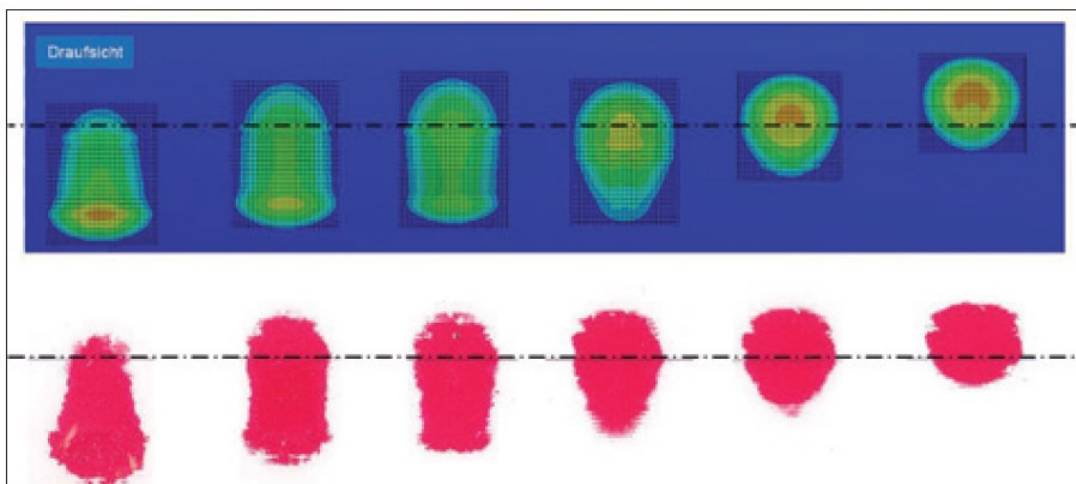


Fig. 2-5-4 Comparison of the contact surfaces: Numerical simulation vs. bench tests [47]. The upper part shows an exemplary contact area from FE calculations. The lower part shows the corresponding experimentally determined contact area impressions (both for the wheel/rail combination S1002/60E2).

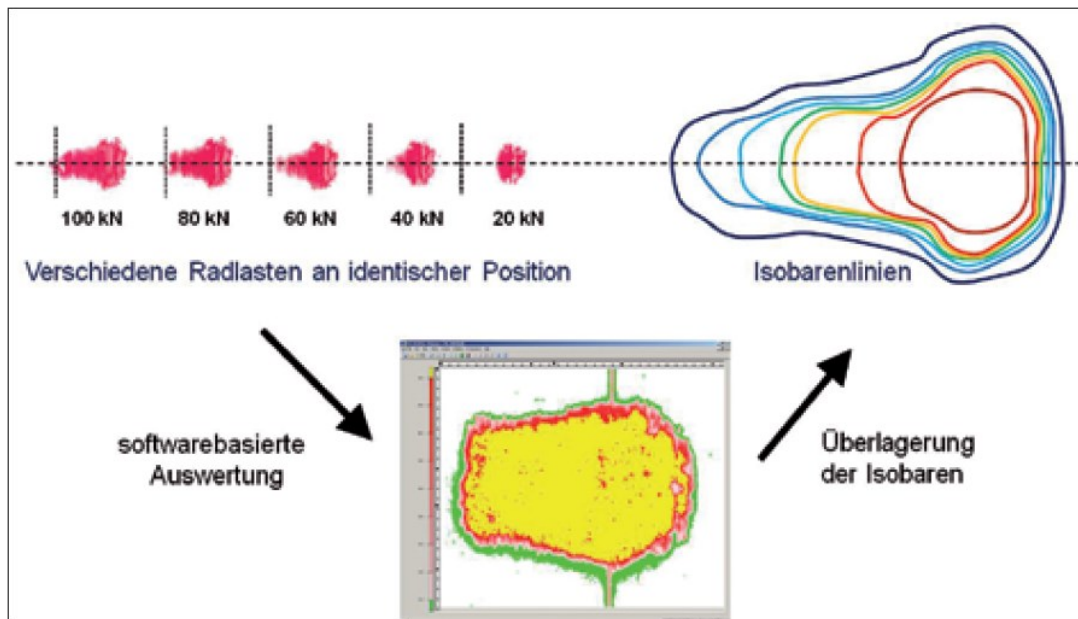


Fig. 2-5-5 Principle for the determination of contact pressure distribution [47]. The software makes it possible to filter out the beginning of the red discolouration at the edge of the contact area. This is shown in the centre of the figure. Here, the transition between the green and red areas corresponds to the 50 MPa isobar. This method is acceptable because the "initial contact point" does not move with increasing wheel load. This procedure gives a qualitative view of the pressure distribution in the contact area (the right of the figure).

Of course, the evaluation method by intentionally inserting a third material such as a carbon sheet, replica sheet, or pressure-sensitive paper between the wheel and the rail disturbs the original wheel-rail contact itself. Therefore, it is difficult to make dynamic measurements focusing on friction behaviour by the use of this technique.

Poole [50] evaluated the contact area between the rolling wheel and rail in the unique way. He set up a block with an array of holes in the rail head of a full-scale wheel-rail test machine, and evaluated the contact area by passing the wheel through the holes while supplying compressed air and monitoring the pressure changes (Fig. 2-5-6). As a result, the variation of contact length with number of wear cycles was obtained (Fig. 2-5-7).

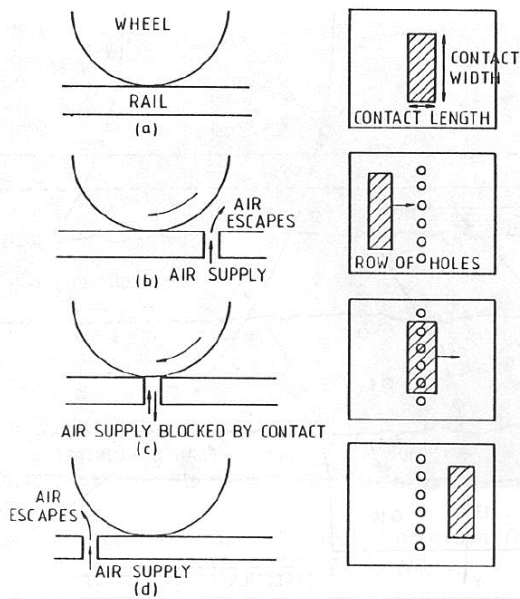


Fig. 2-5-6 An air pressure method for measuring contact areas [50].

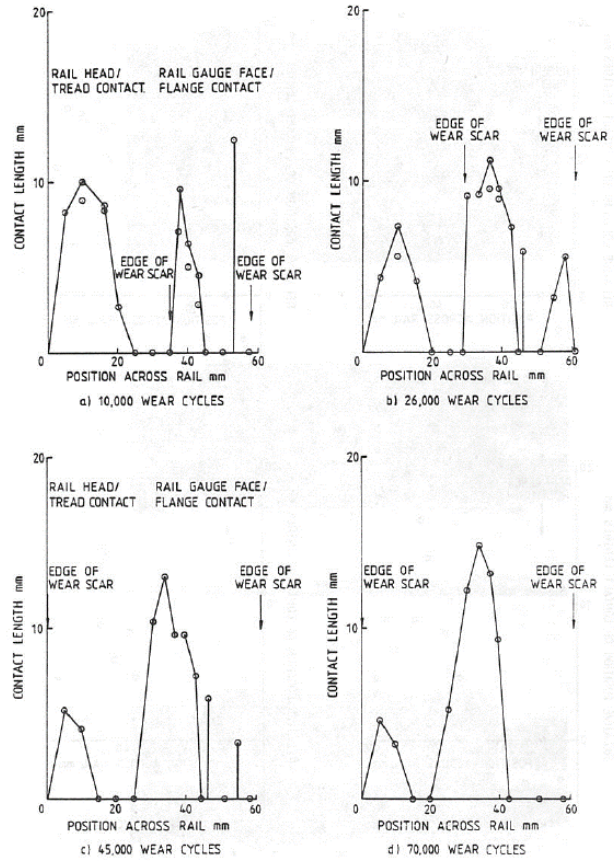


Fig. 2-5-7 Variation of contact length with the number of wear cycles for 27.7 kN lateral load, 80 kN normal load and 19.5 mrad yaw angle [50].

Hung *et al.* [51] measured stress inside the rail using an OFDR (Optical Frequency Domain Reflectometry) FBG (Fiber Bragg Grating) sensor aiming to evaluate the wheel-rail contact condition. This system can measure the longitudinal strains of sensors embedded in the rails in a one-dimensional distribution (Fig. 2-5-8) and obtain the strains in the rail that occur when the wheel passes through the rail (Fig. 2-5-9).



Fig. 2-5-8 Embedded FBG sensors in the rail [51]. The FBG sensors were inserted into 1 mm diameter holes made by electrical discharge machining. The holes were made at two depths of 13 mm and 18 mm.

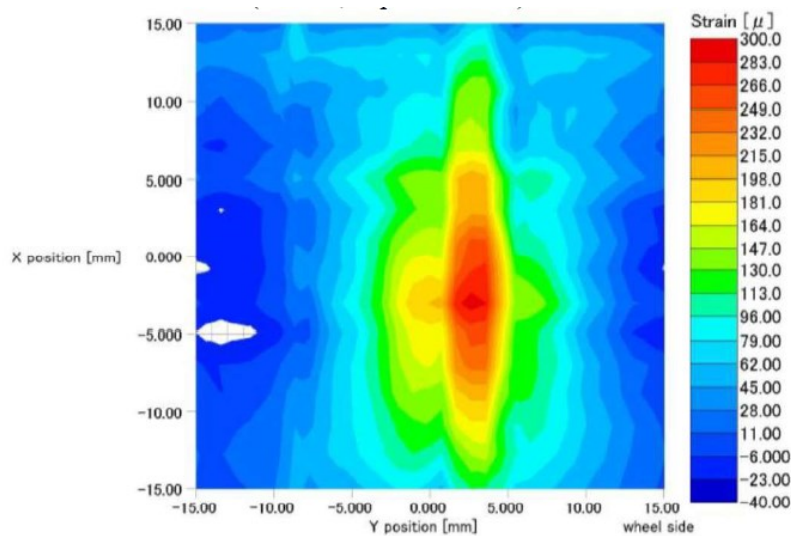


Fig. 2-5-9 Distribution of strains in the rail measured by FBG sensor (Depth: 13 mm) [51]. A three-dimensional distribution map was prepared with a 2mm pitch in the longitudinal direction and 16 sections in the lateral direction.

Poole and Huang *et al.* found their measurements to be in general agreement with the results of Hertz theoretical and FEM numerical calculations, respectively. Although they provide the rough contact geometry of the wheel and rail, more sensitive tribological information to evaluate the frictional behaviour during running-in have not been provided.

2.6 Ultrasound reflectometry

In addition to the experimental evaluation method for wheel-rail contact surfaces introduced in Section 2.5, there are recent examples of the use of ultrasound. Before referring to them, the development of evaluation methods for contact interface using ultrasonics is described first.

2.6.1 Acoustic impedance and reflection coefficient

Acoustic impedance is a numerical expression of the ease of sound propagation. It can be determined by the density of the material, ρ and the velocity, c of sound in the material as Equation (5) [52].

$$z = \rho c \quad (5)$$

At the interface between materials with different acoustic impedances, only a part of a sound wave transmits at the interface and the rest of it is reflected. The reflectivity for ultrasound at an interface where the materials adhere to each other without any cavities, R , can be represented as in Equation (6) and it varies depending on the difference in the acoustic impedances of the two materials.

$$R = \frac{z_2 - z_1}{z_2 + z_1} \quad (6)$$

In this equation, z_1 and z_2 are the acoustic impedances of the materials in contact. Therefore, when the acoustic impedances of the two materials in contact are the same, all the sound wave transmits at the interface without any loss and no reflection occurs ($R=0$). On the other hand, when materials with significantly different acoustic impedances, such as a gas and a solid, are in contact, sound waves are almost completely reflected ($R \approx 1$).

2.6.2 Spring model

It has widely been studied that the intensity of the ultrasonic waves reflected from the contact interface depends on the roughness of the interface and the contact pressure [53]–[56].

A spring model in which the behaviour at the interface between solids in partial contact with each other due to surface roughness is represented by a spring (contact stiffness) to explain the reflective behaviour of ultrasound waves at vertical incidence, obtained from experiments on metal contact surfaces, by changes in contact stiffness [57]–[59].

Schoenberg [60] proposed a model of an imperfectly bonded interface between two elastic media using the concept of "boundary stiffness matrix" which has dimensions stress/length. The displacement across this interface need not be continuous, and the discontinuity of the displacement, or slip, is thought to be linearly related to the continuous stress traction across the interface.

Drinkwater *et al.* [61] also measured the contact stiffness between two aluminium surfaces using ultrasound reflectometry and investigated its frequency dependence. They reported that the reflection coefficient variation with frequency was modelled using the spring model agreed well with the experimental results. When the wavelength of the ultrasound is sufficiently larger than the cavity size at the interface, the reflectivity also depends on the contact stiffness. The contact stiffness is a function of the number, size, and approach of the contact points determined while considering the tiny projections. Because the shape of the unevenness of the surface changes due to elastic and plastic deformation, the measured reflectivity changes as shown in Fig. 2-6-1 as the load is applied. Therefore, it is possible to evaluate the contact condition at the interface by using the reflectivity of ultrasound.

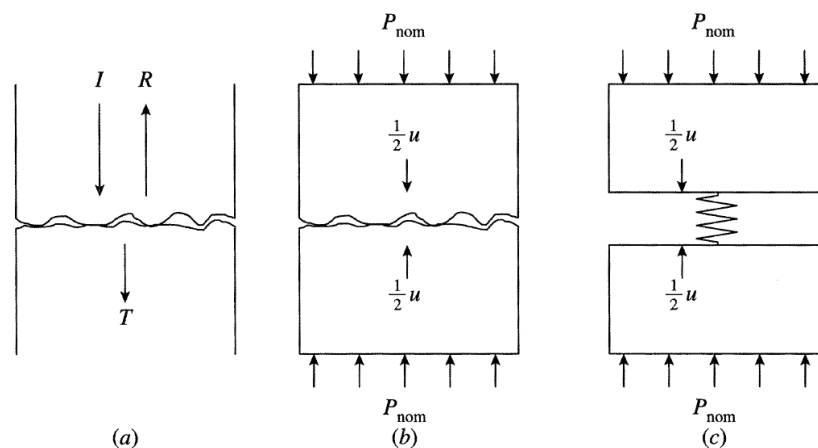


Fig. 2-6-1 Representation of partially contacting interfaces by a spring: (a) geometry of the experimental set-up; (b) static model of the interface; (c) spring model of the interface [61].

The reflectivity of ultrasound was expressed in the following equation [60]:

$$R = \frac{z_2 - z_1 - i\omega(z_1 z_2 / K)}{z_2 + z_1 - i\omega(z_1 z_2 / K)} \quad (7)$$

In the equation, ω and K respectively represent the angular frequency of the ultrasound and the contact stiffness. For the example in this article, the equation can be simplified as

follows because it is assumed that the wheel and the rail are made of the same material ($z_1 = z_2 = z$):

$$|R| = \frac{1}{\sqrt{1 + (2K/\omega z)^2}} \quad (8)$$

Therefore, it is possible to evaluate the contact stiffness K if the reflection coefficient R can be determined in an experiment. Generally, the contact stiffness is defined as a stiffness caused by the surface asperities on the interface the contact stiffness. The intensity of the wave reflected by the interface between steel and air when no load is applied is substantially equivalent to the intensity of the incident wave. It can be used as a simple and effective method for eliminating the influence of the inherent characteristics of the probe and dispersion of the ultrasound.

$$R = \frac{H}{H_0} \quad (9)$$

Biwa *et al.* [62] theoretically pursued the nonlinear pressure dependence of the echo. Dwyer-Joyce *et al.* [63] used ultrasound to investigate changes in contact stiffness at an interface subjected to repeated loading-unloading and captured the transition from plastic to elastic contact. Kim *et al.* [64] also measured the contact condition of the loading-unloading cycles using ultrasound and compared the contact stiffness obtained with the analytical model to obtain the topographic parameters. These parameters were used to predict the real contact area. Gonzalez-Valadez *et al.* [65], [66] measured longitudinal and shear contact stiffness during repeated contact and reported that the ratio was sensitive to roughness and load hysteresis. Gonzalez-Valadez *et al.* [67] used ultrasound to investigate the increase in interfacial stiffness over time and a simplified asperity theory approach to predict the change in contact stiffness over time.

2.6.3 Evaluation for wheel-rail contact

The method of measuring contact conditions by ultrasound has also been applied to the wheel-rail contact interface. Pau *et al.* [68] used a hydraulic cylinder to contact two test specimens cut from a real wheel and rail, respectively, and scanned an ultrasonic probe against the contact area. It is reported that the apparent contact area obtained by binarization of the measured contact surface image is in good agreement with the contact area calculated by Hertz theory (Fig. 2-6-2).

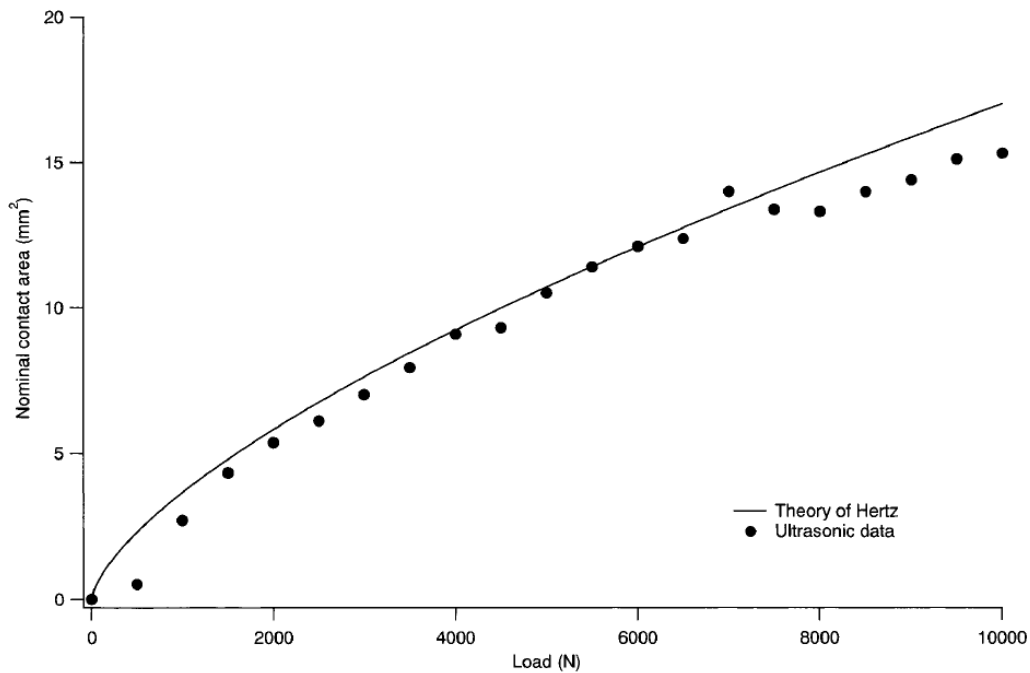


Fig. 2-6-2 Nominal contact area versus applied load: comparison between the experimental data (dot) and Hertz's theory (continuous line) [68].

Pau [69] also applied Królikowski's model [70] to evaluate the real contact area/nominal contact area ratio. Pau found that the RCA increased almost linearly with load, and RCA decreased by about one-seventh as the composite roughness of the wheel-rail system increased by an order of magnitude. Pau *et al.* [71] used ultrasound to measure the shape of the contact patch between rails and wheels that have been machined or artificially made dimples, and investigated the possibility of measuring them (Fig. 2-6-3).

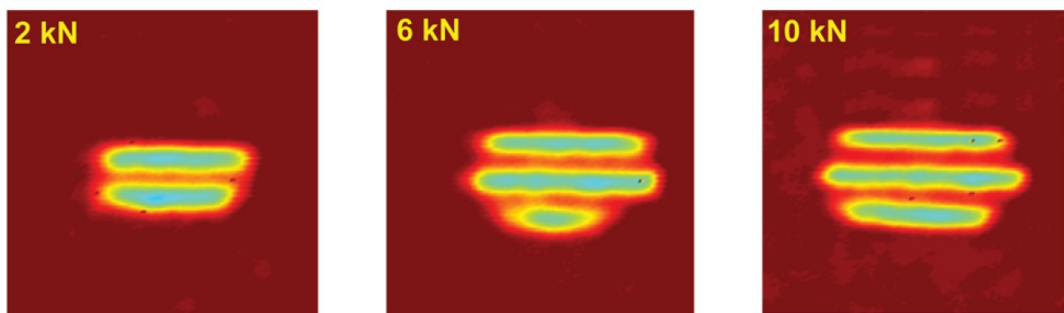


Fig. 2-6-3 Contact maps for the machined wheel [71]. The wheel grooves were 0.5 mm in width, 0.5 mm in depth, with 1.5 mm spacing. The wheel and rail are each cut out near the contact area and pressed statically against each other with a hydraulic jack. The contact area was scanned by a 15 MHz focused immersion ultrasound probe.

Marshall *et al.* [72], [73] measured the distribution of contact stiffness within the wheel-rail contact area, following the previous analysis methods of Drinkwater *et al.* They also found a linearity between contact stiffness and contact pressure, and they applied this relationship to obtain stress distributions (Fig. 2-6-4).

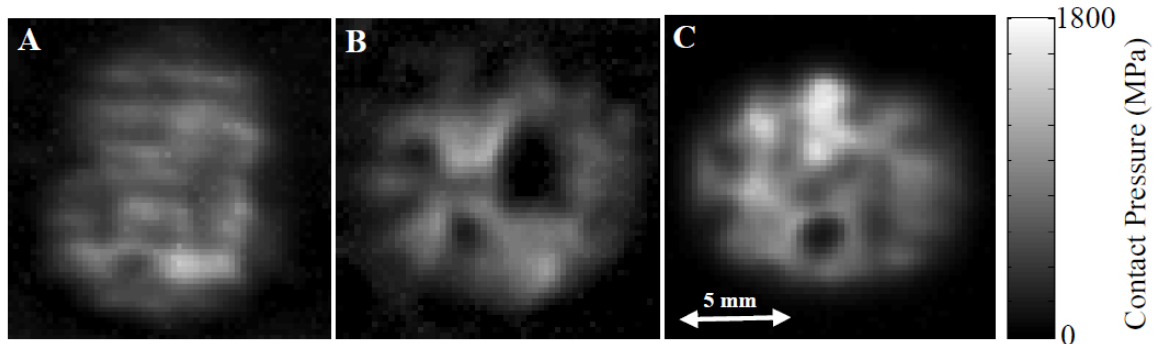


Fig. 2-6-4 Wheel-rail Contact at 65 kN for a) Un-Used; b) Sand Damaged; c) Worn Specimens [72]. The wheel and rail are each cut out near the contact area and pressed statically against each other with a hydraulic jack. The contact area was scanned by a 10 MHz focused immersion ultrasound probe.

Dwyer-Joyce *et al.* [74] investigated the feasibility of using ultrasound on wheels to capture contact conditions. They pressed a set of cut-out wheel and rail together in a biaxial load frame and monitored the reflected signal from the contact interface while varying the normal and lateral loads. The resulting maps of the reflected ultrasound for the applied loads in the two directions were shown (Fig. 2-6-5).

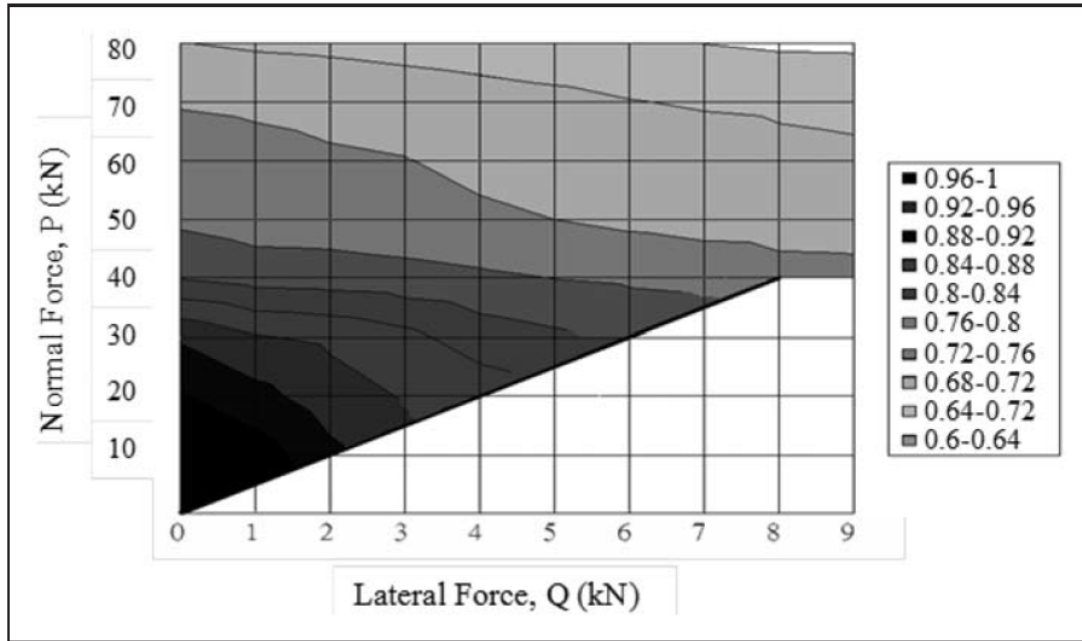


Fig. 2-6-5 Map of the variation of reflection coefficient with normal and lateral loads [74]. A frame and two hydraulic cylinders were used to normally and tangentially load the specimens together. Ultrasonic waves were emitted at the contact area between the rail gauge corner and the wheel flange using 2.25 MHz longitudinal transducer.

Dwyer-Joyce *et al.* [75], Zhou *et al.* [76], [77] and Brunskill *et al.* [78] investigated and realized the measurement of dynamic wheel-rail contact conditions using an array of probes: a line scan was performed with 64 ultrasonic elements arranged in a single row of transducers to monitor wheel-rail contact patches as they passed over the line (Figs. 2-6-6 and 2-6-7). Zhou *et al.* [76] and Brunskill *et al.* [78] inserted the array transducer to the web of rail and evaluated the contact pressure distribution. Figures 2-6-8 and 2-6-9 show the examples of the distributions. These results were obtained by the use of the linear relationship between contact stiffness and contact surface pressure. This method captures the contact condition dynamically and allows for a more precise understanding of frictional phenomena.

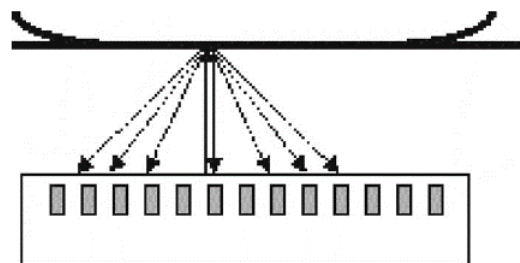


Fig. 2-6-6 An array transducer configured to measure a wheel-rail contact. Since the contact is almost planar, the non-normal reflections are small and neglected [75].

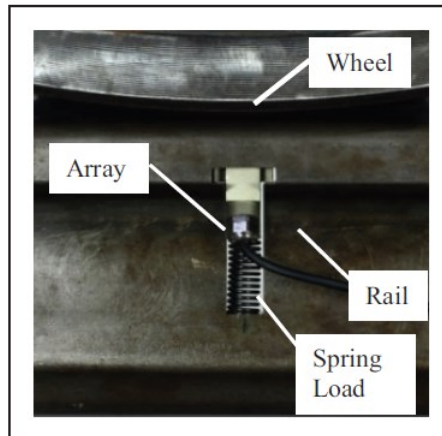


Fig. 2-6-7 The ultrasonic array mounted in a rail section [78]. A 64-element linear array transducer (10MHz) was mounted in a hole cut in the rail.

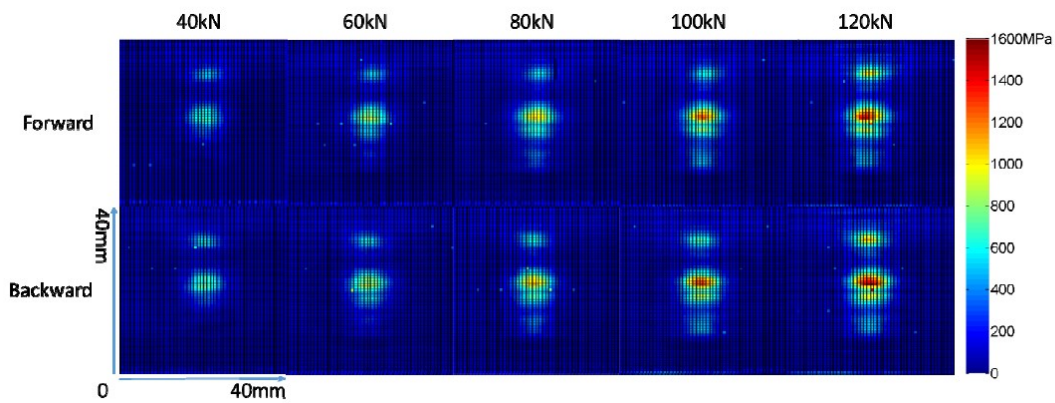


Fig. 2-6-8 The contact area between a rolling wheel and a rail, captured using a 64-element linear array transducer. The rolling speed is 1 mm/s [79].

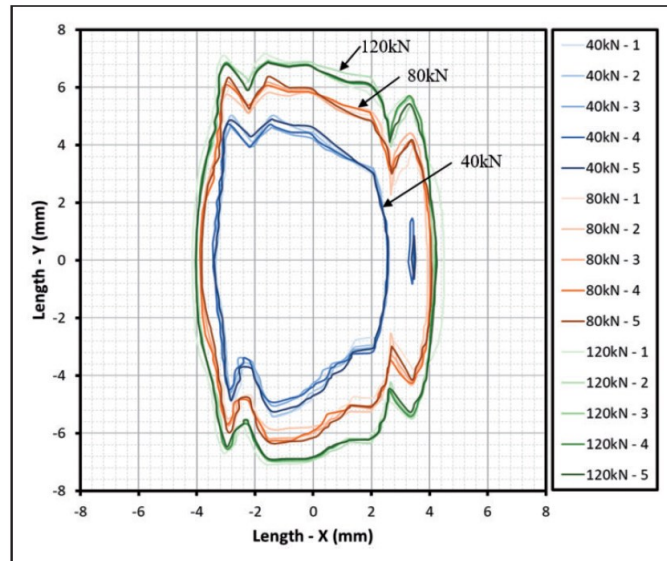


Fig. 2-6-9 200 MPa pressure contours overplotted for five successive passes, at loads of 40 kN, 80 kN, and 120 kN [78]. The contact area between the rolling wheel and the rail was scanned by a linear array transducer (10 MHz).

Furthermore, Zhou *et al.* also investigated a method to measure the contact pressure without adding any pre-machining to the rail [80]. As shown in Fig. 2-6-10, they attached ultrasonic piezoelectric elements directly under the rail head and evaluated the reflection behaviour from the top of the head. Figure 2-6-11 shows the contact pressure distribution of dynamic wheel-rail contact with this method. Although the resolution was not as high as that of Figs. 2-6-8 and 2-6-9, it has the potential to be developed as a field evaluation method.

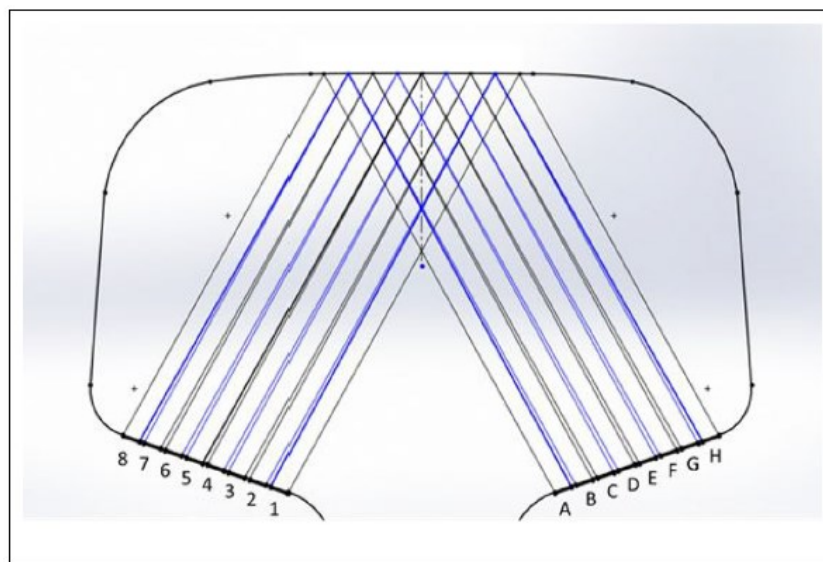


Fig. 2-6-10 The pitch-catch ultrasound measuring technique [80]. The ultrasonic piezoelectric elements (10 MHz) were installed on both sides at the bottom surface of the rail head.

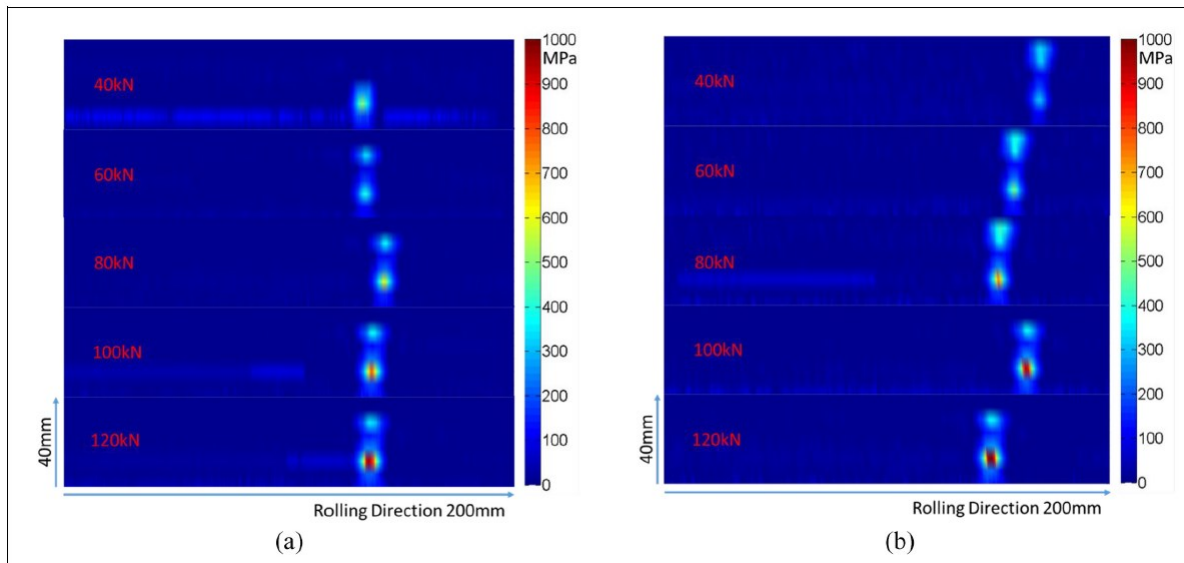


Fig. 2-6-11 Contact pressure distribution of dynamic wheel-rail contact with different loads and different speeds. (a) 5 mm/s.(b) 20 mm/s [80].

2.7 Summary

The literature review covered a wide range of areas, from the basics on wheel-rail contact to flange climb-up derailment, running-in phenomena, and experimental and ultrasonic evaluation methods of the contact interface.

A lot of research on climb-up derailment has already been carried out, both theoretical and experimental, and the methods for evaluating running safety have been brushed up considerably. On the other hand, factors contributing to flange climb-up derailment include high friction coefficients, but it's still being left behind as a factor of uncertainty. In particular, the influence of wheel re-profiling is a matter that is still unclear, and there have been some cases of accidents that occurred after wheel re-profiling in recent years.

There are not many methods to experimentally determine the contact surface and condition of the wheel and rail, and none when it comes to the relationship between surface shape change and friction behaviour.

Meanwhile, the evaluation of the contact interface by ultrasound was found to have potential. The change in contact stiffness with repeated contact has been evaluated by ultrasounds, and the change in contact stiffness was considered to be closely related to the change in the interfacial topography. For application to the wheel-rail interface, this method started with a stationary evaluation approach where the wheels and rails were cut out of blocks. More recently, dynamic evaluations using full-size wheels and rails have become possible.

In wheel-rail studies, the information obtained by ultrasound has been mainly associated with the contact pressure and has not been applied to the evaluation of friction behaviour. A number of studies on the aforementioned running-in phenomena showed that the

interfacial condition changes dramatically during the time between the initiation of the frictional motion of a mechanical element and its reaching a stable state. If the changes of the interfacial condition can be observed in situ by ultrasound, it could provide a breakthrough in understanding the increase of friction coefficient during the wheel running-in process. It may also allow for more accurate prediction and control of the occurrence of climb-up derailments.

References

- [1] S. Iwnicki, M. Spiryagin, C. Cole, and T. McSweeney, *Handbook of railway vehicle dynamics*. CRC press, 2020.
- [2] G. H. Cope, *British Railway Track: Design, Construction and Maintenance sixth edition*. 1993.
- [3] J. Piotrowski and H. Chollet, "Wheel-rail contact models for vehicle system dynamics including multi-point contact," *Veh. Syst. Dyn.*, vol. 43, no. 6–7, pp. 455–483, 2005.
- [4] R. Lewis and U. Olofsson, *Wheel-rail interface handbook*. Elsevier, 2009.
- [5] J. J. Kalker, *Three-Dimensional Elastic Bodies in Rolling Contact*. 1990.
- [6] H. Ishida, T. Miyamoto, E. Maebashi, H. Doi, K. Iida, and A. Furukawa, "Safety assessment for flange climb derailment of trains running at low speeds on sharp curves," *Q. Rep. RTRI*, vol. 47, no. 2, pp. 65–71, 2006.
- [7] J. J. O'Shea and A. A. Shabana, "Analytical and numerical investigation of wheel climb at large angle of attack," *Nonlinear Dyn.*, vol. 83, no. 1–2, pp. 555–577, 2016.
- [8] S. Greene *et al.*, "Flange Climb Derailment Criteria and Wheel/Rail Profile Management and Maintenance Guidelines for Transit Operations," *TCRP Rep. 71 Track-Related Res.*, vol. 5, p. 147, 2005.
- [9] K. Ohno, "Research and development for eliminating wheelclimb derailment accidents," *JR East Tech. Rev.*, no. 2, 2003.
- [10] A. Matsumoto, "Investigations and preventions of derailment accidents in Japan," in *Proceedings of the International Symposium on Speed-up, Safety and Service Technology for Railway and Maglev Systems (STECH'12), 17th - 19th September 2012*, 2012.
- [11] H. Ishida, "Driving Safety (Part 1)-Improving Vehicle Safety by Understanding Derailment-," *JREA (in Japanese)*, vol. 49, no. 11, pp. 32062–32063, 2006.
- [12] H. Takai, M. Uchida, H. Muramatsu, and H. Ishida, "Derailment safety evaluation by analytic equations," *Q. Rep. RTRI*, vol. 43, no. 3, pp. 119–124, 2002.
- [13] T. Tanaka, H. Doi, T. Miyamoto, and H. Iijima, "A study of lateral-force estimation equation focusing on moment of a train bogie," *Trans. JSME (in Japanese)*, vol. 82, no. 842, pp. 16-00054-16-00054, 2016.
- [14] Kousoku Sharyou-you Rinnjiku Kenkyuu Iinkai (Research Committee on Wheel-set for High-speed Vehicles), *Tetsudo Rinjiku (Railway wheel-set) (in Japanese)*, Second. Maruzen Planet, 2011.
- [15] K. Handa, Y. Kimura, and Y. Mishima, "Ferrite and spheroidized cementite ultrafine microstructure formation in an Fe-0.67 Pct C steel for railway wheels under simulated service conditions," *Metall. Mater. Trans. A Phys. Metall. Mater. Sci.*, vol. 40, no. 12, pp. 2901–2908, 2009.

- [16] Y. Hu *et al.*, "Microstructure evolution of railway pearlitic wheel steels under rolling-sliding contact loading," *Tribol. Int.*, vol. 154, no. July 2020, 2021.
- [17] "Keeping on track." [Online]. Available: https://www.sandvik.coromant.com/en-gb/mww/pages/t_keepingontrack.aspx. [Accessed: 23-Jun-2020].
- [18] "Railway turning, re-turning and new wheel turning." [Online]. Available: <https://www.sandvik.coromant.com/sitecollectiondocuments/downloads/global/technical guides/en-gb/c-1020-019.pdf>. [Accessed: 23-Feb-2020].
- [19] H. Iijima *et al.*, "Investigation of the cause and verification of countermeasure for a low-speed flange climb derailment that occurred in the Oku station," *Tech. Rev. JR East (in Japanese)*, no. 29, pp. 21–26, 2009.
- [20] H. Takai, "Practical Methods for Evaluating the Safety of Railway Vehicles against Climb Derailment and Their Applications," Thesis of The University of Tokyo (in Japanese), 2013.
- [21] J. T. S. Board, "Railway Accident Investigation Report RA2007-6," 2007.
- [22] J. T. S. Board, "Railway Accident Investigation Report RA2008-02," 2008.
- [23] R. A. I. Branch, "Rail Accident Report, Locomotive derailment at Ordsall Lane Junction, Salford, 23 January 2013," 2014.
- [24] R. A. I. Branch, "Safety digest, Locomotive derailment at Doncaster, 21 December 2018," 2019.
- [25] A. W. J. de Gee and G. W. Rowe, *Glossary of Terms and Definitions in the Field of Friction, Wear, and Lubrication: Tribology*. Organization for Economic Co-operation and Development, Paris, 1969.
- [26] F. Hirano, "Running-in Process of Metals," *J. Japan Soc. Lubr. Eng. (in Japanese)*, vol. 30, no. 5, pp. 377–384, 1985.
- [27] P. J. Blau, *Friction and wear transitions of materials*. Noyes publications, 1989.
- [28] P. J. Blau, "A model for run-in and other transition in sliding friction.," vol. 109, no. July, pp. 537–543, 1986.
- [29] P. J. Blau, "On the nature of running-in," *Tribol. Int.*, vol. 38, no. 11–12, pp. 1007–1012, Nov. 2005.
- [30] P. J. Blau, *Friction science and technology*. New York : M. Dekker, 1996.
- [31] P. J. Blau, "How common is the steady-state? The implications of wear transitions for materials selection and design," *Wear*, vol. 332–333, pp. 1120–1128, May 2015.
- [32] K. J. Stout, T. G. King, and D. J. Whitehouse, "Analytical techniques in surface topography and their application to a running-in experiment," *Wear*, vol. 43, no. 1, pp. 99–115, 1977.

- [33] T.A.Spedding, W.Watson, T.G.King, and K.J.Stout, "Sampling variation in surface profile skewness and kurtosis measurements," in *Proceedings of the 8th Leeds-Lyon Symposium on Tribology*, 1981, pp. 49–57.
- [34] T. A. Spedding, T. G. King, W. Watson, and K. J. Stout, "The pearson system of distributions: Its application to non-gaussian surface metrology and a simple wear model," *J. Tribol.*, vol. 102, no. 4, pp. 495–500, 1980.
- [35] J. Lundmark, E. Hoglund, and B. Prakash, "Running-in Behaviour of Rail and Wheel Contacting Surfaces," *Int. Conf. Tribol.*, no. September, pp. 1–12, 2006.
- [36] J. Lundmark, E. Kassfeldt, J. Hardell, and B. Prakash, "The influence of initial surface topography on tribological performance of the wheel/rail interface during rolling/sliding conditions," *Proc. Inst. Mech. Eng. Part F J. Rail Rapid Transit*, vol. 223, no. 2, pp. 181–187, 2009.
- [37] K. S. Baek, K. Kyogoku, and T. Nakahara, "An experimental investigation of transient traction characteristics in rolling-sliding wheel/rail contacts under dry-wet conditions," *Wear*, vol. 263, no. 1-6 SPEC. ISS., pp. 169–179, 2007.
- [38] K. S. Baek, K. Kyogoku, and T. Nakahara, "An experimental study of transient traction characteristics between rail and wheel under low slip and low speed conditions," *Wear*, vol. 265, no. 9–10, pp. 1417–1424, 2008.
- [39] T. Nakahara, K. S. Baek, H. Chen, and M. Ishida, "Relationship between surface oxide layer and transient traction characteristics for two steel rollers under unlubricated and water lubricated conditions," *Wear*, vol. 271, no. 1–2, pp. 25–31, 2011.
- [40] M. Mesaritis *et al.*, "A laboratory demonstration of rail grinding and analysis of running roughness and wear," *Wear*, vol. 456–457, no. April, p. 203379, 2020.
- [41] J. Stow and P. Allen, "A Good Practice Guide for Managing the Wheel-Rail Interface of Light Rail and Tramway Systems," *Off. Rail Regul. Manchester*, Jan. 2008.
- [42] T. Ban, H. Kakishima, K. Iida, E. Maebashi, H. Ishida, and M. Ishida, "A study on the coefficient of friction between rail gauge corner and wheel flange focusing on wheel machining," *Proc. Int. Wheel. Congr.*, 2004.
- [43] H. Doi, T. Miyamoto, J. Suzumura, J. Nakahashi, H. Chen, and T. Ban, "Change in Surface Condition of Turned Wheel and Effectiveness of Lubrication Turned against Flange Climb Derailment," *Q. Rep. RTRI*, vol. 53, no. 2, pp. 70–76, 2012.
- [44] A. Kataori, K. Doi, H. Iijima, S. Momosaki, and S. Matsumoto, "The Influence of the Wheel/Rail Contact Point Condition on Friction Coefficient," *9th World Conf. Railw. Res.*, 2011.
- [45] H. I. Andrews, "The contact between a locomotive driving wheel and the rail," *Wear*, vol. 2, no. 6, pp. 468–484, 1959.
- [46] S. Kumar and B. R. Rajkumar, "Laboratory investigation of wheel rail contact stresses for U.S. Freight cars," *J. Manuf. Sci. Eng. Trans. ASME*, vol. 103, no. 2, pp. 246–255, 1981.

- [47] O. Kleiner and C. Schindler, "Geometrie und Druckspannungen im Rad/Schiene-Kontakt," *El-Eisenbahningenieur*, no. 4, pp. 9–12, 2011.
- [48] J. Lekue, F. Dörner, and C. Schindler, "On the Source of the Systematic Error of the Pressure Measurement Film Applied to Wheel-Rail Normal Contact Measurements," *J. Tribol.*, vol. 140, no. 2, pp. 1–4, 2018.
- [49] J. Lekue, F. Dörner, and C. Schindler, "Multiscale Finite Element Modeling of Wheel–Rail Rough Normal Contact Measurements Using Pressure Measurement Film," *Tribol. Trans.*, vol. 61, no. 5, pp. 972–978, 2018.
- [50] W. Poole, "The measurement of the contact area between opaque objects under static and dynamic rolling conditions," in *Proceedings of Contact Mechanics and Wear of Rail/Wheel Systems II*, 1986, pp. 59-72.
- [51] C. Hung *et al.*, "Experiments to Measure Stress with the Wheel / Rail Contact Using Embedded FBG Sensors," in *The Transportation and Logistics Conference (in Japanese)*, p. 3208.
- [52] L. E. Kinsler and A. R. Frey, *Fundamentals of acoustics*. John Wiley & Sons, 1950.
- [53] T. Arakawa, "A study on the transmission and reflection of an ultrasonic beam at machined surfaces pressed against each other," *Mater. Eval.*, vol. 41, pp. 714–719, 1983.
- [54] M. Geiger, U. Engel, and F. Vollertsen, "In Situ Ultrasonic Measurement of the Real Contact Area in Bulk Metal Forming Processes," *CIRP Ann. - Manuf. Technol.*, vol. 41, no. 1, pp. 255–258, 1992.
- [55] Y. Minakuchi, K. Yoshimine, T. Koizumi, and T. Hagiwara, "Contact Pressure Measurements by Means of Ultrasonic Waves: On a Method of Quantitative Measurement," *Bull. JSME*, vol. 28, no. 235, pp. 40–45, 1985.
- [56] M. Pau, F. Aymerich, and F. Ginesu, "Measurements of nominal contact area in metallic interfaces: A comparison between an ultrasonic method and a pressure-sensitive film," *Wear*, vol. 249, no. 5–6, pp. 533–535, 2001.
- [57] K. Kendall and D. Tabor, "An Ultrasonic Study of the Area of Contact between Stationary and Sliding Surfaces," *Proc. R. Soc. A Math. Phys. Eng. Sci.*, vol. 323, no. 1554, pp. 321–340, 1971.
- [58] H. G. Tattersall, "The ultrasonic pulse-echo technique as applied to adhesion testing," *J. Phys. D. Appl. Phys.*, vol. 6, pp. 819–832, 1973.
- [59] J. Królikowski and J. Szczepek, "Prediction of contact parameters using ultrasonic method," *Wear*, vol. 148, no. 1, pp. 181–195, 1991.
- [60] M. Schoenberg, "Elastic wave behavior across linear slip interfaces," *J. Acoust. Soc. Am.*, vol. 68, no. 5, pp. 1516–1521, 1980.
- [61] B. W. Drinkwater, R. S. Dwyer-Joyce, and P. Cawley, "A study of the interaction between ultrasound and a partially contacting solid—solid interface," *Proc. R. Soc. London. Ser. A Math. Phys. Eng. Sci.*, vol. 452, no. 1955, pp. 2613–2628, Jan. 1996.

- [62] S. Biwa, S. Nakajima, and N. Ohno, "On the acoustic nonlinearity of solid-solid contact with pressure-dependent interface stiffness," *J. Appl. Mech. Trans. ASME*, vol. 71, no. 4, pp. 508–515, 2004.
- [63] R. S. Dwyer-Joyce, B. W. Drinkwater, and A. M. Quinn, "The Use of Ultrasound in the Investigation of Rough Surface Interfaces," *J. Tribol.*, vol. 123, no. 1, p. 8, 2001.
- [64] J. Y. Kim, A. Baltazar, and S. I. Rokhlin, "Ultrasonic assessment of rough surface contact between solids from elastoplastic loading-unloading hysteresis cycle," *J. Mech. Phys. Solids*, vol. 52, no. 8, pp. 1911–1934, 2004.
- [65] R. S. Dwyer-Joyce and M. Gonzalez-Valadez, "Ultrasonic Determination of Normal and Shear Interface Stiffness and the Effect of Poisson's Ratio," *Transient Process. Tribol.*, pp. 143–149, 2004.
- [66] M. Gonzalez-Valadez, A. Baltazar, and R. S. Dwyer-Joyce, "Study of interfacial stiffness ratio of a rough surface in contact using a spring model," *Wear*, vol. 268, no. 2–3, pp. 373–379, 2010.
- [67] M. Gonzalez-Valadez and R. S. Dwyer-Joyce, "Asperity Creep Measured by the Reflection of Ultrasound at Rough Surface Contact," *J. Tribol.*, vol. 131, no. 2, p. 021410, 2009.
- [68] M. Pau, F. Aymerich, and F. Ginesu, "Ultrasonic measurements of nominal contact area and contact pressure in a wheel-rail system," *Proc. Inst. Mech. Eng. Part F J. Rail Rapid Transit*, vol. 214, no. 4, pp. 231–243, 2000.
- [69] M. Pau, "Estimation of real contact area in a wheel-rail system by means of ultrasonic waves," *Tribol. Int.*, vol. 36, no. 9, pp. 687–690, 2003.
- [70] J. Królikowski and J. Szczepek, "Phase shift of the reflection coefficient of ultrasonic waves in the study of the contact interface," *Wear*, vol. 157, no. 1, pp. 51–64, 1992.
- [71] M. Pau, "Ultrasonic waves for effective assessment of wheel-rail contact anomalies," *Proc. Inst. Mech. Eng. Part F J. Rail Rapid Transit*, vol. 219, no. 2, pp. 79–90, 2005.
- [72] M. B. Marshall, R. Lewis, R. S. Dwyer-Joyce, O. Olofsson, and S. Björklund, "Measuring Wheel/Rail Contact Stresses using Ultrasound," *14th Int. Wheel. Congr.*, pp. 17–21, 2004.
- [73] M. B. Marshall, R. Lewis, R. S. Dwyer-Joyce, U. Olofsson, and S. Björklund, "Experimental Characterization of Wheel-Rail Contact Patch Evolution," *J. Tribol.*, vol. 128, no. 3, pp. 493–503, 2006.
- [74] R. S. Dwyer-Joyce, C. Yao, R. Lewis, and H. Brunskill, "An ultrasonic sensor for monitoring wheel flange/rail gauge corner contact," *Proc. Inst. Mech. Eng. Part F J. Rail Rapid Transit*, vol. 227, no. 2, pp. 188–195, 2013.
- [75] R. S. Dwyer-Joyce, C. Yao, J. Zhang, R. Lewis, and B. W. Drinkwater, "Feasibility Study for Real Time Measurement of Wheel-Rail Contact Using an Ultrasonic Array," *J. Tribol.*, vol. 131, no. 4, p. 041401, 2009.

- [76] L. Zhou, H. Brunskill, R. Lewis, M. Pletz, W. Daves, and S. Scheriau, "Real time Measurement of Dynamic Wheel-Rail Contacts Using Ultrasonic Reflectometry," *ASME J. Tribol.*, vol. 141, no. 6, 2019.
- [77] R. Zhou, L., Marshall, M.B., Lewis, "Ultrasonic Wheel-Rail Contact Assessment at an Insulated Block Joint," *Int. J. Railw. Technol.*, vol. 6, no. 4, pp. 29–49, 2017.
- [78] H. Brunskill, A. Hunter, L. Zhou, R. Dwyer Joyce, and R. Lewis, "An evaluation of ultrasonic arrays for the static and dynamic measurement of wheel–rail contact pressure and area," *Proc. Inst. Mech. Eng. Part JJ. Eng. Tribol.*, vol. 234, no. 10, pp. 1580–1593, 2020.
- [79] L. Zhou, H. P. Brunskill, R. Lewis, M. B. Marshall, and R. S. Dwyer-Joyce, "Dynamic characterisation of the wheel/rail contact using ultrasonic reflectometry," *Civil-Comp Proc.*, vol. 104, pp. 1–13, 2014.
- [80] L. Zhou, H. P. Brunskill, and R. Lewis, "Real-time non-invasive measurement and monitoring of wheel–rail contact using ultrasonic reflectometry," *Struct. Heal. Monit.*, vol. 0, no. 0, p. 1475921719829882.

3 UNDERSTANDING THE CHANGE OF FRICTION COEFFICIENT AND SURFACE CONDITION AFTER WHEEL RE-PROFILING

Paper 1

Tribological aspects to optimize traction coefficient during running-in period using surface texture

S. Fukagai^{a, c}, L. Ma^b, R. Lewis^a,

^a Leonardo Centre for Tribology, Department of Mechanical Engineering, University of Sheffield, Sheffield, UK

^b Sorby Centre, Department of Materials Science and Engineering, University of Sheffield, Sheffield, UK

^c Railway Technical Research Institute, Tokyo, Japan

Abstract

Risk of wheel-climb derailment increases if the traction coefficient in the wheel/rail contact is too high. This has been observed to happen more just after wheel turning. This novel work investigates how the traction coefficient rises during the running-in period, when textured surfaces are used to simulate a freshly turned wheel. Running-in curve of traction coefficient showed a momentary rise and a peak value of traction coefficient was observed to decrease with the increase in the magnitude of the wheel surface texture. The change of the subsurface hardness and the microstructure were also dependent on the initial surface texture coincidentally and the work-hardening layer of the textured surface was thicker than that of smooth surface. A mechanism model of the effects of surface texture on traction characteristics during the running-in was presented. The work will allow recommendations of wheel turning to be made to help reduce the problem of wheel-climb derailment.

Published in *Wear* Vol 424-425 (2019) 223-232, ISSN 0043-1648

3.1 Introduction

Since the frictional condition between railway wheel and rail has an important role in the transmission of the driving force and braking force, it should be kept at a high level to secure the appropriate acceleration performance and braking distance. On the other hand,

the risk of wheel climb derailment will be increased if the traction coefficient is too high at sharp curves because it generates a greater force in the lateral direction, namely toward to the outside of a curve. The force presses the wheelset against the gauge corner of the outer rail and could cause the flange to climb up [1]–[3]. Therefore, it is important to understand the phenomenon and appropriately control the friction condition. The general method to control the friction condition is the application of lubrication between the wheel and rail. However, installation of lubrication equipment or work by hand at the depot would make an additional expense and a significant contamination around the bogie. Moreover, excessive lubrication causes slips.

A railway wheel experiences re-profiling several times during its whole life to reset it to the designed profile from the worn profile or to remove damage, such as wheel flats and cracks. And it is known that some derailments have occurred relatively soon after the re-profiling of wheels [4]–[7]. Just after the re-profiling, there are machining marks which depend on the shape of the cutting tool and the feed rate at the wheel surface. Some reports mention the possibility that the rougher surface leads to a higher traction coefficient and it increases the risk of flange climb derailment [6]–[8]. Namely, they indicate that the spike-like machining marks cause an increase of traction during the running-in period as they plough into the rail material. Therefore, a smooth surface is recommended at the finishing of wheel machining sometimes [6], [8]. On the other hand, there is another opinion that mentions that the traction force is increased with the deformation of machining marks and increase in real contact area [4], which means that adhesion predominantly affects the increase. Though the mechanism for the traction behaviour during running-in has not been clarified well, there are experimental results using a twin-disk test machine to investigate the influence of the surface texture on the traction characteristics as follows.

Yamamoto *et al.* reported that the traction coefficient of the interface between wheel tread/top of rail could be reduced by optimizing the texture using twin disk tests [9], [10]. They indicated that the application of these textures to a wheel during turning might reduce the risk of derailment. Therefore, there is a possibility to optimize the surface treatment of wheels by the use of the existing re-profiling equipment with the more detailed investigation about the mechanism. Especially, which friction condition between wheel flange/rail gauge corner contact would relate best to the wheel climb derailment. Lundmark *et al.* carried out some case studies of frictional behaviour using different initial roughness and reported that the combination of a rough wheel disk and a smooth rail disk showed the lowest traction coefficient [11]. As a possible reason, the influence of a small difference in the hardness of the work-hardened layer of a rough wheel was indicated. It is well known that the transitions in frictional behaviour during running-in are influenced by not only the change of surface topography. They can also relate to changes in surface composition, microstructure and third-body layer, depending on the

environment. Blau also indicated that the crystallographic reorientation and the surface conformity could be possible causes to characterize the running-in behaviour on metal-metal friction [12], [13]. Baek *et al.* reported that the work-hardening and tribochemical reactions near the surface affect the transition of the traction coefficient differently between dry and wet conditions [14]–[16]. However, it has not been fully understood. To control the traction characteristics and provide a better solution to the flange climb derailment, understanding the behaviour at the interface of wheel/rail during the running-in period and generalizing the model is important.

The aim of this work was to investigate the effects of applying surface texture on traction characteristics during the running-in period and to analyze the tribological mechanisms causing the effect under dry conditions. The tests were carried out using a twin-disk machine. Conditions that simulated the wheel flange/rail gauge corner contact were used. After the tests, the used disks were investigated using an optical surface measurement system (InfiniteFocusSL, Alicona) and a contact-type roughness meter (Surfcorder SE3500, Kosaka Laboratory Ltd.), a micro-Vickers hardness testing machine (Durascan, Struers), optical microscope (Axio Observer, ZEISS), an FEG-SEM (Inspect F50, FEI) with EBSD (Oxford Instrument) and an XPS surface analysis instrument (Supra, Kratos Analytical). The wear debris generated during the test was also collected and the amount was investigated. Finally, mechanistic modelling was presented to explain the effect of surface texture. These findings might inform rail service providers about optimal wheel profiling methods and surface treatments to reduce the likelihood of wheel climb derailments.

3.2 Methodology

3.2.1 Apparatus

Figure 3-1 shows a schematic diagram of the twin-disk rolling-sliding test machine [9], [10], [14]–[16], which is equipped with a small wheel disk and rail disk, and Table 3-1 shows the performance of the experimental apparatus. The wheel disk and the rail disk are connected to separate servomotors. These motors rotate independently and the slip ratio between the disks is prescribed by setting different rotational speeds for each motor. The braking motor is supported by a linear guide that can move in the axial direction. The vertical load is applied to the test disks by use of a coil spring.

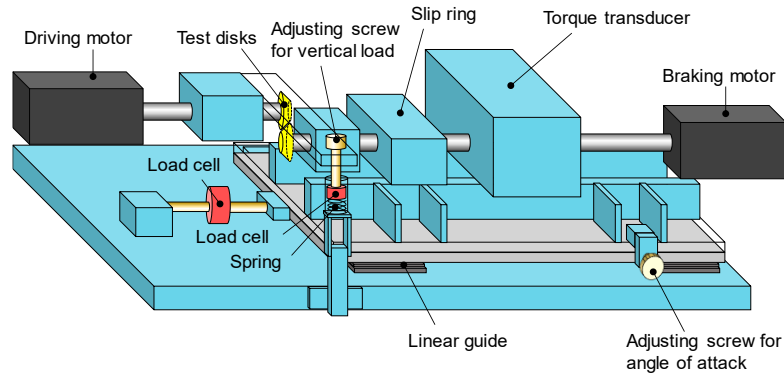


Fig. 3-1 Schematic diagram of the twin-disk rolling-sliding test machine.

Table 3-1 Performance of the experimental apparatus

Rotational speed (rpm)	0~4000
Vertical load (kN)	0~0.5
Slip ratio (%)	0~5
Angle of attack (°)	-3 to +3

3.2.2 Test disks

Figure 3-2 shows the shape and dimension of the test disks. They were cut from actual railway wheels and rails; SSW-Q3S (JIS E 5402) and 50N (JIS E 1101) for the wheel and rail, respectively. In order to simulate the wheel flange/rail gauge corner contact, the wheel disk was made to be a “conical” shape and the rail disk was made to be a “crowned” shape. The straight section of actual wheel flange is 60 -70 degrees. However, the contact between wheel flange and rail gauge corner will take place at not only the straight section, but also the flange root. Therefore, the angle will change from approximately 0 to 70 degrees. Since this is the first trial to evaluate the traction coefficient in the direction for the derailment, the taper angle of wheel disk was chosen as 45 degrees for manufacturing reasons in this study. The shape was designed to have the same radius, 30 mm, at the contact point. Figure 3 shows the surface profiles of the test disks which were obtained using a contact-type roughness meter. Three different types of wheel disks were prepared through surface finishing operations. Disk-A is the most smooth surface which was acquired by grinding. Since the railway wheel is generally re-profiled by use of a machining tool, the micro-texture disks B and C were applied this technique; 0.5 mm/rev and 1.0 mm/rev tools pitch were used for disk-B and disk-C, respectively. The direction of machining was parallel to the direction of disk rotation. This means that the machining marks were oriented across the direction of rotation to simulate the actual machining

situation of the wheel. Rail disks had just one type of surface which was acquired by grinding. Table 3-2 shows the characteristics of disk surfaces. The roughness values were obtained using a roughness meter.

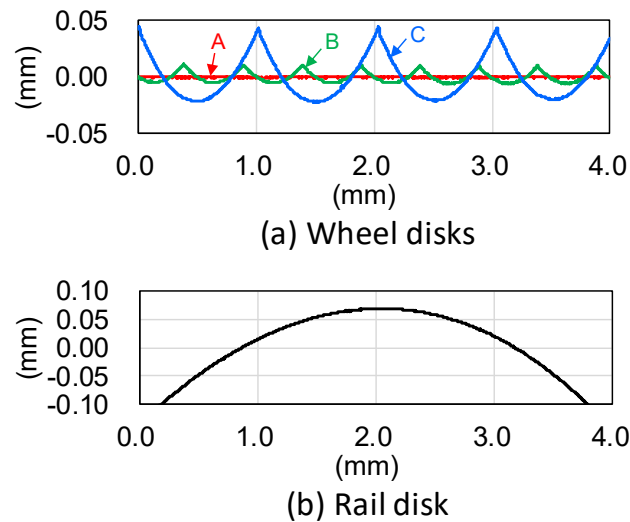


Fig. 3-3 Surface profile of test disks.

Table 3-2 Characteristics of the disk surface

	Pitch of machining (mm)	Ra (μm)	Pz (μm)
Wheel disk-A	-	0.2	2.2
Wheel disk-B	0.5	3.5	16.7
Wheel disk-C	1.0	6.2	67.1
Rail disk	-	1.1	-

3.2.3 Test procedure

Table 3-3 shows the experimental conditions. In general, the Hertzian maximum contact pressure at the wheel flange/ rail gauge corner is up to 2700 MPa [17]. Accordingly, the standard contact pressure was set at 2200 MPa. The standard speed was set at 0.16 m/s; this was done to avoid resonance in the experimental apparatus. As will be described later, it was necessary to stop the test at a characteristic stage to examine the specimen. In determining the speed, consideration was also given to making the test speed slow enough to allow the machine to stop properly at the stages. From the considerations of

the contact situation at the wheel flange/rail gauge corner, the standard slip ratio and angle of attack were set at 2% and 1°, respectively. These values were defined by the results of preliminary simulations of a derailment.

Table 3-3 Experimental conditions

Rotational speed (rpm, m/s)	100, 0.16
Vertical load (kN) / Hertzian maximum contact pressure (MPa)	0.3 kN / 2200
Slip ratio (%)	2
Angle of attack (°)	+1
Room temperature (°C)	14.3 - 21.1
Room humidity (RH%)	30 - 34

The surfaces of the test disks were washed with petroleum ether in an ultrasonic washing vessel before the experiments to remove contaminants such as oil and dust. Figure 3-4 shows a set of wheel and rail disks after attachment on the experimental apparatus. In the experimental apparatus vertical load V and lateral load L were measured; but for detecting the traction coefficient in the lateral direction, these were used to determine the normal force N and the lateral traction force in the lateral direction F_y with the following equations:

$$N = V \cos \alpha + L \sin \alpha, \quad (1)$$

$$F_y = V \sin \alpha - L \cos \alpha \quad (2)$$

where α is the contact angle (45° in this experiment).

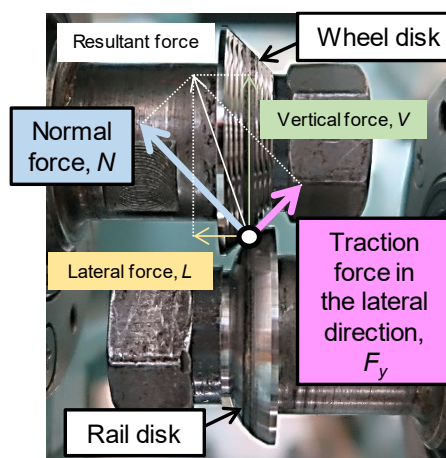


Fig. 3-4 A set of wheel disk and rail disk after attaching on the experimental apparatus.

The surface profile was measured at different stages, the detail of the stage is to be mentioned in the next section, using an optical surface measurement system that had a vertical resolution of 50 nm and a contact-type roughness meter that had a vertical resolution of 200 nm. For the quantification of the plastic deformation by means of hardness, HV0.05 hardness profiles were performed from the deformed near-surface zone into the bulk using a micro-Vickers hardness testing machine. The metallic structures of cross-sections were observed by an optical microscope and FEG-SEM with EBSD. Samples were prepared by rough grinding, diamond suspension polishing followed by colloidal silica polishing. The acceleration voltage of SEM and EBSD was 20 keV. The spot size was 5 μm and the aperture size was 3 μm . The chemical composition on the surface was analyzed by an XPS surface analysis instrument with a monochromated aluminium source. An Ar_{500}^+ at 20 keV source was used to etch away the surface for 300 seconds, and then restricted high-resolution scans were collected over the O 1s and Fe $2p_{3/2}$ regions. This was repeated 10 times to build up a depth profile. The Ar_{500}^+ source at 20 keV has been shown to have an etch rate of 8.3 nm/min through Ta_2O_5 on Ta. During the experiments, a tray was left under the specimens and the amount of wear particles was evaluated.

3.3 Results

3.3.1 Effect of initial surface texture on traction coefficient

Figure 3-5 shows the change of traction coefficient in the lateral direction with running time. The tests were carried out three or four times at the same condition and it was shown that there was the reproducibility for every type of wheel disk. It was found that the change of traction coefficient depends on the initial surface texture. Though every type of wheel disk showed a momentary rise in traction coefficient during running-in, the rougher the initial surface profile was, the smaller the peak value of traction coefficient was. Figure 3-6 shows the schematic patterns of the traction coefficient curve in Fig. 5. "Stage-I" means the condition before the test, "stage-II" means the condition around the peak of the traction coefficient and "stage-III" means the condition after the test. The rougher the initial surface profile was, the longer time took it to reach the peak value. Hereinafter, the analysis of the disks for each characteristic stage (I, II and III) was carried out. Here, the analysis for stage-II was carried out by discontinuing a test after confirming the reproducibility of the change of traction coefficient.

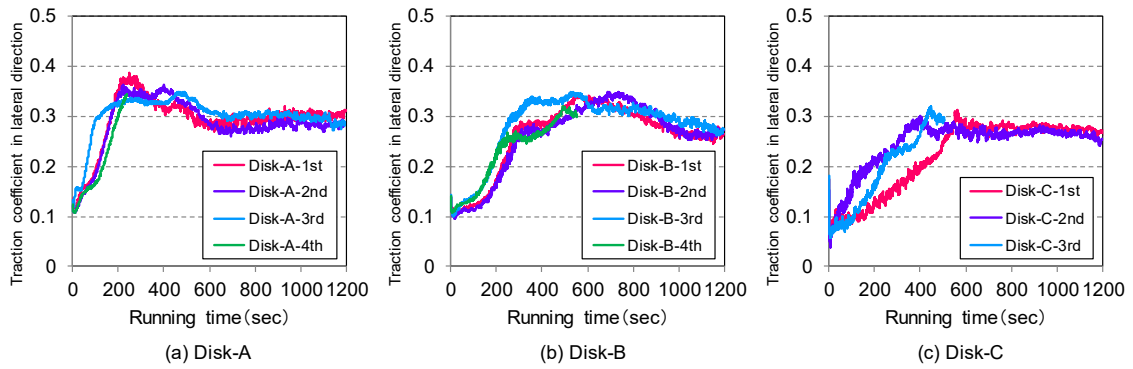


Fig. 3-5 Change of traction coefficient in the lateral direction with running time.

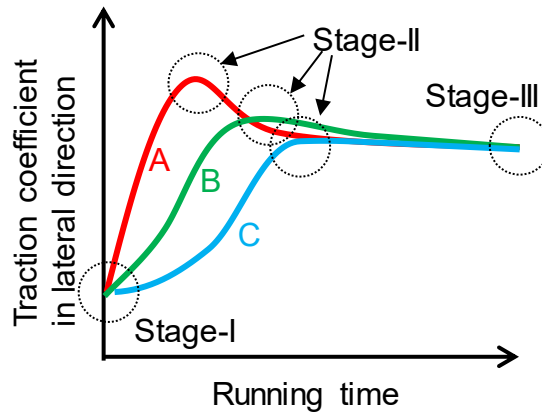
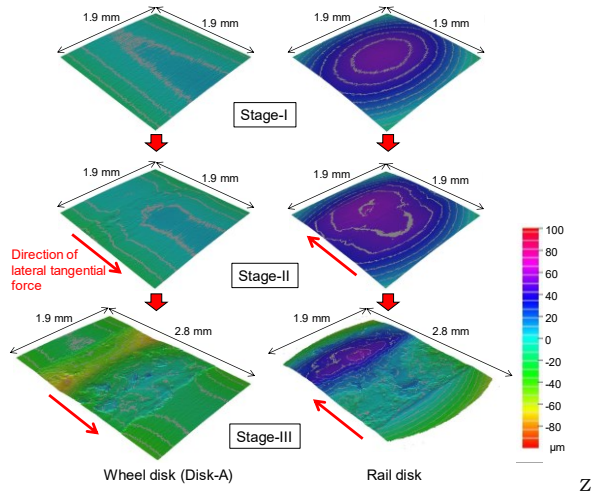


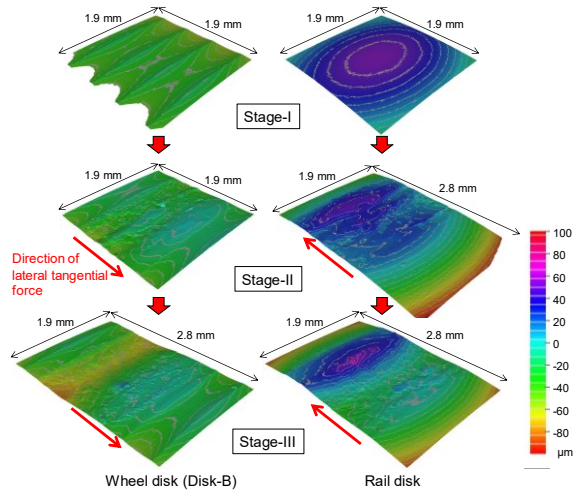
Fig. 3-6 Schematic patterns of the traction coefficient curves in Fig. 3-5.

3.3.2 Surface texture

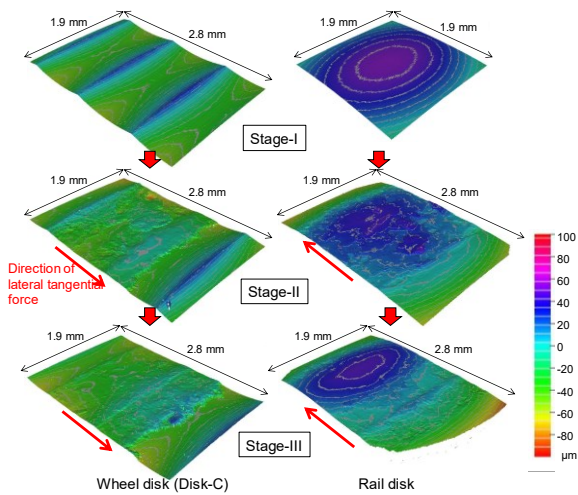
Figure 3-7 shows the change of surface topography of wheel disk and rail disk for each stage which was obtained using an optical surface measurement system. It is clearly shown that the surface deformation increased with the progress of the stage and the direction of plastic flow corresponded to that of traction force in the lateral direction for every type of wheel disks. The initial ridges of disk-B and disk-C were almost made flat at stage-II. Though disk-B and -C seems to proceed the conformity with the progress of stage, the surface of disk-A at stage-III seems to be rougher than that at stage-II.



(a) Wheel disk-A and rail disk



(b) Wheel disk-B and rail disk



(c) Wheel disk-C and rail disk

Fig. 3-7 Change of surface topography of wheel disk and rail disk for each stage.

Figure 3-8 shows the surface profile of test disks for each initial surface profile and stage which was obtained using the contact-type roughness meter. It was found that the surface shapes of the wheel disk and the rail disk went close to the similar shapes each other by the generation of traction force in the lateral direction. It appeared this conformation of the surface profile progressed with the progress of stages and the shape at the stage-III was similar in all initial surface profiles.

Disk-C showed that more or less only one spike was in contact. The radius of the actual rail gauge corner is 13 mm, and the machining pitch of an actual wheel is about 1 – 2 mm. The radius of this rail specimen was 10 mm, and the machining pitches of the wheel specimen were 0.5 and 1 mm.

The contact load is much smaller than that of an actual vehicle and the total energy is also smaller. However, since Hertzian pressure equivalent to that of an actual vehicle is generated, a relative comparison of the local influence of the initial surface geometry on the running-in phenomenon at the contact area is considered possible. In a previous study using the same testing machine [15], the temperature change of the specimens was investigated, but even under the similar test conditions, the temperature rise of the specimens was less than 50°C, so the temperature effects of different scales of specimens are considered to be small.

One author reported that the actual contact shape was made of a few strips by tests using a full-scale wheel/rail contact machine and the result of this study agrees with that [18].

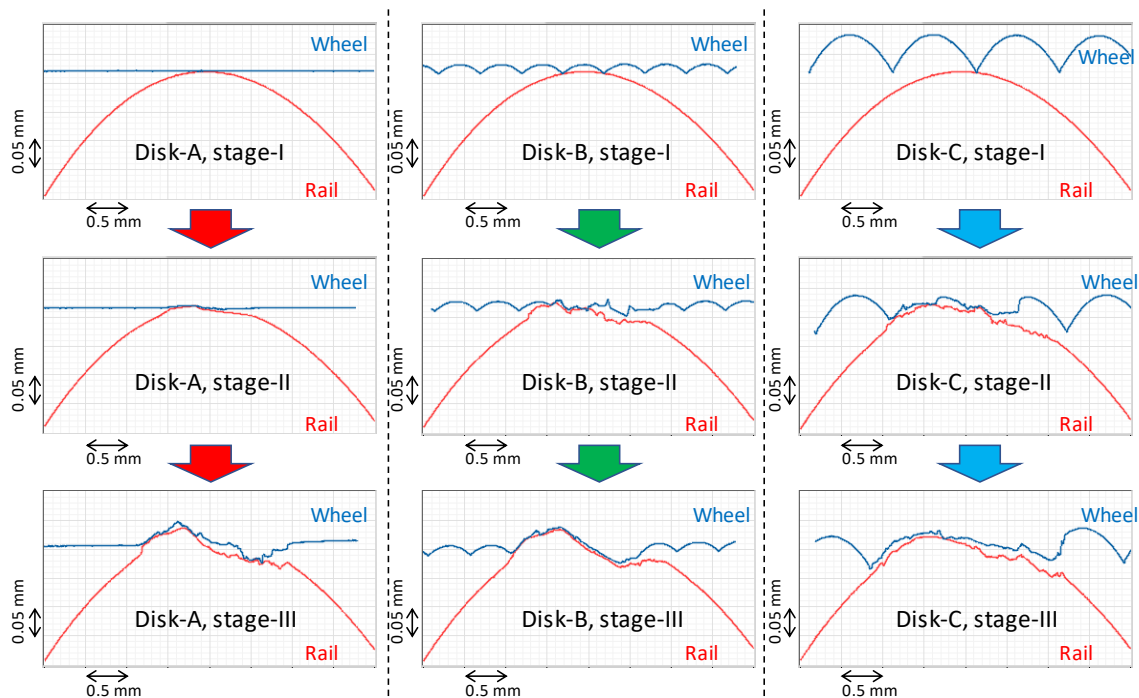


Fig. 3-8 Surface profile of test disks for each initial surface profile and stage.

3.3.3 Hardness

Figure 3-9 shows the depth profile of the hardness of test disks for each initial surface profile and stage. Comparing depth profiles of all disks at stage-II (orange line), it was found that the largest increase of hardness of the area closest to the surface was on disk-C followed in order by disk-B and disk-A. The cause of the increase for the disk-C and disk-B seems to be the larger plastic deformation of the ridges which will be followed by more work-hardening than disk-A, because the higher the ridges are more easily deformed.

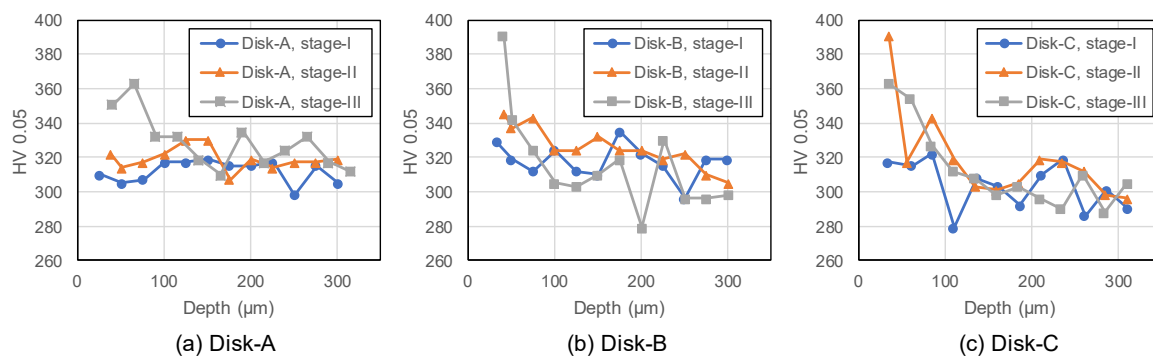


Fig. 3-9 Depth profile of hardness of test disks for each initial surface profile and stage.

3.3.4 Metallic structure

Figure 3-10 shows the metallic structures observed by the optical microscope for each initial surface profile and stage. It is clearly shown that the plastic deformation was increased with the progress of stages for all disks. At stage-II, the depths of plastic flow (white arrows) of disk-B and disk-C were approximately 70 μm . On the other hand, that of disk-A would not be clearly seen beneath the surface. There was no difference among the disks at the point of stage-III, the depth of plastic flow of disk-B and disk-C were approximately 100 μm and that of disk-A was 90 μm . These appearances correspond to the results of the depth profile of hardness.

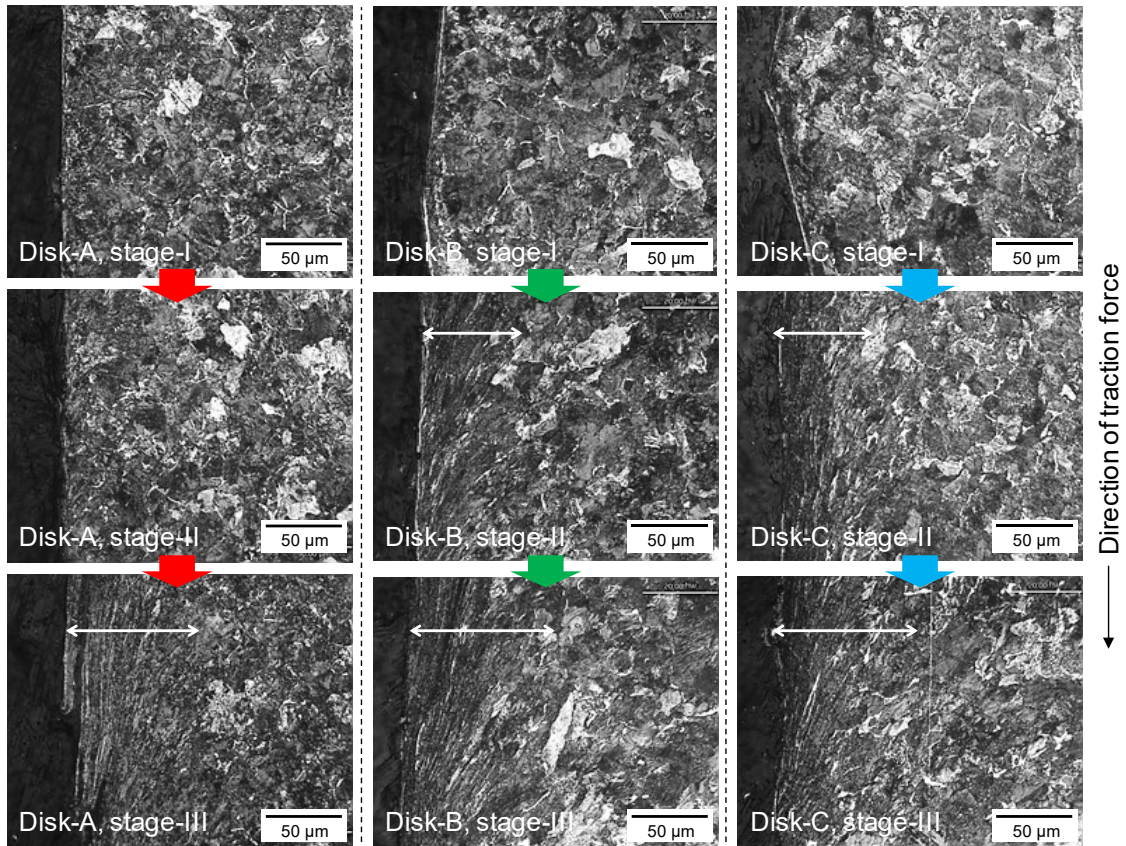


Fig. 3-10 Metallic structures measured by optical microscope for each initial surface profile and stage.

Figure 3-11 shows the sub-surface EBSD plots for wheel disk-A and disk-C at stage-II; (i) shows the inverse pole figure (IPF) for a visualisation of the structure of lattice domains (grains) with grain boundaries (low-angle ($>5^\circ$) grain boundaries LAGB area thin black line and high-angle ($>15^\circ$) grain boundaries HAGB area bold black line); (ii) shows the combined plot of pattern quality and grain boundaries (low-angle ($>5^\circ$) grain boundaries LAGB area thin red line and high-angle ($>15^\circ$) grain boundaries HAGB area bold black line); (iii) shows the local misorientation for the intergranular deformation (rainbow-scale from 0° to 5°).

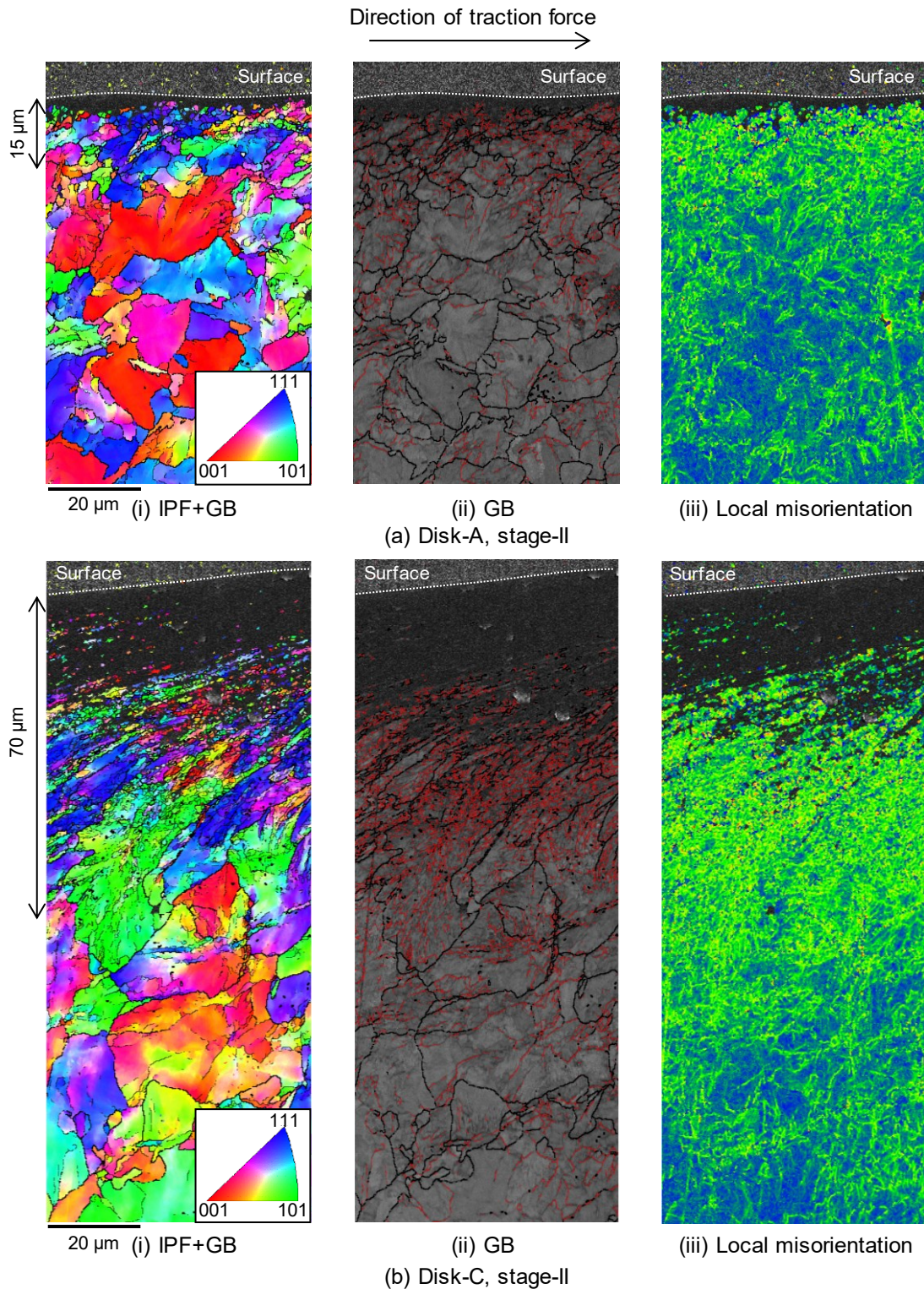


Fig. 3-11 Sub-surface EBSD plots for wheel disk-A and disk-C at stage-II.

It was clearly found that both generated plastic flow in the direction of the traction force, even in disk-A which was not confirmed in Fig. 3-10. Figure 3-11 (i) and (ii) show that the closer to the surface, the smaller the grain size was and Fig. 3-11 (iii) shows that the closer

to the surface, the more significant the strain that was generated for both disks. It appeared that the closer to the top surface, the more the data are missing, it means that the increase of dislocation density and significant decrease of grain size occurred by the large shear stress. These results visualize the formation of pronounced plastic flow. The thickness of the layer which was affected by the plastic flow of disk-C was approximately 70 μm and that of disk-A was more significant thinner, at approximately 15 μm .

3.3.5 Amount of wear particle

Figure 3-12 shows the amount of wear particles during the experiment which was captured under the disks. These results show that there was almost no generation of wear particles between stage-I and stage-II and a large amount was generated between stage-II and stage-III. It would indicate that the surface roughness was deformed plastically until completing the conformation of surfaces and the wear started after that. There is almost no difference in the amount of wear particles throughout the experiments, from disk-A to disk-C. Figure A-1 in Appendix A shows the microscope image of wear particles in each test. Wear particles were collected after stage-III. The image was obtained using a digital microscope VHX-5000 (Keyence). Most forms are flaky and rounded. There is little difference between tests A, B and C.

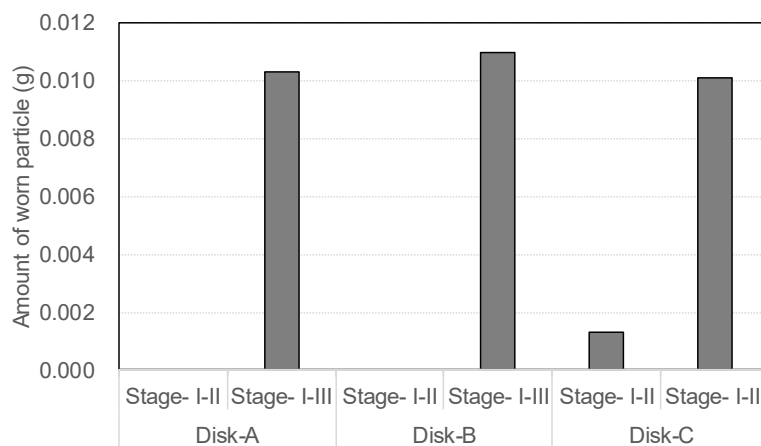


Fig. 3-12 Amount of wear particles during the experiments which were caught under the disks.

3.3.6 Chemical composition

Figure 3-13 shows the depth profile of the oxygen concentration to iron concentration for each initial surface profile and stage which was obtained using XPS. The depth profiles were collected from the same area. Though there was a slight difference in the oxygen concentration profile for each initial surface profile at stage-I, it is possible that a scattering of initial surface conditions caused the difference. On the other hand, there was

no difference at stage-II and -III. It indicates that the oxidation state became similar soon after starting the test and progressed in the almost same way during each test. There is a tendency for the oxidation to increase with the progress of the test in all disks.

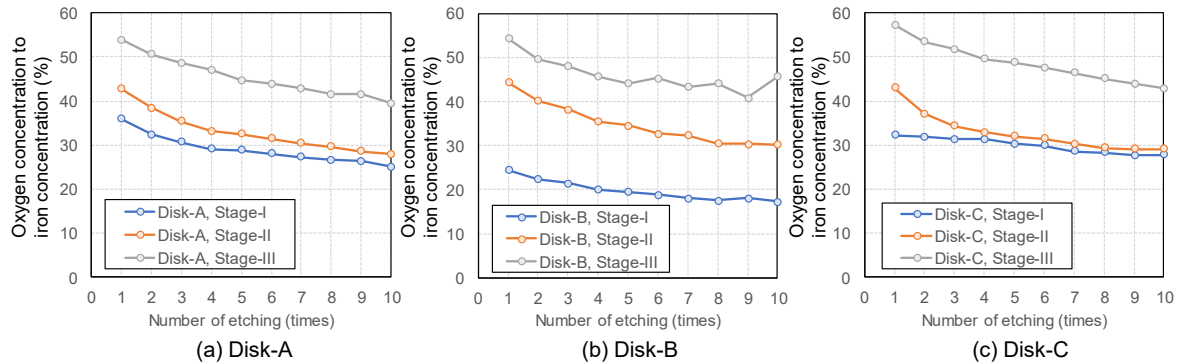


Fig. 3-13 Depth profile of the oxygen concentration to iron concentration for each initial surface profile and stage.

Figure 3-14 shows the high-resolution Fe 2p spectrum for the wear track on samples for stage-III. The iron oxide can be distinguished by the peak positions within the Fe 2p high-resolution spectra, and also by the presence and position of additional satellite peaks [19] which are generated by the excitation of outer-shell electrons following the excitation of the core electron. Fe_3O_4 is not expected to show a satellite feature whilst Fe_2O_3 is expected to show a significant feature at 719 eV. Regarding the Fe 2p_{3/2} XPS peak positions, this peak is expected at 711.0 eV for Fe_2O_3 , 710.6 eV for Fe_3O_4 and approximately 709.0 eV for FeO. Fe metal is expected at approximately 706.7 eV. The Fe 2p spectra shown here for the wear tracks appear to show little or no satellite features, suggesting the oxide is predominantly Fe_3O_4 and this is consistent with the Fe 2p_{3/2} peak position at approximately 710.6 eV for these samples.

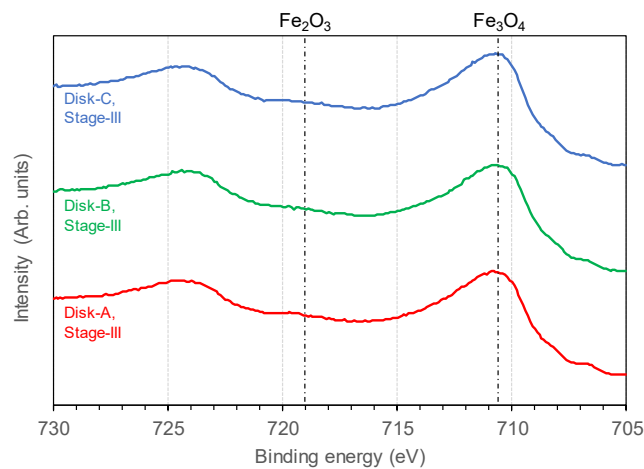


Fig. 3-14 High-resolution Fe 2p spectrum for the wear track on samples of stage III.

3.4 Discussion

The results of the twin-disk tests which simulated the wheel flange/rail gauge corner contact showed that the machining pitch of the wheel strongly influences the traction characteristics during the running-in period. The larger the machining pitch was, the smaller the peak value of the traction coefficient was. As mentioned in Chapter 1, it is sometimes believed that the spike-like machining marks cause an increase of traction during the running-in period. However, the results of this work contradict this and show that rougher wheel surfaces give lower traction coefficients.

Doi *et al.* [4] mentioned the possibility, that the traction coefficient could rise when the machining pattern was worn out from the results of field tests, and it agrees with the results of these laboratory tests. On the other hand, Kataori *et al.* [5] mentioned that the influence on the rise of the traction coefficient by the different machining pitch did not appear in the field tests. However, it might be hidden by the dispersion of the test conditions, such as the presence of dust, humidity, temperature and surface condition of actual wheel and rail because making steady test conditions at field sites is quite difficult. Since the test conditions for these laboratory tests were well controlled, it is thought that the influence was elicited.

As the results of microstructural analysis for the surface showed, the evolution of plastic flow was found on every type of specimen around the near-surface region with the progress of the stages. At stage-II, the samples which had a longer machining pitch showed a deeper range of plastic flow beneath the contact point. In the plastic flow layer, dislocations accumulate and are constrained, resulting in strain hardening. Corresponding to this evolution of plastic flow, the depth profile of the hardness indicated that the long pitch surface generated more significant work-hardening than the ground surface. Figure 3-15 shows a schematic model of the effects of surface texture on traction characteristics during the running-in period.

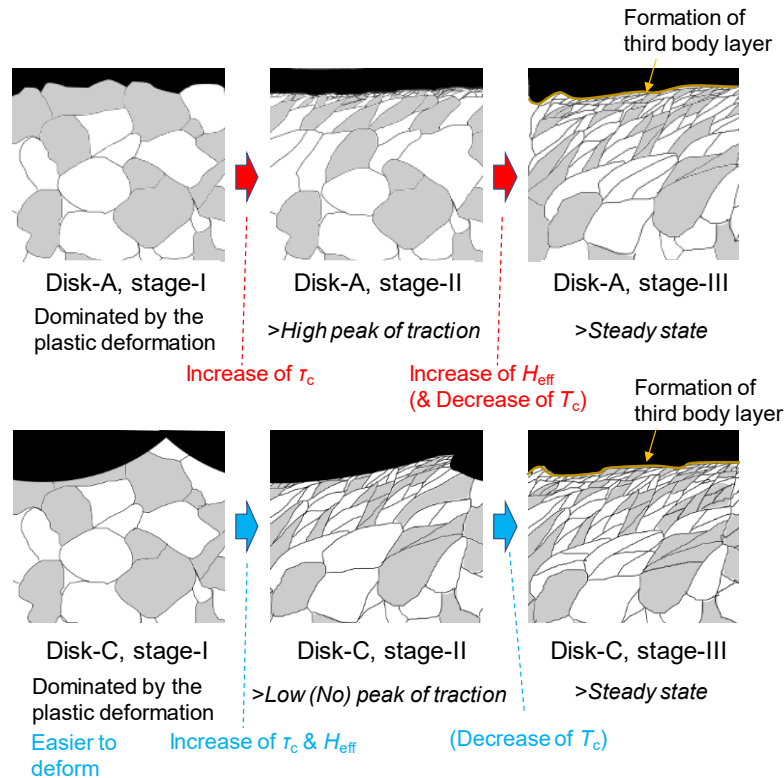


Fig. 3-15 Schematic model of the effects of surface texture on traction characteristics during the running-in period.

From stage-I to stage-II, the surface asperities were deformed plastically and the resistance to deformation was dependant on the traction force. The fact that the amount of wear particles was extremely small between stage-I and stage-II indicates that the surface was undergoing plastic deformation. It is also known that the presence of significant flow in the bulk gives a saturation of coefficient of friction with the increase of contact pressure [20]–[22]. Here, disk-B and disk-C, which had a machined surface, produced higher contact pressure than disk-A because of their conformational factor and suppressed the increase in traction coefficient. Comparing metallic structures of all kinds of disks at stage II, it was found that disk-A had a quite small magnitude of plastic flow compared with disk-B and disk-C. It is thought that disk-B and disk-C were more easily plastically deformed earlier than disk-A.

From stage-II to stage-III, the traction coefficient decreased in the case of disk-A, and slightly decreased and maintained in the case of disk-B and disk-C. In order to discuss the phenomenon, the Bowden-Tabor model on boundary friction [23] was applied the same as used by Halling [24] and Baek *et al.* [14]. Since the interfacial state is considered to change gradually from plastic to elastic contact, the traction coefficient can be expressed by the following formula with the concept of adhesion [14]:

$$\mu = \frac{\tau_c}{H_{\text{eff}}} \quad (3)$$

where, τ_c is the shear strength of the contact interface and H_{eff} is the effective hardness. The effective hardness is the hardness involving the surface layer and it is different from the hardness of either the layer or substrate material. The effective hardness depends on the thickness of the surface layer and it closes to the layer hardness with an increase of thickness. In the case of disk-C (and B), (i) the plastic deformation near the surface dramatically evolves and a thick plastic flow layer is quickly formed between stage-I and stage-II, (ii) traction coefficient makes a settlement with the high τ_c and H_{eff} between stage-II and stage-III. On the other hand, in the case of disk-A, (i) plastic deformation progresses relatively slowly and a thin plastic flow layer is formed between stage-I and stage-II, (ii) traction coefficient shows a high value because of high τ_c and low H_{eff} and it decreases with an additional evolution of plastic deformation, which increases H_{eff} , between stage-II and stage-III.

As shown in Fig. 3-11, the top surface for both (a) Disk-A and (b) Disk-C showed significant deformation at stage-II, and similar grain size, grain boundaries and local misorientation. On the other hand, there was a significant difference in the depth of plastic flow. The depth of plastic flow of Disk-C, 70 μm , was approximately five times larger than that of Disk-A, 15 μm . It means that the difference of effective hardness H_{eff} is larger than that of shear strength τ_c between disk-A and disk-C.

In Fig. 3-7, the changes in surface topography show that there are no specific linear marks in the tangential direction for any of the specimens. This does not support the dominance of abrasive wear as one of the main factors of wear. The presence of flaky, round wear particles, shown in Appendix A, is rather in line with the mechanism of formation of adhesive particles: the notion that the asperities adhere to each other on contact and that the tips of the asperities plastically deform and adhere to the mating surface, finally separating as wear particles [25]. On the other hand, a plastic flow layer is observed below the surface layer in Figs. 3-10 and 3-11, which indicates the accumulation of dislocations and may remain a dominant factor for fatigue wear.

The generation of a third-body layer, which consisted of oxides such as magnetite, was another factor to make a reduction in traction coefficient for all disks. It has been reported that the existence of a third body layer would influence the traction characteristic [26] and especially magnetite could work as a self-lubricated film and prevent the increase in traction coefficient [16], [27].

3.5 Conclusions

Investigations on a twin-disk test machine revealed a tribological phenomenon between the textured wheel and rail materials during the running-in period. The results of experiments and analysis are summarized as follows:

1. The twin-disk tests, which simulated the wheel flange/rail gauge corner contact, showed that the machining pitch of the wheel strongly influences the traction characteristics during the running-in period. The larger the machining pitch was, the smaller the peak value of the traction coefficient was. It is sometimes believed that the spike-like machining marks cause an increase of traction during the running-in period. However, the results of this work contradict this and show that rougher wheel surfaces give lower traction coefficients.
2. The microstructural analysis around the near-surface region of the characteristic stages, such as before test (stage-I), around the peak point of traction coefficient (stage-II), after the test (stage-III), showed that evolution of plastic flow was found on every type of specimen with the progress of stages.
3. At stage-II, the samples which had a longer machining pitch showed a deeper range of plastic flow beneath the contact point. Corresponding to this evolution of plastic flow, the depth profile of hardness indicated that the long pitch surface generated more significant work-hardening than the unmachined surface.

Based on the above results, a mechanistic model of the effects of surface texture on traction characteristics during the running-in period was proposed. It is considered that the major factors causing a decrease in the transient traction coefficient are plastic deformation of the surface texture and the difference of peak value was generated by the difference in the depth of plastic flow. Above results indicate that there might be an appropriate texture or surface treatment to reduce the risk of flange climb derailment during running-in.

References

- [1] W. C. Shust and J. A. Elkins, "Wheel forces during flange climb part I - track loading vehicle tests," in *Railroad Conference, 1997., Proceedings of the 1997 IEEE/ASME Joint.*, 1997, pp. 137–147.
- [2] H. Ishida, T. Miyamoto, E. Maebashi, H. Doi, K. Iida, and A. Furukawa, "Safety assessment for flange climb derailment of trains running at low speeds on sharp curves," *Q. Rep. RTRI*, vol. 47, no. 2, pp. 65–71, 2006.
- [3] A. Matsumoto *et al.*, "Improvement of bogie curving performance by using friction modifier to rail/wheel interface verification by full-scale rolling stand test," *Wear*, vol. 258, no. 7–8, pp. 1201–1208, 2005.
- [4] H. Doi, T. Miyamoto, J. Suzumura, J. Nakahashi, H. Chen, and T. Ban, "Change in Surface Condition of Turned Wheel and Effectiveness of Lubrication Turned against Flange Climb Derailment," *Q. Rep. RTRI*, vol. 53, no. 2, pp. 70–76, 2012.
- [5] A. Kataori, K. Doi, H. Iijima, S. Momosaki, and S. Matsumoto, "The Influence of the Wheel/Rail Contact Point Condition on Friction Coefficient," *9th World Conf. Railw. Res.*, 2011.
- [6] S. Greene *et al.*, "Flange Climb Derailment Criteria and Wheel/Rail Profile Management and Maintenance Guidelines for Transit Operations," *TCRP Rep. 71 Track-Related Res.*, vol. 5, p. 147, 2005.
- [7] S. Iwnicki, M. Spiriyagin, C. Cole, and T. McSweeney, *Handbook of railway vehicle dynamics*. CRC press, 2020.
- [8] J. Stow and P. Allen, "A Good Practice Guide for Managing the Wheel-Rail Interface of Light Rail and Tramway Systems," *Off. Rail Regul.*, 2008.
- [9] D. Yamamoto and H. Chen, "A Fundamental Study on Fine Unevenness and Tangent Force on Wheel Tread of Railway Vehicle (Relations between Environmental Condition and Tangent Force Characteristics with a Two-Disk Rolling Machine)," *Trans. JAPAN Soc. Mech. Eng. Ser. C*, vol. 77, no. 781, pp. 3211–3222, 2011.
- [10] D. Yamamoto and H. Chen, "Influence of the fine unevenness of wheel tread on the running stability of railway vehicle," *Trans. JAPAN Soc. Mech. Eng. Ser. C*, vol. 79, no. 803, 2013.
- [11] J. Lundmark, E. Kassfeldt, J. Hardell, and B. Prakash, "The influence of initial surface topography on tribological performance of the wheel/rail interface during rolling/sliding conditions," *Proc. Inst. Mech. Eng. Part F J. Rail Rapid Transit*, vol. 223, no. 2, pp. 181–187, 2009.
- [12] P. J. Blau, "On the nature of running-in," *Tribol. Int.*, vol. 38, no. 11–12, pp. 1007–1012, Nov. 2005.
- [13] P. J. Blau, *Friction and wear transitions of materials*. Noyes publications, 1989.

- [14] K. S. Baek, K. Kyogoku, and T. Nakahara, "An experimental study of transient traction characteristics between rail and wheel under low slip and low speed conditions," *Wear*, vol. 265, no. 9–10, pp. 1417–1424, 2008.
- [15] K. S. Baek, K. Kyogoku, and T. Nakahara, "An experimental investigation of transient traction characteristics in rolling-sliding wheel/rail contacts under dry-wet conditions," *Wear*, vol. 263, no. 1-6 SPEC. ISS., pp. 169–179, 2007.
- [16] T. Nakahara, K. S. Baek, H. Chen, and M. Ishida, "Relationship between surface oxide layer and transient traction characteristics for two steel rollers under unlubricated and water lubricated conditions," *Wear*, vol. 271, no. 1–2, pp. 25–31, 2011.
- [17] R. Lewis and U. Olofsson, *Wheel-rail interface handbook*. Elsevier, 2009.
- [18] S. Fukagai, T. Ban, K. Makino, M. Kuzuta, Y. Kubota, and H. Chen, "Measurement of contact area between wheel flange and rail gauge corner using ultrasonic technique," *9th Int. Conf. Contact Mech. Wear Rail/Wheel Syst.*, pp. 92–97, 2012.
- [19] T. Yamashita and P. Hayes, "Analysis of XPS spectra of Fe²⁺ and Fe³⁺ ions in oxide materials," *Appl. Surf. Sci.*, vol. 254, no. 8, pp. 2441–2449, 2008.
- [20] M. C. Shaw, A. Ber, and P. A. Mamin, "Friction Characteristics of Sliding Surfaces Undergoing Subsurface Plastic Flow," *J. Basic Eng.*, vol. 82, no. 2, pp. 342–345, 1960.
- [21] T. Wanheim, N. Bay, and A. S. Petersen, "A theoretically determined model for friction in metal working processes," *Wear*, vol. 28, no. 2, pp. 251–258, May 1974.
- [22] T. Nellesmann, N. Bay, and T. Wanheim, "Real area of contact and friction stress at high pressure sliding contact," *Wear*, vol. 43, pp. 45–53, 1977.
- [23] D. Tabor, "Junction Growth in Metallic Friction : The Role of Combined Stresses and Surface Contamination," *Proc. R. Soc. London . Ser. A*, vol. 1266, no. May 2016, pp. 378–393, 1959.
- [24] J. Halling, "Surface coatings materials conservation and optimum tribological performance," *Tribol. Int.*, vol. 12, no. 5, pp. 203–208, 1979.
- [25] J. P. Davim, Ed., *Tribology for engineers : a practical guide*. Elsevier, 2011.
- [26] A. Meierhofer, C. Hardwick, R. Lewis, K. Six, and P. Dietmaier, "Third body layer-experimental results and a model describing its influence on the traction coefficient," *Wear*, vol. 314, no. 1–2, pp. 148–154, 2014.
- [27] S. R. Pearson, P. H. Shipway, J. O. Abere, and R. A. A. Hewitt, "The effect of temperature on wear and friction of a high strength steel in fretting," *Wear*, vol. 303, no. 1–2, pp. 622–631, 2013.

Appendix A

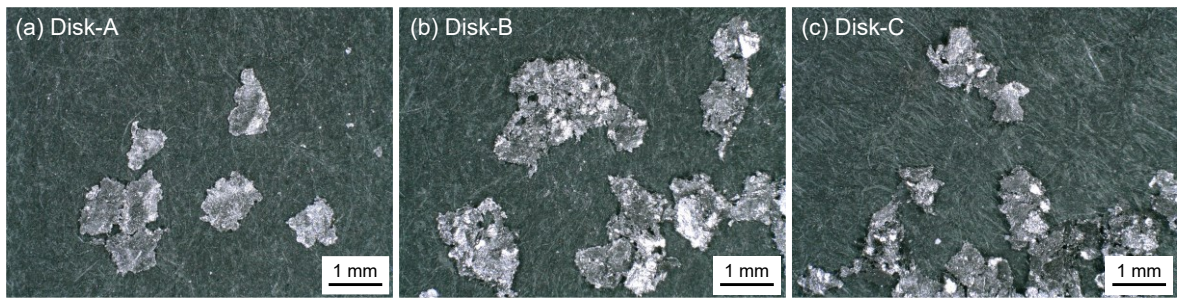


Fig. A-1 Microscope image of wear particles in each test. Wear particles were collected after stage-III.

4 IN-SITU EVALUATION OF A SLIDING INTERFACE WITH DIFFERENT ROUGHNESS CONDITIONS USING ULTRASOUND REFLECTOMETRY

Paper 2

In-situ evaluation of a sliding interface with different roughness conditions using ultrasound reflectometry

S. Fukagai^{a,b}, M. Watson^b, H. P. Brunskill^b, A. K. Hunter^b, M.B. Marshall^b, R. Lewis^b

^a Railway Technical Research Institute, Tokyo, Japan

^b Department of Mechanical Engineering, University of Sheffield, Sheffield, UK

Abstract

Understanding the dynamic condition of the interface between a railway wheel and rail is important to reduce the risks and consider the effectiveness of countermeasures for tribological problems. Traditionally the difficulty in obtaining accurate non-destructive interfacial measurements has hindered systematic experimental investigations. Recently an ultrasound reflectometry technique has been developed as a direct observation method of a rolling-sliding interface, however the topography dependence under the high contact pressures in a wheel-rail contact has not been clarified. For this reason, a novel in-situ measurement of the contact stiffness using ultrasound reflectometry was carried out for three different levels of roughness. A contact pressure equivalent to that in a wheel-rail interface was achieved by using a high-pressure torsion test approach. The dynamic change of contact stiffness with sliding was measured using ultrasound and the influence of roughness was investigated. The measured changes were validated using a newly developed numerical simulation, and mechanisms to explain the observed behaviour were proposed in terms of fracture and plastic deformation of the asperity bonds. These findings could help in understanding the traction characteristics for different roughness conditions and also assist in understanding damage mechanisms better, such as wear and rolling contact fatigue.

Submitted to Proceedings of the Royal Society A

4.1 Introduction

The wheel and the rail play vital roles in rail operation, such as bearing the vehicle load, guiding the vehicle and transmitting the driving and braking forces. To achieve these roles, the wheel and the rail roll/slide against each other under extremely high contact pressure conditions. Due to the severe contact condition, the interface is the origin of a number of tribological problems during operation. For example, when contaminants, such as water, oil or fallen leaves, get into the interface, the interaction can lead to wheel spin and brake lock-up. Such significant slipping can cause not only performance problems in terms of delays and safety issues from over-running (past signals at danger or a station), but also thermal damage and abnormal deformation of wheel and rail [1], [2]. Also, it is known that high friction coefficient and slip at curves could lead to severe wear and deformation of wheel and rail [3], [4], high energy consumption [5] and wheel-rail noise [6], [7]. Additionally, it increases the risk of a wheel climb derailment occurring [8]–[10].

To consider effective countermeasures for the problems mentioned above and to reduce the risks, it is important to understand the dynamic conditions in the interface. However, the difficulty in obtaining accurate non-destructive interfacial measurements has hindered systematic experimental investigations.

Use of pressure-sensitive films is one potential method to evaluate the contact area and stress [11], [12]. However, these films will change the tangential load due to their different frictional properties and they act as a “gasket” so change the load distribution in the interface. Practical implementation is also difficult because the film disintegrates under high-pressure and shear between the wheel and the rail. A method using a Fiber Bragg Grating (FBG) sensor which is embedded in the rail to evaluate the distribution of wheel-rail contact pressure has also been reported [13]. Although the contact pressure can be evaluated by measuring the strain in the rail in this method, there is difficulty in investigating the tribological phenomenon at the interface.

Recently, ultrasonic techniques have been used to observe the contact between wheel and rail [14]–[21]. Though there are spatial resolution limits and considerations of transducer positioning to ensure the sound waves reflect off the area of interest, this technique can be used to non-invasively and directly observe the contact. When an ultrasonic wave strikes the interface between the wheel and rail, it is partially transmitted and partially reflected. The proportion of the wave reflected depends on the stiffness of the contact [22], [23]. This approach has been used to determine the contact pressure distribution in wheel-rail contacts and the influence of wear profile, roughness and surface defects on the contact patch [15], [17]. Also, this actual distribution of the contact pressure could be applied to the simulation of wear and damage propagation with consideration of surface topography [24], [25].

The authors have already investigated the influence of the topography on the friction behaviour between the wheel and rail in dry condition focusing on the mechanisms of

flange climb derailments [26]. As a result, it was found that the initial topography affected the friction behaviour during running-in. Though these results indicate that the dynamic evolution of the surface asperities relates to the friction behaviour, these findings were based on the surface investigation when the test was stopped intermittently. The authors also investigated the relationship between the change in contact condition and the change in friction coefficient by scanning the contact surface with a linear array ultrasonic transducer attached to a full-scale wheel-rail contact rig [27]. The friction coefficient tends to increase as the contact stiffness, evaluated from the echo amplitude of the ultrasound, increases. In order to understand this phenomenon in more detail, it is necessary to capture in real time how the topography of the interface changes from time to time. Recently, a fundamental study to investigate the interfacial condition with micro-periodic vibration using ultrasonic waves was reported [28]. This study showed that the reflection coefficient dynamically changed with the progress of the friction mode, such as static to macro-slip. However, the experiments were carried out under a 10 MPa contact pressure, which is much lower than the wheel-rail contact pressure, and the influence of topography has still not been investigated. If the ultrasonic technique could be applied to a sliding interface which simulates the slip component of the wheel-rail interface, it will enable clarification of how the interfacial topography between the wheel and rail with extremely high contact pressure changes with frictional motion.

The aim of this work was to understand the influence of the roughness on the dynamic friction behaviour between the wheel and rail. To achieve a contact pressure equivalent to that in a wheel-rail interface, a high-pressure torsion (HPT) test approach was used. The HPT testing equipment is capable of applying horizontal relative motion (sliding) to two surfaces in contact with each other, while achieving a high contact pressure. The contact area is large enough to evaluate the contact stiffness using ultrasonic waves. Tiny piezoelectric elements which generate the ultrasonic waves were bonded to one of the test specimens. Ultrasonic reflection from the interface was used to conduct in-situ evaluation of the contact condition, particularly contact stiffness. Transient loading conditions and displacement were also measured during the test. Following these measurements, and the changes of contact stiffness with contact pressure, sliding distance were reproduced numerically.

4.2 Methodology

4.2.1 HPT testing equipment

Figure 4-1 shows the appearance of the HPT testing equipment. This equipment is capable of making contact between two specimens with a constant normal stress and then rotating the bottom specimen in the direction parallel to the contact interface. It uses load cells for tension, compression, and torque to measure the compressing load and the

torque; and uses a rotary variable differential transformer to measure the rotation speed. Table 4-1 lists the specifications of the HPT testing equipment.

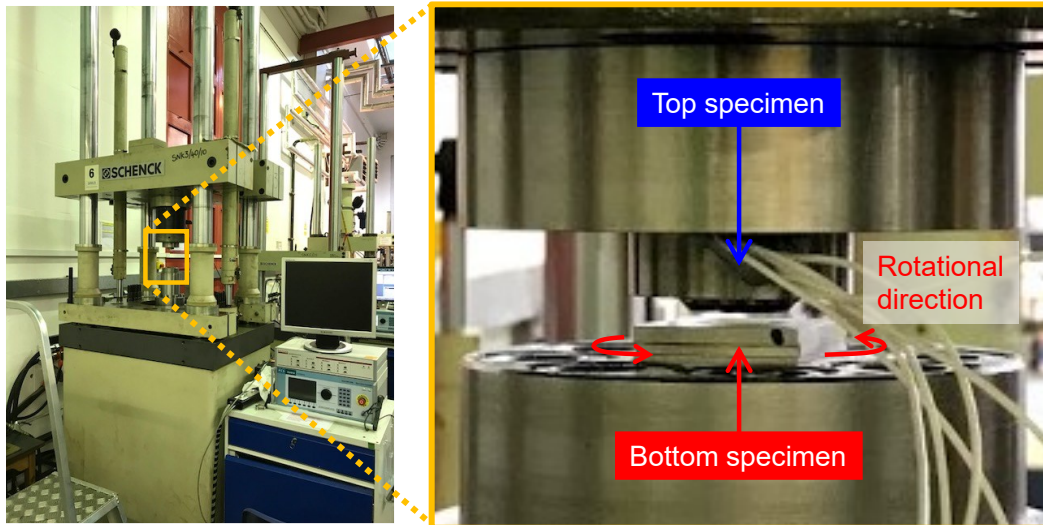


Fig. 4-1 Appearance of the HPT equipment.

Table 4-1 Specifications of the HPT testing equipment

Item	Value
Axial load (tensile and compression)	± 400 kN
Movable range in axial direction	± 25 mm
Torque	± 1000 Nm
Movable range in rotational direction	± 40 degrees

Figure 4-2 shows the initial design of specimens for the HPT testing equipment. Specimens are installed in the top and bottom parts of the equipment and a pair of the specimens is used as a unit. The top specimen is shaped in a cylindrical form. The bottom specimen is shaped in a rectangular solid form. Both specimens are reset by grinding, blasting or cutting the contact surface for each test. Therefore, although the height and other dimensions of the samples vary slightly from test to test, the contact area were measured for each test to define about the same contact pressure. Figure 4-3 shows a schematic of the HPT testing equipment. The contact shape can be seen as an annular shape. The annular contacts were used so that typical contact pressures could be achieved at the loading capacity of the apparatus. The test specimens are to be as parallel as possible so that a uniform pressure is obtained at each radius of the annular contact.

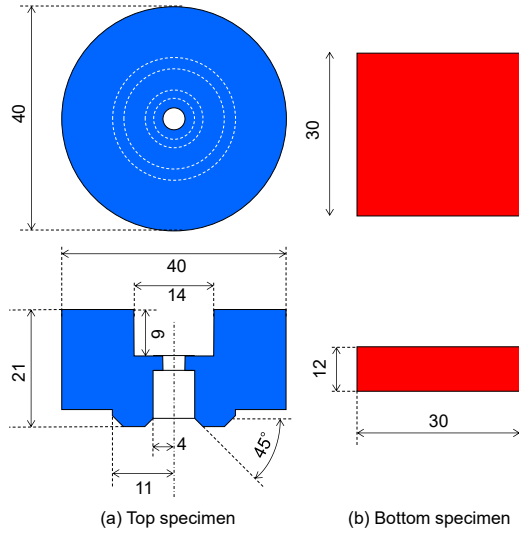


Fig. 4-2 Initial design of specimens for the HPT test.

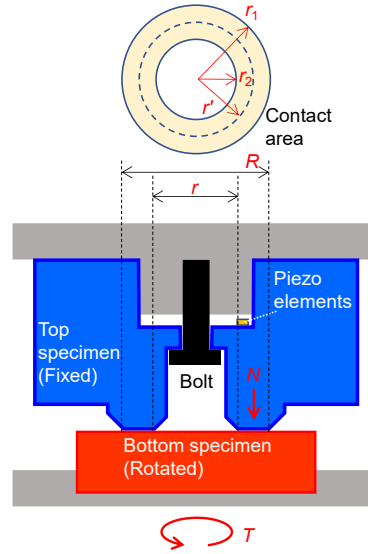


Fig. 4-3 Schematic of the HPT testing equipment.

The relationship between the normal load N and the normal stress p_N is represented as in Equation (1):

$$p_N = \frac{N}{\pi(r_1^2 - r_2^2)} \quad (1)$$

In Equation (1), r_1 and r_2 respectively represent the outer and inner diameters of the hollow circle of the contact area. The relation between the torque T and the tangential load S can be represented as in Equation (2):

$$S = \frac{T}{\frac{2}{3} \left(\frac{r_1^3 - r_2^3}{r_1^2 - r_2^2} \right)} \quad (2)$$

In addition, the relationship between the tangential load S and the tangential stress p_s can be represented as in Equation (3):

$$p_s = \frac{S}{\pi(r_1^2 - r_2^2)} \quad (3)$$

4.2.2 Ultrasonic measurement

Figure 4-4 shows the measurement principle of contact stiffness using ultrasound waves. At the interface between materials with different acoustic impedances, only a part of a sound wave transmits at the interface and the rest of it is reflected back. The reflectivity for ultrasound at an interface where the materials adhere to each other without any cavities, R , can be represented as in Equation (4) and it varies depending on the difference in the acoustic impedances of the two materials.

$$R = \frac{z_2 - z_1}{z_2 + z_1} \quad (4)$$

In this equation, z_1 and z_2 are the acoustic impedances of the materials in contact. The acoustic impedance is determined by the product of the density of the material and the acoustic velocity in the material. Therefore, when the acoustic impedances of the two materials in contact are the same and if the interface is hypothetically perfectly conformal, all the sound wave will transmit at the interface without any loss and no reflection occurs ($R=0$). On the other hand, when materials with significantly different acoustic impedances, such as a gas and a solid, are in contact, sound waves are almost completely reflected ($R \approx 1$).

Because the surface of an actual material is not a completely flat plane and has minute asperities and undulations, cavities are generated at the interface. When the wavelength of the ultrasound is sufficiently larger than the cavity size at the interface, the proportion of the reflected wave also depends on the contact stiffness. The contact stiffness is a function of the number, size, and approach of the contact points determined while considering the minute asperities [22]. Because the topographies of the surface changes due to elastic and plastic deformation, the measured reflectivity changes as shown in Figure 4-4 as load is applied. Therefore, it is possible to evaluate the contact condition at the interface by using the reflectivity of ultrasound.

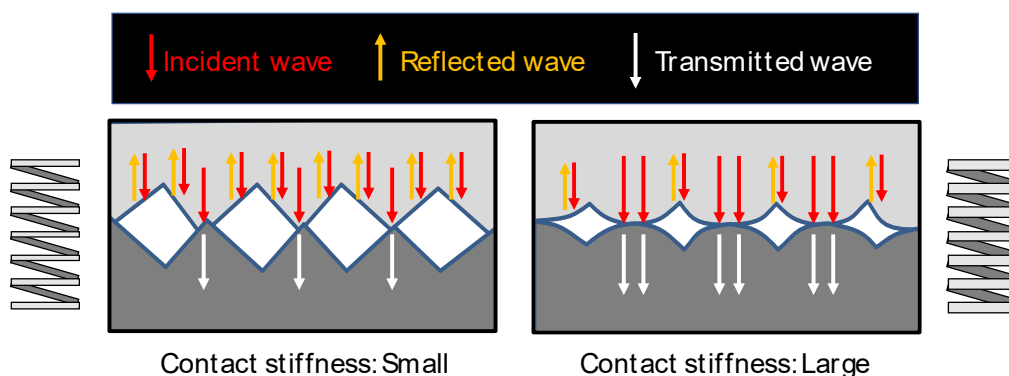


Fig. 4-4 Measurement principle of contact stiffness using ultrasound wave.

Schoenberg [29] adopted the spring interface model to express the reflectivity of ultrasound in the following equation:

$$R = \frac{z_2 - z_1 - i\omega(z_1 z_2 / K)}{z_2 + z_1 - i\omega(z_1 z_2 / K)} \quad (5)$$

In the equation, ω and K respectively represent the angular frequency of the ultrasound and the contact stiffness. For the example in this article, the equation can be simplified as follows because it is assumed that the wheel and the rail are made of the same material ($z_1 = z_2 = z$):

$$|R| = \frac{1}{\sqrt{1 + (2K/\omega z)^2}} \quad (6)$$

Therefore, it is possible to evaluate the contact stiffness K if the reflection coefficient R can be determined in an experiment. Generally, the contact stiffness is defined as the normal or tangential stress generated when the relative distance between two surfaces in contact via surface asperities changes by a unit length in each direction. The contact stiffnesses for each direction are expressed as in the following equations:

$$K_N = \frac{dp_N}{du_N} \quad (7)$$

$$K_T = \frac{dp_T}{du_T} \quad (8)$$

where, u_N represent the distance between mean lines of the surfaces in contact and u_T represents the surface tangential displacement, respectively. As shown in the equation below, the reflectivity is represented by the ratio between the intensities of the reflected wave when a load is applied and that when no load is applied:

$$R = \frac{H}{H_0} \quad (9)$$

where H and H_0 are the reflected wave intensity with load applied and no contact, respectively. The intensity of the wave reflected by the interface between steel and air when no load is applied is assumed to be equivalent to the intensity of the incident wave. It can be used as a simple and effective method for eliminating the influence of the inherent characteristics of the probe and attenuation/dispersion of the ultrasound.

4.2.3 Specimens

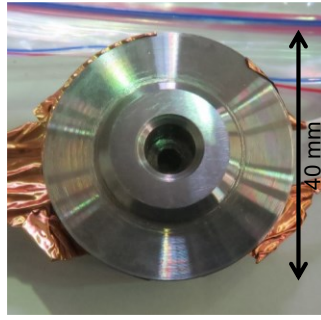
The top and the bottom specimens were made from ER8 (EN13262:2009) wheel material and R260 (EN13674-1:2011) rail material, respectively. Table 4-2 shows the hardness for the specimens. The hardness values are the average for 5 measurements. The measurements were conducted using a Mitutoyo hardness testing machine HV-110 and test force was 5 kgf.

Table 4-2 Hardness of the specimens

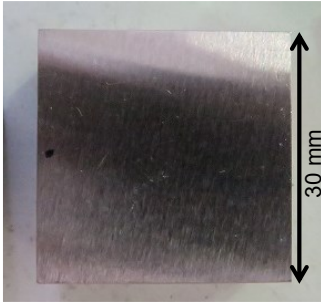
	R8T Wheel (top) specimen	R260 Rail (bottom) specimen
Hardness HV(5)	267(± 8)	285(± 9)

Note: The values in brackets indicate standard deviation.

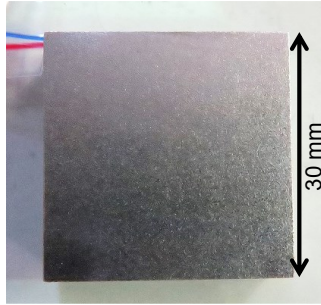
The surface type of the top specimens was finished by grinding in all tests to obtain a reproducible and constant surface geometry. On the other hand, surface types of bottom specimens were different for each test. Three different roughnesses were achieved by grinding, sandblasting and machining, respectively which gave increasingly large values for the root-mean-square of roughness, R_q . Figure 4-5 shows the appearance of the specimen contact surfaces. Different surface finishes, such as cutting and sandblasting, may have different degrees of residual stress, but as the intensity of reflected wave is divided by the value before contact, as shown in equation (9), the influence is considered to be small.



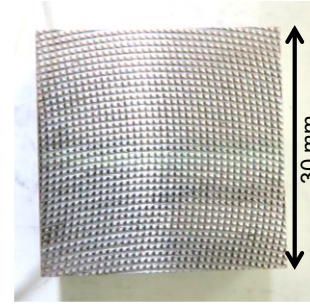
(a) Top specimen



(b) Bottom specimen:
Low roughness



(c) Bottom specimen:
Medium roughness



(d) Bottom specimen:
High roughness

Fig. 4-5 Appearance of specimens on the contact side.

Table 4-3 lists the values of the root-mean-square of roughness and the composite roughness. The value of the root-mean-square of roughness, R_q , is the average value for 5 measurements. The value of the combined roughness, σ , is calculated using equation (10);

$$\sigma = \sqrt{R_{qt}^2 + R_{qb}^2} \quad (10)$$

where R_{qt} and R_{qb} are the root mean square roughness of the top and bottom specimens, respectively.

Table 4-3 Roughnesses of specimen's surface before the tests

Roughness	Measurement direction	Root-mean-square of roughness, R_q (μm)		Composite roughness for each direction, σ (μm)
		Top specimen	Bottom specimen	
Low	Circumferential	0.5	0.7	0.8
	Radial	0.6	0.6	0.9
Medium	Circumferential	0.3	1.4	1.5
	Radial	0.4	1.5	1.6
High	Circumferential	0.6	7.4	7.4
	Radial	0.7	8.0	8.1

For all the contact tests, specimens were soaked in 2-propanol and washed in an ultrasonic bath before the measurement. Miniature piezoelectric elements were bonded to the top specimen to generate ultrasonic waves that reflected off the contact interface and they also measure the reflected wave. Figure 4-6 shows the longitudinal and transverse piezoelectric elements which were attached on the back of the top specimen.

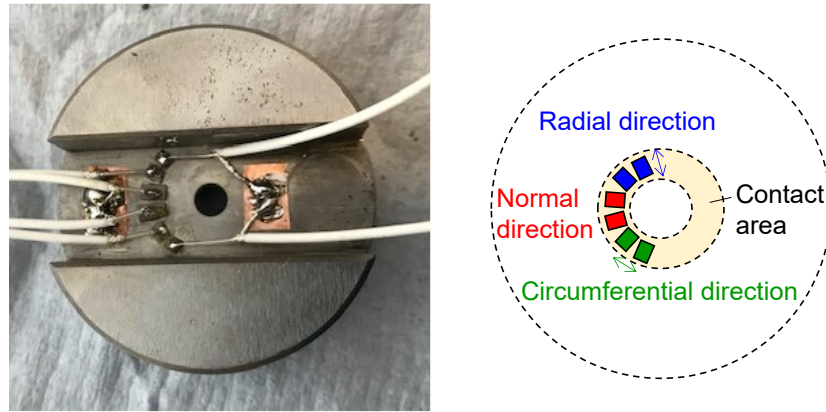


Fig. 4-6 Piezoelectric elements attached on the back of the top specimen.

The piezoelectric elements were used to determine the contact stiffness in the normal, circumferential, and radial direction. Measurements were taken in these different directions as there is a possibility that the contact stiffnesses in different directions will show different behaviour with application of the normal and tangential force. Of course, it is possible that the friction conditions may be slightly different at each measurement position, but this should provide useful information on whether there are obvious differences between directions. The piezoelectric elements for measurement of the transverse waves were installed in directions parallel (circumferential direction) and perpendicular (radial direction) to the friction direction. Piezoelectric elements with a central frequency of 5 MHz, were used for both the measurements of longitudinal and transverse waves. In this test, a "Pitch-Catch" method was employed in which different piezoelectric elements are used for activation and reception of the ultrasound. For the measurement, there is another method that is referred to as "Pulse-Echo" in which the same piezoelectric element is used for transmission and reception of the ultrasound. However, this method is inferior to the "Pitch-Catch" method in terms of accuracy because the transmitted wave remains as a noise (Fig. 4-7).

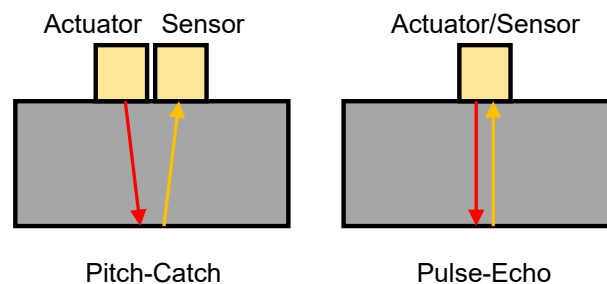


Fig. 4-7 Difference between "Pitch-Catch" and "Pulse-Echo".

4.2.4 Test procedure

Figure 4-8 shows a schematic example of a loading cycle. The test was conducted using the following procedure:

1. A normal stress is applied after inserting a pressure-sensitive paper between the specimens to check that the load is uniformly distributed on the contact area.
2. After making the specimens directly contact with each other, the normal stress is increased gradually to approximately 600MPa.
3. While keeping the top specimen in the specified position, the tangential stress is applied. (Phase-I)
4. The bottom specimen is rotated. (Phase-II)
5. The tangential stress is gradually released. (Phase-III)
6. After releasing the torque, the specimens are separated.

During steps 2 to 6, the contact stiffnesses are measured by using ultrasound.

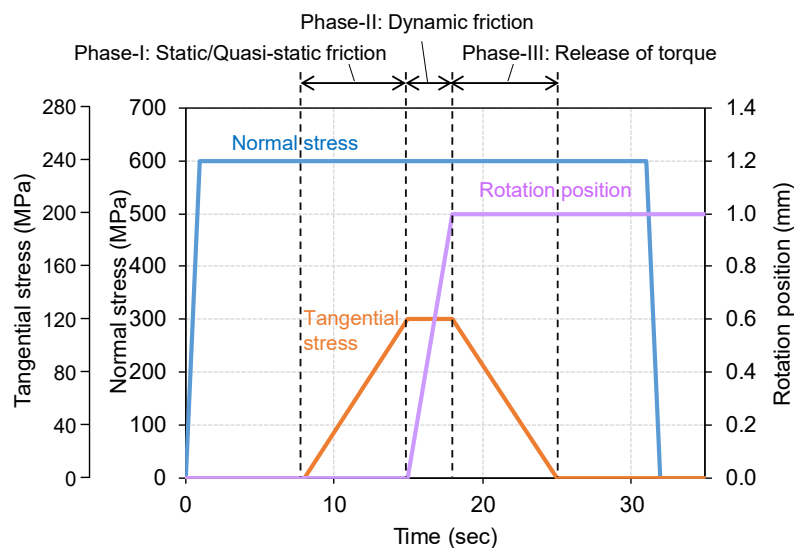


Fig. 4-8 Schematic example of a loading cycle.

4.2.5 Numerical simulation

In order to verify whether changes in contact stiffness can occur in the test conditions, numerical contact simulations based on a Boundary Element Method (BEM) with the half space approximation were conducted and the results were compared with the experimental results. The numerical calculations were conducted using three-dimensional surface topography data measured by a non-contact surface profiler (InfiniteFocus, Alicona) before test cycles, as shown in Fig. 4-9. In the calculations, the (b) Bottom specimen: Low roughness was used instead of the (a) Top specimen, because there were awkward gaps in the top one. Both were ground finishes and were judged to

have similar surface topography as the roughness in both directions, circumferential and radial, was almost identical, as shown in Table 4-3.

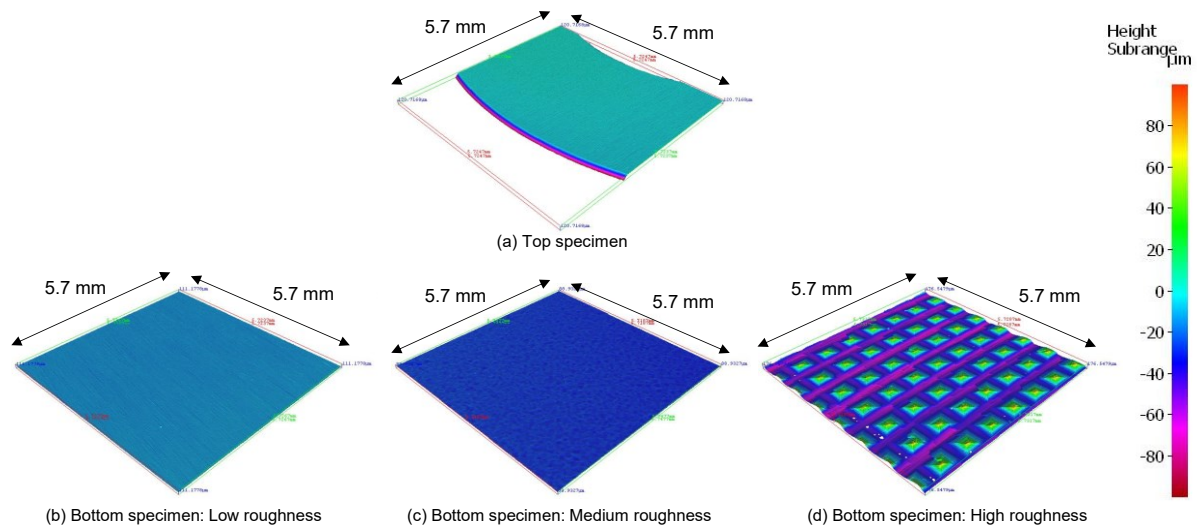


Fig. 4-9 Three-dimensional surface topography of the specimens before test cycles.

The boundary element formulation for a normal contact converts the problem of finding displacement at the surface points given a set of pressures on each of the surface points, to a convolution between the surface pressures and a 'short-form' influence matrix which depends on the material properties of the surface and the discretisation grid. Alternatively, this process can be thought of as a matrix multiplication between a vector of pressures and a 'long form' influence matrix. In practice, the convolution method is almost always used as this allows the process to be accelerated by completing the convolution in Fourier space (if $x(t) \otimes h(t) = y(t)$, then $X(f)H(f) = Y(f)$) [30].

For contact between two surfaces, these influence matrices can be summed to give the total deformation of the pair of surfaces due to a set of mutual loads. In general, for a rough surface contact the inverse problem is solved, finding the loads required to produce deformation in the surfaces so that the surfaces do not penetrate each other. The domain of this solution is confined to areas of the surface where this load is positive. This can be solved by a suitable conjugate gradient method.

In this work the domain of the solution is further confined to areas where the normal surface pressure is less than a limiting pressure, based on the material hardness as given by [31]. Areas which contact, but would require a load larger than this critical load to not penetrate, are allowed to penetrate and the critical load is applied. This constraint has been added to the BCCG method given in [32]. After each time step of the simulation this penetration is removed as plastic wear.

When the normal contact problem has been solved, the contact stiffness must be found. At any point, the response of the system to small perturbations of load can be thought of as linear providing the perturbation is not large enough to change the domain of the

solution (the points of the discrete surface profile which are in contact). In practice we can set the domain of the solution, removing the minimum and maximum load constraints and find the pressures on the currently contacting nodes required to produce a unit deformation of those nodes. The sum of these pressures is the contact stiffness as given by [33]. However, this total stiffness includes all of the deformation from the infinite half space as well as the contact region:

$$M \otimes L^1 = D^1 \quad (11)$$

$$D_i^1 = 1 : i \in \text{Contact} \quad (12)$$

$$L_i^1 = 0 : i \notin \text{Contact} \quad (13)$$

$$k_{all} = \frac{\Delta l}{\Delta d} = \frac{\sum_{i=0} L_i^1 a}{1} = a \sum_{i=0} L_i^1 \quad (14)$$

In the ultrasound community it is common to define the contact stiffness as the load per unit gap closure. This is a different but related quantity. Previous studies have found this quantity by perturbing the system with a small load and directly measuring the change in gap height from the simulation result [34]. However, the accuracy of this solution is likely to be extremely poor as the total load results are the result of a double optimisation procedure, optimising for the interference between the surfaces and again for the pressures required to accommodate the set interference. Below it is shown that the gap definition of contact stiffness can be linked to the total stiffness:

$$\lim_{\Delta l \rightarrow 0} \frac{\Delta l}{\Delta \bar{G}} = k_{gap} \quad (15)$$

$$\Delta G_i = G_i^0 - G_i^{\Delta l} = G_i^0 - (G_i^0 + D_i - \Delta d) \quad (16)$$

$$\Delta G_i = D_i - \Delta d \quad (17)$$

As the system is linear, the following can be written:

$$\Delta d = \frac{\Delta l}{k_{all}} \quad (18)$$

$$D_i = \frac{D_i^1 \Delta l}{a \sum_{i=0} L_i^1} \quad (19)$$

$$\Delta G_i = \left(\frac{D_i^1 - 1}{k_{all}} \right) \Delta l \quad (20)$$

$$k_{gap} = \frac{\Delta l}{\Delta \bar{G}} = \left(\frac{k_{all}}{D^1 - 1} \right) \quad (21)$$

Clearly, when the entire surface is in contact $D_i^1=1: \forall i$ and this gap stiffness tends to infinity as expected. This method can also be used to calculate the contact stiffness in either the loading or unloading directions, by excluding nodes which are at the maximum pressure the loading stiffness will be found.

These equations were solved for a 1024 by 1024 grid, using the experimentally measured surface profiles shown above. The code used to solve the models has been added to “Slippy” (version 0.1.4), an open source contact modelling package. The code used to generate these models is provided in the additional material.

4.3 Results

4.3.1 Change in the contact stiffness during normal force loading

Figure 4-10 shows the relationship between the normal stress and the contact stiffness which was measured during normal loading (step 2 in test procedure). It indicates that the contact stiffness has a positive correlation with the normal stress on the contact area for all the directions and all the different roughness cases. This result coincides with many previous reports [15], [35], [36] and it indicates the suitability of this experiment to evaluate the contact stiffness.

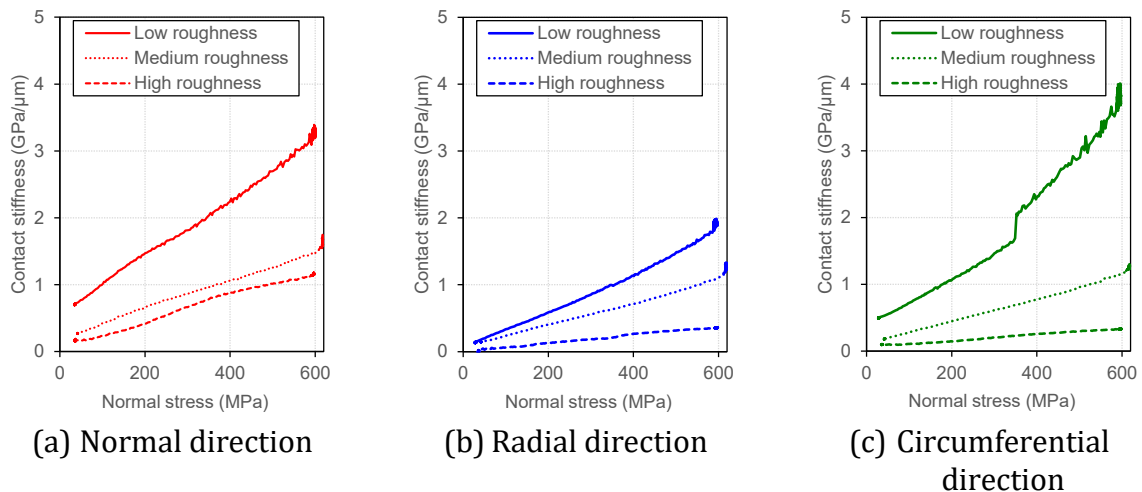


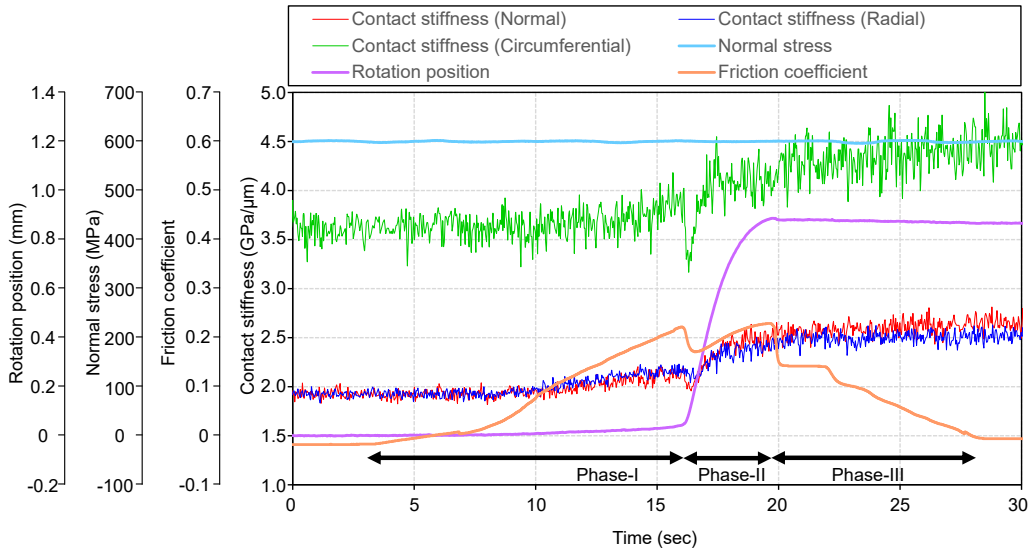
Fig. 4-10 Relationship between the normal stress and the contact stiffness which was measured during the normal stress loaded (step 2 in test procedure).

4.3.2 Change in the contact stiffness under tangential force

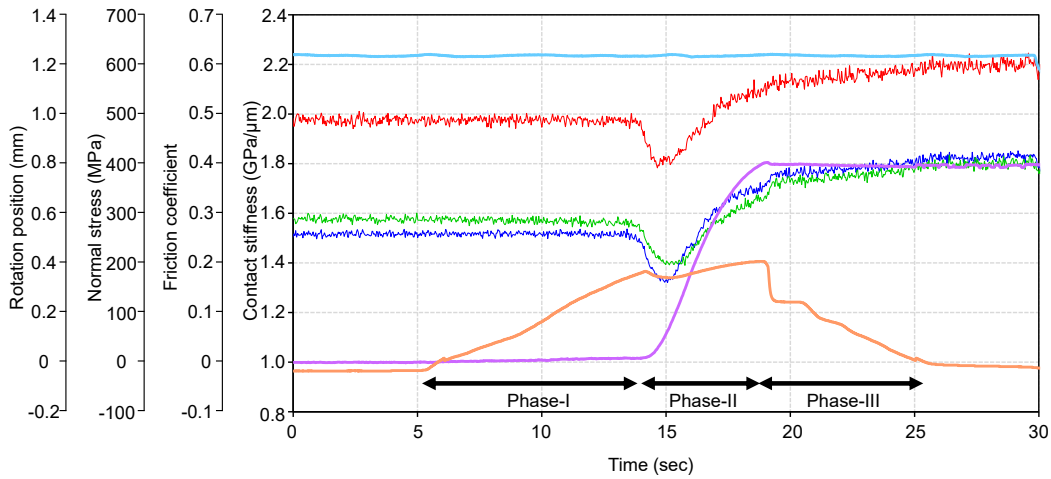
Figure 4-11 shows the changes in the contact stiffness, friction coefficient, normal stress and rotation position with the time, obtained from steps 3 and 4 of the test procedure. Here, the positive stress value is defined as the stress in the compression direction for normal stress. In Phase-I, there was little or no sliding while the friction coefficient

increased. For this period, the specimens were assumed to be in a static or a quasi-static contact condition except for the possibility of the rig being slightly twisted, and the contact stiffnesses remained at almost constant level or slightly increased. In Phase-II, the rotation position rapidly increased. At the same time, the contact stiffness rapidly decreased at the onset of slip, then slightly increased after that in the case of low and medium roughness. On the other hand, in the case of the highest roughness, the contact stiffness no longer showed the dip and the rotation curve rises gently with the friction force. In Phase-III, though the rotation stopped and the friction coefficient decreased as the tangential stress was released, the contact stiffness kept a constant level or slightly increased. At the same time, a slight restoration of the rotational position was found. It is considered that a spring back (relaxation) at the contact interface occurred.

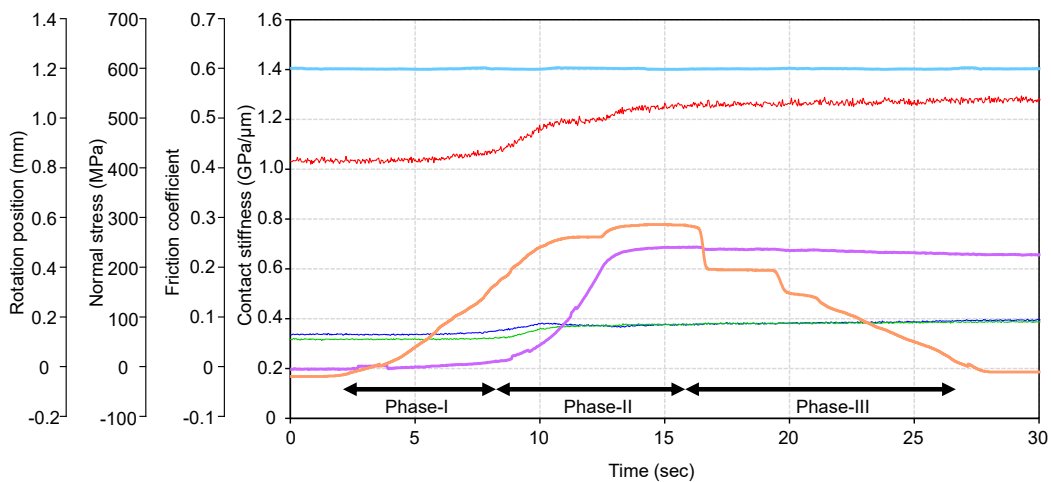
In all cases of roughness, though the friction coefficient decreased to zero when the tangential stress was released after rotation, the friction coefficient showed a negative value before Phase-I. It is considered that a slight misalignment in the horizontal direction between the specimen and the testing equipment generated tiny slip even when only normal stress was applied.



(a) Low roughness



(b) Medium roughness



(c) High roughness

Fig. 4-11 Changes in the parameters with testing time, parameters: contact stiffness, tangential stress, normal stress, rotation position (steps 3 to 5 in test procedure).

Figure 4-12 shows the relationship between the sliding distance and the contact stiffness while the tangential stress was applied and Fig. 4-13 shows that has been normalized by the contact stiffness before the application of tangential stress as the initial value. It indicates a positive correlation exists between them, especially at low and medium roughness. It is considered that the dynamic tangential force caused flattening of the asperities or locking of asperities at the interface and these increased the contact stiffness. At high roughness, the contact stiffness increased in the early stages of sliding, but then the stiffness curve became flat with sliding.

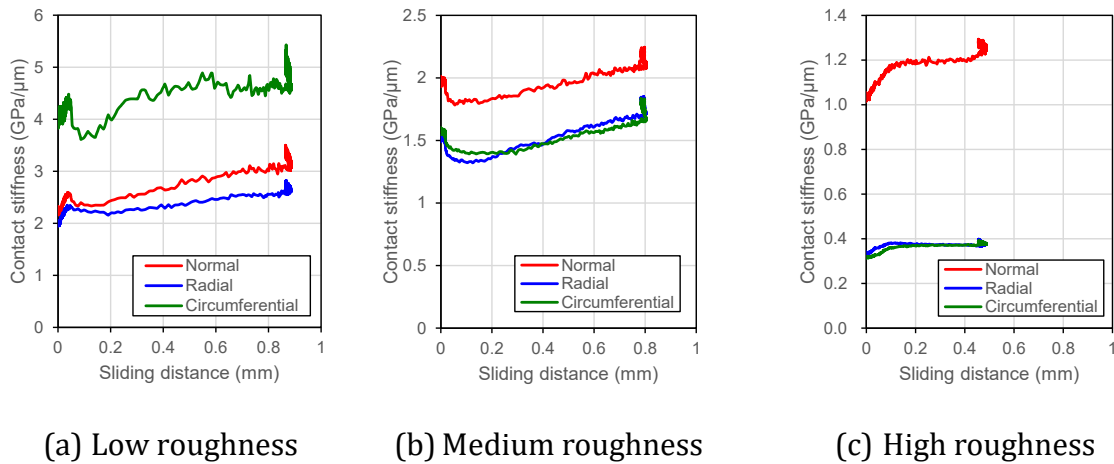


Fig. 4-12 Relationship between the sliding distance and the contact stiffness.

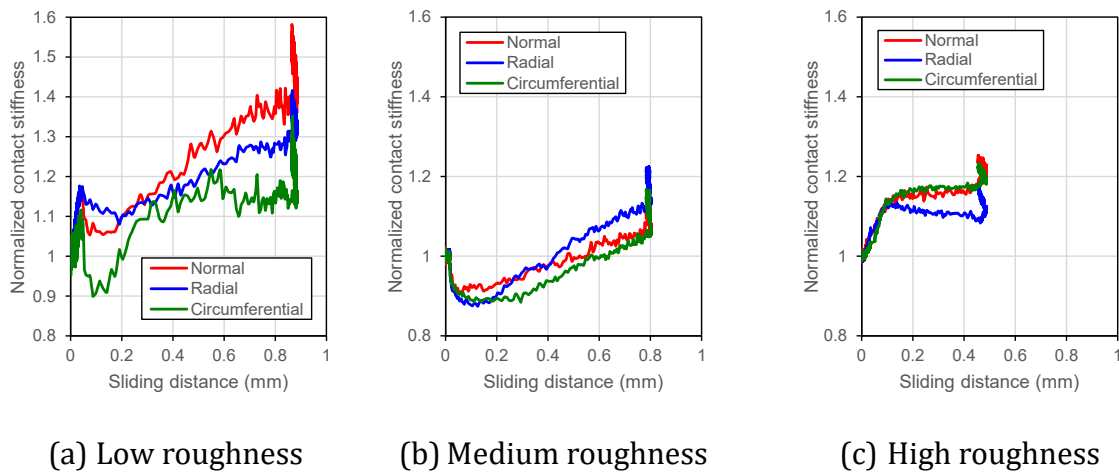


Fig. 4-13 Relationships between the sliding distance and normalized contact stiffness.

4.3.3 Change in the contact stiffness during normal force unloading

Figure 4-14 shows the relationship between the normal contact stress and the contact stiffness which was measured during the normal stress unloading (step 6 in test procedure). The overall contact stiffness was higher than that of loading, but this would be due to the increase in contact stiffness with slip, as shown in Fig. 4-11. It was found

that the change of contact stiffness follows a different path in the procedure of loading and unloading. Although the contact stiffness during loading showed the more linear-like increase, it showed a square root-like function or an asymptote with decrease of normal stress in the procedure of unloading. Drinkwater *et al.* and Dwyer-Joyce *et al.* conducted loading-unloading cycles measuring contact stiffness and reported hysteresis trends [36], [37] and they indicated that the possible influence of the plasticity of asperities occurs in the loading cycle.

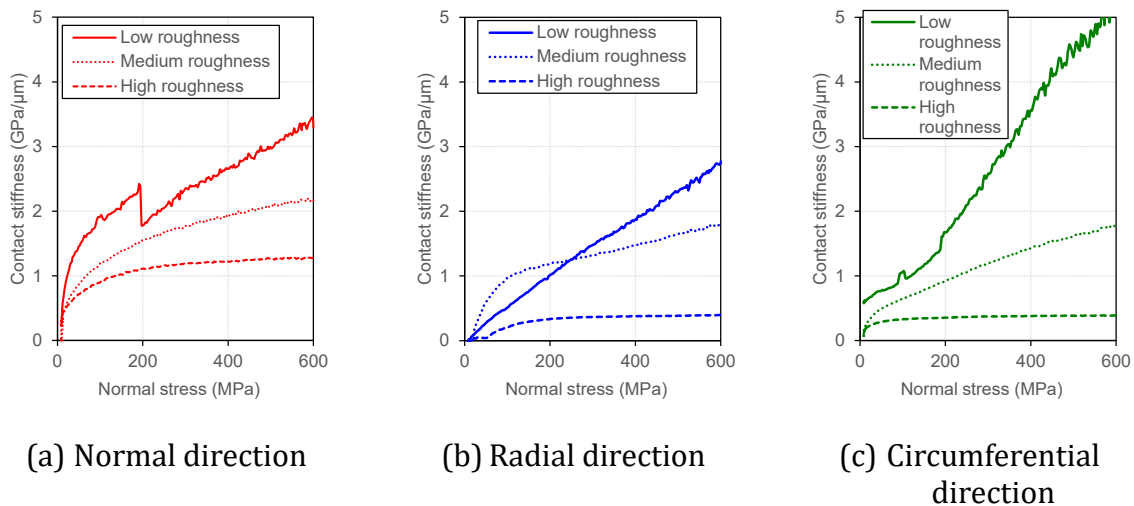


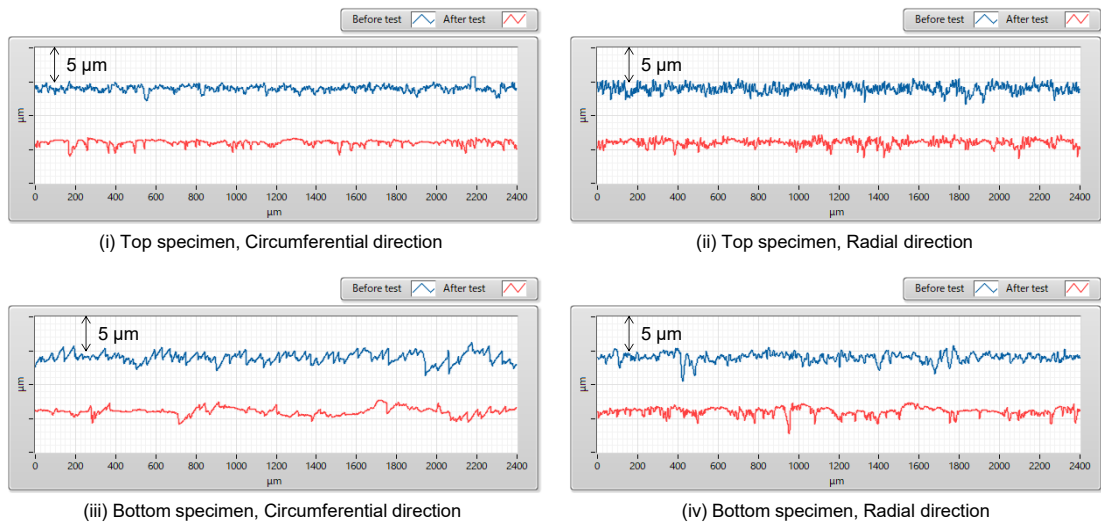
Fig. 4-14 Relationship between the normal stress and the contact stiffness which was measured during the normal stress unloaded (step 6 in test procedure).

4.3.4 Change in the roughness profile after the cycle

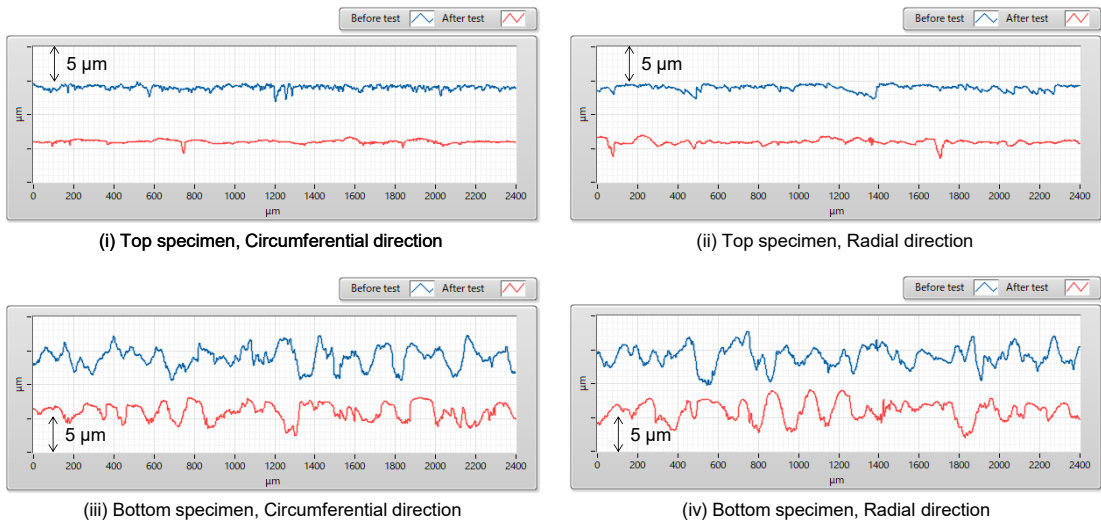
Table 4-4 lists the values of the root-mean-square of roughness, R_q , and the composite roughness. Figure 4-15 shows the roughness profiles of the top and bottom specimens measured before and after the test which were measured using a contact-type roughness meter (Mitutoyo SurfTest SJ-210). Comparing the roughness values before the test indicated in Table 4-3 and those after the test indicated in Table 4-4, there was little difference in the roughness values for the low and medium roughness conditions before and after the test. However, in the roughness curves, it was found that the shape of the summits of the asperities have been rounded and flattened after the test in the cases of low and medium roughness. On the other hand, the roughness values of the top specimen in the case of high roughness increased significantly. With regard to the roughness profile, it is considered that the asperities of the bottom specimen were stuck and transcribed to the top specimen in the case of high roughness.

Table 4-4 Roughnesses of specimen's surface after the tests

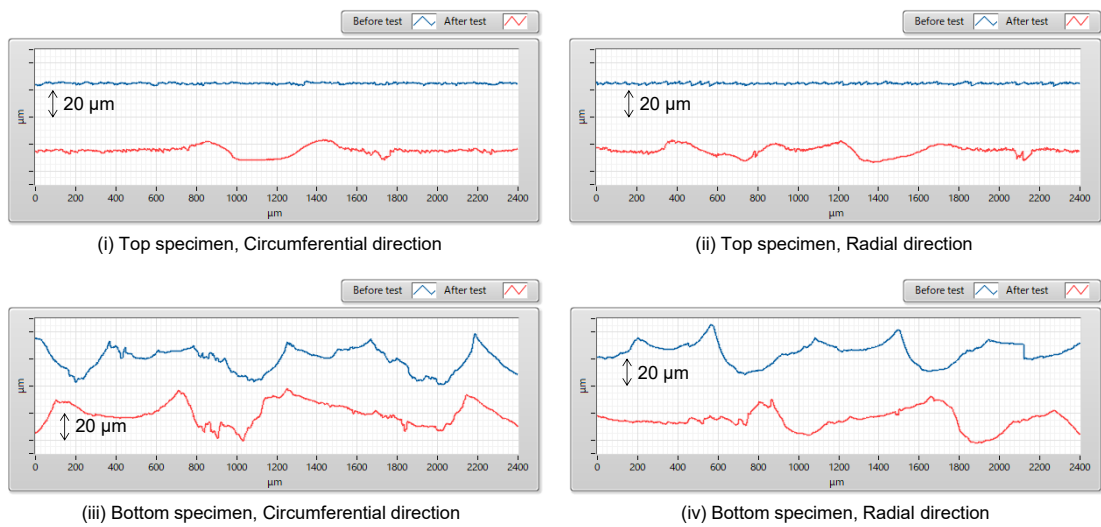
Roughness	Measurement direction	Root-mean-square of roughness, Rq (μm)		Composite roughness for each direction (μm)
		Top specimen	Bottom specimen	
Low roughness	Circumferential	0.3	0.6	0.6
	Radial	0.4	0.7	0.8
Medium roughness	Circumferential	0.2	1.3	1.3
	Radial	0.4	1.4	1.5
High roughness	Circumferential	2.5	7.0	7.4
	Radial	3.6	6.2	7.2



(a) Low roughness



(b) Medium roughness



(c) High roughness

Fig. 4-15 Roughness profiles of the top and bottom specimens before and after the tests.

Figure 4-16 shows photographs of the contact surfaces of the specimens after the test. For all roughness conditions, a circular contact area is clearly shown on the surface of the bottom specimen after the test. At the high roughness condition, the surface of the top specimen after the test shows a dotted pattern, which is thought to be the imprint of the asperities of the bottom specimen. At lower roughness levels, localised wear marks were observed at the outer circular edge of the contact area, but not at higher roughness levels. In the areas of wear marks, a metallic sheen can be seen.

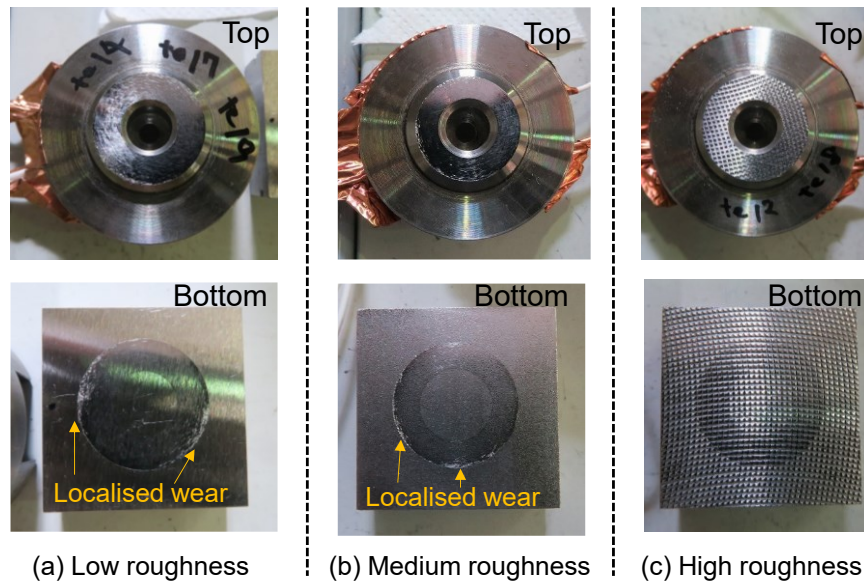


Fig. 4-16 Photographs of the contact surfaces of the specimens after the tests.

4.3.5 Comparison of experimental and numerical simulation results

Figure 4-17 shows the changes in normal contact stiffness simulated by the same test cycle as in the experiment. The real contact area is not evenly distributed across the apparent contact area. Close to the edges the local pressure is higher, leading to a higher real contact area. This can be true both for the real and simulated contact. As such in order to be compared to the measured results, the domain of the contact stiffness calculation is reduced to a patch in the centre of the apparent contact area.

The size of this patch greatly influences the result of the calculation, larger patches include more of the edge and give a higher contact stiffness. This is most pronounced for smoother surfaces. Because of this, results from two different sized areas are shown: 2.5mm square and 1.25mm square. These sizes represent the projected size of the sensor if the emitter is considered as an area or point source, respectively.

The contact stiffness tends to be higher for a 2.5mm square than for a 1.25mm square. As mentioned above, this is because the greater area is more affected by the locally higher contact stiffness at the edge. In the following sections, the experimental and numerical results of the individual steps will be compared.

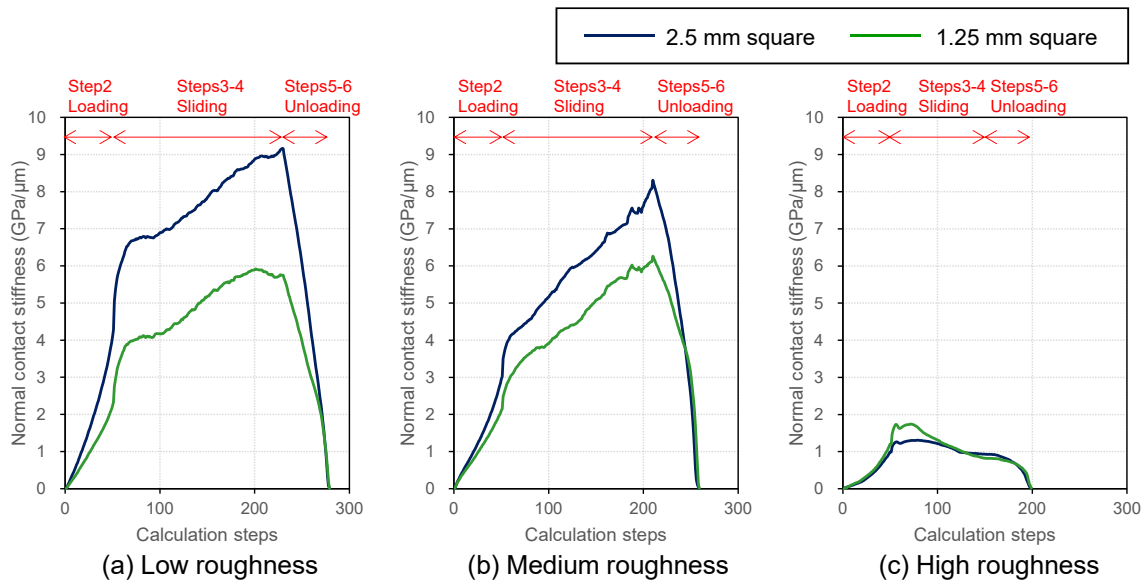


Fig. 4-17 Changes in normal contact stiffness simulated by the same test cycle as in the experiment.

Figure 4-18 shows the contact stiffnesses in the normal direction during loading (step 2) estimated by the numerical calculation with those by experiment. For all roughness conditions, the numerical simulations reproduced the increasing trend of normal contact stiffness with increasing pressure.

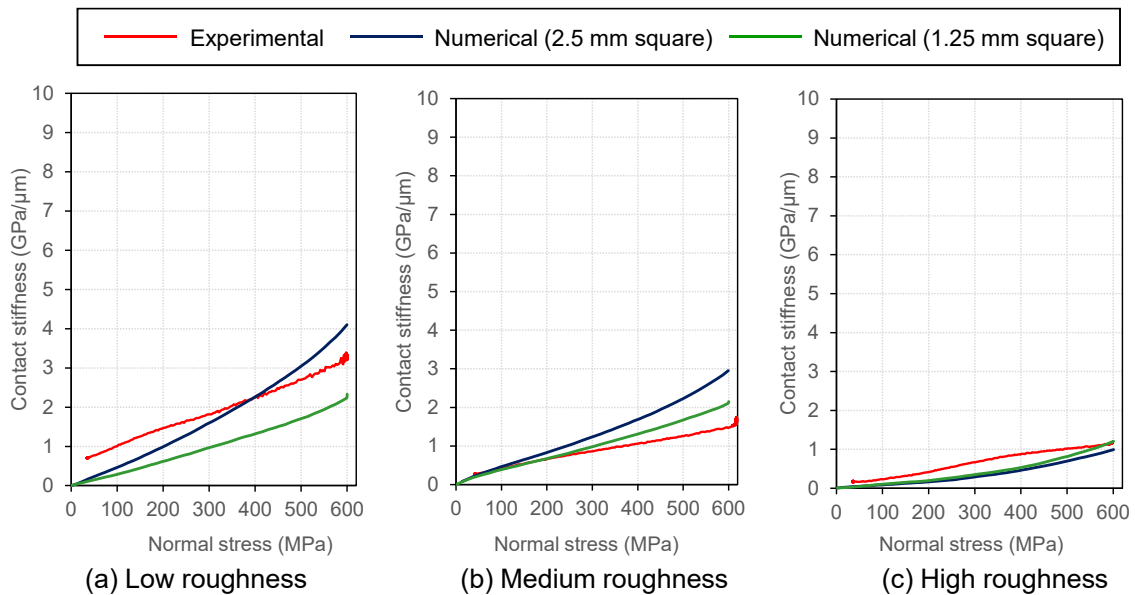


Fig. 4-18 Contact stiffnesses in normal direction during loading estimated by the numerical calculation with those by experiment.

Figure 4-19 compares the contact stiffness in the normal direction estimated by the numerical calculation during sliding (steps 3-4) with the experimental one. For the two smoother surfaces, the numerical prediction rapidly increases during sliding as material

is removed to account for plastic deformation. As shown this leads to a large over prediction by the end of the sliding step. For the higher roughness this effect is counteracted by the surfaces becoming less conformal.

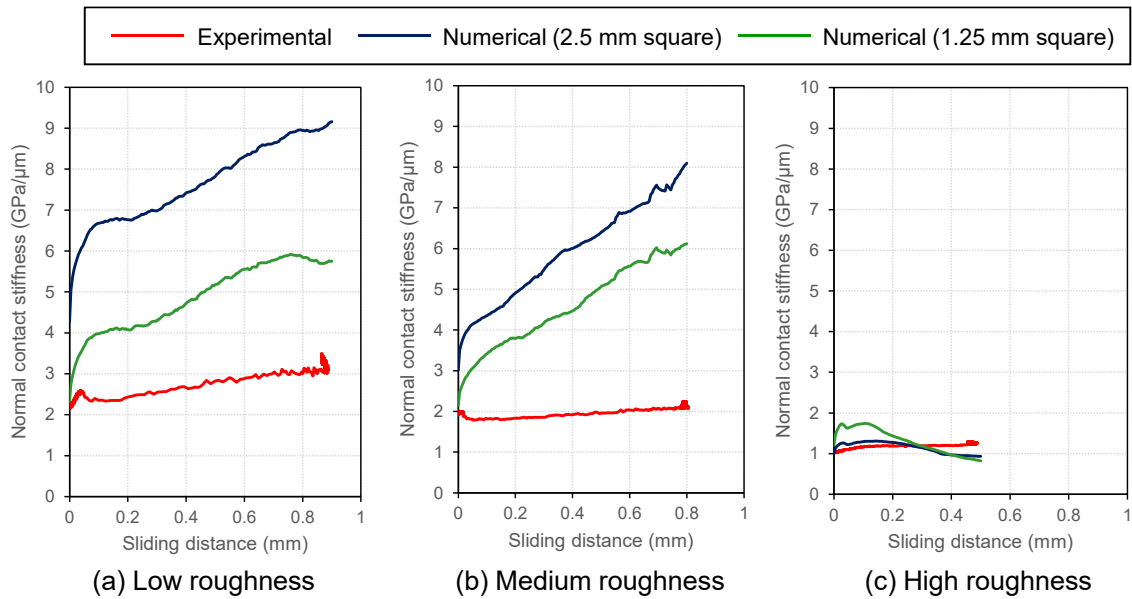


Fig. 4-19 Contact stiffnesses in normal direction during sliding estimated by the numerical calculation with those by experiment.

Figure 4-20 compares the contact stiffnesses in the normal direction during unloading (steps 5-6) estimated by the numerical calculation with those measured during the experiment. As in the sliding step, and for the same reasons, the magnitude of the stiffness is higher for the model in all but the roughest case. However, the form of the result is generally well captured, this result is not simply the opposite of the loading curve as the surface become more conformal due to plastic deformation.

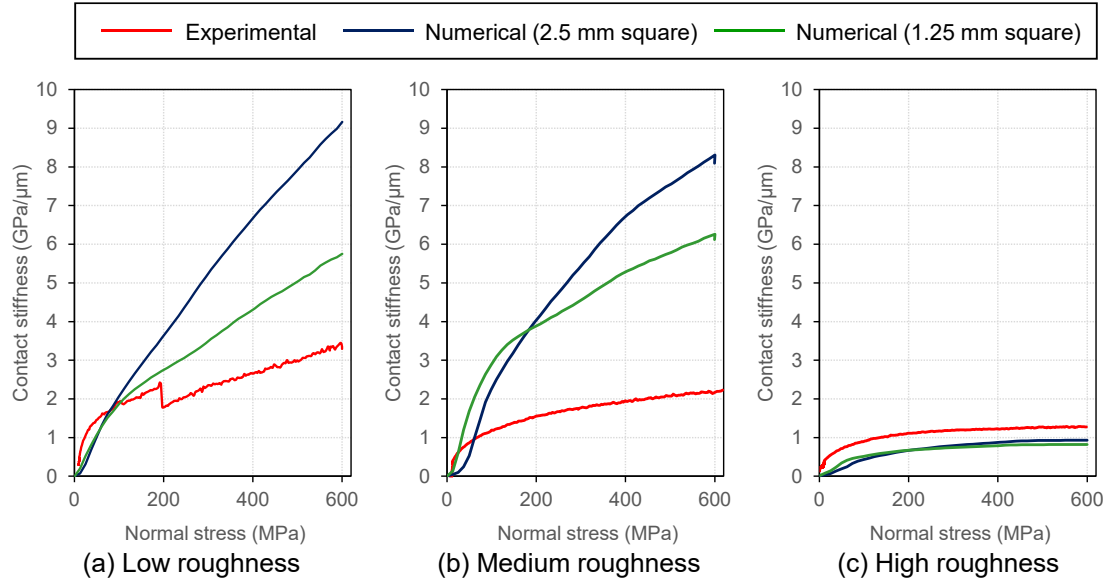


Fig. 4-20 Contact stiffnesses in normal direction during unloading estimated by the numerical calculation with those by experiment.

4.4 Discussion

Figures 4-12 and 4-13 showed the increase of contact stiffness around the end of the rotation. To investigate this phenomenon from another aspect, the work by the friction was evaluated. Figure 4-21 shows the relationship between the testing time and the work which was done by the tangential load. The work, W was calculated by the following equation:

$$W = \int_{L_0}^{L_1} |S| dL \quad (22)$$

where, L is the accumulation distance and calculated by the following equation:

$$L = \int_{t_0}^{t_1} |l| dt \quad (23)$$

where, l is the rotation distance, t_0 is the time when the tangential stress was applied and t_1 is the time when the tangential stress was released. The relationships were almost the same for all cases of roughness. However, it is found that the increase of the work energy in the case of high roughness is more gradual than that in the cases of low and medium roughness.

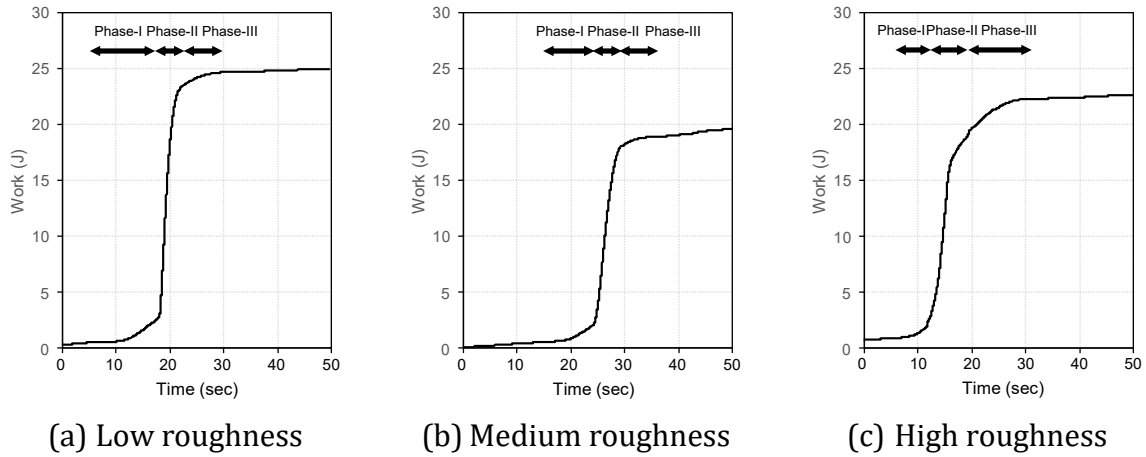


Fig. 4-21 Relationships between the accumulated rotation distance and the work.

Figure 4-22 shows the relationship between the work and the normalized contact stiffness. It is found that the normalized contact stiffness basically increased with the work for all roughnesses. However, they dropped around 2-5 J in the cases of low and medium roughness before rising again. This period is relevant to the beginning of Phase-II, the dynamic friction. On the other hand, there was no drop in the case of high roughness. Pesaresi *et al.* [28] also reported a decrease of the contact stiffness after a macro-slip. It is thought that the accumulation of work energy caused micro destruction of the interface and it led friction to drop, before rising again as new asperity junctions began to form in the cases of low and medium roughness. On the other hand, in the case of high roughness, it is thought that the plastic deformation of the asperities preceded the conformation and it suppressed the destruction of the interface.

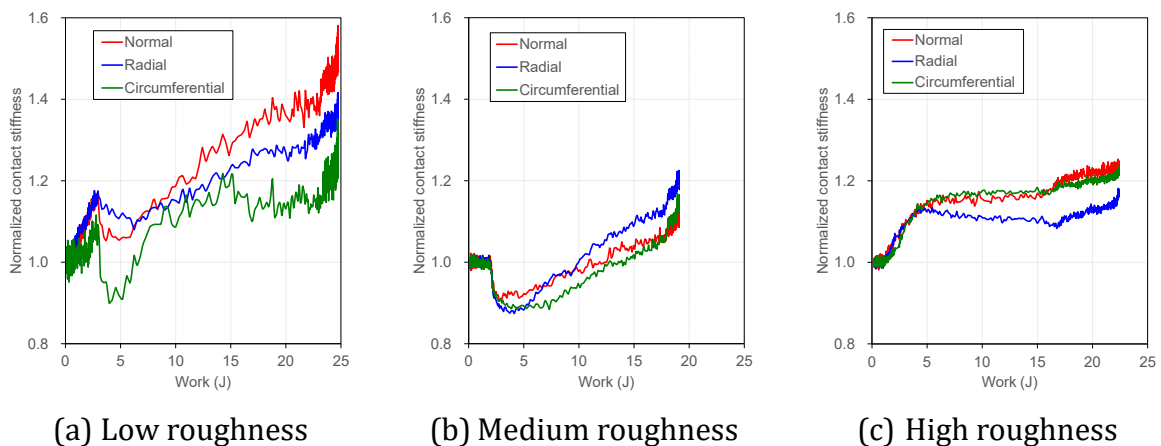


Fig. 4-22 Relationships between the work and the normalized contact stiffness.

Figure 4-23 shows a schematic representation of the proposed mechanism for the change at the interface when the dynamic friction occurs. In the case of low/medium roughness, the tips of asperities are plastically deformed and make conformed contacts at individual

bonds due to the material similarity of the two bodies in contact. As the tangential load is applied and the Coulomb limit is approached, interfacial fracture begins to occur at each bond [38], and friction and stiffness simultaneously drop. This fracture is thought to occur microscopically at first, but quickly propagates to the entire interface as a macro-slip [39]. With macro-slip, new asperity junctions form (un-deformed asperities, previously not in contact), and stiffness and friction begin to rise. In (a) low roughness and (b) medium roughness in Fig.4-16, metallic sheen was observed at the localised wear marks, which may be due to the exposure of the metallic substrate by wear.

On the other hand, in the case of high roughness, macroscale effects (i.e. each large machined peak) dominate as opposed to individual asperities (microscale). The tips of asperities also conformed, but the penetration of asperities is greater than the smoother interface because of the higher local pressure [40]. With the application of tangential load, the asperities plastically deform rather than break bonds owing to the interlocking of the tips due to penetration and the greater heights of asperities. In the field of metal forming, it is widely known that bulk plastic deformation occurs during shearing as the contact pressure increases [41], [42]. Considering the greater asperity as a separated bulk body, it is possible that the plastic deformation of the asperity took precedence over the micro-slip. Hence, the contact stiffness gradually increases as a consequence from static/quasi-static friction to the dynamic friction.

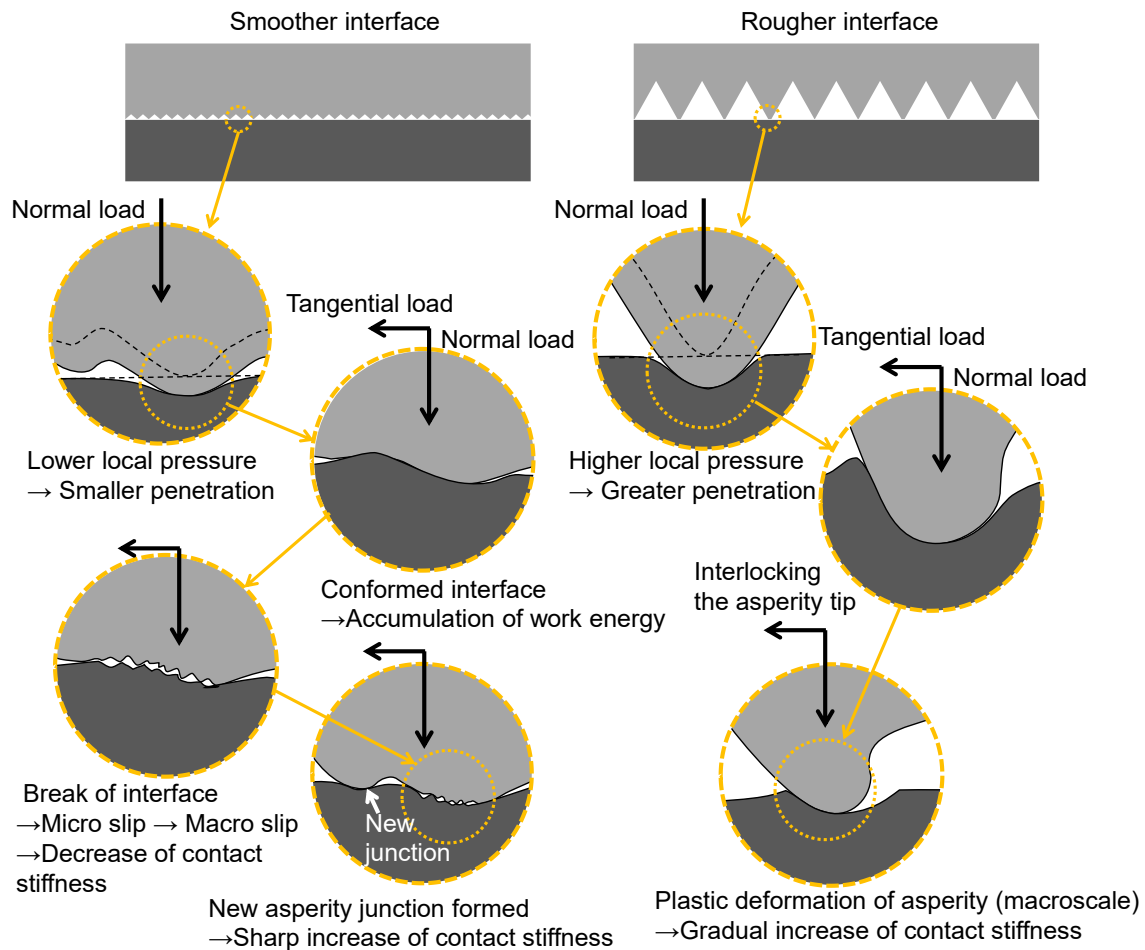


Fig. 4-23 Schematic representation of the proposed mechanism of the change at the interface when the dynamic friction occurs.

Figure 4-24 shows the relationship between the tangential contact stress and the normalized contact stiffness from quasi-static to dynamic friction. It should be noted that the contact stiffness was normalized as the initial value by the contact stiffness before the application of tangential stress. It was found that most of those increased with the tangential stress as well as the normal stress dependency in Figs. 4-10 and 4-14. In the low and the medium roughness condition, the normalized contact stiffness was partly below 1 because there was a large drop in contact stiffness at the beginning of sliding, as shown in Fig. 4-12. The dependency on tangential stress showed more scattering compared with the normal stress. It is thought that the change of surface asperities at sliding interface is more complicated than the purely compressed interface which was constrained in the loading direction, because the friction joints could separate with relative motion. However, according to the previous reports [26], [43], it is considered that Figure 4-24 might show the running-in phenomenon during which the friction force rises with a conforming and smoothing surface.

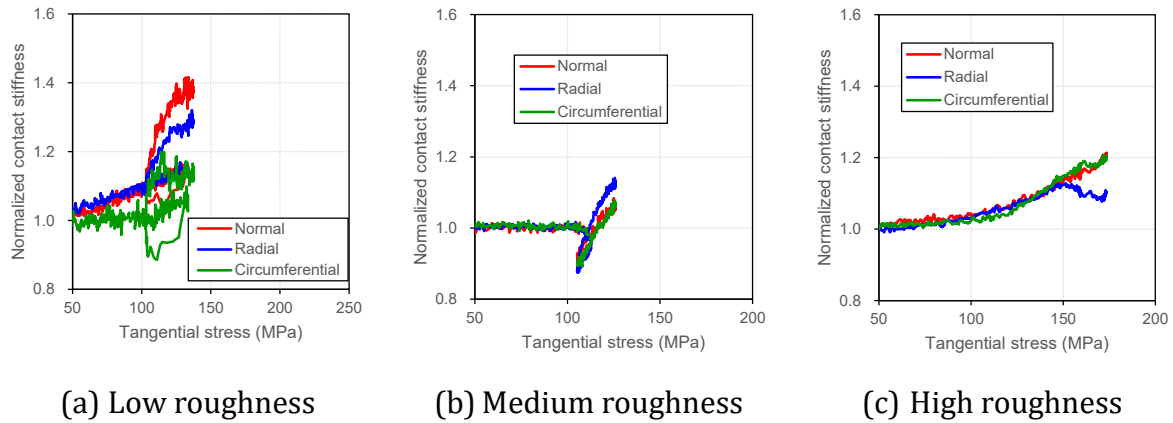


Fig. 4-24 Relationships between the tangential stress and normalized contact stiffness from quasi-static to dynamic friction.

4.5 Conclusions

Aiming to understand the influence of the roughness on the dynamic friction behaviour between the wheel and rail, ultrasonic reflectometry was applied to the HPT test approach, and in-situ evaluation of the contact condition was carried out. From the results of evaluation, the following conclusions can be drawn:

- (1) The application of the ultrasound reflectometry to the HPT test approach enabled in-situ evaluation of the friction interface under extremely high contact pressure and gave the information about continuous change of interfacial topographies and contact stiffnesses with friction. It is thought that this technique can be applied not only to the wheel-rail interface, but also to general high contact pressure interfaces.
- (2) The change of the contact stiffnesses during the process in which the static/quasi-static friction mode transitions to the dynamic friction mode could be evaluated. A transient drop of the contact stiffness was observed at the beginning of the dynamic friction mode at the smoother interface. The contact stiffnesses increased along with the dynamic friction motion regardless of the direction. In addition, it was found that the contact stiffnesses did not change significantly while the tangential stress was released and rapidly decreases while the normal stress was released.
- (3) There was the positive relationship between the sliding distance and the contact stiffnesses. It was considered to indicate that the wear and plastic deformation of the asperities progressed and conformed along with the increase of the sliding distance. The dependency of the direction on the contact stiffness was not significant and they were considered to change almost uniformly.
- (4) The results of numerical simulation showed that the effect of initial roughness on the increase in contact stiffness with increasing contact pressure and sliding distance could be generally reproduced. Also, it was thought that the accumulation of work energy excited break of conformed interface at the beginning of the dynamic friction at the smoother interface. On the other hand, it was thought that the plastic deformation of the asperities preceded the conformation at the rougher interface.

References

- [1] D. I. Fletcher and S. H. Sanusi, "The potential for suppressing rail defect growth through tailoring rail thermo-mechanical properties," *Wear*, vol. 366–367, pp. 401–406, 2016.
- [2] J. Ahlström and B. Karlsson, "Microstructural evaluation and interpretation of the mechanically and thermally affected zone under railway wheel flats," *Wear*, vol. 232, no. 1, pp. 1–14, 1999.
- [3] R. Lewis *et al.*, "Mapping railway wheel material wear mechanisms and transitions," *Proc. Inst. Mech. Eng. Part F J. Rail Rapid Transit*, vol. 224, no. 3, pp. 125–137, 2010.
- [4] U. Olofsson and T. Telliskivi, "Wear, plastic deformation and friction of two rail steels - A full-scale test and a laboratory study," *Wear*, vol. 254, no. 1–2, pp. 80–93, 2003.
- [5] S. Kumar, G. Yu, and A. C. Witte, "Wheel-rail resistance and energy consumption analysis of cars on tangent track with different lubrication strategies," *Proc. IEEE/ASME Jt. Railr. Conf.*, pp. 129–136, 1995.
- [6] D. T. Eadie, M. Santoro, and J. Kalousek, "Railway noise and the effect of top of rail liquid friction modifiers: Changes in sound and vibration spectral distributions in curves," *Wear*, vol. 258, no. 7–8, pp. 1148–1155, 2005.
- [7] S. Fukagai, T. Ban, M. Ogata, M. Ishida, and A. Namura, "Development of wheel/rail Friction Moderating System (FRIMOS)," *Q. Rep. RTRI (railw. Tech. Res. Institute)*, vol. 49, no. 1, 2008.
- [8] W. C. Shust and J. A. Elkins, "Wheel forces during flange climb part I - track loading vehicle tests," in *Railroad Conference, 1997., Proceedings of the 1997 IEEE/ASME Joint.*, 1997, pp. 137–147.
- [9] H. Ishida, T. Miyamoto, E. Maebashi, H. Doi, K. Iida, and A. Furukawa, "Safety assessment for flange climb derailment of trains running at low speeds on sharp curves," *Q. Rep. RTRI*, vol. 47, no. 2, pp. 65–71, 2006.
- [10] A. Matsumoto *et al.*, "A new measuring method of wheel-rail contact forces and related considerations," *Wear*, vol. 265, no. 9–10, pp. 1518–1525, 2008.
- [11] O. Kleiner and C. Schindler, "Geometrie und Druckspannungen im Rad/Schiene-Kontakt," *El-Eisenbahningenieur*, no. 4, pp. 9–12, 2011.
- [12] F. Dörner, C. Körblein, and C. Schindler, "On the accuracy of the pressure measurement film in Hertzian contact situations similar to wheel-rail contact applications," *Wear*, vol. 317, no. 1–2, pp. 241–245, 2014.
- [13] C. Hung, H. Doi, K. Nunotani, and S. Lin, "Experiments to measure stress with the wheel/rail contact using embedded FBG sensors," in *9th International Conference on Contact Mechanics and Wear of Rail/Wheel Systems*, 2012, pp. 752–757.

- [14] M. Pau, "Estimation of real contact area in a wheel-rail system by means of ultrasonic waves," *Tribol. Int.*, vol. 36, no. 9, pp. 687–690, 2003.
- [15] M. B. Marshall, R. Lewis, R. S. Dwyer-Joyce, U. Olofsson, and S. Björklund, "Experimental Characterization of Wheel-Rail Contact Patch Evolution," *J. Tribol.*, vol. 128, no. 3, pp. 493–503, 2006.
- [16] R. S. Dwyer-Joyce, C. Yao, J. Zhang, R. Lewis, and B. W. Drinkwater, "Feasibility Study for Real Time Measurement of Wheel-Rail Contact Using an Ultrasonic Array," *J. Tribol.*, vol. 131, no. 4, p. 041401, 2009.
- [17] M. Pau and B. Leban, "Ultrasonic assessment of wheel-rail contact evolution exposed to artificially induced wear," *Proc. Inst. Mech. Eng. Part F J. Rail Rapid Transit*, vol. 223, no. 4, pp. 353–364, 2009.
- [18] R. S. Dwyer-Joyce, C. Yao, R. Lewis, and H. Brunskill, "An ultrasonic sensor for monitoring wheel flange/rail gauge corner contact," *Proc. Inst. Mech. Eng. Part F J. Rail Rapid Transit*, vol. 227, no. 2, pp. 188–195, 2013.
- [19] H. Brunskill, A. Hunter, L. Zhou, R. Dwyer Joyce, and R. Lewis, "An evaluation of ultrasonic arrays for the static and dynamic measurement of wheel–rail contact pressure and area," *Proc. Inst. Mech. Eng. Part J J. Eng. Tribol.*, vol. 234, no. 10, pp. 1580–1593, 2020.
- [20] L. Zhou, H. P. Brunskill, R. Lewis, M. B. Marshall, and R. S. Dwyer-Joyce, "Dynamic characterisation of the wheel/rail contact using ultrasonic reflectometry," *Civil-Comp Proc.*, vol. 104, pp. 1–13, 2014.
- [21] L. Zhou, H. P. Brunskill, and R. Lewis, "Real-time non-invasive measurement and monitoring of wheel–rail contact using ultrasonic reflectometry," *Struct. Heal. Monit.*, vol. 0, no. 0, p. 1475921719829882.
- [22] K. Kendall and D. Tabor, "An Ultrasonic Study of the Area of Contact between Stationary and Sliding Surfaces," *Proc. R. Soc. A Math. Phys. Eng. Sci.*, vol. 323, no. 1554, pp. 321–340, 1971.
- [23] H. G. Tattersall, "The ultrasonic pulse-echo technique as applied to adhesion testing," *J. Phys. D. Appl. Phys.*, vol. 6, pp. 819–832, 1973.
- [24] A. Rovira, A. Roda, M. B. Marshall, H. Brunskill, and R. Lewis, "Experimental and numerical modelling of wheel-rail contact and wear," *Wear*, vol. 271, no. 5–6, pp. 911–924, 2011.
- [25] M. Pau, B. Leban, and M. Guagliano, "Propagation of Sub-surface Cracks in Railway Wheels for Wear-induced Conformal Contacts," *J. Mech. Syst. Transp. Logist.*, vol. 3, no. 1, pp. 226–235, 2010.
- [26] S. Fukagai, L. Ma, and R. Lewis, "Tribological aspects to optimize traction coefficient during running-in period using surface texture," *Wear*, vol. 424–425, no. January, pp. 223–232, 2019.

- [27] S. Fukagai, H. P. Brunskill, A. K. Hunter, R. S. Dwyer-Joyce, and R. Lewis, "Transitions in rolling-sliding wheel/rail contact condition during running-in," *Tribol. Int.*, 2019.
- [28] L. Pesaresi, A. Fantetti, F. Cegla, L. Salles, and C. W. Schwingshackl, "On the Use of Ultrasound Waves to Monitor the Local Dynamics of Friction Joints," *Exp. Mech.*, vol. 60, no. 1, pp. 129–141, 2020.
- [29] M. Schoenberg, "Elastic wave behavior across linear slip interfaces," *J. Acoust. Soc. Am.*, vol. 68, no. 5, pp. 1516–1521, 1980.
- [30] R. Pohrt and Q. Li, "Complete boundary element formulation for normal and tangential contact problems," *Phys. Mesomech.*, vol. 17, no. 4, pp. 334–340, 2014.
- [31] A. Azam, A. Dorgham, A. Morina, A. Neville, and M. C. T. Wilson, "A simple deterministic plastoelastohydrodynamic lubrication (PEHL) model in mixed lubrication," *Tribol. Int.*, vol. 131, no. October 2018, pp. 520–529, 2019.
- [32] E. A. H. Vollebregt, "The Bound-Constrained Conjugate Gradient Method for Non-negative Matrices," *J. Optim. Theory Appl.*, vol. 162, no. 3, pp. 931–953, 2014.
- [33] R. Pohrt and V. L. Popov, "Contact stiffness of randomly rough surfaces," *Sci. Rep.*, vol. 3, pp. 1–6, 2013.
- [34] D. Nowell, D. Mulvihill, H. Brunskill, M. Kartal, and R. Dwyer-Joyce, "Measurement and modelling of interface stiffness in frictional contacts," in *Proceedings of 5th World Tribology Congress, WTC 2013*, 2013.
- [35] M. Gonzalez-Valadez, A. Baltazar, and R. S. Dwyer-Joyce, "Study of interfacial stiffness ratio of a rough surface in contact using a spring model," *Wear*, vol. 268, no. 2–3, pp. 373–379, 2010.
- [36] B. W. Drinkwater, R. S. Dwyer-Joyce, and P. Cawley, "A study of the interaction between ultrasound and a partially contacting solid—solid interface," *Proc. R. Soc. London. Ser. A Math. Phys. Eng. Sci.*, vol. 452, no. 1955, pp. 2613–2628, Jan. 1996.
- [37] R. S. Dwyer-Joyce, B. W. Drinkwater, and A. M. Quinn, "The Use of Ultrasound in the Investigation of Rough Surface Interfaces," *J. Tribol.*, vol. 123, no. 1, p. 8, 2001.
- [38] E. Rabinowicz, "The nature of the static and kinetic coefficients of friction," *J. Appl. Phys.*, vol. 22, no. 11, pp. 1373–1379, 1951.
- [39] S. Maegawa, A. Suzuki, and K. Nakano, "Precursors of global slip in a longitudinal line contact under non-uniform normal loading," *Tribol. Lett.*, vol. 38, no. 3, pp. 313–323, 2010.
- [40] N. Nagase, S. Shido, and I. Yarita, "The effect of lubricant on microwear of dull rolls in temper rolling by 4 hi rolling mill," *ISIJ Int.*, vol. 49, no. 6, pp. 874–880, 2009.
- [41] M. C. Shaw, A. Ber, and P. A. Mamin, "Friction Characteristics of Sliding Surfaces Undergoing Subsurface Plastic Flow," *J. Basic Eng.*, vol. 82, no. 2, pp. 342–345, 1960.

- [42] T. Wanheim, N. Bay, and A. S. Petersen, "A theoretically determined model for friction in metal working processes," *Wear*, vol. 28, no. 2, pp. 251–258, May 1974.
- [43] P. J. Blau, "On the nature of running-in," *Tribol. Int.*, vol. 38, no. 11–12, pp. 1007–1012, Nov. 2005.

5 TRANSITION OF THE FRICTION BEHAVIOUR AND INTERFACE TOPOGRAPHY DUE TO REPEATED HIGH-PRESSURE CONTACT AND SLIDING

Paper 3

Transition of the friction behaviour and interface topography due to repeated high-pressure contact and sliding

S. Fukagai^{a,b}, M.B. Marshall^b, R. Lewis^b

^a Railway Technical Research Institute, Tokyo, Japan

^b Department of Mechanical Engineering, University of Sheffield, Sheffield, UK

Abstract

A rapid increase in the friction coefficient can occur during the running-in between the wheel and rail. Although it has been found that the running-in process depends on the initial topography, the difficulty in obtaining accurate non-destructive interfacial measurements has hindered systematic investigations. In this work, four interfaces, which have different initial topographies, were continuously monitored using ultrasound reflectometry until they became conformed. A contact pressure representative of that in a wheel-rail interface was achieved by using a high-pressure torsion test approach. The transition of contact stiffness and friction coefficient with repeated sliding and their relationship were investigated. Based on the experimental results, a mechanism model for the running-in process of the contact interface was proposed. These findings will help in understanding the running-in process of the wheel-rail interface and assist in managing the wheel and rail properly to improve safety.

To be submitted

5.1 Introduction

The wheel and the rail play vital roles in rail operation, such as bearing the vehicle load, guiding the vehicle and transmitting the driving and braking forces. To achieve these

roles, the wheel and the rail roll and slide against each other under extremely high contact pressure conditions. Due to the severe contact condition, the interface is the origin of a number of tribological problems during operation. For example, when contaminants, such as water, oil or fallen leaves, get into the interface, the interaction leads to wheel spin and brake lock-up sometimes. Such significant sliding can cause not only performance problems in terms of delays and safety issues from over-running (past signals at danger or station), but also thermal damage and abnormal deformation of wheel and rail [1], [2]. Also, it is known that high friction coefficient and slip at curves could lead to severe wear and deformation of wheel and rail [3], [4], high energy consumption [5] and wheel-rail noise [6], [7]. Additionally, it increases the risk of a wheel climb derailment occurring [8]–[10].

One parameter that has a significant impact on these problems is the friction coefficient. The friction coefficient is a system-dependent value, and it is generally known that the value depends on various environmental conditions, e.g., temperature, humidity, contamination, etc. Surface topography may be one of the influencing factors. For example, it has been reported that wheels with lathe cutting marks just after wheel re-profiling are prone to derailment [11]–[13]. However, the effect of such topography is still not well understood. The authors have already investigated the influence of the topography on the friction behaviour between the wheel and rail in dry condition focusing on the mechanism of the flange climb-up derailment [14]. As a result, it was found that the initial topography strongly affected the friction behaviour during running-in (Figure 5-1). Though these results indicate that the evolution of the surface asperities strongly relates with the friction behaviour, these findings were based on surface investigations when the test was stopped intermittently. Therefore, the difficulty in obtaining accurate non-destructive interfacial measurements has hindered systematic investigations.

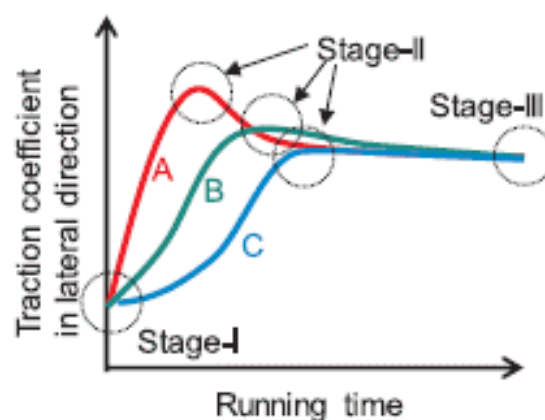


Fig. 5-1 Schematic patterns of the traction coefficient curves at the twin-disks tests during running-in [14]; the initial roughness is greater in the order of C, B, and A.

Recently, ultrasound techniques have been used to observe the contact between wheel and rail [15]–[22]. Though there are spatial resolution limits and considerations of transducer positioning to ensure the sound waves reflect off the area of interest, this technique can be used to non-invasively and directly observe the contact. When an ultrasound wave strikes the interface between the wheel and rail, it is partially transmitted and partially reflected. The proportion of the wave reflected depends on the stiffness of the contact [23], [24]. This approach has been used to determine the contact pressure distribution in wheel-rail contacts and the influence of wear profile, roughness and surface defects on the contact patch [16], [18]. Also, this actual distribution of the contact pressure could be applied to the simulation of wear and damage propagation with consideration for surface topography [25], [26].

The authors applied the ultrasound reflectometry to an actual wheel-rail interface and monitored the changes in the interface condition during repeated rolling and sliding [27]. The results showed that there was a correlation between the change in friction coefficient and contact stiffness with repeated rolling-sliding, and a near linear relationship was obtained. Additionally, the authors also applied the ultrasonic measurement technique to the high-pressure torsion (HPT) test and investigated the dynamic change of contact stiffness with sliding [28]. As a result, it was found that the deformation of surface asperities and frictional behaviour due to sliding differed depending on the surface topography. The above report is limited to the measurement of friction during one test cycle, but if an interface where friction is repeated can be continuously monitored, the mechanism of the continuously changing friction coefficient during the running-in as shown in Fig. 5-1 may be revealed.

The aim of this work was to investigate what is happening at the wheel-rail interface during the running-in process and how the behaviour influences the evolution of friction. To achieve a contact pressure equivalent to the wheel-rail contact, a high-pressure torsion test approach was used. Tiny piezoelectric elements which activate the ultrasound wave were attached to the one of the specimens. Ultrasonic reflection from the interface was used to conduct the in-situ evaluation of the contact condition, particularly contact stiffness. Transient loading condition and friction coefficient were also measured during the test. Following these measurements, the changes of contact stiffness with repetitive sliding cycles and the running-in mechanism were proposed.

5.2 Methodology

5.2.1 HPT testing equipment

Since the details of the high-pressure torsion test equipment and ultrasonic measurement are described in previous works [28], [29] only the basic structure is explained here. Figure 5-2 shows the appearance of the HPT testing equipment. This

equipment is capable of making contact between two specimens with a constant normal pressure and then rotating the bottom specimen in the direction parallel to the contact interface. It uses load cells for tension, compression, and torque to measure the compressing load and the torque; and uses a rotary variable differential transformer to measure the rotation speed. Table 5-1 lists the specifications of the HPT testing equipment.

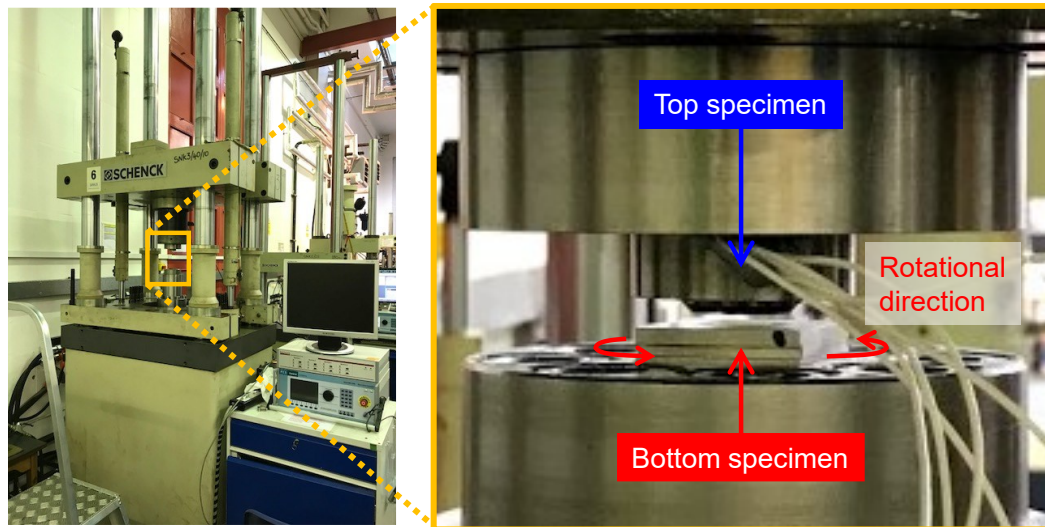


Fig. 5-2 Appearance of the HPT equipment.

Table 5-1 Specifications of the HPT testing equipment

Item	Value
Axial load (tensile and compression)	± 400 kN
Movable range in axial direction	± 25 mm
Torque	± 1000 Nm
Movable range in rotational direction	± 40 degrees

5.2.2 Ultrasonic measurement

Since the details of the ultrasonic measurement of the interface are described in many previous studies [16], [20], [27], [29]–[31] only the basic principle is explained here. Figure 5-3 shows the measurement principle of contact stiffness using ultrasound wave. At the interface between materials with different acoustic impedances, only a part of a sound wave transmits at the interface and the rest of it is reflected back. The reflectivity for ultrasound at an interface where the materials adhere to each other without any cavities, R , can be represented as in Equation (1) and it varies depending on the difference in the acoustic impedances of the two materials.

$$R = \frac{z_2 - z_1}{z_2 + z_1} \quad (1)$$

In this equation, z_1 and z_2 are the acoustic impedances of the materials in contact. The acoustic impedance is determined by the product of the density of the material and the acoustic velocity in the material. Therefore, when the acoustic impedances of the two materials in contact are the same and if the interface is hypothetically perfectly conformal, all the sound wave will transmit at the interface without any loss and no reflection occurs ($R=0$). On the other hand, when materials with significantly different acoustic impedances, such as a gas and a solid, are in contact, sound waves are almost completely reflected ($R \approx 1$).

Because the surface of an actual material is not a completely flat plane and has minute asperities and undulations, cavities are generated at the interface. When the wavelength of the ultrasound is sufficiently larger than the cavity size at the interface, the proportion of the reflected wave also depends on the contact stiffness. The contact stiffness is a function of the number, size, and approach of the contact points determined while considering the minute asperities [23]. Because the topographies of the surface changes due to elastic and plastic deformation, the measured reflectivity changes as shown in Figure 5-3 as the load is applied. Therefore, it is possible to evaluate the contact stiffness at the interface by using the reflectivity of ultrasound.

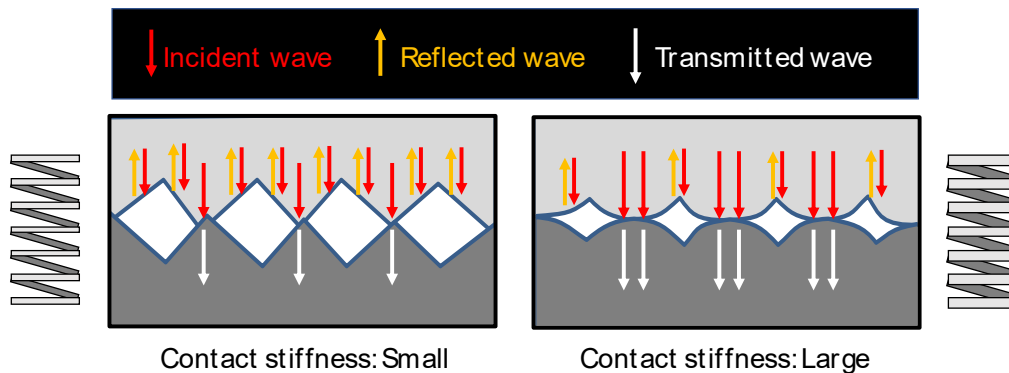


Fig. 5-3 Measurement principle of contact stiffness using ultrasound wave.

5.2.3 Specimens

The top and the bottom specimens were made from ER8 (EN13262:2009) and R260 (EN13674-1:2011), respectively. Table 5-2 shows the hardness for the specimens. The hardness values are the average for 5 measurements. The measurements were conducted by a Mitutoyo HV-110 machine and the test force was 5 kgf.

Table 5-2 Hardness of the specimens

	R8T Wheel (top) specimen	R260 Rail (bottom) specimen
Hardness HV(5)	267(± 8)	285(± 9)

Note: The values in brackets indicate standard deviation.

The surface type of the top specimens remained constant for all tests and was achieved by grinding. On the other hand, the surface types of bottom specimens were varied. Four different roughness' were used: a low roughness specimen achieved by sand blasting and medium and large roughness specimens achieved by machining, which gave increasingly high values. Figure 5-4 shows the appearance of specimens on the contact surface.

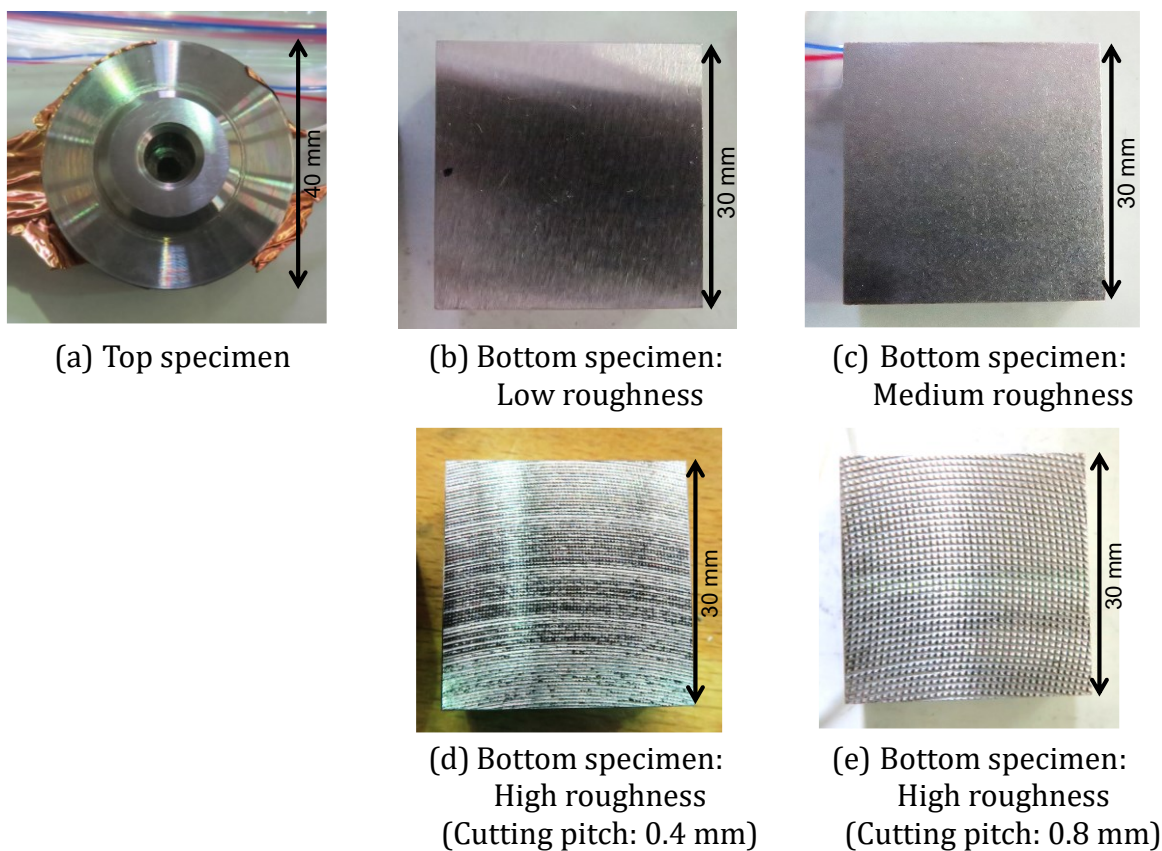


Fig. 5-4 Appearance of specimens on the contact side.

Table 5-3 lists the values of the root-mean-square of roughness which were measured using a contact-type roughness meter (Mitsutoyo Surf Test SJ-210) and the composite roughness. The value of the root-mean-square of roughness is the average value for 5 measurements. The value of the combined roughness, σ , is calculated using equation (2);

$$\sigma = \sqrt{R_{qt}^2 + R_{qb}^2} \quad (2)$$

where R_{qt} and R_{qb} are the root mean square roughness of the top and bottom specimens, respectively.

Table 5-3 Roughness' of specimen's surface before the tests for topography dependence

Topography	Normal pressure (MPa)	Measurement direction	Root-mean-square of roughness, Rq (μm)		Composite roughness for each direction, σ (μm)
			Top specimen	Bottom specimen	
Low roughness	600	Circumferential	0.5	0.7	0.8
		Radial	0.6	0.6	0.9
Medium roughness	600	Circumferential	0.3	1.4	1.5
		Radial	0.4	1.5	1.6
High roughness (0.4 mm)	600	Circumferential	0.6	5.7	5.8
		Radial	0.8	2.7	2.8
High roughness (0.8 mm)	600	Circumferential	0.6	7.4	7.4
		Radial	0.7	8.0	8.1
	300	Circumferential	2.3	7.3	7.7
		Radial	2.3	8.9	9.2
	900	Circumferential	0.3	10.2	10.2
		Radial	0.3	9.7	9.7

For all the contact tests, specimens were soaked in 2-propanol before the measurement and then washed in an ultrasound cleaner. Piezoelectric elements were attached to the top specimen to reflect the ultrasound towards the contact interface and measure the reflected wave. Figure 5-5 shows the piezoelectric element which was attached on the back of the top specimen. The piezoelectric elements were attached to respectively measure the longitudinal and transverse waves to determine the contact stiffness in the normal, tangential direction, because there is a possibility the contact stiffness' in different directions show varying characteristic behaviour with the application of the normal and tangential pressure. The piezoelectric elements for the measurement of the transverse waves were installed in directions parallel (circumferential direction) and perpendicular (radial direction) to the friction direction. Piezoelectric elements with a

central frequency of 5 MHz were used for both the measurements of longitudinal and transverse waves. In this test, a "Pitch-Catch" method was employed in which different piezoelectric elements are used for activation and reception of the ultrasound. For the measurement, there is another method that is referred to as "Pulse-Echo" in which the same piezoelectric element is used for transmission and reception of the ultrasound. However, this method is inferior to the "Pitch-Catch" method in terms of accuracy because the transmitted wave remains as a noise.

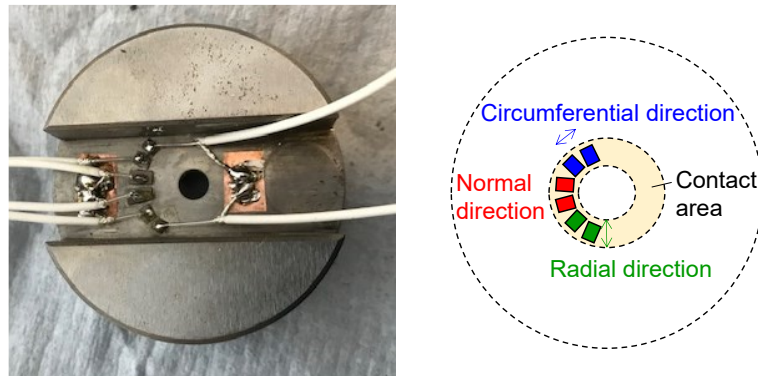


Fig. 5-5 Piezoelectric element which is attached on the back of the top specimen.

5.2.4 Test procedure

The test was conducted using the following procedure:

1. A normal pressure is applied after inserting a pressure-sensitive paper between the specimens to check that the load is uniformly distributed on the contact surface.
2. After making the specimens directly contact with each other, the pressure on the contact surface is increased gradually to approximately 600MPa (Additionally, 300 MPa in the case of high roughness).
3. While keeping the top specimen in the specified position, the bottom specimen is rotated.
4. After releasing the torque, the specimens are separated.
5. Back to step 2.

During steps 2 to 4, the contact stiffness is measured by using ultrasound with normal force (normal pressure), torque (tangential pressure), and the rotational position of the specimen (Fig. 5-6). Steps 2 to 5 were repeated until 15 cycles and the roughnesses of top and bottom specimens were measured after the 1st, 5th, 10th and 15th cycle. The roughnesses were measured five times for each of the radial and circumferential directions of the specimen rotation and the average value was evaluated.

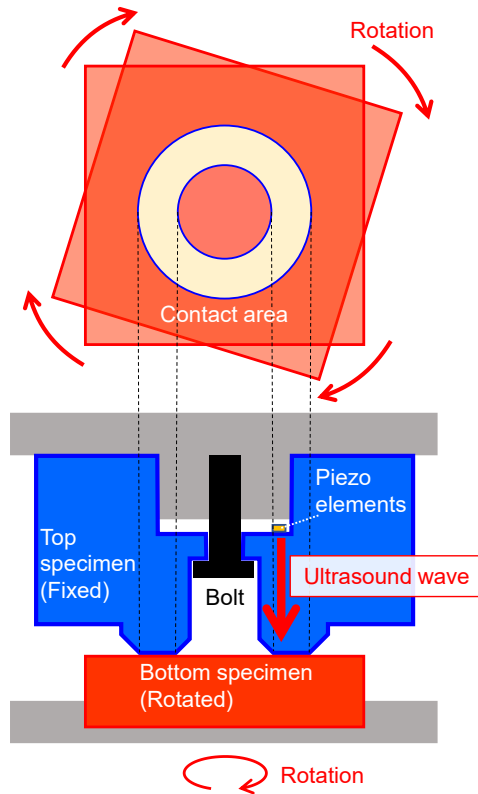


Fig. 5-6 Contact between top and bottom specimens and rotation of bottom specimen.

Figure 5-7 shows a schematic example of a change of contact pressure and sample rotation position between test steps 2-4. Normal force (normal pressure), torque (tangential pressure) and contact stiffness for each test cycle were evaluated by calculating the average value for a given time. In order to eliminate making an arbitrary evaluation, the time interval was standardized as 3 seconds before the signal to start the release of torque was sent, and the average value during that time was obtained.

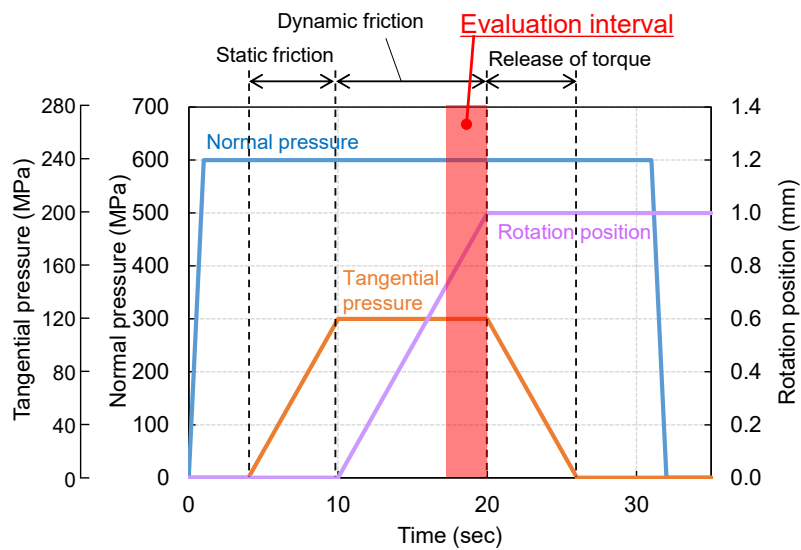


Fig. 5-7 Schematic example of a loading cycle.

5.3 Results

5.3.1 Topography dependence on contact stiffness and friction coefficient during running-in

Figure 5-8 shows the change of friction coefficient with test cycles for different initial roughness. It is found that the lower the initial roughness, the faster the friction coefficient rises, and the peak friction coefficient is higher for lower initial roughness. It can also be seen that the friction coefficient reaches around 0.6 in the final state of the 15th cycle for all roughness conditions. These tendencies of change coincide well with the patterns which were obtained from the results using a twin-disk machine (Figure 5-1).

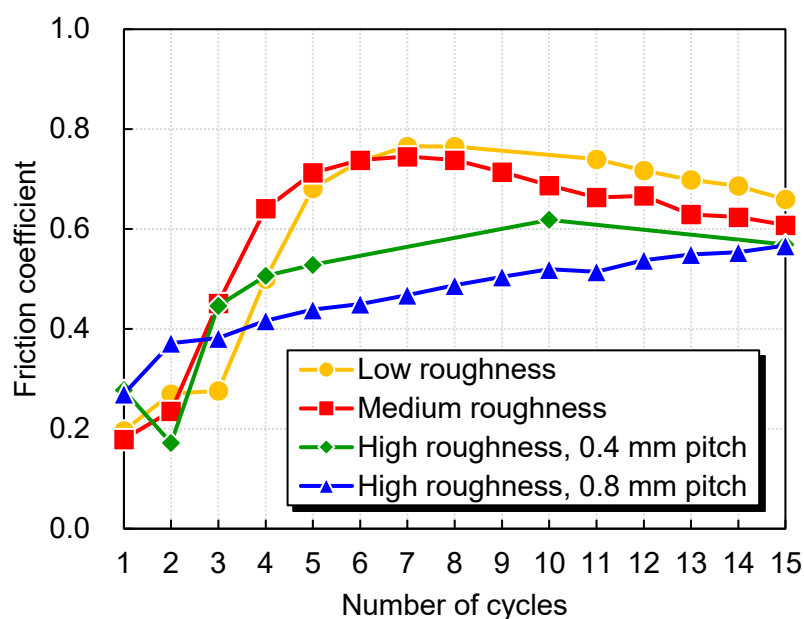


Fig. 5-8 Change of friction coefficient with test cycles for different initial roughness.

Figure 5-9 shows the changes of contact stiffness and friction coefficient with testing cycles for different initial roughness. It is found that the stiffness in the cases of low and medium roughness peaked in the early cycles, the 4th-5th, then dropped until the 8th-10th test cycle, then tapered off until the 15th test cycle. In the case of high roughness, 0.4 mm pitch, the contact stiffness rose gradually until the 5th or 10th cycle, then kept constant or tapered until the 15th test cycle. In the case of high roughness, 0.8 mm pitch, the stiffness gradually increased through all the test cycles. A generally good correlation was obtained between the contact stiffness and the friction coefficient. The friction coefficient was at its maximum at about the same time as the contact stiffness was at its maximum.

By comparing the changes in all roughness conditions, it was observed that the lower the initial roughness, the faster the increase in contact stiffness and the higher the peak contact stiffness for all cycles. For all roughness conditions, normal stiffness was higher than the shear stiffnesses after the 6th cycle. This is in agreement with previous studies

such as Gonzalez-Vadez *et al.* [32]. Furthermore, in this experiment, the shear stiffness in the circumferential direction tended to be higher than that in the radial direction for most of the test cycles, especially for smoother surfaces. This is due to the possibility that the roughness is directional and that when the shearing load is added, the asperities are more likely to interlock in the circumferential direction than in the radial direction.

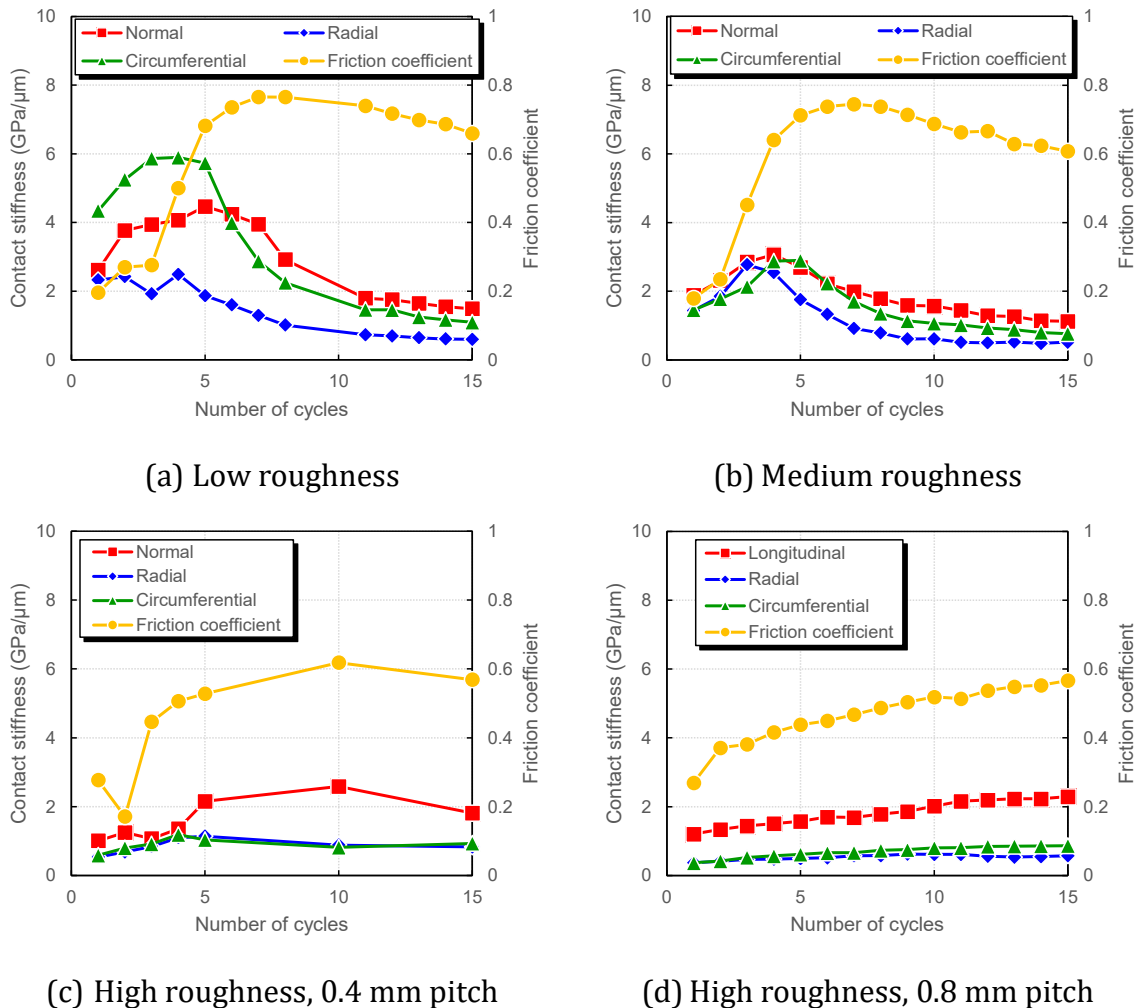


Fig. 5-9 Changes of contact stiffness and friction coefficient with test cycles for different initial roughness.

Figure 5-10 shows the relationship between normal contact stiffness and friction coefficient during cycles. Although there is a generally positive correlation between the friction coefficient and the contact stiffness, the correlation appears to be dependent on the initial topography conditions. The higher the initial roughness, the more linear the relationship between contact stiffness and friction coefficient, and the lower the initial roughness, the more gradual the relationship between the contact stiffness and the friction coefficient at the beginning of cycles. In other words, at the beginning of the cycle with low roughness, a small tangential (friction) force caused a large increase in contact stiffness.

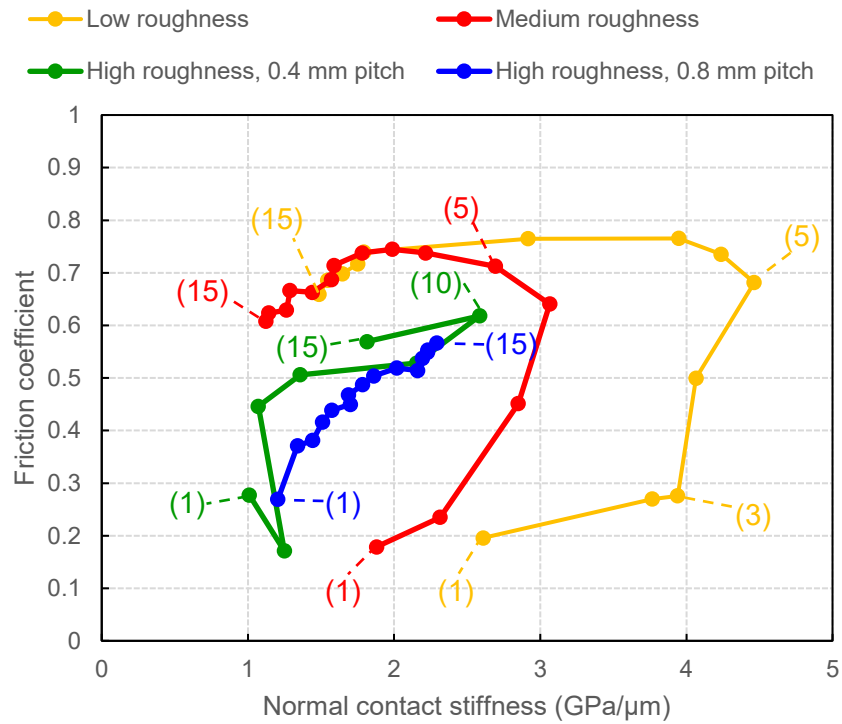


Fig. 5-10 Relationship between normal contact stiffness and friction coefficient during cycles. The number in brackets is the cycles.

5.3.2 Contact pressure dependence on contact stiffness and friction coefficient during running-in

Figure 5-11 shows the change of friction coefficient with test cycles for different contact pressures under high roughness conditions (0.8 mm pitch). In the case of 600 and 900 MPa, there was a reversal of the high and low values when the number of cycles was low, but basically, the friction coefficient in the running-in process increased with the increase in contact pressure.

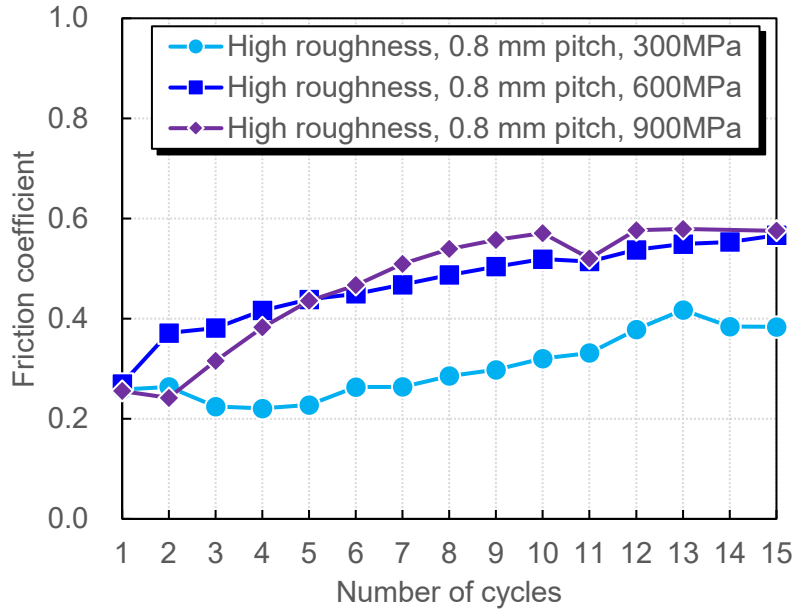


Fig. 5-11 Change of friction coefficient with test cycles for different contact pressure under high roughness conditions (0.8 mm pitch).

Figure 5-12 shows the changes of the contact stiffness and friction coefficient with testing cycle for different contact pressure under high roughness conditions (0.8 mm pitch). Here, the result of normal stiffness under the condition of 900 MPa contact pressure is missing due to sensor failure. It is found that the contact stiffness increases with the contact pressure. It is known that the contact stiffness depends on the contact pressure and increases with the contact pressure [16], [33]–[36]. However, the present result further shows that the higher the contact pressure, the greater the slope of the increase in contact stiffness with increasing number of cycles. Furthermore, the slope of the shear stiffness in the circumferential direction is even larger than that in the radial direction.

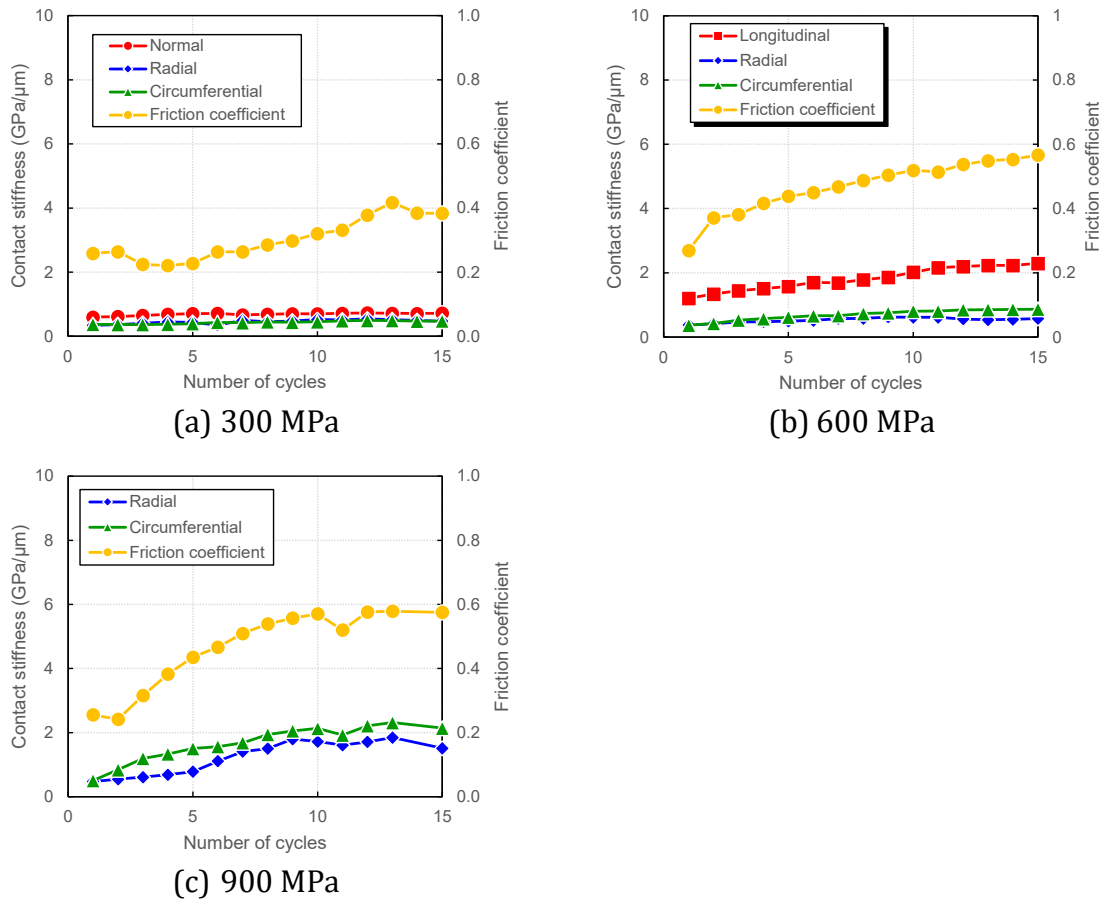
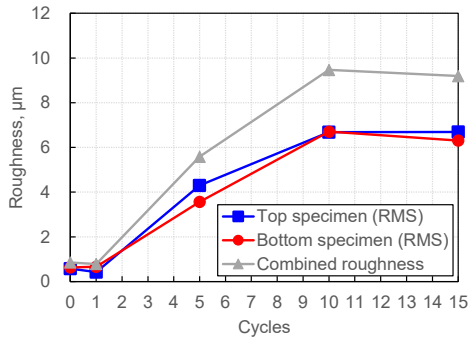


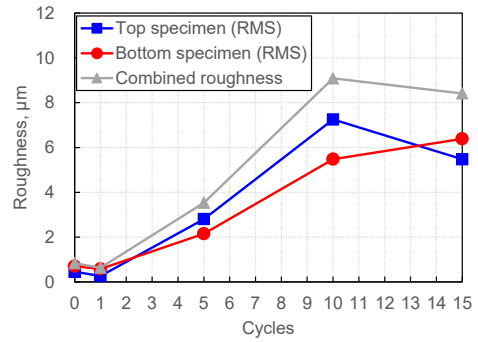
Fig. 5-12 Changes of contact stiffness and friction coefficient with test cycles for different contact pressure under high roughness conditions (0.8 mm pitch). (The result of normal stiffness under the condition of 900 MPa contact pressure is missing due to sensor failure.)

5.3.3 Change in the surface roughness during repetitive cycles

Figure 5-13 shows the changes of the root mean square roughness and combined roughness with test cycles in different initial roughness. In the case of low and medium roughness, the roughness of the top and bottom specimens changed in a similar manner. These roughness values increased after the 5th cycle and then increased slowly or remained constant until the 15th cycle. The combined roughness also changed in the same way as the individual roughness of the top and bottom specimens. In the case of high roughness, the roughness of the bottom specimen was higher than that of the top specimen before the test, but as the number of cycles increased, the roughness of the bottom specimen decreased and that of the top specimen increased, finally reaching the same level after the 15th cycle. The combined roughness increased with the number of cycles in the radial direction of 0.4 mm pitch, but the others remained almost constant. The final combined roughness after the 15th cycle was lower in the circumferential direction than in the radial direction for all initial roughness conditions.

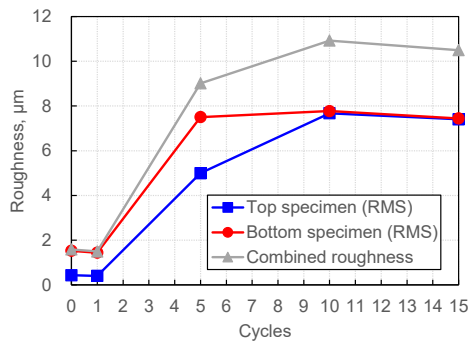


(i) Radial direction

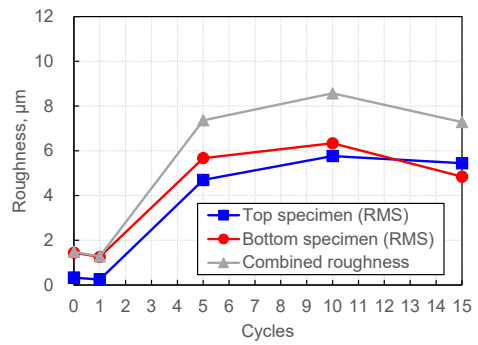


(ii) Circumferential direction

(a) Low roughness

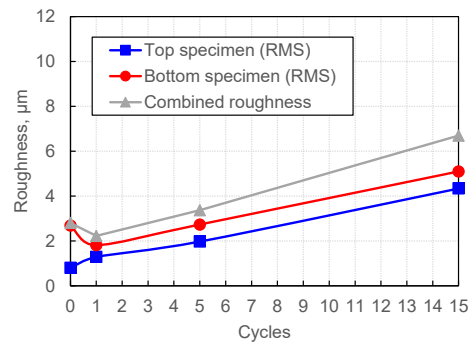


(i) Radial direction

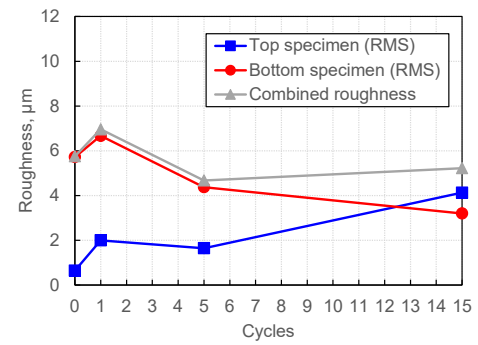


(ii) Circumferential direction

(b) Medium roughness

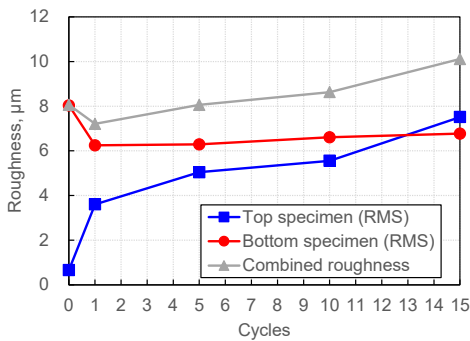


(i) Radial direction

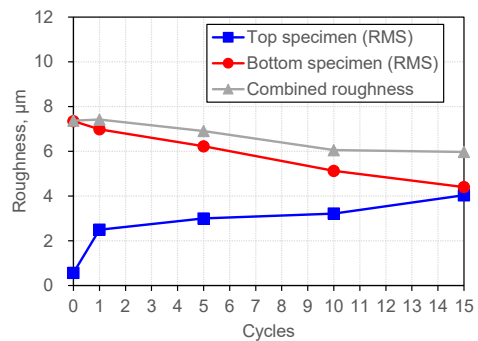


(ii) Circumferential direction

(c) High roughness, 0.4 mm pitch



(i) Radial direction



(ii) Circumferential direction

(d) High roughness, 0.8 mm pitch

Fig. 5-13 Changes of the root mean square roughness and combined roughness with test cycles in different initial roughness.

Figure 5-14 shows the changes of the root mean square roughness and combined roughness with test cycles for different contact pressure, under high roughness conditions (0.8 mm pitch). For all contact pressure conditions, the roughness values of the bottom and top specimens approached each other as the number of cycles increased, and the higher the contact pressure, the faster these values approached each other. The final combined roughness values in the circumferential direction were lower than those in the radial direction. Appendix B shows the roughness profiles of the top and bottom specimens measured with the progress of cycles.

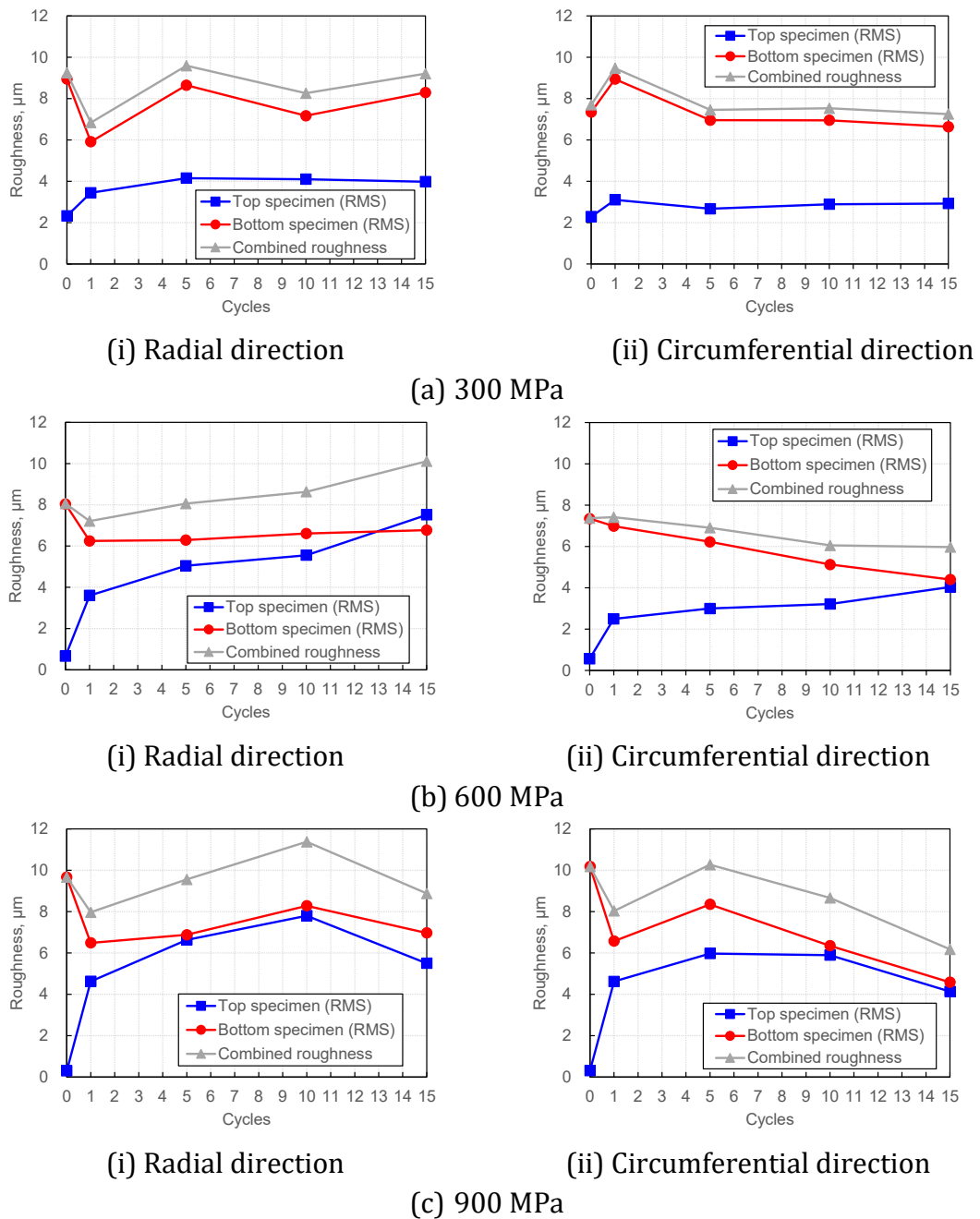


Fig. 5-14 Changes of the root mean square roughness and combined roughness with test cycles in different contact pressure under high roughness conditions (0.8 mm pitch).

5.4 Discussion

From Figs. 5-8 and 5-9, the running-in process can be divided into two main phases; a phase in which the friction coefficient and the contact stiffness are increasing (Phase-I) and decreasing (Phase-II). The distinction between these two phases was clear when the initial roughness was low or medium, but tended to become blurred when the initial roughness was high. This may be due to the elastic-plastic response of the interface influenced by differences in the initial roughness. Based on the whole results, mechanisms for how the surfaces evolve with the repetition of cycles can be proposed. Figure 5-15 shows a schematic diagram of the running-in process of the interface.

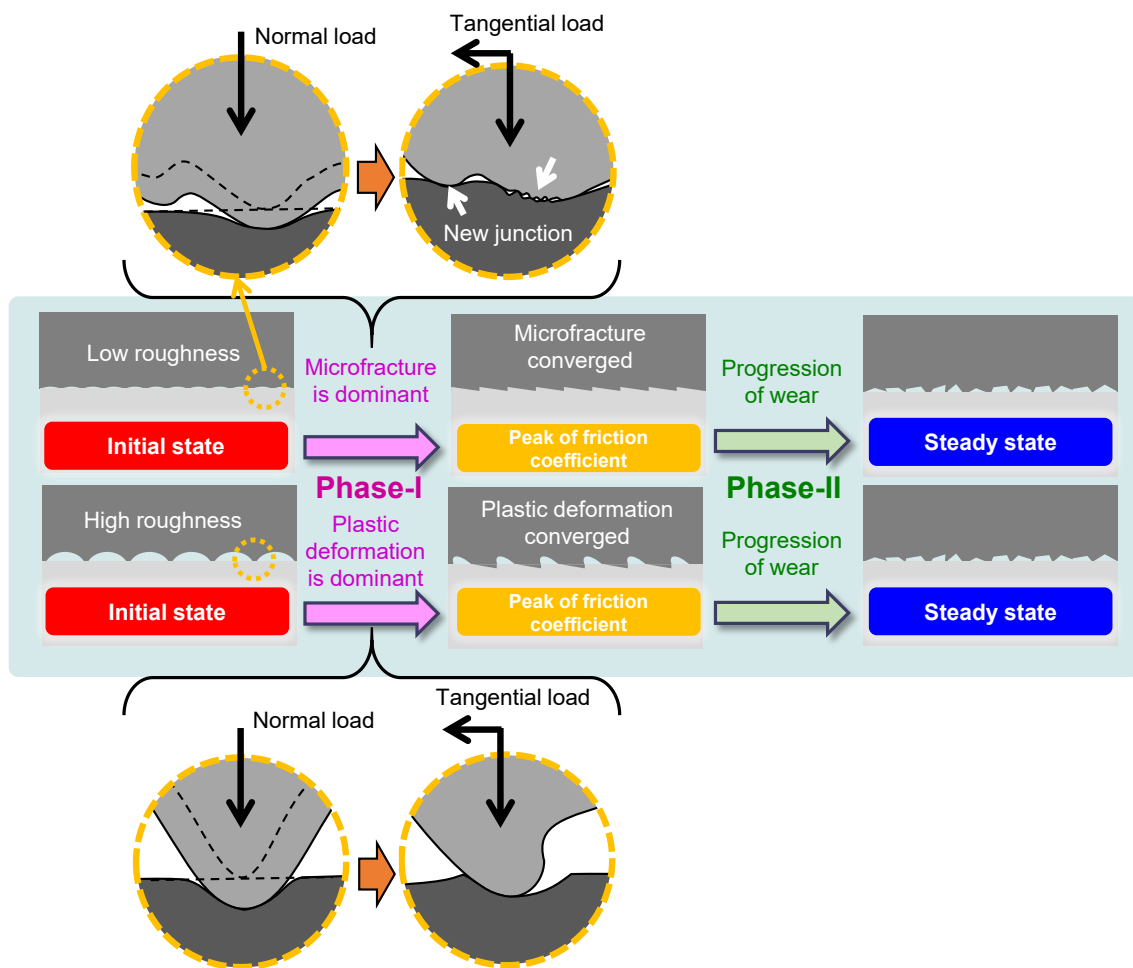


Fig. 5-15 Schematic mechanism of the difference of the interfacial condition during running-in between low initial roughness and high initial roughness.

In the cases of low and medium roughness, the process was considered as follows;

- i. As seen previously for a single cycle [28], asperity junctions form between the surfaces resisting tangential motion. As the Coulomb limit is approached, microscopic fracture occurs, leading to a drop in friction and contact stiffness.
- ii. Whilst fracture is microscopic at first, macro-slip quickly propagates to the entire interface [37], and undeformed asperities, previously not in contact, form new junctions. Stiffness then begins to rise [28], implying an increase in the deformation resistance of the interface, in turn leading to an increase in the coefficient of friction. The fractured junctions also expose fresh metal beneath the original surface, which similarly contributes to an increase in friction coefficient. Hence this process results in the observed overall rise in friction and stiffness over the first cycle.
- iii. With repeat cycles, the process continues. Each time the Coulomb limit is reached, interface damage occurs, followed by the formation of new junctions, as yet more previously undeformed asperities come into contact. Whilst the damaged junctions are weaker and of lower stiffness, the addition of new junctions into the contact leads to a continued net rise in both the interface stiffness and coefficient of friction.
- iv. Finally with continued cycles, the surfaces reach a point of conformity, with all asperities having become part of the contact. At this point stiffness and coefficient of friction are maximized.
- v. With continued motion and no new asperities available, wear continues at asperity junctions, leading to a drop in stiffness as damage accrues. However, as a fresh metal surface is also exposed continuously, the decrease in the friction coefficient is somewhat gradual, given this removal of material aids junction strength.

i~iii correspond to Phase-I and iv to Phase-II.

In the cases of high roughness, the process was considered as follows;

- i. The tips of asperities also conformed, but the penetration of asperities (i.e. each large machined peak) is greater than the smoother interface because of the higher local pressure [37].
- ii. With the application of tangential load, the asperities plastically deform rather than break bonds owing to the interlocks of the tips by the penetration and the greater heights of asperities. Once the Coulomb limit is passed and macro-slip occurs, plastic deformation and rounding of surface peaks accelerates [28].
- iii. With continued macro-slip, continued deformation and rounding occur at a gradual rate, and stiffness and friction coefficient rise slowly.
- iv. As the plastic deformation of the asperities converges, the micro-slips begin to increase. Throughout this process changes in measured roughness and contact stiffness are marginal, given the wear that occurs is not on the scale of the overall initial surface topography.

i~iii correspond to Phase-I and iv to Phase-II. In the case of 0.4 mm pitch, Phase-II was reached earlier than in the case of 0.8 mm pitch, and partial fracture (micro-slip) was considered to have increased after 10th cycle. However, the peak contact stiffness was not as high as for low and medium roughness, indicating that the micro-slip occurred

partially before the whole asperities were deformed plastically and were expected to spread gradually over the whole contact area.

In Fig. 4-16(c), the surface of the top specimen after the test showed indentations which were probably formed by the contact with the initial asperities of the bottom specimen. The roughness curve of the top specimen after 1st cycle, shown in Table B.4 in Appendix, also shows similar indentations. These results support i.

The contact pressure dependency on the running-in process on contact stiffness and friction coefficient would also support this mechanism. The increase in contact stiffness and friction coefficient was more gradual when the contact pressure was lower (300 MPa). The reason for this is thought to be that the decrease in contact pressure caused more gradual deformation of the surface asperities and a more gradual increase in the friction coefficient.

It is considered that wear debris are easily ejected from the system in the twin disk machines [14], whereas they are less likely to be ejected in the HPT machines. Such wear debris may have been trapped into the gaps formed by the surface asperities, also making the interface stiffer at the peak of the friction coefficient. In the case of the low/medium initial roughness, the same phenomenon could also have contributed to the increased contact stiffness in the early stages, such as i to iv. However, the effect of the above mentioned wear debris in these HPT tests does not seem to be dominant in the mechanism, because the friction coefficient increased despite the fact that there was almost no ejected debris in the early stages before the friction coefficient reached its peak in the twin disk tests [14].

Roughness is clearly a strong driver for friction changes in the running-in process, and in the measured data, obvious links also exist between the roughness state and the steady-state friction. Whilst it would have been desirable to measure the roughness after every cycle and microanalysis of worn surfaces, and this is something to be considered in the future, further analysis of the pre- and post-test data recorded can help to clarify the trends observed.

Fragmented roughness data is one such analysis approach that can be undertaken to investigate the data further. Figure 5-16 shows the change of the power spectral density (PSD) obtained from the circumferential roughness curve of the bottom specimens with the increase in the number of cycles in the case of low and high roughness (0.8 mm pitch, 600 MPa) case. It should be noted that these are not the true measured values, but the pseudo-roughness curves obtained by connecting the roughness curves measured five times for 2.4 mm each, and then performing the Fast Fourier Transform. At the PSD before the test, for the high roughness conditions, there are characteristic peaks around the spatial frequencies of 1.25×10^{-3} , which correspond to the fly cutting pitch. For the low roughness conditions, no characteristic peaks were observed.

It can be seen that the characteristic peaks of high roughness gradually decrease with the increase in the number of cycles until the 15th cycle. This can be attributed to the gradual plastic deformation of the cutting marks due to normal and tangential pressures. In addition, after the 10th cycle, a slight increase in PSD is observed in the region of spatial frequency 10^{-2} and above. This is considered to be due to the formation of fine unevenness in the order of several tens of micrometres by the wear.

In the low roughness case, the PSD decreased slightly after the first cycle at a spatial frequency of about 1×10^{-2} , and transformed into a topography with a PSD peak at a spatial frequency of about 2 to 4×10^{-3} from the 5th to the 10th cycle. These peaks are considered to be transient, as they are rarely seen in the beginning and are reduced after the final 15th cycle. This may suggest that large frictional forces resulted in relatively large scale surface breakdown and caused the decrease the contact stiffness during Phase-II. It should be noted that for the two cases with very different initial roughnesses, a similar surface topography was eventually reached.

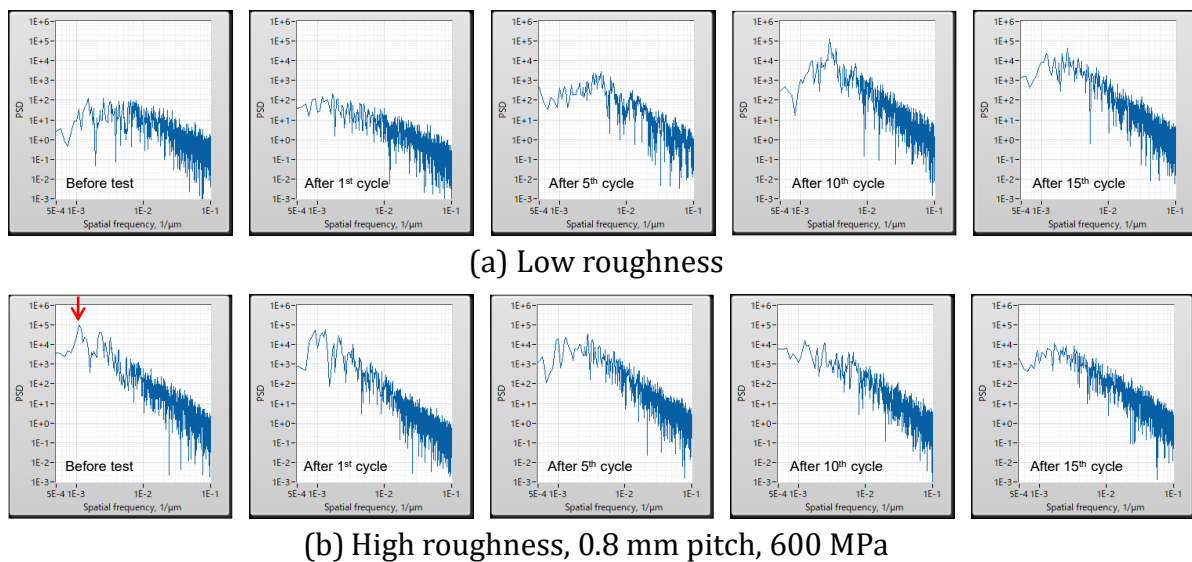


Fig. 5-16 Change of the power spectral density (PSD) obtained from the circumferential roughness curve of the bottom specimens with the increase in the number of cycles. The arrow in (b) refers to the frequencies that can be attributed to the fly cut.

5.5 Conclusions

Aiming to understand the difference in the running-in behaviour of a wheel-rail interface under different initial roughness conditions and its effect on the friction coefficient, ultrasound reflectometry was applied to the high-pressure torsion test. The high-pressure torsion test cycle was repeated up to 15 times and the change in friction coefficient was monitored and the change in contact stiffness was measured in situ using ultrasound. The following conclusions can be drawn:

- (1) The lower the initial roughness, the faster the friction coefficient rose, and the higher

the peak friction coefficient value was. These tendencies coincided well with those seen using a twin-disk machine in a previous study [14]. Also, it is found that the rate of increase of friction coefficient in the case of high roughness under 300MPa was lower than 600 MPa and 900 MPa.

- (2) In the low roughness condition, the friction coefficient increased with contact stiffness at the beginning of the cyclic test, reached a peak, and then decreased with contact stiffness. While, the change of contact stiffness in the case of high roughness condition linked with that of friction coefficient over the whole test. The change of roughness represented well that of contact stiffness.
- (3) A mechanism model during the running-in process of the contact interface was proposed as follows; for low initial roughness, the surface fracture was considered to be the dominant factor in increasing the friction coefficient and contact stiffness, whereas for high initial roughness, the plastic deformation of the asperities was considered to be the dominant factor.

References

- [1] D. I. Fletcher and S. H. Sanusi, "The potential for suppressing rail defect growth through tailoring rail thermo-mechanical properties," *Wear*, vol. 366–367, pp. 401–406, 2016.
- [2] J. Ahlström and B. Karlsson, "Microstructural evaluation and interpretation of the mechanically and thermally affected zone under railway wheel flats," *Wear*, vol. 232, no. 1, pp. 1–14, 1999.
- [3] R. Lewis *et al.*, "Mapping railway wheel material wear mechanisms and transitions," *Proc. Inst. Mech. Eng. Part F J. Rail Rapid Transit*, vol. 224, no. 3, pp. 125–137, 2010.
- [4] U. Olofsson and T. Telliskivi, "Wear, plastic deformation and friction of two rail steels - A full-scale test and a laboratory study," *Wear*, vol. 254, no. 1–2, pp. 80–93, 2003.
- [5] S. Kumar, G. Yu, and A. C. Witte, "Wheel-rail resistance and energy consumption analysis of cars on tangent track with different lubrication strategies," *Proc. IEEE/ASME Jt. Railr. Conf.*, pp. 129–136, 1995.
- [6] D. T. Eadie, M. Santoro, and J. Kalousek, "Railway noise and the effect of top of rail liquid friction modifiers: Changes in sound and vibration spectral distributions in curves," *Wear*, vol. 258, no. 7–8, pp. 1148–1155, 2005.
- [7] S. Fukagai, T. Ban, M. Ogata, M. Ishida, and A. Namura, "Development of wheel/rail Friction Moderating System (FRIMOS)," *Q. Rep. RTRI (railw. Tech. Res. Institute)*, vol. 49, no. 1, 2008.
- [8] W. C. Shust and J. A. Elkins, "Wheel forces during flange climb part I - track loading vehicle tests," in *Railroad Conference, 1997., Proceedings of the 1997 IEEE/ASME Joint.*, 1997, pp. 137–147.
- [9] H. Ishida, T. Miyamoto, E. Maebashi, H. Doi, K. Iida, and A. Furukawa, "Safety assessment for flange climb derailment of trains running at low speeds on sharp curves," *Q. Rep. RTRI*, vol. 47, no. 2, pp. 65–71, 2006.
- [10] A. Matsumoto *et al.*, "A new measuring method of wheel-rail contact forces and related considerations," *Wear*, vol. 265, no. 9–10, pp. 1518–1525, 2008.
- [11] S. Greene *et al.*, "Flange Climb Derailment Criteria and Wheel/Rail Profile Management and Maintenance Guidelines for Transit Operations," *TCRP Rep. 71 Track-Related Res.*, vol. 5, p. 147, 2005.
- [12] R. A. I. Branch, "Rail Accident Report, Locomotive derailment at Ordsall Lane Junction, Salford, 23 January 2013," 2014.
- [13] R. A. I. Branch, "Safety digest, Locomotive derailment at Doncaster, 21 December 2018," 2019.

- [14] S. Fukagai, L. Ma, and R. Lewis, "Tribological aspects to optimize traction coefficient during running-in period using surface texture," *Wear*, vol. 424–425, no. January, pp. 223–232, 2019.
- [15] M. Pau, "Estimation of real contact area in a wheel-rail system by means of ultrasonic waves," *Tribol. Int.*, vol. 36, no. 9, pp. 687–690, 2003.
- [16] M. B. Marshall, R. Lewis, R. S. Dwyer-Joyce, U. Olofsson, and S. Björklund, "Experimental Characterization of Wheel-Rail Contact Patch Evolution," *J. Tribol.*, vol. 128, no. 3, pp. 493–503, 2006.
- [17] R. S. Dwyer-Joyce, C. Yao, J. Zhang, R. Lewis, and B. W. Drinkwater, "Feasibility Study for Real Time Measurement of Wheel-Rail Contact Using an Ultrasonic Array," *J. Tribol.*, vol. 131, no. 4, p. 041401, 2009.
- [18] M. Pau and B. Leban, "Ultrasonic assessment of wheel-rail contact evolution exposed to artificially induced wear," *Proc. Inst. Mech. Eng. Part F J. Rail Rapid Transit*, vol. 223, no. 4, pp. 353–364, 2009.
- [19] R. S. Dwyer-Joyce, C. Yao, R. Lewis, and H. Brunskill, "An ultrasonic sensor for monitoring wheel flange/rail gauge corner contact," *Proc. Inst. Mech. Eng. Part F J. Rail Rapid Transit*, vol. 227, no. 2, pp. 188–195, 2013.
- [20] H. Brunskill, A. Hunter, L. Zhou, R. Dwyer Joyce, and R. Lewis, "An evaluation of ultrasonic arrays for the static and dynamic measurement of wheel–rail contact pressure and area," *Proc. Inst. Mech. Eng. Part JJ. Eng. Tribol.*, vol. 234, no. 10, pp. 1580–1593, 2020.
- [21] L. Zhou, H. P. Brunskill, R. Lewis, M. B. Marshall, and R. S. Dwyer-Joyce, "Dynamic characterisation of the wheel/rail contact using ultrasonic reflectometry," *Civil-Comp Proc.*, vol. 104, pp. 1–13, 2014.
- [22] L. Zhou, H. P. Brunskill, and R. Lewis, "Real-time non-invasive measurement and monitoring of wheel–rail contact using ultrasonic reflectometry," *Struct. Heal. Monit.*, vol. 0, no. 0, p. 1475921719829882.
- [23] K. Kendall and D. Tabor, "An Ultrasonic Study of the Area of Contact between Stationary and Sliding Surfaces," *Proc. R. Soc. A Math. Phys. Eng. Sci.*, vol. 323, no. 1554, pp. 321–340, 1971.
- [24] H. G. Tattersall, "The ultrasonic pulse-echo technique as applied to adhesion testing," *J. Phys. D. Appl. Phys.*, vol. 6, pp. 819–832, 1973.
- [25] A. Rovira, A. Roda, M. B. Marshall, H. Brunskill, and R. Lewis, "Experimental and numerical modelling of wheel-rail contact and wear," *Wear*, vol. 271, no. 5–6, pp. 911–924, 2011.
- [26] M. Pau, B. Leban, and M. Guagliano, "Propagation of Sub-surface Cracks in Railway Wheels for Wear-induced Conformal Contacts," *J. Mech. Syst. Transp. Logist.*, vol. 3, no. 1, pp. 226–235, 2010.

- [27] S. Fukagai, H. P. Brunskill, A. K. Hunter, R. S. Dwyer-Joyce, and R. Lewis, "Transitions in rolling-sliding wheel/rail contact condition during running-in," *Tribol. Int.*, vol. 149, no. August 2018, p. 105679, 2020.
- [28] S. Fukagai, M. Watson, H. P. Brunskill, A. K. Hunter, M. B. Marshall, and R. Lewis, "In-situ evaluation of a sliding interface with different roughness conditions using ultrasound reflectometry," *Submitt. to Proc. R. Soc. A*, 2021.
- [29] M. Evans, W. A. Skipper, L. Buckley-Johnstone, A. Meierhofer, K. Six, and R. Lewis, "The development of a high pressure torsion test methodology for simulating wheel/rail contacts," *Tribol. Int.*, vol. 156, no. September 2020, p. 106842, 2021.
- [30] B. W. Drinkwater, R. S. Dwyer-Joyce, and P. Cawley, "A study of the interaction between ultrasound and a partially contacting solid—solid interface," *Proc. R. Soc. London. Ser. A Math. Phys. Eng. Sci.*, vol. 452, no. 1955, pp. 2613–2628, Jan. 1996.
- [31] R. S. Dwyer-Joyce, "The application of ultrasonic NDT techniques in tribology," *Proc. Inst. Mech. Eng. Part J J. Eng. Tribol.*, vol. 219, no. 5, pp. 347–366, 2005.
- [32] M. Gonzalez-Valadez, A. Baltazar, and R. S. Dwyer-Joyce, "Study of interfacial stiffness ratio of a rough surface in contact using a spring model," *Wear*, vol. 268, no. 2–3, pp. 373–379, 2010.
- [33] B. Drinkwater, R. Dwyer-Joyce, and P. Cawley, "A Study of the Transmission of Ultrasound Across Real Rough Solid-Solid Interfaces," in *Review of Progress in Quantitative Nondestructive Evaluation: Volume 14*, D. O. Thompson and D. E. Chimenti, Eds. Boston, MA: Springer US, 1995, pp. 1829–1836.
- [34] R. S. Dwyer-Joyce, B. W. Drinkwater, and A. M. Quinn, "The Use of Ultrasound in the Investigation of Rough Surface Interfaces," *J. Tribol.*, vol. 123, no. 1, p. 8, 2001.
- [35] J. Y. Kim, A. Baltazar, and S. I. Rokhlin, "Ultrasonic assessment of rough surface contact between solids from elastoplastic loading-unloading hysteresis cycle," *J. Mech. Phys. Solids*, vol. 52, no. 8, pp. 1911–1934, 2004.
- [36] S. Biwa, S. Hiraiwa, and E. Matsumoto, "Stiffness evaluation of contacting surfaces by bulk and interface waves," *Ultrasonics*, vol. 47, no. 1–4, pp. 123–129, Dec. 2007.
- [37] N. Nagase, S. Shido, and I. Yarita, "The effect of lubricant on microwear of dull rolls in temper rolling by 4 hi rolling mill," *ISIJ Int.*, vol. 49, no. 6, pp. 874–880, 2009.

Appendix B

Table B.1 Change of roughness profiles of the top and bottom specimens with the progress of the cycles in the case of low roughness when the contact stress is 600 MPa.

		Top/Bottom	Circumferential direction	Radial direction
Initial	Top			
	Bottom			
After 1st cycle	Top			
	Bottom			
After 5th cycle	Top			
	Bottom			
After 10th cycle	Top			
	Bottom			
After 15th cycle	Top			
	Bottom			

Table B.2 Change of roughness profiles of the top and bottom specimens with the progress of the cycles in the case of medium roughness when the contact stress is 600 MPa.

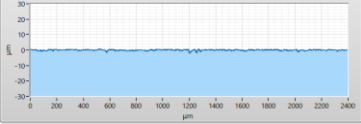
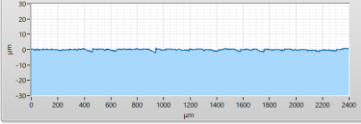
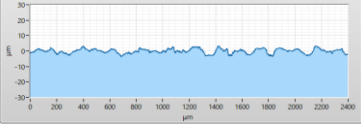
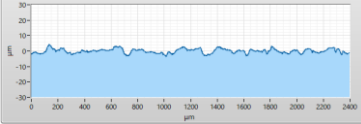
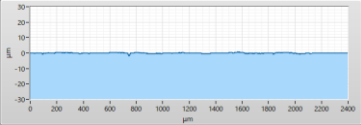
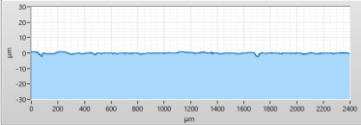
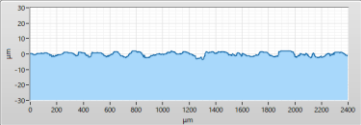
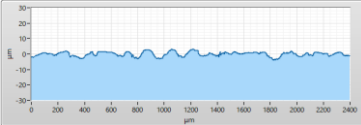
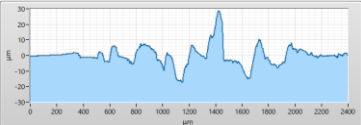
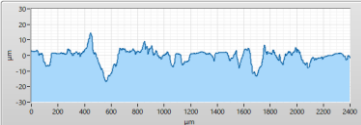
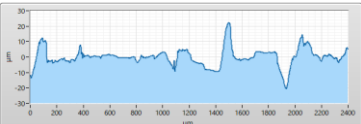
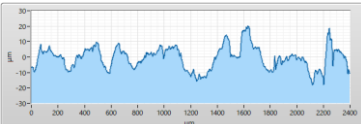
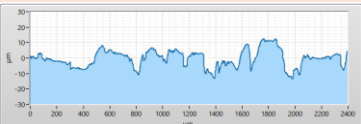
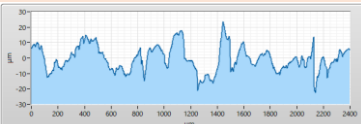
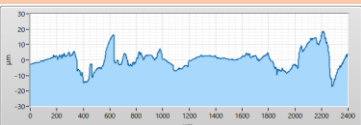
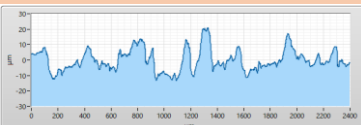

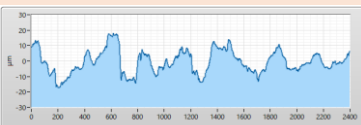

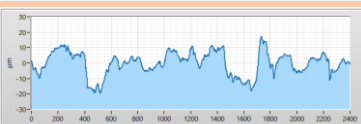
	Top/Bottom	Circumferential direction	Radial direction
Initial	Top		
	Bottom		
After 1st cycle	Top		
	Bottom		
After 5th cycle	Top		
	Bottom		
After 10th cycle	Top		
	Bottom		
After 15th cycle	Top		
	Bottom		

Table B.3 Change of roughness profiles of the top and bottom specimens with the progress of the cycles in the case of high roughness (0.4 mm pitch) when the contact stress is 600 MPa.

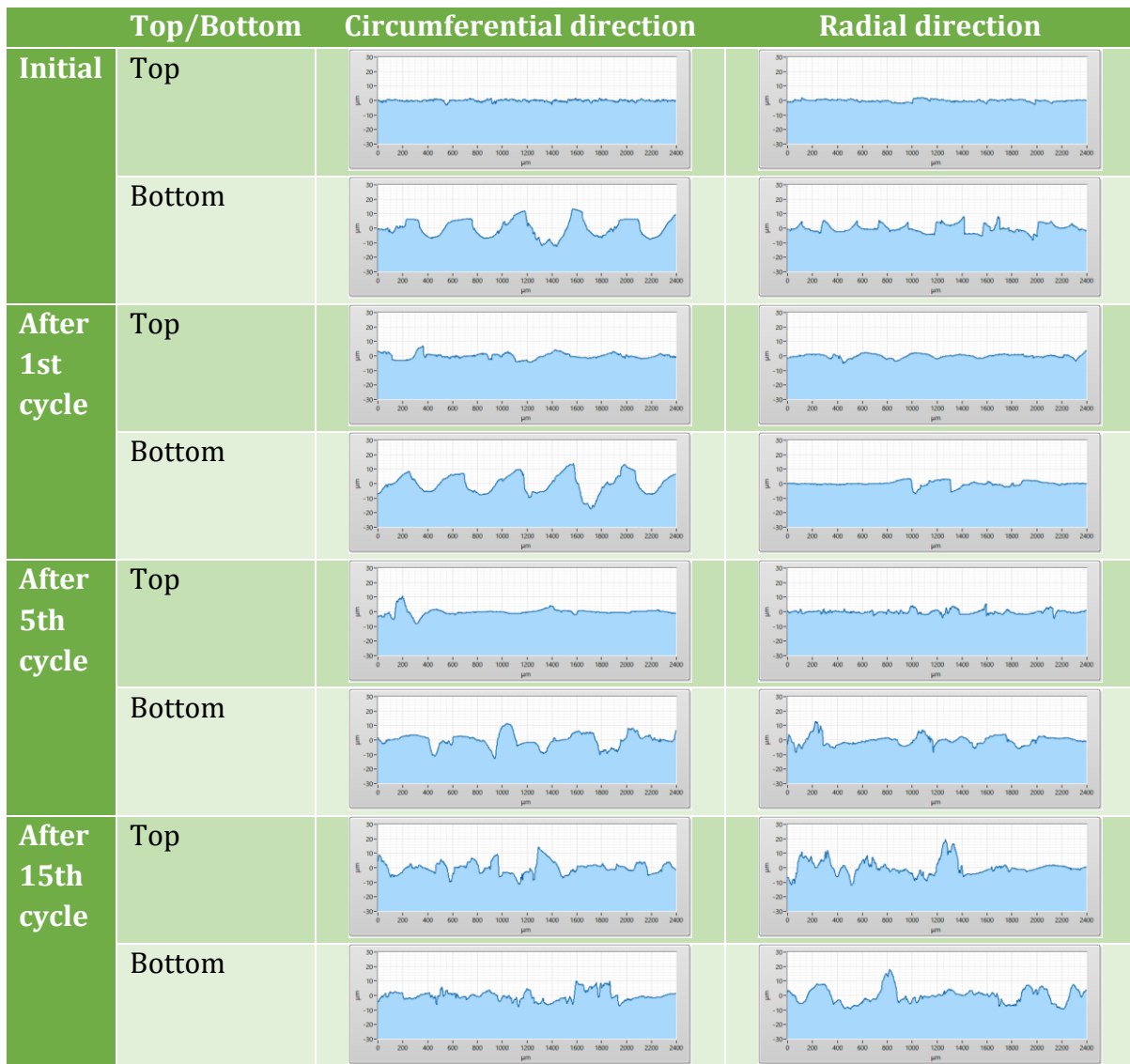


Table B.4 Change of roughness profiles of the top and bottom specimens with the progress of the cycles in the case of high roughness (0.8 mm pitch) when the contact stress is 600 MPa.

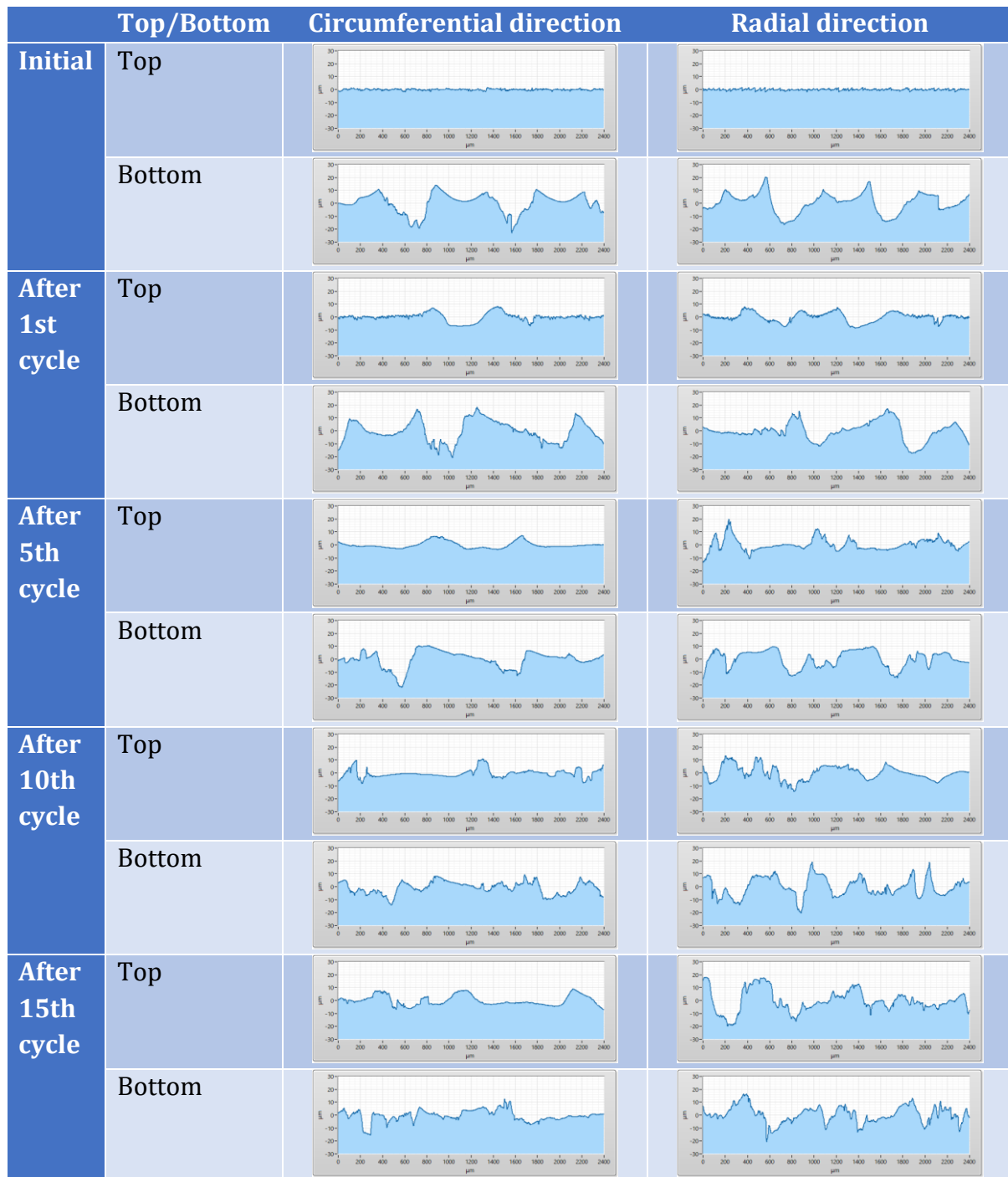


Table B.5 Change of roughness profiles of the top and bottom specimens with the progress of the cycles in the case of high roughness (0.8 mm pitch) when the contact stress is 300 MPa.

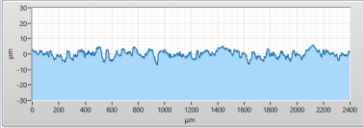
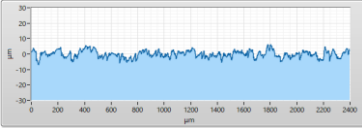
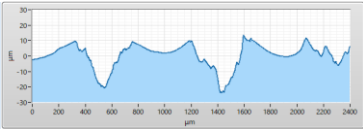
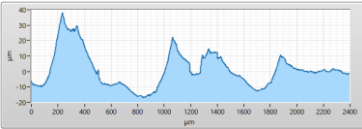
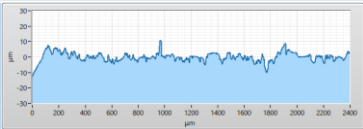
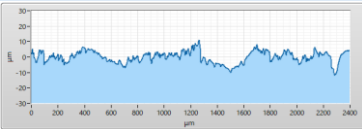
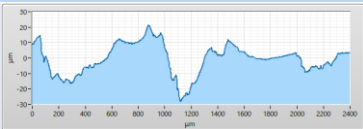
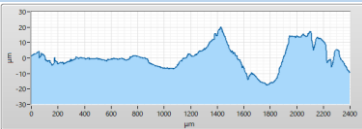
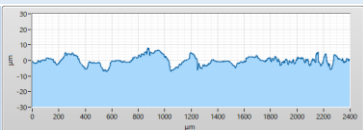
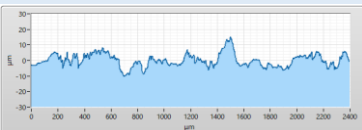
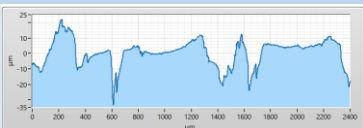
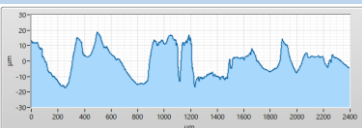
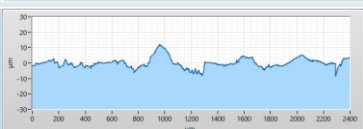
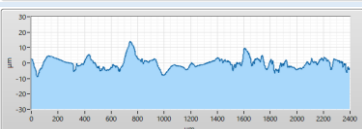
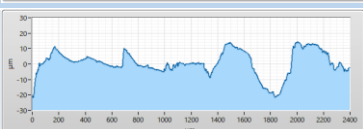
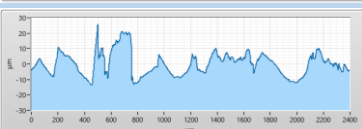
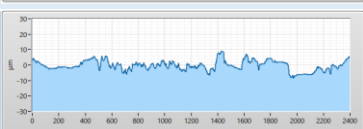
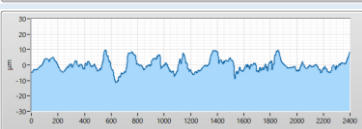
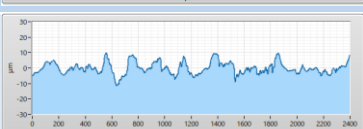
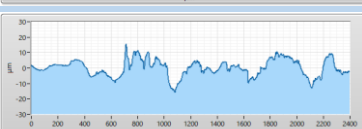
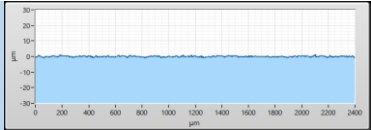
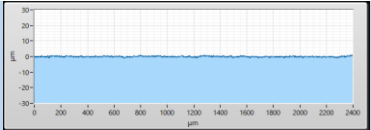
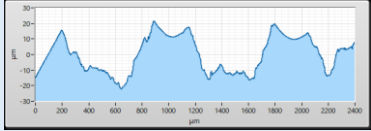
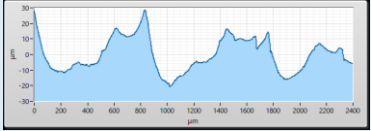
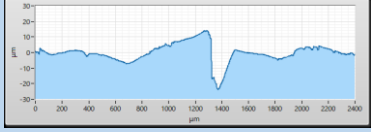
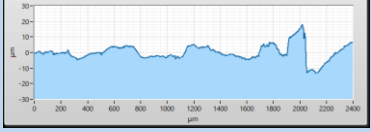
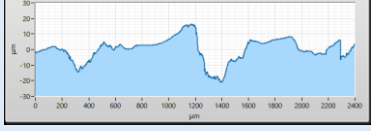
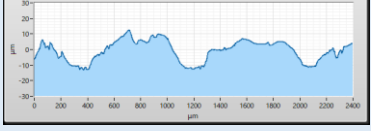
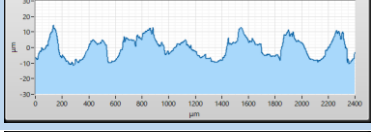
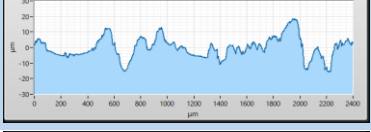
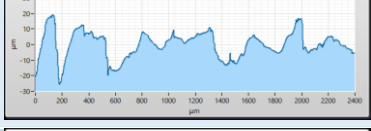
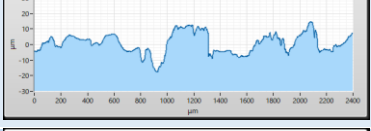
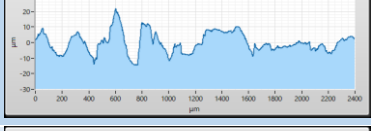
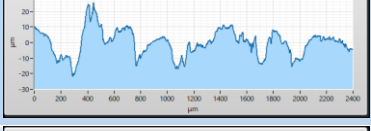
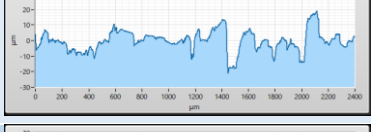
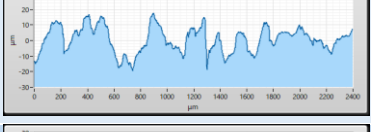
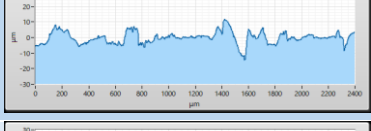
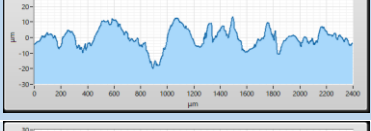
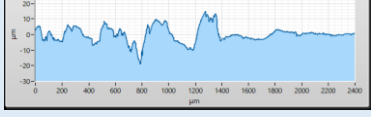
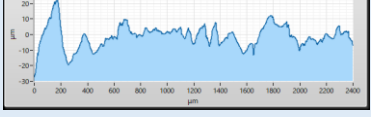
	Top/Bottom	Circumferential direction	Radial direction
Initial	Top		
	Bottom		
After 1st cycle	Top		
	Bottom		
After 5th cycle	Top		
	Bottom		
After 10th cycle	Top		
	Bottom		
After 15th cycle	Top		
	Bottom		

Table B.6 Change of roughness profiles of the top and bottom specimens with the progress of the cycles in the case of high roughness (0.8 mm pitch) when the contact stress is 900 MPa.

		Top/Bottom	Circumferential direction	Radial direction
Initial	Top			
	Bottom			
After 1st cycle	Top			
	Bottom			
After 5th cycle	Top			
	Bottom			
After 10th cycle	Top			
	Bottom			
After 15th cycle	Top			
	Bottom			

6 APPLYING THE EVALUATION TECHNIQUE USING ULTRASOUND REFLECTOMETRY TO THE ACTUAL WHEEL- RAIL INTERFACE

Paper 4

Transitions in rolling-sliding wheel/rail contact condition during running-in

S. Fukagai^{a,b}, H. P. Brunskill^a, A. K. Hunter^a, R. S. Dwyer-Joyce^a, R. Lewis^a

^aLeonardo Centre for Tribology, Department of Mechanical Engineering, University of Sheffield, Sheffield, UK

^bRailway Technical Research Institute, Tokyo, Japan

Abstract

The risk of wheel-climb derailment increases if the traction coefficient in the wheel/rail contact is too high. This has been observed to happen more frequently just after wheel machining. This work investigates how the traction coefficient rises with the evolution of the wheel/rail interface during the running-in. Experiments were performed using a full-scale wheel/rail contact rig and an ultrasonic array transducer mounted in the rail. Results were used to determine the stiffness of the contact interface. Contact stiffness appeared to be positively correlated with the traction coefficient. Owing to the conforming of the interface, contact stiffness increases before the traction coefficient rises. The work will allow recommendation of wheel machining to be made to help reduce the problem of wheel-climb derailment.

Published in Tribology International Vol 149 (2020), 105679

6.1 Introduction

Since the frictional condition between the wheel and rail plays a vital role in the transmission of driving force and braking force, it should be kept at an optimum level to secure the proper acceleration performance and braking distance. On the other hand, it is known that high traction coefficient and slip at curves could lead to severe wear and

deformation of wheel and rail, energy consumption and squealing noise [1]. It also increases the risk of a wheel climb derailment occurring [2]–[4].

Nakahara *et al.* reported that the traction between a wheel and rail changes with a train traffic passage even in the dry condition [5] and showed some transient traction curves using twin-disk testing which indicated that traction coefficient varies with the evolution of surface roughness during running-in [6]. Blau also addressed the tribological behaviour during running-in and reported typical examples of friction force transition curves [7]. Notably, it was mentioned that the friction force tends to increase significantly in the case of dry contact after the start of sliding contact. In these cases, it is commonly recognized that one of the main causes for such a transition is the evolution of surface topography with cyclic contacts [6], [7]. Lundmark *et al.* [8] and Yamamoto and Chen [9], [10] also reported that transitions in traction coefficient are strongly influenced by the initial topography.

A railway wheel experiences re-profiling several times during its life to reset it to the designed profile from the worn profile or to remove damage, such as a wheel flat, cracks. And it is known that some derailments have occurred relatively soon after the re-profiling of wheels [11]–[14]. Just after re-profiling, the wheel surface has a large roughness which is caused by the machining marks. Some reports mention the possibility that the rougher surface leads to a higher traction coefficient, and so increases the risk of flange climb derailment [13]–[15]. Specifically, they indicate that the spike-like machining marks cause an increase in traction during running-in as they plough into the rail material. Therefore, a smooth surface is recommended at the finishing of wheel machining [13], [15]. On the other hand, there is another opinion that traction force is increased with the deformation of machining marks and increase in real contact area [11]. As the wheel and rail experience cyclic rolling-sliding with tangential force, the surface topography changes and therefore the interfacial condition alters dramatically during running-in. Therefore, it is important to understand how this interfacial condition evolves over time to understand the potential mechanisms for wheel climb derailment. However, the difficulty in obtaining accurate non-destructive interfacial measurements has hindered systematic experimental investigations. An increased understanding of these effects might inform rail service providers about optimal wheel profiling methods and lubrication programs to reduce the likelihood of wheel climb derailment.

Pressure-sensitive films can be used to observe contact area and stress in a static contact. However, these films can cause over-prediction of the contact area owing to the thickness of the film and changes in tangential force due to its different frictional properties. Practical implementation is also difficult because the film disintegrates under high-pressure and shear between the wheel and the rail. Recently, ultrasonic techniques have been used to observe the contact between wheel and rail [16]–[20]. Though there are spatial resolution limits and considerations of transducer positioning to ensure the sound waves reflect off the area of interest, this technique can be used to non-invasively and directly observe the contact. When an ultrasonic wave strikes the interface between the

wheel and rail, it is partially transmitted and partially reflected. The proportion of the wave reflected depends on the stiffness of the contact [21], [22]. This approach has been used to determine the contact pressure distribution in wheel-rail contacts and the influence of wear, roughness and surface defects on the contact patch [17], [19]. This actual distribution of the contact pressure could apply to the simulation of wear amount and damage propagation with consideration for surface topography [23], [24].

Recently, dynamic ultrasonic measurement of a rolling-sliding contact has been achieved [25], [26]. Using this method, the dynamic contact in rolling-sliding can be obtained for repeated cycles. Information about the contact condition under the cyclic tangential force might lead to the clarification of mechanisms causing the tribological transition curve during running-in.

The aim of this work was to understand and characterize the tribological behaviour between wheel and rail during running-in. Ultrasonic reflection was used to evaluate interface condition in a rolling-sliding contact, particularly contact stiffness over time as running-in occurs. The experiments were performed using a full-scale dynamic wheel/rail contact-testing machine and a 64 element ultrasonic array transducer mounted in the rail. The transient traction coefficient was also measured during the test. Following these measurements, a comparison between contact stiffness and traction coefficient was carried out.

6.2 Methodology

6.2.1 Full-scale dynamic wheel/rail rig

Figure 6-1 shows a schematic diagram of the full-scale dynamic wheel/rail contact rig [25], [27], which was equipped with a full-scale wheel loaded onto a traversing rail. It could apply a normal force of up to 200 kN and tangential force of up to 60 kN using servo-controlled hydraulic cylinders. The rail was pushed and pulled at a velocity of up to 100 mm/s in the longitudinal direction. The wheel could be unconstrained so that its rotation was a result of the friction force between the wheel and the rail, and it could also be forced to rotate slightly faster by the movement of an actuator which was connected to it via a chain. The difference in speed generated the tangential force. Each hydraulic cylinder had a load cell mounted in-line facilitating the measurement of traction coefficient from the division of tangential force by the normal force.

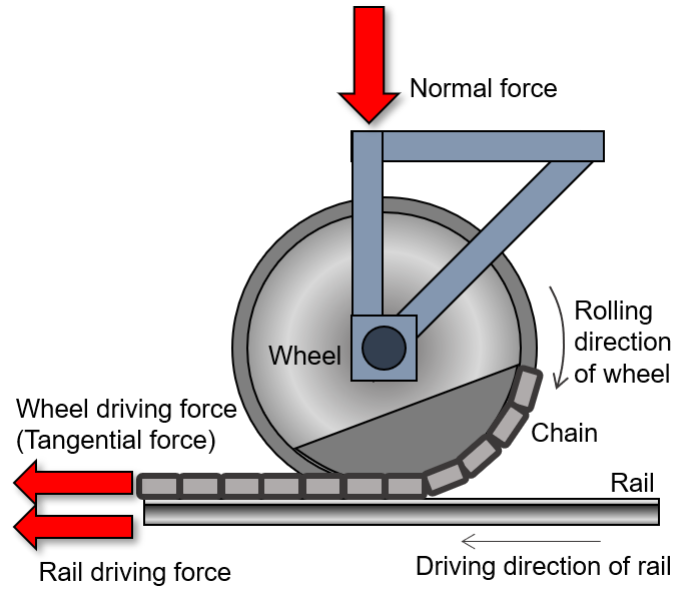


Fig. 6-1 Schematic diagram of the full-scale dynamic wheel/rail contact rig.

Figure 6-2 shows a photograph of the ultrasonic array transducer and a schematic of the set-up. The transducer was mounted in a hole that was made in the rail in the direction parallel to the sleeper. Hence, the contact area could be scanned with the passage of the wheel on the rail where the transducer was mounted. The array transducer consisted of 64 piezo elements arranged linearly each with a width of 0.5 mm and a constant pitch of 0.6 mm. The sampling interval in the rolling direction was determined by the ultrasonic array scanning frequency and the wheel rolling velocity. Since the scanning frequency was approximately 14 Hz and the rolling speed for these tests was 10 mm/s, the sampling interval in the rolling direction was approximately 0.7 mm. The frequency of the ultrasonic wave was 5 MHz.

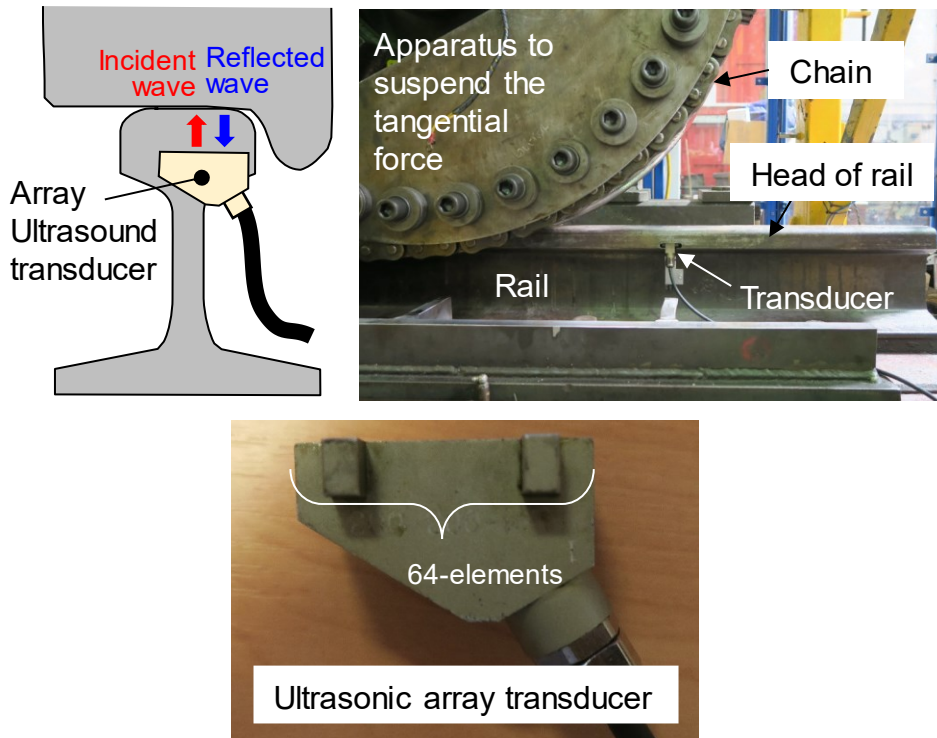


Fig. 6-2 Ultrasound array transducer and schematic of the set-up.

6.2.2 Ultrasound technique

At an interface of two dissimilar materials, part of the incident ultrasonic wave is transmitted through the interface and the other part is reflected. For an interface of two dissimilar materials perfectly bonded, the proportion of the reflected wave, described by the reflection coefficient R , is dependent on the acoustic impedance mismatch between the two materials and is given by [28]:

$$R = \frac{z_2 - z_1}{z_2 + z_1} \quad (1)$$

where z_1 and z_2 are the acoustic impedances (which are the products of density and acoustic velocity) of the contacting materials. Therefore, for two perfectly bonded identical materials, the interface would have no reflection ($z_1=z_2$, $R=0$) and the entire wave is transmitted (without any losses). Conversely, an ultrasonic wave is almost completely reflected at an interface between two materials with substantially different acoustic impedances, as in the case of a solid and a gas ($R \approx 1$).

Real engineering interfaces are inherently rough and micro and macroscopic air gaps are formed at an interface. Presuming the length of the ultrasonic wave is long relative to the

size of the air gaps the whole interface behaves as a single reflector and therefore R is also dependent on the contact stiffness of the interface [21], [22]. The contact stiffness, K , is a function of the surface topography, surface material properties and the contact pressure and has a significant influence on the contact dynamics. As the surface topography changes due to elastic and plastic deformation, the measured reflection coefficient R will change accordingly as shown in Fig. 6-3. The contact stiffness could vary from zero for a pair of surfaces just in contact to infinity when they are perfectly bonded. In principle, the degree of conformity at the interface can be determined by measuring the reflection coefficient of the ultrasonic wave.

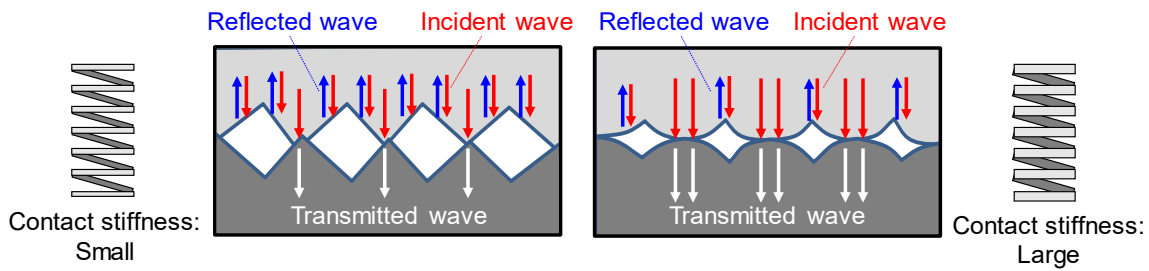


Fig. 6-3 Principle of measurement.

Schoenberg [28] used an interface 'spring model' to show how the reflection coefficient is related to contact stiffness:

$$R = \frac{z_1 - z_2 - i\omega(z_1 z_2 / K)}{z_1 + z_2 - i\omega(z_1 z_2 / K)} \quad (2)$$

where ω is the angular frequency of the ultrasound and K is the interfacial contact stiffness. The contact stiffness is defined as the stiffness due to asperity contact per unit area of an interface, as shown in the following equation:

$$K = -\frac{dp}{du} \quad (3)$$

where p is the nominal contact pressure and u is the distance between the surface mean lines. In the case of present work, the materials on both sides of the interface are similar ($z_1=z_2=z$), then equation (2) reduces to:

$$|R| = \frac{1}{\sqrt{1 + (2K/\omega z)^2}} \quad (4)$$

Therefore, if the reflection coefficient, R , can be experimentally obtained, the contact stiffness, K can be estimated. Generally, normal contact stiffness can be distinguished from shear contact stiffness depending on the loading direction. The contact stiffness in this paper means the normal contact stiffness unless otherwise specified.

Many researchers [16]–[20] have obtained the reflection coefficient R as the ratio of the reflected ultrasonic wave amplitude under load, H , to that when unloaded with no material in contact, H_0 (the reference).

$$R = \frac{H}{H_0} \quad (5)$$

When unloaded, the contact is effectively steel against air and so the wave can be assumed to be fully reflected and thus H_0 is equivalent to the incident wave amplitude. This is a simple practical way to obtain the reflection coefficient and removes the influence of transducer characteristics, ultrasonic wave scattering and attenuation.

6.2.3 Test rail and wheel

Figure 6-4 shows the profile of test rail and wheel which were measured using a non-contact profile measurement device (CW40, CALIPRI). The type of the test rail was UIC60A (EN 13674-1) at a length of 1200 mm and that of the test wheel was P8 (EN 13715) at a diameter of 920mm. Since the rail and the wheel were used for full-scale contact tests before this test, both had been slightly worn. There were two choices for contact location on the rail by inverting the direction of the rail in the rig. Two roughness conditions were prepared on each side of the rail (Fig. 6-4(a)). On one side, a rough surface topography was created by intentionally running the rig in a high traction force rolling-sliding condition. On the other side of the rail, the surface was prepared by polishing with sandpaper predominantly along the longitudinal direction to create a smoother surface. The contact location on the wheel was fixed (Fig. 6-4(b)) and the surface of the wheel was not specially prepared.

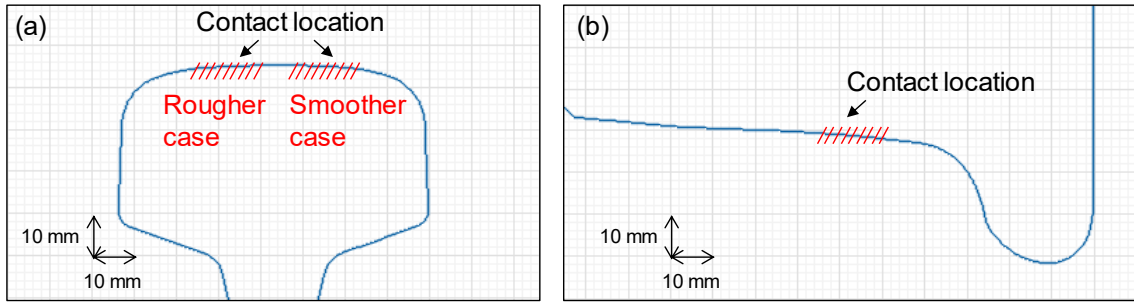


Fig. 6-4 Measured profile of test rail and wheel and contact location, (a) rail, (b) wheel.

Silicon polymer replicas (Microset 101 Fluid and NP10 Nozzle) were used to copy the surface topography of rail and wheel. After obtaining the replica, the roughness and surface topography were analyzed using an optical surface measurement system (InfiniteFocus, Alicona). Figure 6-5 shows the initial surface profile of rail and wheel for each case. The plus and minus sign of these profiles have been reversed to be the same as the actual surface because the profiles were obtained from the replica. The measurements were carried out five times per direction, lateral and tangential. Table 6-1 shows the initial roughness value of rail and wheel which is the mean value of five measurements. It can be seen that the magnitude of rail roughness in the rougher case is significantly larger than that in the smoother case. Therefore, two different wheel-rail combinations with significantly different initial roughness of the rail surface were tested and compared.

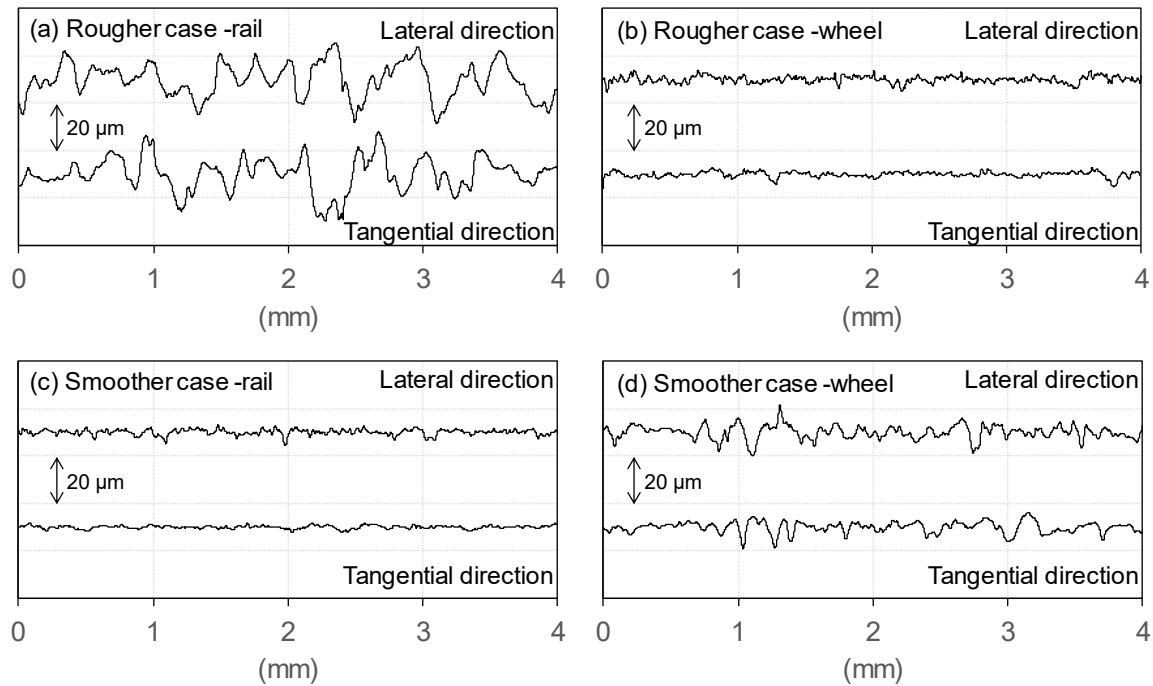


Fig. 6-5 Initial roughness profile of rail and wheel for each test, (a) Rougher case -rail, (b) Rougher case-wheel, (c) Smoother case-rail, (d) Smoother case-wheel.

Table 6-1 Initial roughness (root-mean-square roughness) of test rail and wheel

Case	Roughness, Rq (μm)			
	Rail		Wheel	
	Lateral direction	Tangential direction	Lateral direction	Tangential direction
Rougher case	8.0	6.9	1.5	1.2
Smoother case	1.2	0.8	2.8	2.4

6.2.4 Test procedure

Table 6-2 shows the test conditions. The cyclic contact tests were continued up to 100 cycles in the test of the rougher case and 60 cycles in the smoother case. Both tests were carried out after cleaning the surface with acetone. The measurement of traction coefficient and reflection coefficient were carried out continuously during the cyclic tests. Silicon polymer replicas were used for the evaluation of roughness as mentioned in section 2.3. These replicas were obtained after 100 cycles in the test of the rougher case and after 20 cycles in the test of the smoother case when the increase of traction

coefficient showed saturation with the increase of cycles. The velocity was quite low, 10 mm/sec. Though it is well known that the traction coefficient is influenced by the velocity when fluid, such as water, gets in between the wheel and the rail, this influence is small in the dry condition [29].

Table 6-2 Test conditions

Normal force (kN)	Slip ratio (%)	Velocity (mm/s)	Cycles for the measurement of traction coefficient and reflection coefficient (cycles)	Timing for replicating the surface topography (cycles)
80	3	10 for measurement	1-10, 13-20, 23-30, 33-40, 43-50, 53-60 (63-100, only in rougher case)	After 100 (rougher case) After 20 (smoother case)

6.3 Results

6.3.1 Change of traction coefficient with cyclic rolling

Figure 6-6 shows the relationship between the number of cycles and the traction coefficient. The traction coefficient was calculated as the ratio of tangential force to drive the wheel and the normal force (Fig. 6-1) and the value was extracted at the moment the wheel passed the ultrasonic transducer. Both results of the rougher case and the smoother case showed the increase of traction coefficient with the increase in cycles and it is clearly found that the increase in the smoother case was more rapid than that of the rougher case. In both cases, the traction coefficient reached a plateau of approximately 0.5.

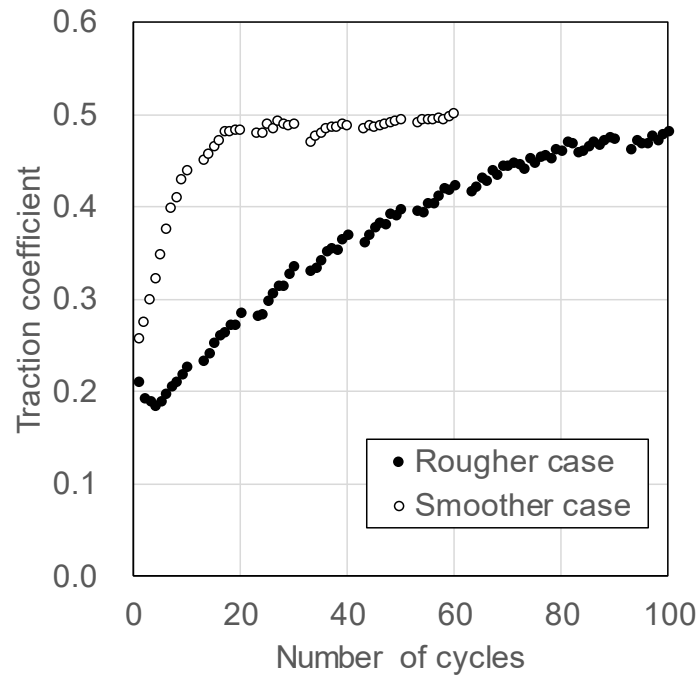


Fig. 6-6 Relationship between number of cycles and traction coefficient.

6.3.2 Change of contact stiffness with cyclic rolling

Reflection coefficient measurements were made continuously during the rolling cycles. The contact stiffness was determined from the measurements using equation (3). Figure 6-7 shows the contact stiffness maps between wheel and rail for the different number of cycles. Here the threshold value of contact stiffness to define the contact area was determined as the value which was calculated by a 10% decrease of reflection coefficient ($R=0.9$). The threshold value was iterated to give the largest value of the reflection coefficient that was unaffected by background noise. This was confirmed by comparing the result with the expected contact shape. The increase of contact stiffness with the increase in cycles can be seen in the change of contours. As the cycles progress, the surfaces are becoming more conformal.

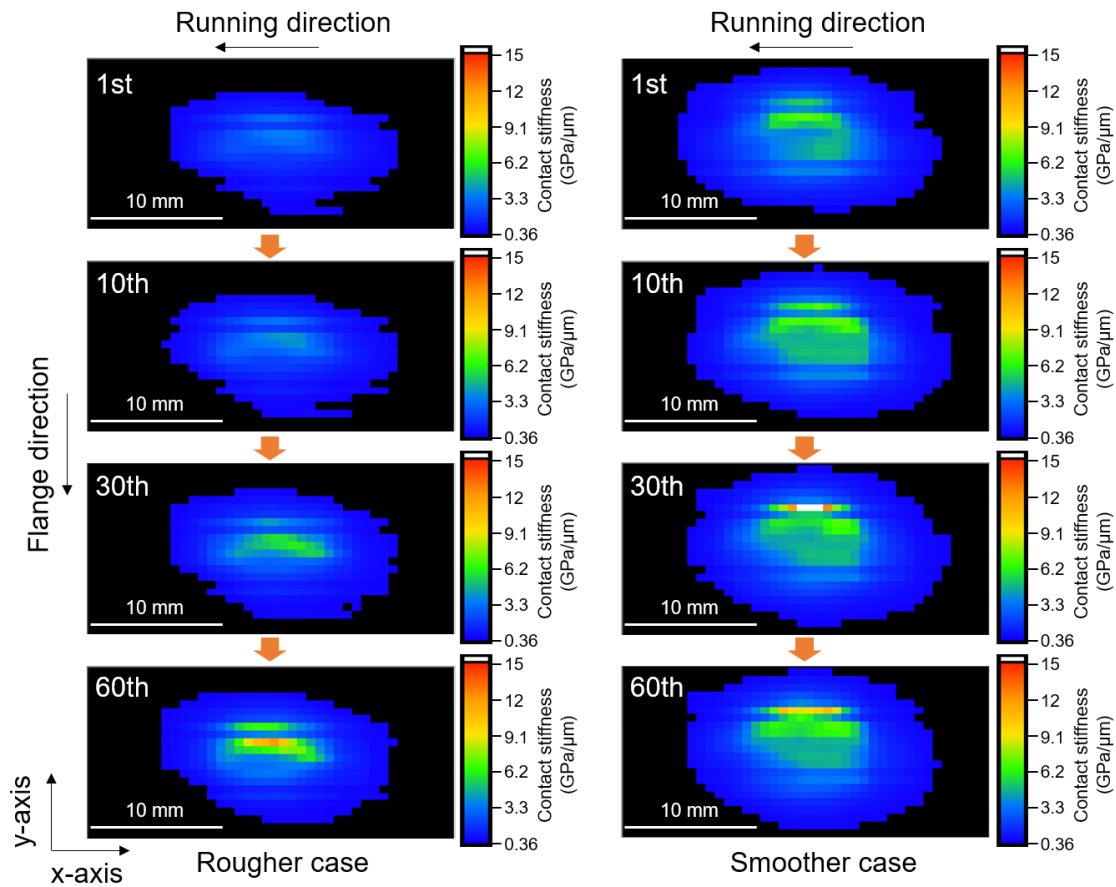


Fig. 6-7 Contact stiffness maps between wheel and rail for the different number of cycles.

Figure 6-8 shows a cross-section through contact stiffness maps. Here, each line was selected to pass through the point which had the maximum contact stiffness. It was found that the increasing tendency is not uniform inside the contact area and there were some peak points that showed a significant increase for both rougher and smoother cases. It is thought that the region of higher contact pressure generates more significant evolution of contact interface.

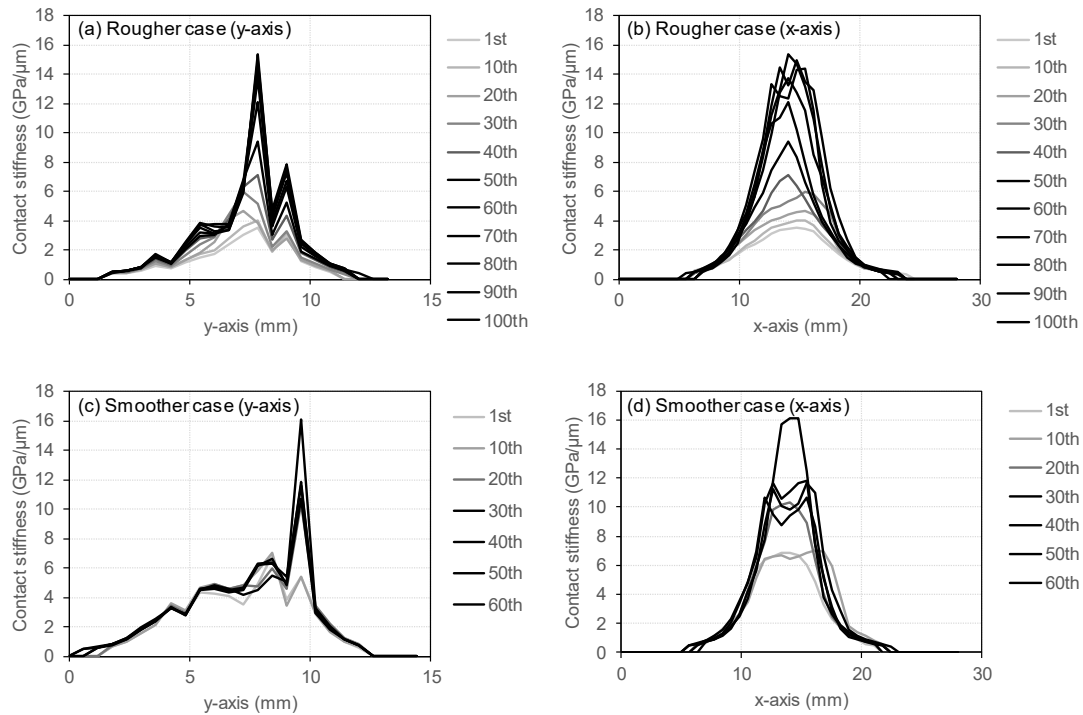


Fig. 6-8 Cross-section through contact stiffness maps, (a) Rougher case along the y-axis, (b) Rougher case along the x-axis, (c) Smoother case along the y-axis, (d) Smoother case along the x-axis.

Figure 6-9 shows the relationship between the mean contact stiffness and the number of cycles. Here, the mean value was calculated using the data which exceeded the threshold value above mentioned. The mean contact stiffness increased with the cyclic rolling and the value of the smoother case saturated more rapidly than that of the rougher case. This tendency was similar to the transition of traction coefficient.

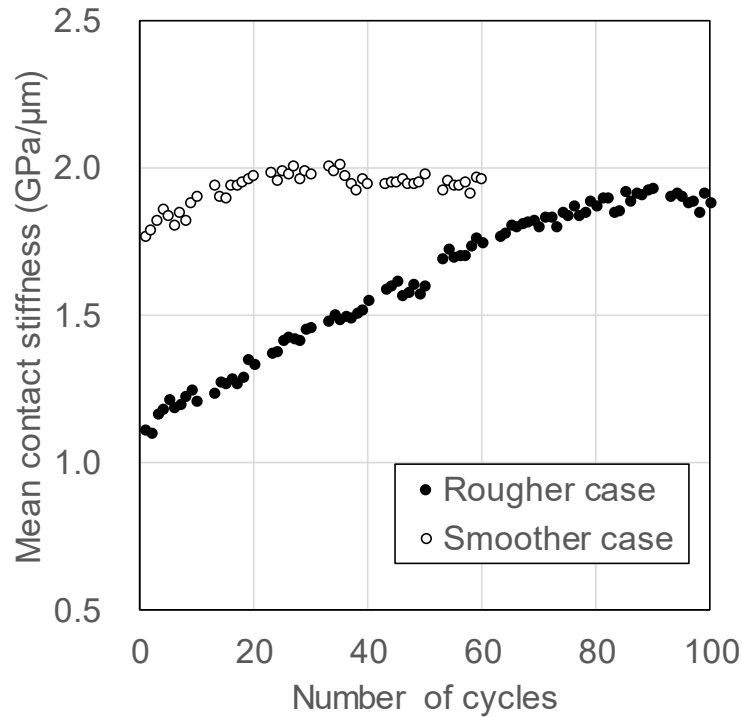


Fig. 6-9 Relationship between number of cycles and mean contact stiffness.

6.3.3 Change of surface topography with cyclic rolling

Figure 6-10 shows a comparison of the surface topography before and after the test cycles. Here, it should be noted that what appears to be a projection is actually a dent because these images were obtained from a replica. Figure 6-10 (a) shows that the initial asperities on the rail in the rougher case were flattened dramatically. Figs. 6-10 (b) and (d) at the wheel after test cycles showed the evolution of stripe-like traces along with the traction force. It is thought that the traction force makes such traces.

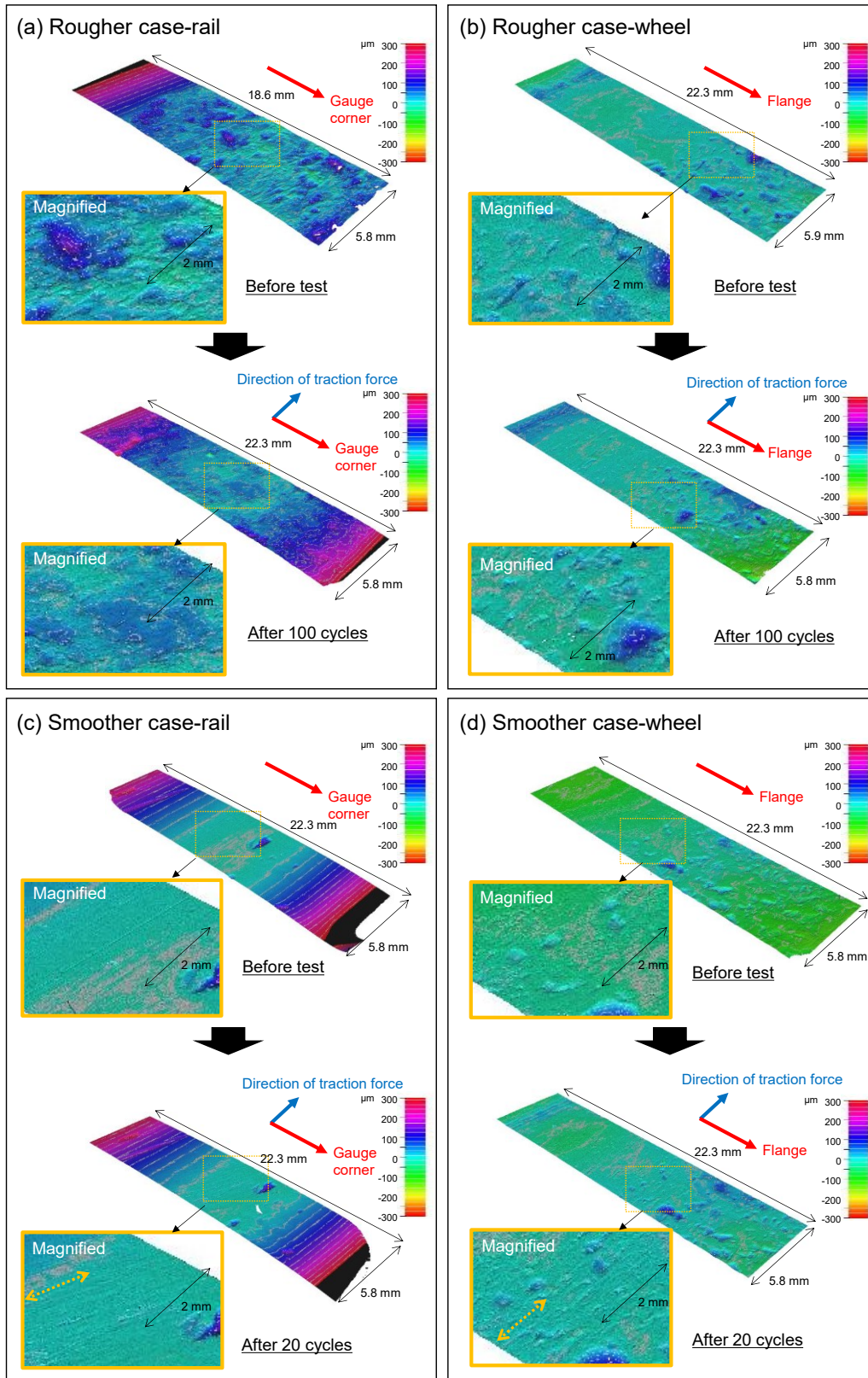


Fig. 6-10 Comparison of the surface topography between before and after test cycles, (a) Rougher case-rail, (b) Rougher case-wheel, (c) Smoother case-rail, (d) Smoother case-wheel.

Figure 6-11 shows a comparison of the profiles before and after the test cycles. The measurement of profiles was carried out in a similar way to that described in section 2.3. Figure 6-11 (a) shows that the initial asperities on the rail in the rougher case were flattened dramatically. On the other hand, Fig. 6-11 (b) shows that the roughness on the wheel in the rougher case slightly increased after the cycles. It is thought that this increase was due to compressions by the asperity summits of the rail surface or the surface texturing by the traction force. Figures 6-11 (c) and (d) show that there was no significant difference before and after the cycles.

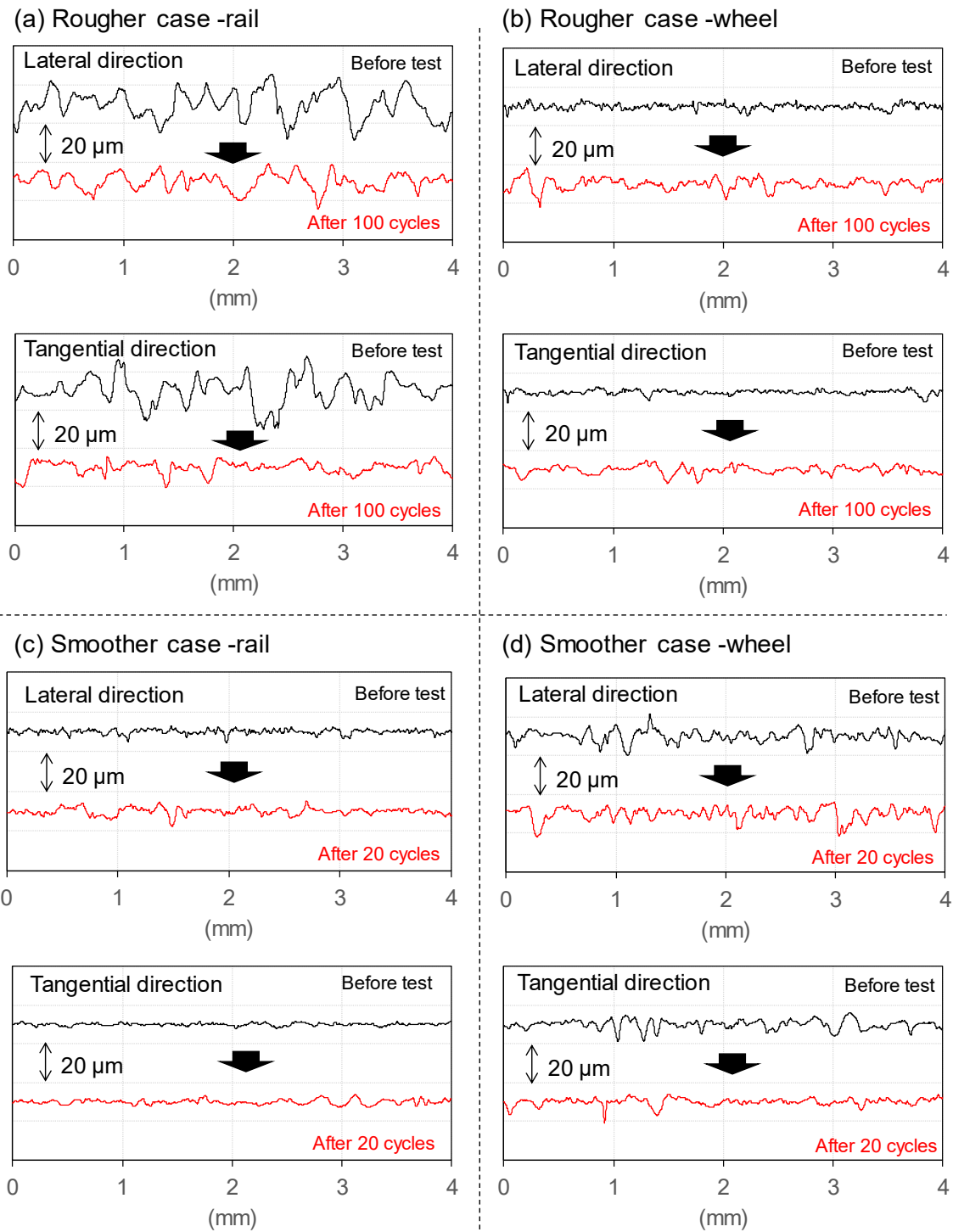


Fig. 6-11 Comparison of the profiles before and after test cycles, (a) Rougher case-rail, (b) Rougher case-wheel, (c) Smoother case-rail, (d) Smoother case-wheel.

Figure 6-12 shows the comparison of root-mean-square roughness value (R_q) for each case, rail/wheel and directions. Here, these were mean values for five measurements and the error bar means the range from the maximum value to minimum value, which is the same as the actual surface (reverse value of replica). Figure 6-12 (a) shows that R_q of rail

in the rougher case dramatically decreased and Fig. 6-12 (b) shows that Rq of wheel in the rougher case slightly increased after the cyclic tests in the rougher case. Figures 6-12 (c) and (d) show that there was no significant difference before and after the cycles in the smoother case.

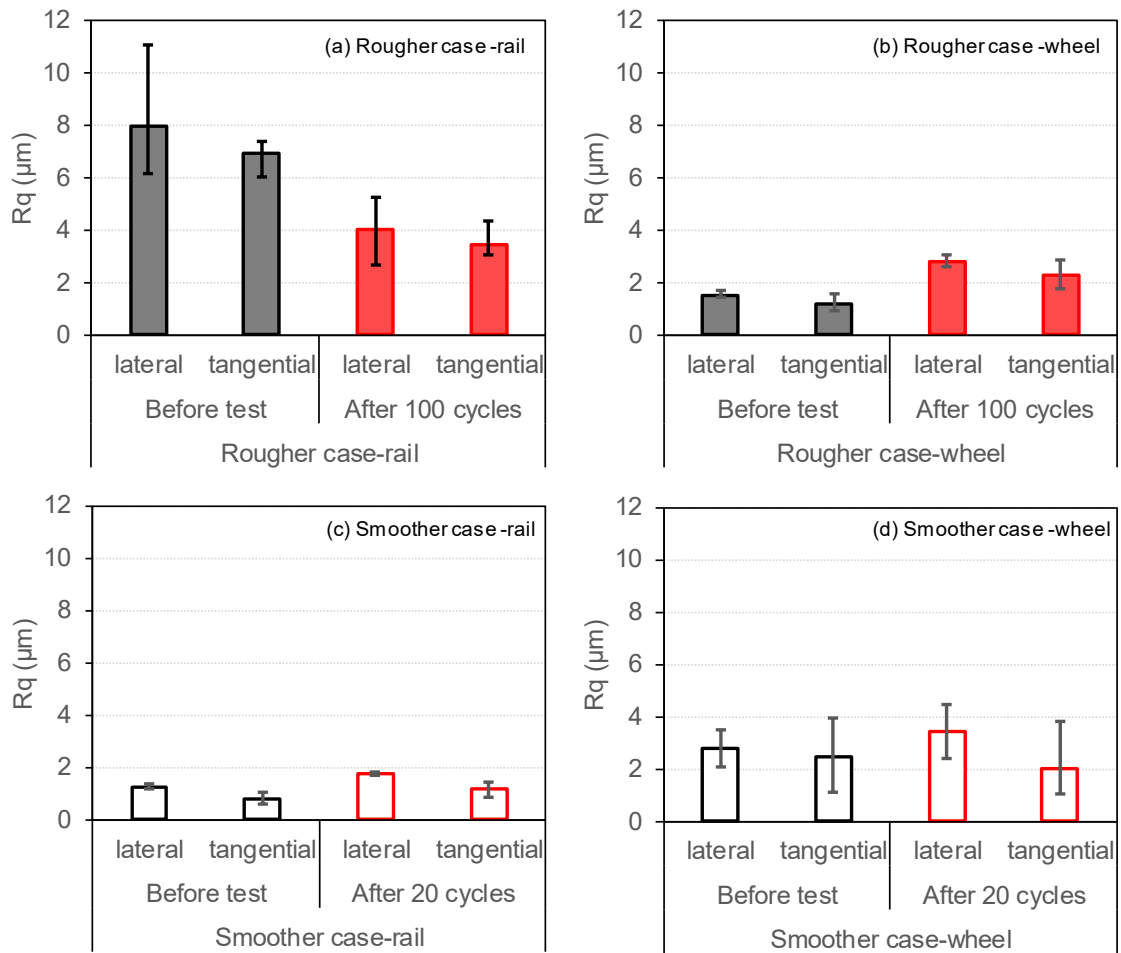


Fig. 6-12 Comparison of the root-mean-square roughness, (a) Rougher case-rail, (b) Rougher case-wheel, (c) Smoother case-rail, (d) Smoother case-wheel.

6.4 Discussion

The continuous evaluation of contact stiffness during the running-in period revealed that contact stiffness increases with an increase in cycles. However, the rate of increase differed from the rougher case to the smoother case. The increase of contact stiffness in the rougher case can be explained by the significant decrease in rail roughness. As the roughness reduces, the surface conforms more and the stiffness increases. Though there was also an increase of contact stiffness in the smoother case, there was no significant change in roughness value. However, in the magnified windows of Figs. 6-10(c) and 6-10(d), although they correspond to approximately the same position on the rail and wheel, there appears to be a slight change in the surface aspect, with a new orientation (yellow dotted lines).

For a more detailed analysis of surface topography, additional parameters, skewness (R_{sk}) and kurtosis (R_{ku}) were evaluated. Figure 6-13 shows a schematic illustration of surface topography with ranging skewness and kurtosis [30]. Skewness is the parameter to evaluate the symmetry of the roughness profile [30], [31]. A zero value of R_{sk} means a symmetrical distribution, a negative value means the profile has an inclined distribution in the upper side of a mean line and a positive value means the profile has an inclined distribution in the lower side of a mean line. Kurtosis is the parameter used to evaluate the sharpness of asperity summits of the roughness profile [30], [31]. If R_{ku} is smaller than three, it means there is a platykurtic distribution and if the value is larger than three, it means there is a leptokurtic distribution.

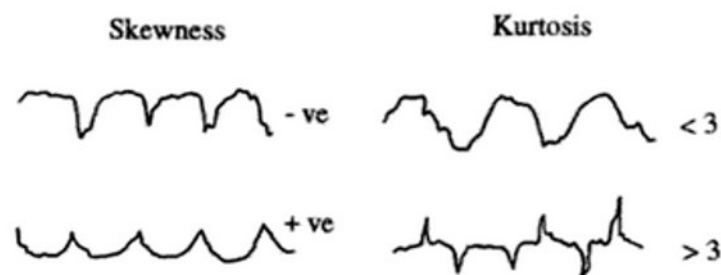


Fig. 6-13 Schematic illustration for surface topography with various skewness and kurtosis [30].

Figures 6-14 (a) and (b) show the comparison for skewness (R_{sk}) of the profile which was shown in Fig. 6-11. In the smoother case, there is a relatively large increase in the lateral direction of the rail before the test to after 20 cycles. Figures 6-14 (c) and (d) show the comparison of kurtosis (R_{ku}) of the profile which was shown in Fig. 6-11. In the smoother case, there is a noticeable difference in the lateral direction on the rail before the test to after 20 cycles. Generally, a grinding process produces grooved surfaces with negative skewness, but high kurtosis values [30]. Since the rail in the smoother case was prepared by polishing using sandpaper, it is reasonable that a negative R_{sk} value and

large R_{ku} value appeared before the test. It is thought that sharp scratching marks were deformed during the running-in period and the change of roughness distribution showed the difference in R_{sk} and R_{ku} after the cyclic test even if the R_q was almost the same. Therefore, this change should have caused a slight increase of contact stiffness in the smoother case.

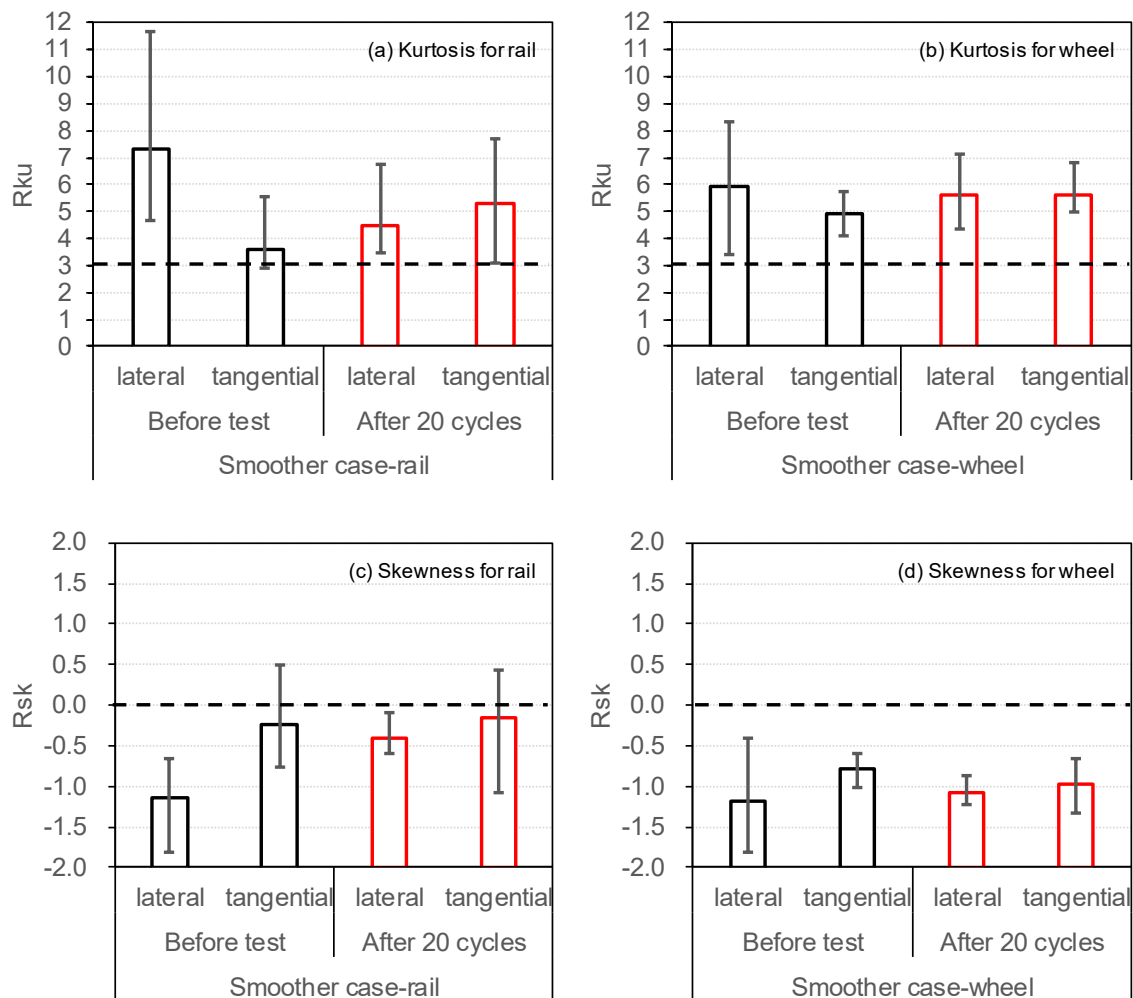


Fig. 6-14 Comparison of the parameters of roughness in smoother case, (a)Kurtosis for rail, (b)Kurtosis for wheel, (c) Skewness for rail, (d) Skewness for wheel.

Figure 6-15 shows the relationship between mean contact stiffness and traction coefficient. The mean contact stiffness in the rougher case appears to have a positive correlation with the traction coefficient and is close to being linear. On the other hand, the relationship in the smoother case was relatively skewed and the traction coefficient is much less dependent on contact stiffness. Contact stiffness is an effect dominated by roughness and deformation under load, while the traction coefficient is much more dependent on surface conditions and contamination, such as water and oxide layer. In the smoother case, the surface condition influences the traction more strongly than the rougher case. It is thought that these influences decreased with the increase of the cyclic number and the wear of the outer surface layer.

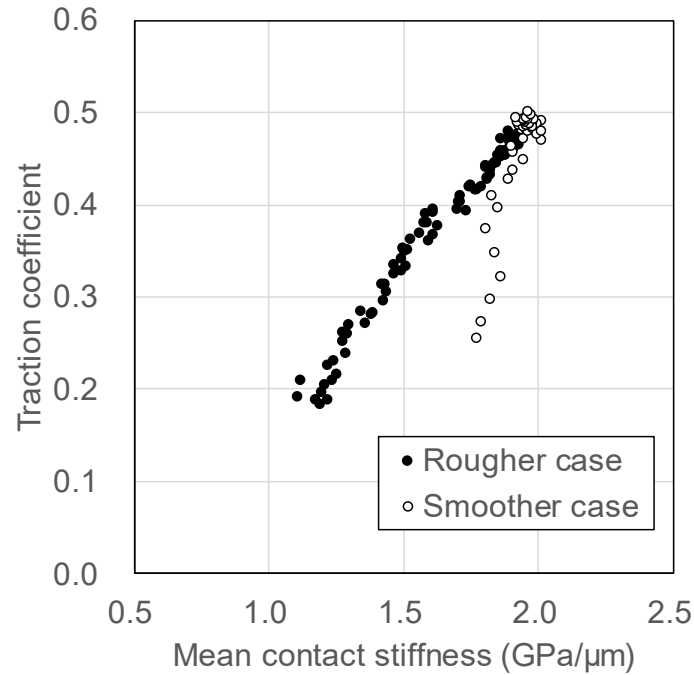


Fig. 6-15 Relationship between mean contact stiffness and traction coefficient.

Figure 6-16 shows a schematic model of the transition of surface roughness and contact stiffness. Here, it is simplified as the contact between a completely flat surface and a rough surface. As mentioned in section 6.2.2, normal contact stiffness can be distinguished from shear contact stiffness depending on the loading direction. Normal contact stiffness increases with the increase of cyclic rolling-sliding contacts and the decrease of roughness. There are several studies that discuss how shear contact stiffness increases with the increase of normal contact stiffness and the ratio of shear stiffness to normal stiffness is nearly constant as a function of Poisson's ratio [32]–[34]. The displacement along the tangential direction, Δx , would be qualitatively dominated by the slip ratio and it was constant, three percent, during this test. Therefore, it is thought that the shear stress increased with the increase of normal contact stiffness as the following equation:

$$\tau = cK \cdot \Delta x \quad (6)$$

where τ is shear stress and c is the ratio of shear stiffness to normal stiffness. As a consequence, there would be a linear-like relationship between normal contact stiffness and traction coefficient.

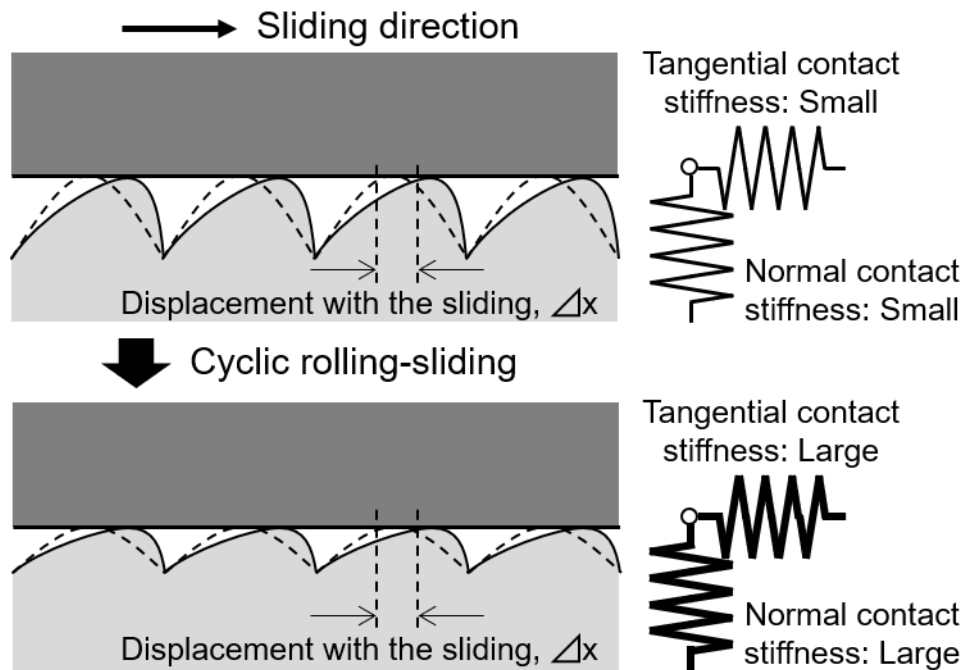


Fig. 6-16 Schematic model of the transition of surface roughness and contact stiffness.

From this relationship, it is thought that the traction coefficient under the smoother surface was larger because the contact stiffness (stiffness of the contact area between two objects) in the smoother case is larger than that in rougher case.

It is believed that the initial surface asperities cause a high traction coefficient by the spike-like effect and a smooth surface is sometimes recommended at the finishing of wheel machining. However, these results revealed that the traction coefficient in the rougher case rose more slowly than that in the smoother case, because the initial contact stiffness was small. Therefore, the initial large roughness at least in the range of this test may not increase the traction coefficient during running-in. After all, the influence of the more large topography, such as machining pattern, should be ensured.

It has already been found that the contact stiffness is affected by the contact pressure. Therefore, the effect of contact pressure should be taken into account for the direct estimation of the traction force/acceleration force using the contact stiffness and it will be a future work.

Oxides will be generated in the contact during testing, but there are currently no real-time methods for assessing this that would enable the layer to be related to friction. Post-test analysis [35] has shown that the ex-situ layers from testing are thicker than those on an actual rail which may be significant, but more work would be needed to investigate this.

6.5 Conclusions

From the measurement of a rolling-sliding contact condition between wheel and rail using ultrasound waves, the following conclusions can be drawn:

1. Both the rougher case and the smoother case showed an increase in traction coefficient with the increase of cycles and it is clearly found that the increase in the smoother case was more rapid than that of the rougher case.
2. Mean contact stiffness which was measured using ultrasonic waves increased with the cyclic rolling and the value of the smoother case saturated more rapidly than that of the rougher case. This tendency was similar to the transition in traction coefficient.
3. Root-mean-square roughness in the rougher case showed that the initial asperity was flattened dramatically after the cyclic rolling-sliding. Though that in the smoother case showed no significant change, there was an increase in skewness and a decrease of kurtosis.
4. Mean contact stiffness appears to have a positive correlation with the traction coefficient and is close to being linear. Based on the above results, a mechanism model of the effects of contact stiffness on traction characteristics during the running-in period was proposed.

References

- [1] R. Lewis and U. Olofsson, *Wheel-rail interface handbook*. Elsevier, 2009.
- [2] W. C. Shust and J. A. Elkins, "Wheel forces during flange climb part I - track loading vehicle tests," in *Railroad Conference, 1997., Proceedings of the 1997 IEEE/ASME Joint.*, 1997, pp. 137–147.
- [3] H. Ishida, T. Miyamoto, E. Maebashi, H. Doi, K. Iida, and A. Furukawa, "Safety assessment for flange climb derailment of trains running at low speeds on sharp curves," *Q. Rep. RTRI*, vol. 47, no. 2, pp. 65–71, 2006.
- [4] A. Matsumoto *et al.*, "A new measuring method of wheel-rail contact forces and related considerations," *Wear*, vol. 265, no. 9–10, pp. 1518–1525, 2008.
- [5] T. Nakahara, K. S. Baek, H. Chen, and M. Ishida, "Relationship between surface oxide layer and transient traction characteristics for two steel rollers under unlubricated and water lubricated conditions," *Wear*, vol. 271, no. 1–2, pp. 25–31, 2011.
- [6] K. S. Baek, K. Kyogoku, and T. Nakahara, "An experimental study of transient traction characteristics between rail and wheel under low slip and low speed conditions," *Wear*, vol. 265, no. 9–10, pp. 1417–1424, 2008.
- [7] P. J. Blau, "On the nature of running-in," *Tribol. Int.*, vol. 38, no. 11–12, pp. 1007–1012, Nov. 2005.
- [8] J. Lundmark, E. Kassfeldt, J. Hardell, and B. Prakash, "The influence of initial surface topography on tribological performance of the wheel/rail interface during rolling/sliding conditions," *Proc. Inst. Mech. Eng. Part F J. Rail Rapid Transit*, vol. 223, no. 2, pp. 181–187, 2009.
- [9] D. Yamamoto and H. Chen, "A Fundamental Study on Fine Unevenness and Tangent Force on Wheel Tread of Railway Vehicle (Relations between Environmental Condition and Tangent Force Characteristics with a Two-Disk Rolling Machine)," *Trans. JAPAN Soc. Mech. Eng. Ser. C*, vol. 77, no. 781, pp. 3211–3222, 2011.
- [10] D. Yamamoto and H. Chen, "Influence of the fine unevenness of wheel tread on the running stability of railway vehicle," *Trans. JAPAN Soc. Mech. Eng. Ser. C*, vol. 79, no. 803, 2013.
- [11] H. Doi, T. Miyamoto, J. Suzumura, J. Nakahashi, H. Chen, and T. Ban, "Change in Surface Condition of Turned Wheel and Effectiveness of Lubrication Turned against Flange Climb Derailment," *Q. Rep. RTRI*, vol. 53, no. 2, pp. 70–76, 2012.
- [12] A. Kataori, K. Doi, H. Iijima, S. Momosaki, and S. Matsumoto, "The Influence of the Wheel/Rail Contact Point Condition on Friction Coefficient," *9th World Conf. Railw. Res.*, 2011.
- [13] S. Greene *et al.*, "Flange Climb Derailment Criteria and Wheel/Rail Profile Management and Maintenance Guidelines for Transit Operations," *TCRP Rep. 71 Track-Related Res.*, vol. 5, p. 147, 2005.

- [14] S. Iwnicki, M. Spiriyagin, C. Cole, and T. McSweeney, *Handbook of railway vehicle dynamics*. CRC press, 2020.
- [15] J. Stow and P. Allen, "A Good Practice Guide for Managing the Wheel-Rail Interface of Light Rail and Tramway Systems," *Off. Rail Regul.*, 2008.
- [16] M. Pau, "Estimation of real contact area in a wheel-rail system by means of ultrasonic waves," *Tribol. Int.*, vol. 36, no. 9, pp. 687–690, 2003.
- [17] M. B. Marshall, R. Lewis, R. S. Dwyer-Joyce, U. Olofsson, and S. Björklund, "Experimental Characterization of Wheel-Rail Contact Patch Evolution," *J. Tribol.*, vol. 128, no. 3, pp. 493–503, 2006.
- [18] R. S. Dwyer-Joyce, C. Yao, J. Zhang, R. Lewis, and B. W. Drinkwater, "Feasibility Study for Real Time Measurement of Wheel-Rail Contact Using an Ultrasonic Array," *J. Tribol.*, vol. 131, no. 4, p. 041401, 2009.
- [19] M. Pau and B. Leban, "Ultrasonic assessment of wheel-rail contact evolution exposed to artificially induced wear," *Proc. Inst. Mech. Eng. Part F J. Rail Rapid Transit*, vol. 223, no. 4, pp. 353–364, 2009.
- [20] R. S. Dwyer-Joyce, C. Yao, R. Lewis, and H. Brunskill, "An ultrasonic sensor for monitoring wheel flange/rail gauge corner contact," *Proc. Inst. Mech. Eng. Part F J. Rail Rapid Transit*, vol. 227, no. 2, pp. 188–195, 2013.
- [21] K. Kendall and D. Tabor, "An Ultrasonic Study of the Area of Contact between Stationary and Sliding Surfaces," *Proc. R. Soc. A Math. Phys. Eng. Sci.*, vol. 323, no. 1554, pp. 321–340, 1971.
- [22] H. G. Tattersall, "The ultrasonic pulse-echo technique as applied to adhesion testing," *J. Phys. D. Appl. Phys.*, vol. 6, pp. 819–832, 1973.
- [23] A. Rovira, A. Roda, M. B. Marshall, H. Brunskill, and R. Lewis, "Experimental and numerical modelling of wheel-rail contact and wear," *Wear*, vol. 271, no. 5–6, pp. 911–924, 2011.
- [24] M. Pau, B. Leban, and M. Guagliano, "Propagation of Sub-surface Cracks in Railway Wheels for Wear-induced Conformal Contacts," *J. Mech. Syst. Transp. Logist.*, vol. 3, no. 1, pp. 226–235, 2010.
- [25] L. Zhou, H. Brunskill, R. Lewis, M. Pletz, W. Daves, and S. Scheriau, "Real time Measurement of Dynamic Wheel-Rail Contacts Using Ultrasonic Reflectometry," *Submitt. to J. Tribol.*, 2018.
- [26] H. P. Brunskill, "The Real-Time Characterisation of Dry Machine Element Contacts Using Ultrasonic Reflectometry," Ph.D. thesis, University of Sheffield, 2013.
- [27] S. R. Lewis, S. Riley, D. I. Fletcher, and R. Lewis, "Optimisation of a railway sanding system for optimal grain entrainment into the wheel–rail contact," *Proceedings of the Institution of Mechanical Engineers, Part F: Journal of Rail and Rapid Transit*, vol. 232, no. 1. pp. 43–62, 2018.

- [28] M. Schoenberg, "Elastic wave behavior across linear slip interfaces," *J. Acoust. Soc. Am.*, vol. 68, no. 5, pp. 1516–1521, 1980.
- [29] T. Ohyama, "Tribological studies on adhesion phenomena between wheel and rail at high speeds," *Wear*, vol. 144, pp. 263–275, 1991.
- [30] B. Bhushan, *Principles and applications to tribology*. John Wiley & Sons, 1999.
- [31] E. S. Gadelmawla, M. M. Koura, T. M. A. Maksoud, I. M. Elewa, and H. H. Soliman, "Roughness parameters," *J. Mater. Process. Technol.*, vol. 123, no. 1, pp. 133–145, 2002.
- [32] H. A. Sherif and S. S. Kossa, "Relationship between normal and tangential contact stiffness of nominally flat surfaces," *Wear*, vol. 151, no. 1, pp. 49–62, 1991.
- [33] J. Królikowski and J. Szczepek, "Assessment of tangential and normal stiffness of contact between rough surfaces using ultrasonic method," *Wear*, vol. 160, no. 2, pp. 253–258, 1993.
- [34] R. S. Dwyer-Joyce and M. Gonzalez-Valadez, "Ultrasonic Determination of Normal and Shear Interface Stiffness and the Effect of Poisson's Ratio," *Transient Process. Tribol.*, pp. 143–149, 2004.
- [35] A. Meierhofer, C. Hardwick, R. Lewis, K. Six, and P. Dietmaier, "Third body layer-experimental results and a model describing its influence on the traction coefficient," *Wear*, vol. 314, no. 1–2, pp. 148–154, 2014.

7 INFLUENCE OF INITIAL ROUGHNESS OF RE-PROFILED WHEELS ON FRICTION COEFFICIENT

Paper 5

Traction Condition between Wheel Flange and Rail Gauge Corner during Running-in

S. Fukagai^{a,b*}, R. Lewis^a

^a Department of Mechanical Engineering, University of Sheffield, Sheffield, UK

^b Railway Technical Research Institute, Tokyo, Japan

Abstract

The risk of wheel-climb derailment increases if the traction coefficient in the wheel/rail contact is too high. This has been observed to happen more frequently just after wheel machining. This work investigates how the traction coefficient rises with the evolution of the machining marks of the wheel during running-in. Experiments were performed using a full-scale rig to simulate the contact between wheel flange and rail gauge corner. The contact area was scanned and visualized using an ultrasonic array transducer mounted in the rail. Results were used to determine the distribution of contact stiffness. The transition of the contact stiffness distribution clarified the process of surface evolution. The increase of traction coefficient with the cyclic rolling/sliding followed an increase of contact stiffness. Also, the rougher wheel showed a reduced increase of contact stiffness during running-in.

Presented in Railway Engineering 2019, Edinburgh, UK

7.1 Introduction

Since the frictional condition between the wheel and rail plays a vital role in the transmission of the driving force and braking force, it should be kept at an optimum level to secure the proper acceleration performance and braking distance. On the other hand, it is known that high traction coefficient and slip at curves could lead to severe wear and deformation of wheel and rail, energy consumption and squealing noise [1]. It also increases the risk of a wheel climb derailment occurring [2]–[4].

Nakahara *et al.* [5] reported that the traction between a wheel and a rail changes with a train traffic passage even in the dry condition and showed some transient traction curves using twin-disk testing which indicated that traction coefficient varies with the evolution of surface roughness during running-in [6]. Blau [7] also addressed that the tribological behaviour during running-in and reported typical examples of friction force transition curves. Notably, it was mentioned that the friction force tends to increase significantly in the case of dry contact after the start of sliding contact. In these cases, it is commonly recognized that one of the main causes for such a transition is the evolution of surface topography with cyclic contacts [6], [7]. Lundmark *et al.* [8] and Fukagai *et al.* [9] also reported that transitions in traction coefficient are strongly influenced by the initial topography.

A railway wheel experiences machining several times during its life to reset it to the designed profile from the worn profile or to remove damage, such as a wheel flat or, cracks. And it is known that some derailments have occurred relatively soon after machining of wheels [10]–[13]. Just after machining, the wheel surface has a large roughness which is caused by the machining marks. Some reports mention the possibility that the rougher surface leads to a higher traction coefficient, and so increases the risk of flange climb derailment [12]–[14]. Specifically, they indicate that the spike-like machining marks cause an increase in traction during running-in as they plough into the rail material. Therefore, a smooth surface is recommended at the finishing of wheel machining [12], [14]. On the other hand, there is another opinion that traction force is increased with the deformation of machining marks and increase in real contact area [10]. As the wheel and rail experience cyclic rolling/sliding with tangential force, the surface topography changes and therefore the interfacial condition alters dramatically during running-in. Therefore, it is important to understand how such an interfacial condition evolves over time to understand the potential mechanisms for wheel climb derailment just after wheel machining. However, the difficulty in obtaining accurate non-destructive interfacial measurements has hindered systematic experimental investigations. An increased understanding of these effects might inform rail service providers about optimal wheel profiling methods and lubrication programs to reduce the risk of wheel climb derailment.

Recently, ultrasonic techniques have been used to observe the contact between wheel and rail [15]–[19]. Though there are spatial resolution limits and considerations of transducer positioning to ensure the sound waves reflect off the area of interest, this technique can be used to non-invasively and directly observe the contact. When an ultrasonic wave strikes the interface between the wheel and rail, it is partially transmitted and partially reflected. The proportion of the wave reflected depends on the stiffness of the contact [20], [21]. Recently, dynamic ultrasonic measurement of a rolling/sliding contact has been achieved [22], [23]. The authors also have investigated

the relationship between the contact stiffness and traction coefficient and revealed that there was a positive relationship on the dynamic contact for repeated cycles [24]. However, the test wheel had no machining marks on its surface. Such large roughness is suspected to cause the spike effect and lead to the increase of traction coefficient. Also, it is expected that the contact shape and contact condition will change more dramatically. Therefore, the information about the contact condition under a cyclic tangential force will help to understand the mechanism causing the tribological transition just after the wheel machining.

This work aimed to understand and characterize the tribological behaviour at the wheel flange just after wheel machining. Ultrasonic reflection was used to evaluate interface condition in a rolling/sliding contact, particularly contact stiffness over time as running-in occurs. The experiments were performed using a full-scale dynamic wheel/rail contact-testing machine and a 64-element ultrasonic array transducer mounted in the rail. The transient traction coefficient was also measured during the test.

7.2 Methodology

7.2.1 Full-scale rig

Figure 7-1 shows a schematic illustration of the full-scale testing machine, which is equipped with an actual wheel and rail loaded upside down on it. It can apply a vertical load of up to 50 kN, a lateral load of up to 40 kN and a rail longitudinal load of up to 20 kN using hydraulic cylinders to push the rail. The rail is moved at a velocity of up to 100 mm/s in the longitudinal direction. Although the wheel exhibits no driving performance, it is rotated by force generated due to the friction between the wheel and the rail. The angle of attack is changeable from -3-degree to +3-degree by adjusting the plate on which the rail is mounted. Figure 7-2 shows an array ultrasound transducer and a schematic of the setting. The transducer was mounted in a hole that was made in the rail in the direction parallel to the wheel flange. Hence, the contact area could be scanned with the passage of the wheel on the rail where the transducer was mounted. The array transducer consisted of 64 piezo elements arranged linearly each with a constant pitch of 0.5mm. However, the sampling interval was improved to 0.25 mm different combinations of group elements. The sampling interval in the rolling direction was determined by the accuracy of the encoder, which was attached to the rail, and it was 0.08 mm.

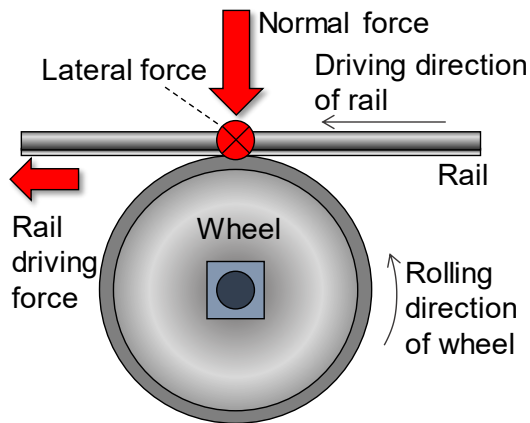


Fig. 7-1 Schematic illustration of the full-scale testing machine.

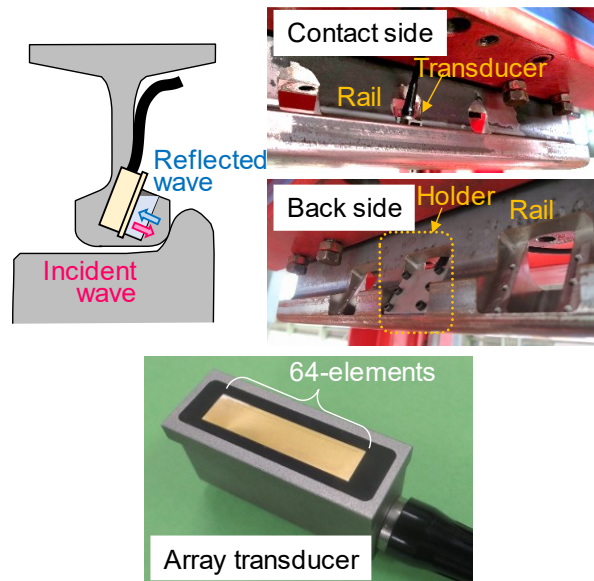


Fig. 7-2 Array ultrasound transducer and schematic of the setting.

Figure 7-3 shows the wheel flange forces acting on the rail gauge corner and the transducer position. The rail contacts the wheel flange at one contact patch around the straight section of the wheel flange. The rail was mounted on the testing machine without an angle of cant. In the test machine a vertical load P and lateral load Q were applied, but for defining the test conditions these were used to determine the normal force N and the lateral tangential force F_y with the following equations:

$$N = P \cos \alpha + Q \sin \alpha , \tag{1}$$

$$F_y = P \sin \alpha - Q \cos \alpha , \tag{2}$$

where α is the contact angle (65° in this experiment).

The longitudinal tangential force F_x was set independently of the vertical load P and lateral load Q . It should be noted that the traction coefficient in the lateral direction, which is described later, means F_y/N .

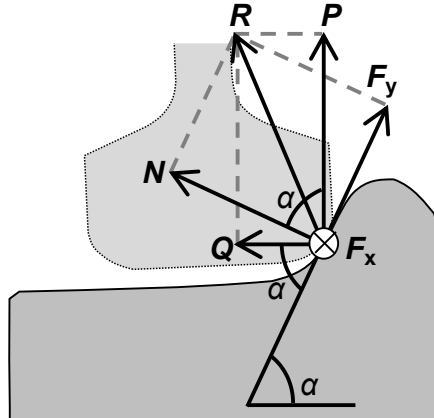


Fig. 7-3 Schematic diagram of the full-scale wheel/rail contact rig.

7.2.2 Ultrasound technique

At an interface of two dissimilar materials, part of the incident ultrasonic wave is transmitted through the interface, and the other part is reflected. For an interface of two dissimilar materials perfectly bonded, the proportion of the reflected wave, described by the reflection coefficient R , is dependent on the acoustic impedance mismatch between the two materials and is given by [25]:

$$R = \frac{z_2 - z_1}{z_2 + z_1} \quad (3)$$

where z_1 and z_2 are the acoustic impedances (which are the products of density and acoustic velocity) of the contacting materials. Therefore, for two perfectly bonded identical materials, the interface would have no reflection ($z_1=z_2$, $R=0$) and the entire wave is transmitted (without any losses). Conversely, an ultrasonic wave is almost completely reflected at an interface between two materials with substantially different acoustic impedances, as in the case of a solid and a gas ($R \approx 1$).

Real engineering interfaces are inherently rough, and micro and macroscopic air gaps are formed at an interface. Presuming the length of the ultrasonic wave is long relatively to the size of the air gaps the whole interface behaves as a single reflector and therefore R is also dependent on the contact stiffness of the interface [20], [21]. The contact stiffness, K , is a function of the surface topography, surface material properties and the contact pressure and has a significant influence on the contact dynamics. As the surface topography changes due to elastic and plastic deformation, the measured reflection coefficient R will change accordingly as shown in Fig. 7-4. The contact stiffness could vary

from zero for a pair of surfaces just in contact with infinity when they are perfectly bonded. In principle, the degree of conformity at the interface can be determined by measuring the reflection coefficient of the ultrasonic wave.

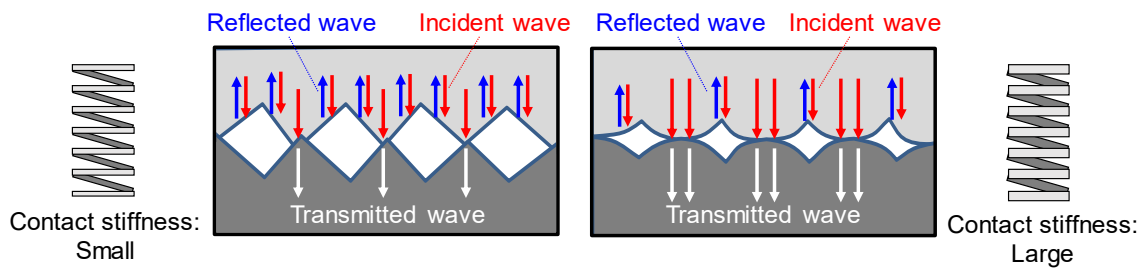


Fig. 7-4 Principle of measurement.

Schoenberg [25] used an interface 'spring model' to show how the reflection coefficient is related to contact stiffness:

$$R = \frac{z_1 - z_2 - i\omega(z_1 z_2 / K)}{z_1 + z_2 - i\omega(z_1 z_2 / K)} \quad (4)$$

where ω is the angular frequency of the ultrasound and K is the interfacial contact stiffness. The contact stiffness is defined as the stiffness due to asperity contact per unit area of an interface, as shown in the following equation.

$$K = -\frac{dp}{du} \quad (5)$$

where p is the nominal contact pressure and u is the distance between the surface mean lines. The interface stiffness depends on the load applied, and hence the contact pressure between them. When the load at the interface is increased the surfaces are pressed closer together with more asperities contacting, thus the stiffness rises. The stiffness in this way is nonlinear and may vary from zero when the surfaces are just touching, to infinity when the surfaces are completely conformal. In the case of present work, the materials on both sides of the interface are similar ($z_1=z_2=z$), then equation (4) reduces to:

$$K = \frac{\omega z}{2} \sqrt{\frac{1}{R^2} - 1} \quad (6)$$

Therefore, if the reflection coefficient, R , can be experimentally obtained, the contact stiffness, K can be estimated. Generally, normal contact stiffness can be distinguished from shear contact stiffness depending on the loading direction. The contact stiffness in this paper means the normal contact stiffness unless otherwise specified.

Many researchers [15]–[19] have obtained the reflection coefficient R as the ratio of the reflected ultrasonic wave amplitude under load, H , to that when unloaded with no material in contact, H_0 (the reference).

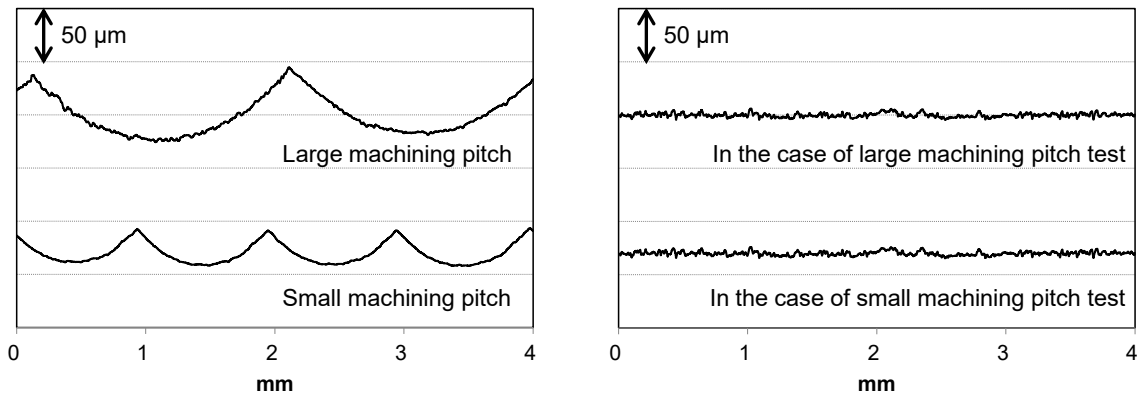
$$R = \frac{H}{H_0} \quad (7)$$

When unloaded, the contact is effectively steel against air, and so the wave can be assumed to be fully reflected and thus H_0 is equivalent to the incident wave amplitude. This is a simple practical way to obtain the reflection coefficient and removes the influence of transducer characteristics, ultrasonic wave scattering and attenuation.

7.2.3 Test rail and wheel

The type of the test rail was 50N (JIS E 1101-2001) at a length of 750 mm and that of the test wheel was SSW-Q3S (JIS E 5402) with a diameter of 860mm. Both the wheel and the rail were new and the profile of the wheel was a “modified arc tread”. The rail contacts the wheel flange at one contact patch around the straight section of the wheel flange.

To investigate the dependency on the initial surface topography, two types of wheel surface were prepared with the different machining pitch; the large machining pitch was 2.0 mm/rev, and the small machining pitch was 1.0 mm/rev. Figure 7-5 shows the initial surface profile of rail and wheel for each case. Resin replicas based on methyl methacrylate (Technovit 3040, Kluzer) were used to copy the surface topography of wheel. After obtaining the replica, the roughness and surface topography were analyzed using a contact-type roughness meter (Surfcorder SE3500, Kosaka Laboratory Ltd.). The plus and minus signs of these profiles were reversed to be the same as the actual surface because the profiles were obtained from the replica. Table 7-1 shows the initial roughness value which is the mean value of three measurements. The roughness of wheel was measured in the radial direction and that of rail was measured in the longitudinal direction.



(a) Wheel

(b) Rail

Fig. 7-5 Initial surface profiles of wheel and rail.

Table 7-1 Initial roughness of test wheel and rail

		Pitch of machining (mm/rev)	Ra (μm)	Pz (μm)
Large machining pitch	Wheel	2.0	2.3	66.5
	Rail	-	1.3	16.9
Small machining pitch	Wheel	1.0	3.4	34.8
	Rail	-	0.9	9.3

7.2.4 Test procedure

Table 7-2 shows the test conditions. The cyclic contact tests were continued up to 120 cycles for both machining pitches. The tests were carried out after cleaning the surface with acetone. The measurement of the traction coefficient in lateral direction and reflection coefficient were carried out continuously during the cyclic tests. Resin replicas were used for the evaluation of roughness after the tests as mentioned in the previous section. The velocity was quite low, approximately 5 mm/sec. Though it is well known that the traction coefficient is influenced by the velocity when fluid, such as water, gets in between the wheel and the rail, this influence is small in the dry condition [26].

Table 7-2 Test conditions

Normal force (kN)	Velocity (mm/s)	Angle of attack (degree)	Number of cycles (cycles)
30	5	1	120

7.3 Results

7.3.1 Change of traction coefficient with cyclic rolling

Figure 7-6 shows the relationship between the number of contacts and the traction coefficient in the lateral direction. Here, the number of contacts was obtained by integrating the number of the right and left directions in reciprocating motion. Since the direction of the movement with a positive attack angle corresponds to the even-number-th contacts, the data of the even-number-th contacts are plotted in Fig. 7-6. The traction coefficient for large machining pitch, initially about 0.35, increased with the number of contacts, and tends to be saturated at about 0.42 at the contact number more than 40. On the other hand, the traction coefficient for small machining pitch, initially about 0.25, increased with the contact number, and it was saturated to be about 0.48 at a contact number of more than 60. From these results, it has become clear that the tendencies of the increase in the traction coefficient with the contact number are different between large machining pitch and small machining pitch. Namely, compared with large machining pitch, the traction coefficient for small machining pitch tends to be saturated at relatively low contact number, and the saturated value for large machining pitch is lower than that for small machining pitch.

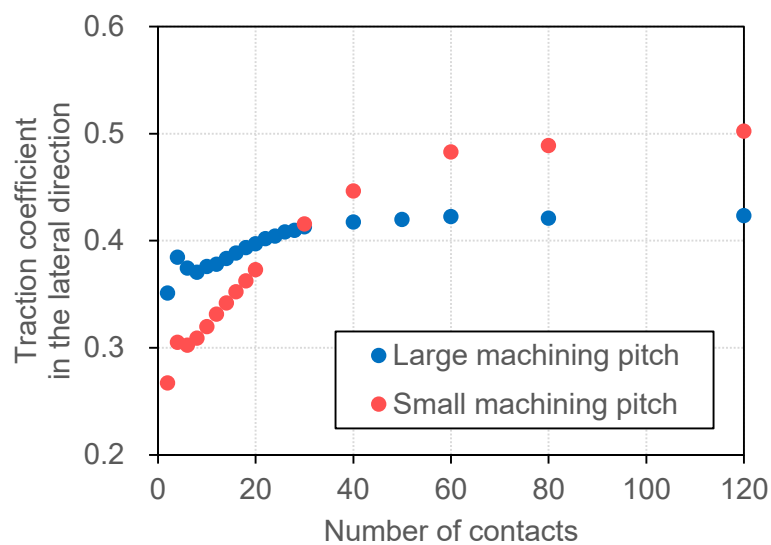


Fig. 7-6 Relationship between number of cycles and traction coefficient.

7.3.2 Change of contact stiffness with cyclic rolling

Figure 7-7 shows the change in the distribution of contact stiffness with the increase in the number of contacts for the large machining pitch and the small machining pitch. From the results of the large machining pitch, it can be found that the distribution of contact stiffness, initially one line at 2nd contact, became two lines at 6th contacts. The distance between two lines almost coincides with that between two ridges of machining marks by wheels described in Fig. 7-5 (machining pitch: 2.0 mm). Therefore, it is suggested that the lines represent the shape of the contact shape that was produced by the contact between the ridges of the machining marks. After 20 contacts, it was observed that the lines changed to the shape of the contact shape composed of bold one line.

For the measurement results of the small machining pitch, on the other hand, a line-shaped contact was not observed from the first contact to the end of the contacts. However, it was observed that the initially existing ellipsoidal contact shape gradually increased.

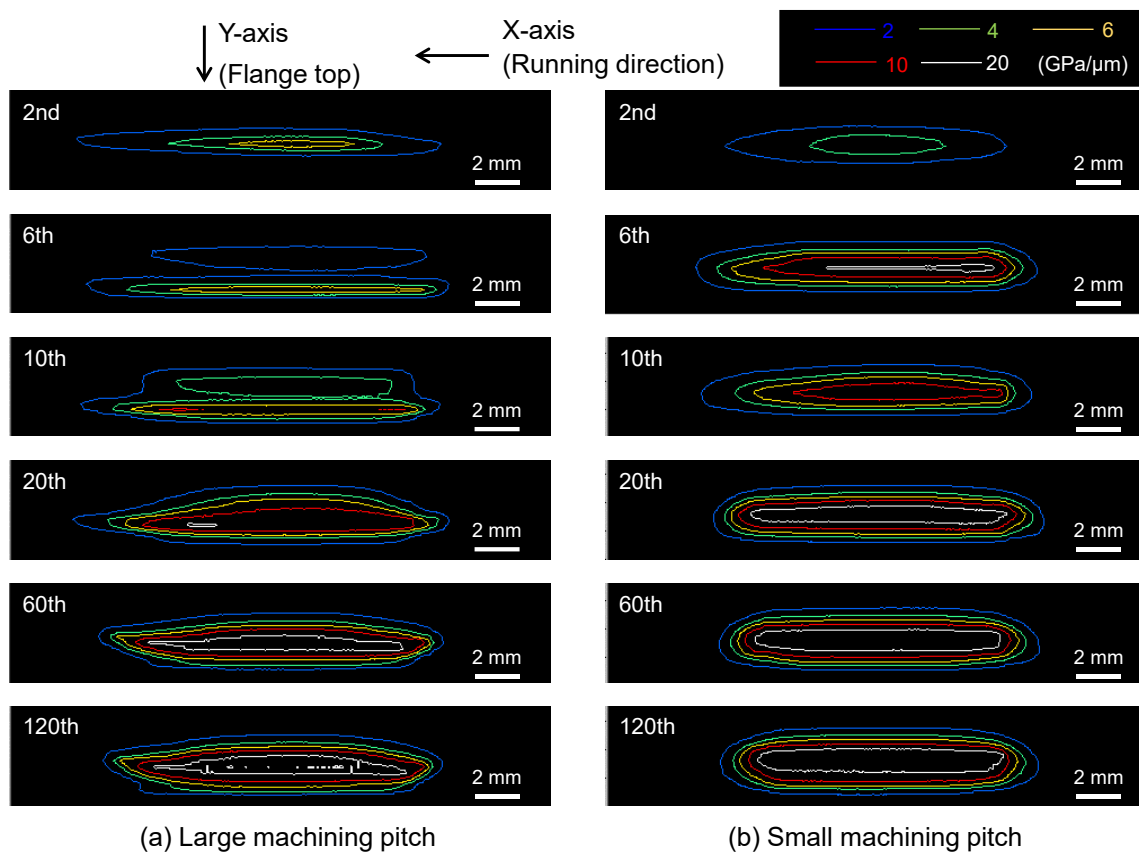


Fig. 7-7 Change in the distribution of contact stiffness with the increase in the number of contacts.

Figure 7-8 presents the relationship between the number of cyclic contacts and the mean contact stiffness in the apparent contact plane. The mean contact stiffness was obtained from the summation of the contact stiffness in the apparent contact area (Fig. 7-7) divided by the number of data in the apparent contact shape. The mean contact stiffness for the large machining pitch, initially about 2 GPa/ μm , tends to increase with the number of contacts. It is also observed that the value reached to be 8 GPa/ μm at around 20 contacts, and then it was saturated. On the other hand, the mean transmittance for the small machining pitch, initially about 2 GPa/ μm like the large machining pitch, tends to increase with the contact number. Then it increased further and finally tends to be saturated at about 14 GPa/ μm .

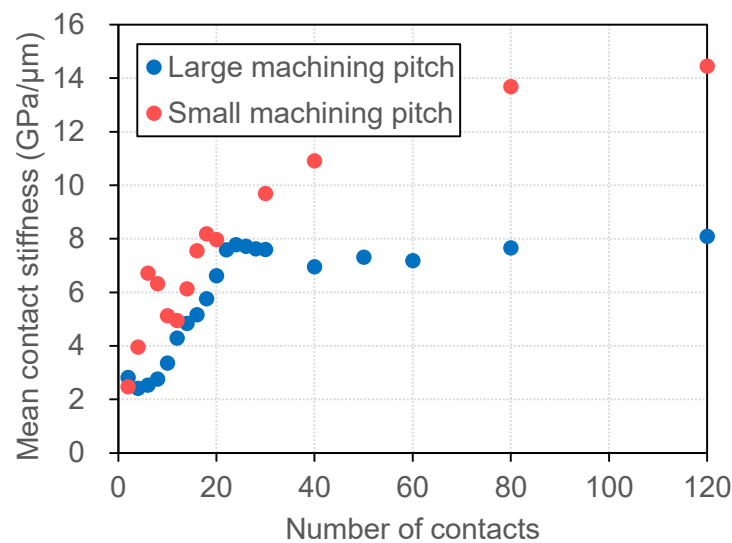


Fig. 7-8 Relationship between number of cycles and mean contact stiffness.

7.3.3 Change of surface topography with cyclic rolling

Figure 7-9 shows the comparison of the profiles before and after the test cycles. The measurement of profiles was carried out in a similar way as mentioned previously. Figures 7-9 (a) and (b)-Wheel show that the initial machining marks were flattened dramatically in both machining pitch. However, the large machining pitch remains some marks compared with the small machining pitch. Figs. 7-9 (c) and (d)-Rail show that the initial asperities were flattened similar extent in both machining pitches.

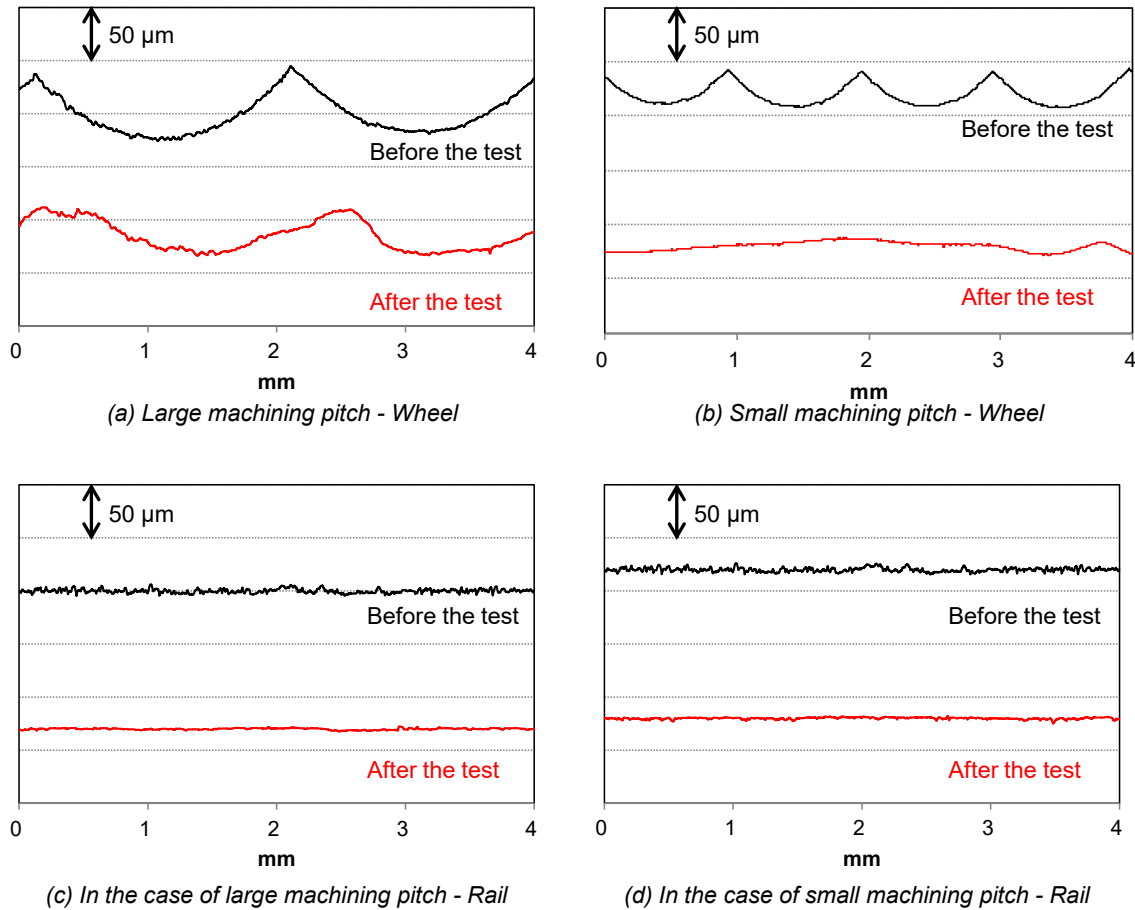


Fig. 7-9 Comparison of the profiles before and after test cycles.

7.4 Conclusions

From the measurement of rolling/sliding contact condition between wheel flange and rail gauge corner using ultrasound wave, the following conclusions can be drawn:

1. For both wheel machining pitches, the large machining pitch and the small machining pitch, showed the increase of traction coefficient with the increase of cycles and it is found that the increase in the small machining pitch was larger than that of the large machining pitch.
2. Mean contact stiffness which was measured using ultrasound wave increased with the cyclic rolling and the value of the small machining pitch saturated larger than that of the large machining pitch. This tendency was similar to the transition of the traction coefficient.
3. The maximum height of surface asperities in both machining pitches showed that the initial asperity was flattened dramatically after the cyclic rolling/sliding. Maximum height after cycles in the large machining pitch remained higher than that in the small machining pitch.

References

- [1] R. Lewis, R. S. Dwyer-Joyce, S. R. Lewis, C. Hardwick, and E. A. Gallardo-Hernandez, "Tribology of the Wheel-Rail Contact: The Effect of Third Body Materials," *Int. J. Railw. Technol.*, vol. 1, no. 1, pp. 167–194, 2012.
- [2] W. C. Shust and J. A. Elkins, "Wheel forces during flange climb part I - track loading vehicle tests," in *Railroad Conference, 1997., Proceedings of the 1997 IEEE/ASME Joint.*, 1997, pp. 137–147.
- [3] H. Ishida, T. Miyamoto, E. Maebashi, H. Doi, K. Iida, and A. Furukawa, "Safety assessment for flange climb derailment of trains running at low speeds on sharp curves," *Q. Rep. RTRI*, vol. 47, no. 2, pp. 65–71, 2006.
- [4] A. Matsumoto *et al.*, "A new measuring method of wheel-rail contact forces and related considerations," *Wear*, vol. 265, no. 9–10, pp. 1518–1525, 2008.
- [5] T. Nakahara, K. S. Baek, H. Chen, and M. Ishida, "Relationship between surface oxide layer and transient traction characteristics for two steel rollers under unlubricated and water lubricated conditions," *Wear*, vol. 271, no. 1–2, pp. 25–31, 2011.
- [6] K. S. Baek, K. Kyogoku, and T. Nakahara, "An experimental study of transient traction characteristics between rail and wheel under low slip and low speed conditions," *Wear*, vol. 265, no. 9–10, pp. 1417–1424, 2008.
- [7] P. J. Blau, "On the nature of running-in," *Tribol. Int.*, vol. 38, no. 11–12, pp. 1007–1012, Nov. 2005.
- [8] J. Lundmark, E. Kassfeldt, J. Hardell, and B. Prakash, "The influence of initial surface topography on tribological performance of the wheel/rail interface during rolling/sliding conditions," *Proc. Inst. Mech. Eng. Part F J. Rail Rapid Transit*, vol. 223, no. 2, pp. 181–187, 2009.
- [9] S. Fukagai, L. Ma, and R. Lewis, "Tribological aspects to optimize traction coefficient during running-in period using surface texture," *Wear*, vol. 424–425, no. January, pp. 223–232, 2019.
- [10] H. Doi, T. Miyamoto, J. Suzumura, J. Nakahashi, H. Chen, and T. Ban, "Change in Surface Condition of Turned Wheel and Effectiveness of Lubrication Turned against Flange Climb Derailment," *Q. Rep. RTRI*, vol. 53, no. 2, pp. 70–76, 2012.
- [11] A. Kataori, K. Doi, H. Iijima, S. Momosaki, and K. Horioka, "Development of Continuous Measurement Equipment for Angle of Attack and Results of Measurements," *JR EAST Tech. Rev.*, no. 19, pp. 46–49.
- [12] S. Greene *et al.*, "Flange Climb Derailment Criteria and Wheel/Rail Profile Management and Maintenance Guidelines for Transit Operations," *TCRP Rep. 71 Track-Related Res.*, vol. 5, p. 147, 2005.
- [13] S. Iwnicki, M. Spiriyagin, C. Cole, and T. McSweeney, *Handbook of railway vehicle dynamics*. CRC press, 2020.

- [14] J. Stow and P. Allen, "A Good Practice Guide for Managing the Wheel-Rail Interface of Light Rail and Tramway Systems," *Off. Rail Regul. Manchester*, Jan. 2008.
- [15] M. Pau, "Estimation of real contact area in a wheel-rail system by means of ultrasonic waves," *Tribol. Int.*, vol. 36, no. 9, pp. 687–690, 2003.
- [16] M. B. Marshall, R. Lewis, R. S. Dwyer-Joyce, U. Olofsson, and S. Björklund, "Experimental Characterization of Wheel-Rail Contact Patch Evolution," *J. Tribol.*, vol. 128, no. 3, pp. 493–503, 2006.
- [17] R. S. Dwyer-Joyce, C. Yao, J. Zhang, R. Lewis, and B. W. Drinkwater, "Feasibility Study for Real Time Measurement of Wheel-Rail Contact Using an Ultrasonic Array," *J. Tribol.*, vol. 131, no. 4, p. 041401, 2009.
- [18] M. Pau and B. Leban, "Ultrasonic assessment of wheel-rail contact evolution exposed to artificially induced wear," *Proc. Inst. Mech. Eng. Part F J. Rail Rapid Transit*, vol. 223, no. 4, pp. 353–364, 2009.
- [19] R. S. Dwyer-Joyce, C. Yao, R. Lewis, and H. Brunskill, "An ultrasonic sensor for monitoring wheel flange/rail gauge corner contact," *Proc. Inst. Mech. Eng. Part F J. Rail Rapid Transit*, vol. 227, no. 2, pp. 188–195, 2013.
- [20] K. Kendall and D. Tabor, "An Ultrasonic Study of the Area of Contact between Stationary and Sliding Surfaces," *Proc. R. Soc. A Math. Phys. Eng. Sci.*, vol. 323, no. 1554, pp. 321–340, 1971.
- [21] H. G. Tattersall, "The ultrasonic pulse-echo technique as applied to adhesion testing," *J. Phys. D. Appl. Phys.*, vol. 6, pp. 819–832, 1973.
- [22] L. Zhou, H. Brunskill, R. Lewis, M. Pletz, W. Daves, and S. Scheriau, "Real time Measurement of Dynamic Wheel-Rail Contacts Using Ultrasonic Reflectometry," *Submitt. to J. Tribol.*, 2018.
- [23] H. P. Brunskill, "The Real-Time Characterisation of Dry Machine Element Contacts Using Ultrasonic Reflectometry," Ph.D. thesis, University of Sheffield, 2013.
- [24] S. Fukagai, H. P. Brunskill, A. K. Hunter, R. S. Dwyer-Joyce, and R. Lewis, "Transitions in rolling-sliding wheel/rail contact condition during running-in," *Tribol. Int.*, 2019.
- [25] M. Schoenberg, "Elastic wave behavior across linear slip interfaces," *J. Acoust. Soc. Am.*, vol. 68, no. 5, pp. 1516–1521, 1980.
- [26] T. Ohyama, "Tribological studies on adhesion phenomena between wheel and rail at high speeds," *Wear*, vol. 144, pp. 263–275, 1991.

8 DISCUSSION

8.1 Test conditions for contact stiffnesses evaluation

Table 8-1 shows the list of conditions for the experimental tests to measure the contact stiffnesses using ultrasonic waves that have been described in Chapters 4 to 7. In Test 1, high-pressure torsion (HPT) tests were conducted, and the contact stiffnesses were evaluated using piezoelectric elements attached to the specimens. In this test, two specimens were placed in contact with each other, and one specimen was twisted and rotated to cause friction. In Test 2, an array-type ultrasonic probe with 64 piezoelectric elements was inserted into the rail head of a full-scale wheel-rail contact test machine owned by The University of Sheffield, and the friction interface of the top of rail and wheel tread passing over the probe was scanned to evaluate the contact stiffness distribution. In Test 3, a phased-array-type ultrasonic probe with 64 piezoelectric elements was mounted on the rail head of a full-scale wheel-rail contact test machine owned by the Railway Technical Research Institute (Japan), and the friction interface of the wheel flange and rail gauge corner passing over the probe was scanned to evaluate the contact stiffness distribution. For more details of each test, the previously published or presented work is available for reference [1]–[4].

Table 8-1 Test conditions for evaluation of contact stiffnesses using ultrasound

		Test 1 [1], [2]	Test 2 [3]	Test 3 [4]
		HPT	FSR-Sheffield	FSR-RTRI
Chapter numbers in this thesis		Chapter 4 and 5	Chapter 6	Chapter 7
Load		110 kN	80 kN	30 kN
Average contact pressure in a contact area		Approx. 0.6 GPa	Approx. 0.5 GPa*	Approx. 0.9 GPa*
Velocity		0.2 mm/sec	10 mm/sec	5 mm/sec
Sliding condition		Sliding	Rolling-sliding	Rolling
Surface finishing		Ground/Blasted/Lathed	Ground/Worn	Lathed
Initial roughness (combined roughness)		Ground: 0.8 μm Blasted: 1.5 μm Lathed (0.4 mm): 5.8 μm Lathed (0.8 mm): 7.4 μm	Ground: 3.0 μm Worn: 8.1 μm	Lathed (1 mm): 4.3 μm Lathed (2 mm): 3.5 μm
Number of cycles		15	100	120
UT	Sensor type	Direct attachment of PZT elements	Array transducer	Phased array transducer
	Frequency	5 MHz	5 MHz	10 MHz
	Measurement mode	Pitch-catch	Pulse-echo	Pulse-echo
	Excitation direction	Normal/Tangential	Normal	Normal

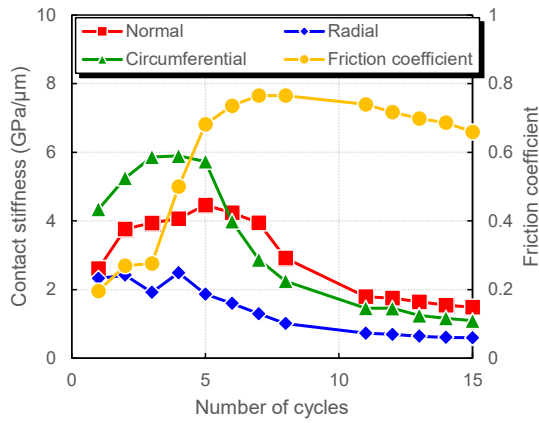
* In the case of the FSR, there is a pressure distribution according to the curvature of the wheel and rail.

8.2 Relationship between contact stiffness and friction coefficient

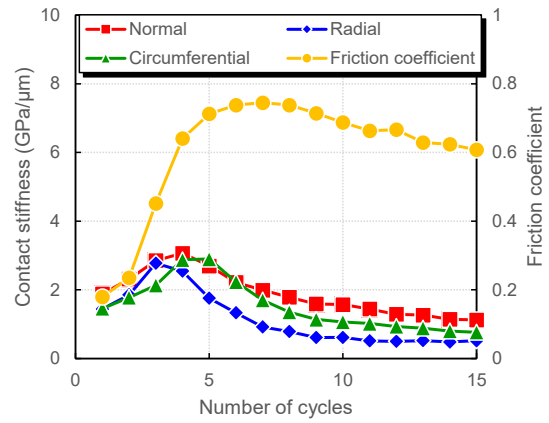
8.2.1 Test 1: HPT

Figure 8-1 shows the changes of contact stiffness and friction coefficient with testing cycles for different initial roughness using the HPT test machine. It was found that the stiffness in the cases of low and medium roughness peaked in the early cycles, 4th-5th, then dropped until the 8th-10th test cycle, then tapered off until the 15th test cycle. In the case of high roughness, 0.4 mm pitch, the contact stiffness rose gradually until the 5th or 10th cycle, then kept constant or tapered until the 15th test cycle. In the case of high roughness, 0.8 mm pitch, the stiffness gradually increased through all the test cycles. A generally good correlation was obtained between the contact stiffness and the friction coefficient. The friction coefficient was at its maximum at about the same time as the contact stiffness was at its maximum.

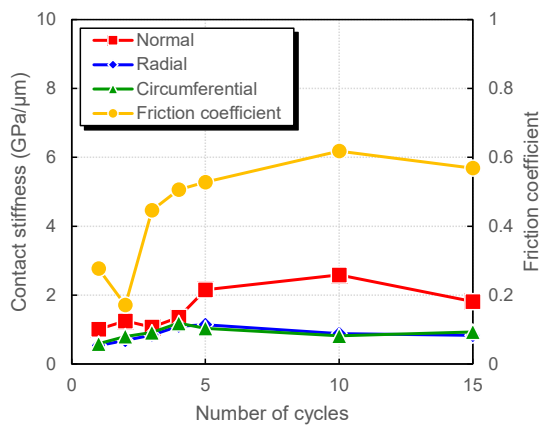
By comparing the changes in all roughness conditions, it was observed that the lower the initial roughness, the faster the increase in contact stiffness and the higher the peak contact stiffness for all cycles.



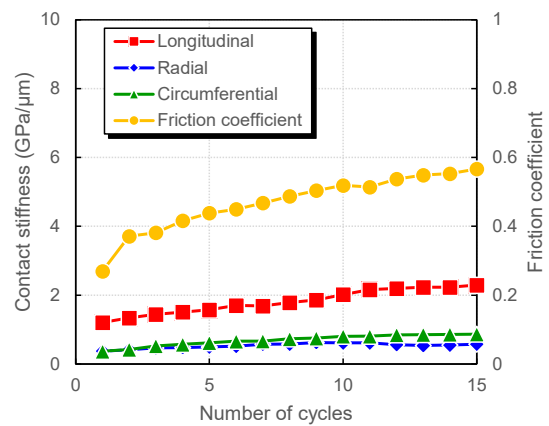
(a) Low roughness
Initial combined roughness: 0.8 μm



(b) Medium roughness
Initial combined roughness: 1.5 μm



(c) High roughness, 0.4 mm pitch
Initial combined roughness: 5.8 μm



(d) High roughness, 0.8 mm pitch
Initial combined roughness: 7.4 μm

Fig. 8-1 Changes of contact stiffness and friction coefficient with test cycles for different initial roughness.

Figure 8-2 shows the relationship between normal contact stiffness and friction coefficient during the cycles with the roughness changes. Although there is a generally positive correlation between the friction coefficient and the contact stiffness, the correlation appears to be dependent on the initial topography conditions. The higher the initial roughness, the more linear the relationship between contact stiffness and friction coefficient, and the lower the initial roughness, the more gradual the relationship between the contact stiffness and the friction coefficient at the beginning of the cycles. As discussed in Chapters 4 and 5, these differences can be attributed to the different friction modes of the running-in process. The micro-fracture of the surface at low initial roughness and the plastic deformation of the asperities at high initial roughness are considered to be the dominant factors during the running-in.

The different friction modes also explain the change in roughness: in the low roughness condition, micro-fracture causes a gradual increase in roughness on both sides at the same time. In contrast, in high roughness conditions, the surface asperities deformed

plastically (reducing the roughness) on the rougher side and they penetrated into the smoother side (increasing the roughness). Through the cycles, the two sides are gradually brought into the same condition.

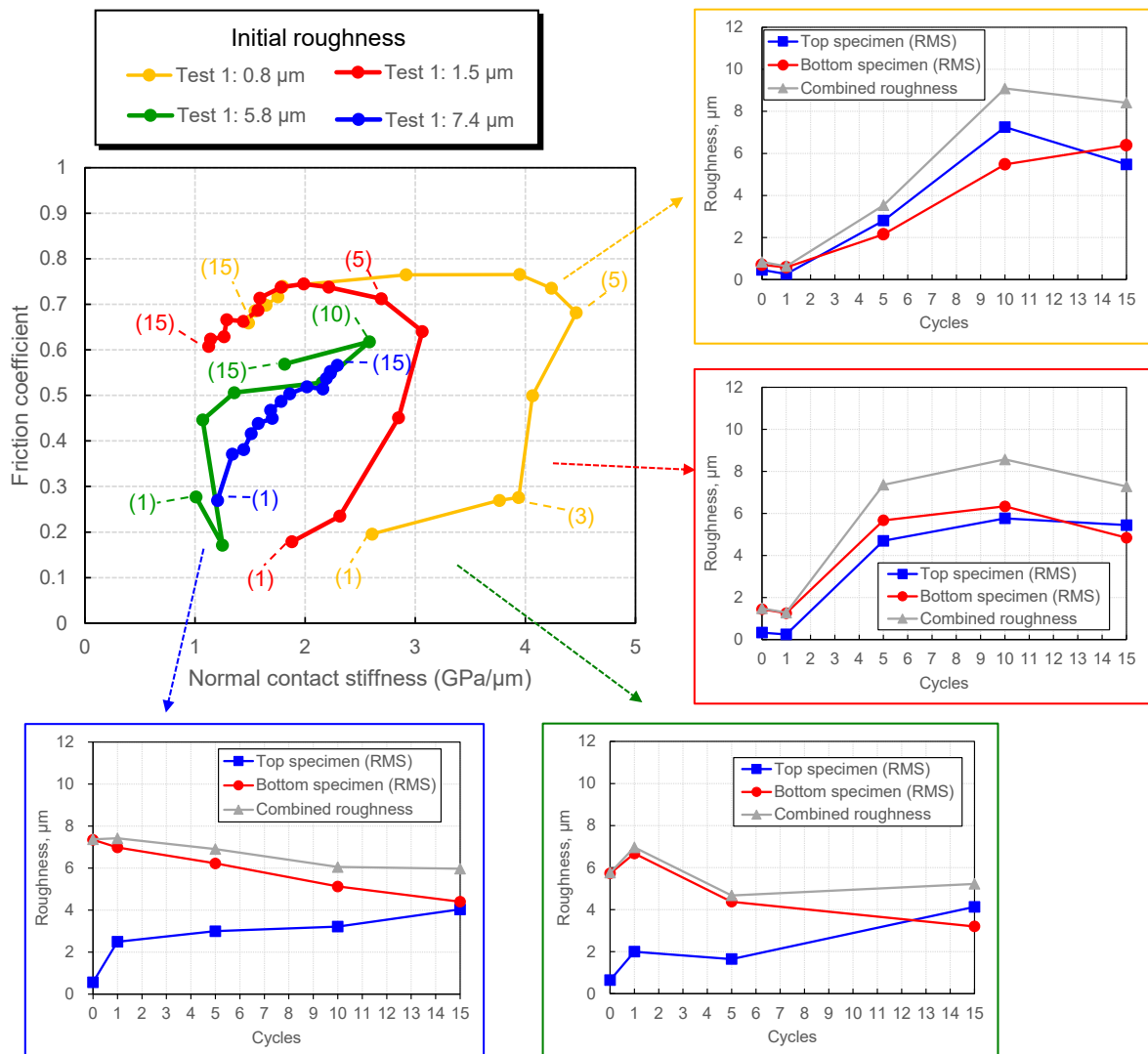
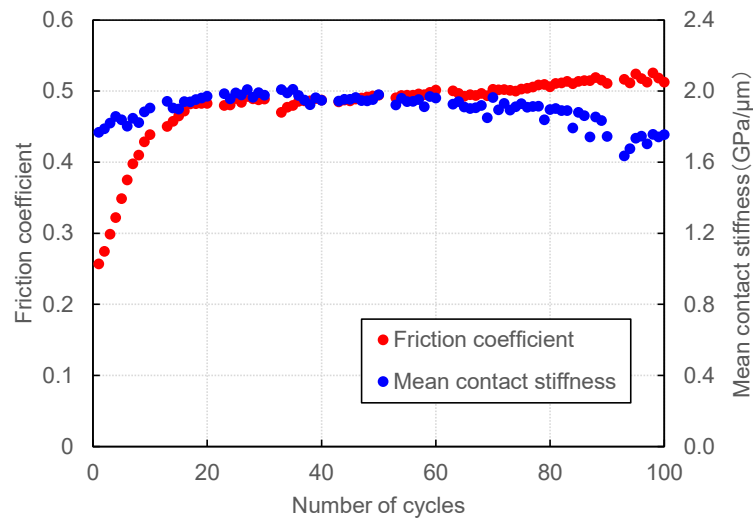


Fig. 8-2 Relationship between normal contact stiffness and friction coefficient during cycles. The number in brackets is the cycles. The changes in RMS roughness and combined roughness of the two specimens in contact are also noted.

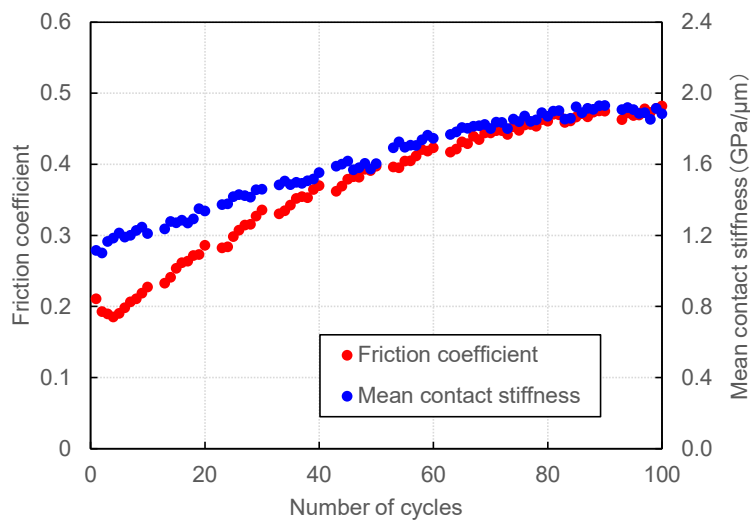
8.2.2 Test 2: FSR at Sheffield

Figure 8-3 shows the changes of contact stiffness and friction coefficient with testing cycles for different initial roughness using the FSR at Sheffield. Here, the results for the smoother case include the results up to the 60th cycle shown in Chapter 6, plus the results for the 60th-100th cycles. The reason for this is that, following the results of the HPT test, it was judged necessary to analyse and add the results for the data after the 60th cycle.

It was found that the stiffness in the smoother case increased slightly from about 1.8 to 2.0 GPa/ μm by the 20th cycle, remained almost constant between 20~70th cycle and decreased slightly to about 1.8 GPa/ μm after the 70th cycle. The coefficient of friction, on the other hand, increased rapidly from about 0.25 to 0.5 by the 20th cycle, and then continued to increase slowly until the 100th cycle. In the rougher case, the contact stiffness continued to increase gradually from about 1.1 to 1.9 GPa/ μm and the friction coefficient from about 0.2 to 0.5, both up to the 100th cycle.



(a) Smoother case
Initial combined roughness: 3.0 μm



(b) Rougher case
Initial combined roughness: 8.1 μm

Fig. 8-3 Relationship between mean contact stiffness and traction coefficient.
(FSR at Sheffield)

Figure 8-4 shows the relationship between (normal) mean contact stiffness and friction coefficient during cycles. In the rougher case, a good linear relationship was found between the contact stiffness and the friction coefficient. On the other hand, in the smoother case, the contact stiffness tends to increase and then to decrease. The linear increase at high initial roughness and the curve trend at low initial roughness are in agreement with the HPT results.

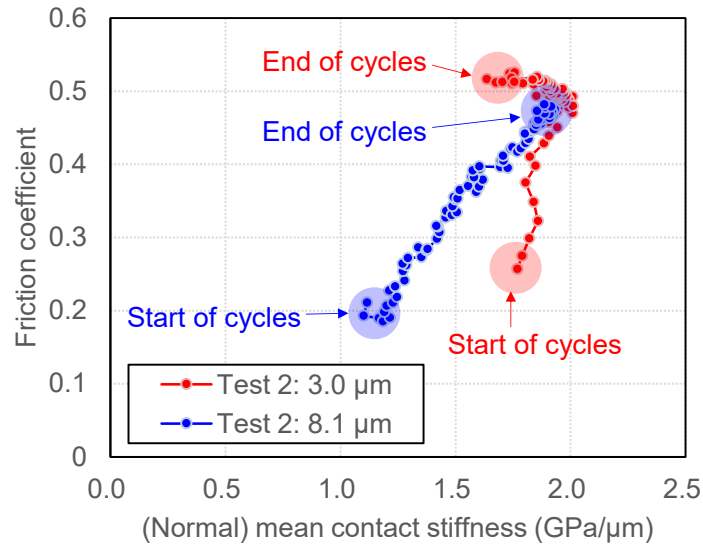
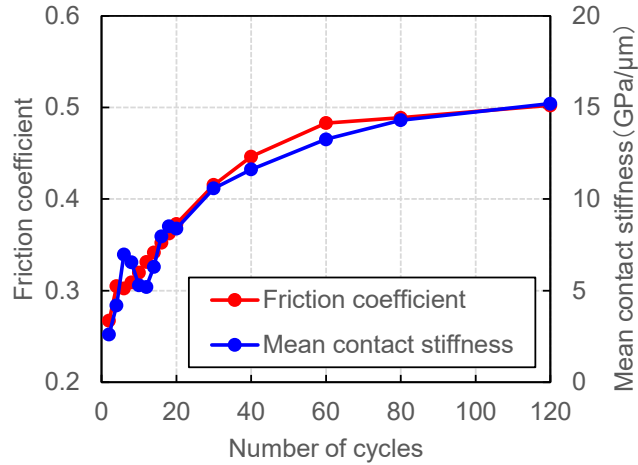


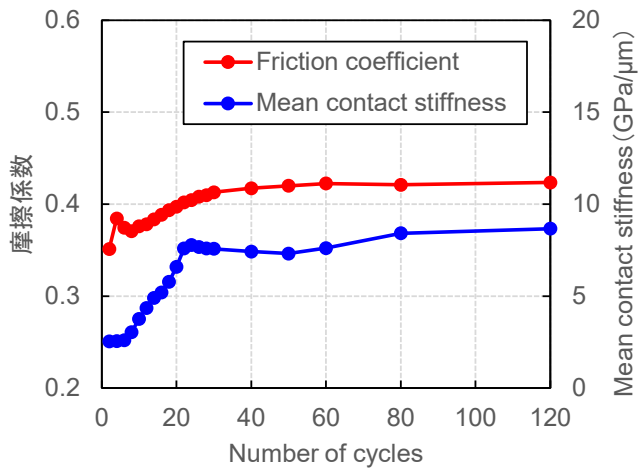
Fig. 8-4 Relationship between (normal) mean contact stiffness and friction coefficient during cycles in the case of FSR at Sheffield.

8.2.3 Test 3: FSR at RTRI

Figure 8-5 shows the changes of contact stiffness and friction coefficient with testing cycles for different initial roughness using the FSR at RTRI. For the machining pitch of 1 mm, the contact stiffness continued to increase gradually from about 3 to 15 GPa and the friction coefficient from about 0.25 to 0.5, both up to the 120th cycle. For the machining pitch of 2 mm, the contact stiffness increased from 2.5 to 8 GPa/μm and the friction coefficient from 0.35 to 0.41 by the 20th to 30th cycle, after that they remained almost constant.



(a) Machining pitch: 1 mm, Initial combined roughness: 4.3 μm



(b) Machining pitch: 2 mm, Initial combined roughness: 3.5 μm

Fig. 8-5 Relationship between mean contact stiffness and traction coefficient. (FSR at RTRI)

Figure 8-6 shows the relationship between (normal) mean contact stiffness and friction coefficient during cycles. For both machining pitches 1 and 2 mm, a linear relationship was found between the contact stiffness and the friction coefficient.

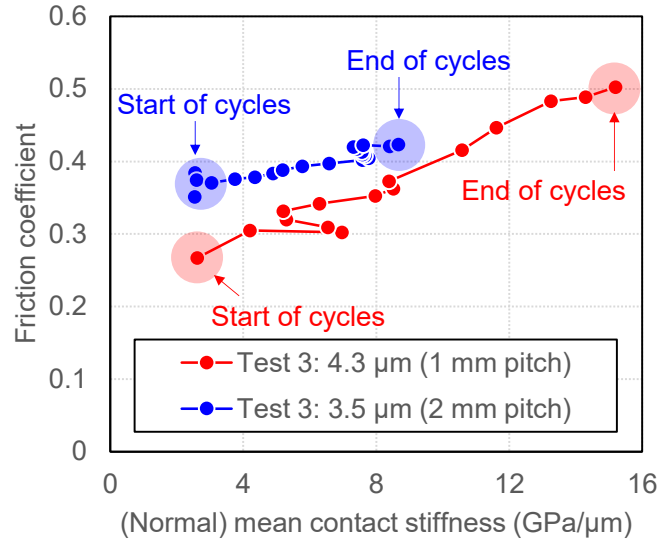


Fig. 8-6 Relationship between (normal) mean contact stiffness and friction coefficient during cycles in the case of FSR at RTRI.

8.2.4 General trend

The results of Test 1, 2 and 3 showed that there is a generally positive correlation between contact stiffness and friction coefficient. During the running-in process of the friction interface, the friction coefficient increases with the number of friction cycles, regardless of the initial roughness, and at the same time the contact stiffness increases. As discussed in more detail in the HPT part of Chapters 4 and 5, the mechanism of the increase seems to depend to some extent on the roughness. In brief, the micro-slip and surface fracture of the interface at lower initial roughness and the macroscopic plastic deformation of the high asperities at higher initial roughness are considered to be the main factors that increase the friction coefficient and contact stiffness, respectively. However, these factors are always mixed, and the impact will likely depend on the initial roughnesses. On the other hand, the reduction in the friction coefficient was attributed to the macroscopic wear of the surface, where the growth of wear particles caused an increase in the surface roughness, which suppressed the contact stiffness and the friction coefficient.

Test 1 was carried out on a small specimen under simplified friction conditions, but showed results for a range of roughness conditions. It is clearly shown that the stepwise differences in initial roughness result in stepwise differences in the running-in process.

Test 2, in which random initial roughness of different sizes was formed on actual wheels and rails, is in general agreement with Test 1, showing the characteristics described above for the smoother and rougher cases respectively. It is very important to note that the rolling-slip condition with full-scale wheels and rails shows the same trend as in the simplified Test 1.

Test 3 is an actual re-profiled wheel and rail test, where the characteristics of the "rougher case" were shown well. It is thought that the contact stiffness and friction coefficient increase with plastic deformation of the machined roughness asperities. The contact stiffness of Test 3 was much higher than that of the other two tests. The reason for this is that the contact pressure is higher in Test 3 than in the other two tests. The friction conditions are also milder because there is no speed difference (slip) between the direction of rotation of the wheel and the longitudinal direction of the rail, which means that there is less surface fracture leading to a decrease in contact stiffness.

8.3 Recommendation to the practical operation

It should be noted in the above results that, for wheel-rail friction, a higher initial roughness did not result in a higher friction coefficient. This is not consistent with the "spike-like" effect, which has been considered as one of the mechanisms to increase the friction coefficient during wheel climb-up derailment. The "spike-like" surface implied an abrasive action, where the friction coefficient increased as the roughness asperities of the wheel plough into the rail. However, the experimental results showed that a lower initial roughness tended to lead to a rather rapid increase in the friction coefficient, with a higher maximum value.

In each of the repeated tests, the friction coefficient tended to increase not just after the start of the test, but after some continuation of the friction test. The results of this thesis also showed that the contact stiffness increases when the friction coefficient increases during the running-in process of the wheel-rail interface. This is thought to be due to the fact the interface is temporarily in a stiffer contact condition, resulting in a higher frictional force.

The running-in operation of machinery and equipment is commonly carried out under lubrication. In this sense, the situation where metal surfaces are conformed without lubrication, as in the case of wheels and rails, is unusual. In particular, it is well known that contact between similar metals can cause strong adhesion [5], so it is advisable to take measures, such as applying lubricant, to conform the contact surfaces as gently as possible.

As described in Section 2.3, the higher the friction coefficient between the wheel flange and the rail gauge corner, the greater the risk of wheel climb-up and derailment. The above contact position is therefore the target for lubrication to prevent derailment. However, it is difficult to predict when the friction coefficient and contact stiffness will increase on an actual vehicle, because the number of times the wheel flange contacts the rail and the condition of the contact depends on the individual vehicle and the route it travels.

On the other hand, there is a report [6] that investigated the change in flange roughness through running a test on a sharp curve using an actual vehicle, and it was reported that

after wheel re-profiling, the roughness decreased (machining marks were deformed) up to about the 5th time through a curve, and then increased after about the 30th time (Figs. 8-7 and 8-8).

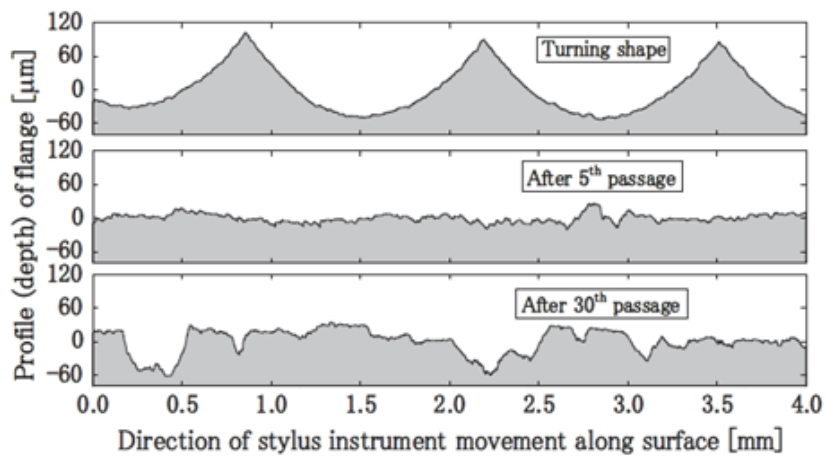


Fig. 8-7 Change of surface profile of the wheel flange with increasing number of passages at a sharp curve after wheel re-profiling. (Machining feed rate: 1.5mm/rev) [6].

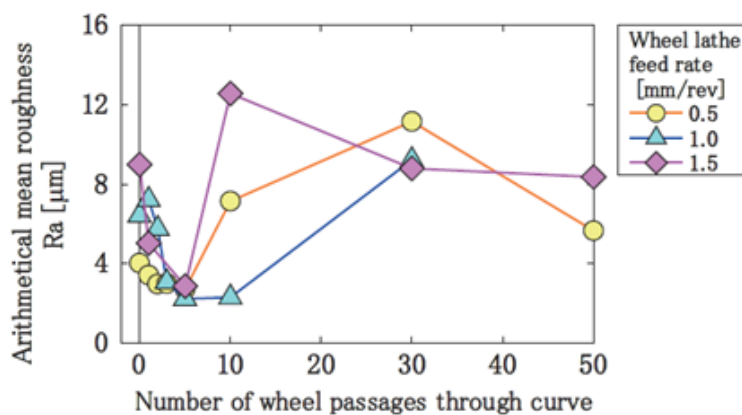


Fig. 8-8 Change of arithmetical mean roughness, Ra, of the wheel flange with increasing number of passages at a sharp curve after wheel re-profiling [6].

This trend is consistent with the changes in contact conditions shown in Tests 1 to 3. Based on the findings of this thesis, it is possible that the contact stiffness and friction coefficient increased at the time when the roughness of the wheel had initially decreased and the asperities disappeared. This suggests that it would be more effective to lubricate the wheel flanges just after wheel re-profiling, as the friction coefficient may increase after wheel re-profiling over a relatively short distance, such as 5 passes through a sharp curve.

References

- [1] S. Fukagai, M. Watson, H. P. Brunskill, A. K. Hunter, M. B. Marshall, and R. Lewis, "In-situ evaluation of a sliding interface with different roughness conditions using ultrasound reflectometry," *Submitt. to Proc. R. Soc. A*, 2021.
- [2] S. Fukagai, M. B. Marshall, and R. Lewis, "Transition of the friction behaviour and interface topography due to repeated high-pressure contact and slide," *To be Submitt.*
- [3] S. Fukagai, H. P. Brunskill, A. K. Hunter, R. S. Dwyer-Joyce, and R. Lewis, "Transitions in rolling-sliding wheel/rail contact condition during running-in," *Tribol. Int.*, vol. 149, no. August 2018, p. 105679, 2020.
- [4] S. Fukagai and R. Lewis, "Traction condition between wheel flange and rail gauge corner during running-in," in *Proceedings of the 15th international conference on railway engineering*, 2019.
- [5] F. P. Bowden and L. Leben, "The nature of sliding and the analysis of friction," *Proc. R. Soc. Lond. A*, vol. 169, pp. 371–391, 1939.
- [6] H. Doi, T. Miyamoto, J. Suzumura, J. Nakahashi, H. Chen, and T. Ban, "Change in Surface Condition of Turned Wheel and Effectiveness of Lubrication Turned against Flange Climb Derailment," *Q. Rep. RTRI*, vol. 53, no. 2, pp. 70–76, 2012.

9 CONCLUSIONS

The aim of this work was reducing the incidence of climb-up derailments and further improving the safety of the railways. The phenomenon of climb-up derailment is thought to occur when the balance of the frictional (adhesive) forces between the wheel flange and the rail - the source of traction on the railway - deviates from a certain range. Considering the tendency of derailments to occur, the balance may also become unstable, especially just after the wheels have been re-profiled. Further basic knowledge of the tribological mechanisms at the wheel-rail interface after wheel re-profiling was needed to improve railway safety. The findings are as follows:

(1) Understanding the friction trend after wheel re-profiling

The twin-disk tests, simulating a freshly machined wheel, revealed how the friction coefficient changes during the running-in period. The running-in curve of the friction coefficient showed a momentary rise and a peak value was observed to decrease with the increase in magnitude of the wheel surface texture. The change of the subsurface hardness and the microstructure were also dependent on the initial surface texture coincidentally and the work-hardening layer of the textured surface was thicker than that of smooth surface.

(2) Evaluating the transition of the slip interface during the running-in using ultrasound reflectometry

The application of ultrasound reflectometry to a slip interface enabled the in-situ evaluation of contact stiffness changes. A contact pressure representative of that in a wheel-rail interface was achieved by using a high-pressure torsion (HPT) test approach. The dynamic change of contact stiffness was found to be dependent on the initial surface topography, indicating that the friction mode can be different. The change of the friction coefficient during the repeated slip test was in general agreement with the trend of the twin-disk tests, and the dynamic evaluation of the contact stiffness provided a more detailed understanding of the interfacial change during the running-in process. The micro-fracture of the surface at low initial roughness and the plastic deformation of the asperities at high initial roughness are considered to be the dominant factors to the running-in.

(3) Applying the evaluation technique using ultrasound reflectometry to the actual wheel-rail interface

Tests with the full-scale rig enabled to understand the changes in the running-in process in the actual wheel-rail contact area. The ultrasound measurement using arrayed probe provided the change of the contact stiffness distribution in the contact area. It revealed how the contact stiffness distribution within the contact area changes with repeated wheel rolling. The change of the mean value of contact stiffness showed the similar trend with HPT tests, and the friction coefficient increased with increasing contact stiffness. In the tests with the re-profiled wheels, it was possible to understand the behaviour of the friction coefficient increasing with the plastic deformation of the machining marks.

(4) Management of the re-profiled wheel

To sum up the above findings, for wheel-rail friction, a higher initial roughness did not result in a higher friction coefficient. This is not consistent with the "spike-like" effect, which has been considered as one of the mechanisms to increase the friction coefficient during wheel climb-up derailment. The "spike-like" surface implied an abrasive action, where the friction coefficient increased as the roughness asperities of the wheel plough into the rail. However, the experimental results showed that a lower initial roughness tended to lead to a rather rapid increase in the friction coefficient, with a higher maximum value. In each of the repeated tests, the friction coefficient tended to increase not just after the start of the test, but after some continuation of the friction test. The results of this thesis also showed that the contact stiffness increases when the friction coefficient increases during the running-in process of the wheel-rail interface. This is thought to be due to the fact that the interface is temporarily in a stiffer contact condition, resulting in a higher frictional force. Therefore, it was thought that the lubrication of the wheel flange just after the wheel re-profiling would be effective in preventing the wheel climb-up derailment, as the friction coefficient could be high when clean metal surfaces are exposed by machining.